Influence of Smart CutTM process' technological steps on the thickness uniformity of SOI wafers: Multi-Scale approach

Pablo E. Acosta-Alba

To cite this version:

Pablo E. Acosta-Alba. Influence of Smart CutTM process' technological steps on the thickness uniformity of SOI wafers: Multi-Scale approach. Materials Science [cond-mat.mtrl-sci]. Université Paul Sabatier - Toulouse III, 2014. English. NNT : . tel-01060076

HAL Id: tel-01060076
https://theses.hal.science/tel-01060076

Submitted on 2 Sep 2014

THÈSE

En vue de l'obtention du

DOCTORAT DE L'UNIVERSITÉ DE TOULOUSE

Délivré par : *l'Université Toulouse 3 Paul Sabatier (UT3 Paul Sabatier)*

Présentée et soutenue le *Date de défense (27/05/2014)* **par :**

Pablo Eduardo ACOSTA ALBA

Influence of Smart Cut™ technological steps on thickness uniformity of *SOI* wafers : Multi-Scale approach

JURY

François Rieutord	CEA-INAC, Grenoble	Rapporteur
Pierre Müller	CiNam, Marseille	Rapporteur
Daniel Alquier	LMP, Tours	Examinateur
Vincent Paillard	CNRS-CEMES, Toulouse	Examinateur
Marc Respaud	LPCNO-INSA, Toulouse	Examinateur
Didier Dutartre	ST Microelectronics, Crolles	Examinateur
Alain Claverie	CNRS-CEMES, Toulouse	Directeur de thèse
Oleg Kononchuk	SOITEC, Bernin	Co-directeur de thèse

École doctorale et spécialité :

SDM : Nano-physique, nano-composants, nano-mesures - COP 00

Unité de Recherche :

CEMES/CNRS UPR 8011

Anyone who has never made a mistake has never tried anything new.

Albert Einstein

Remerciements

Ce travail de recherche a été réalisé dans le cadre d'une collaboration entre la société Soitec à Grenoble et le laboratoire CEMES-CNRS (Centre d'Elaboration de Matériaux et d'Etudes Structurales) à Toulouse et ce grâce à une convention CIFRE.

Je tiens donc à remercier d'une part, Carlos Mazuré de m'avoir accueilli au sein du service R&D de Soitec et d'autre part, Alain Claverie de m'avoir accueilli au CEMES-CNRS.

Je voudrais également remercier Daniel Alquier, Vincent Paillard, Marc Respaud et Didier Dutartre d'avoir examiné mon travail de thèse. Je suis aussi très reconnaissant et honoré que François Rieutord et Pierre Müller aient accepté d'être rapporteurs de ce manuscrit et je les remercie très sincèrement.

Au-delà d'être directeur de mon laboratoire d'accueil, Alain Claverie a été mon directeur de thèse. Malgré la distance il a toujours été disponible pour me guider, me conseiller et m'aider. Il a été particulièrement présent lors de la rédaction de ce manuscrit, et je tiens à lui présenter mes remerciements le plus sincères pour avoir veiller à la précision et à la clarté de chacun de chapitres.

Je voudrais aussi remercier Oleg Konunchuck, qui a encadré ce travail au sein de Soitec. Il a toujours su assurer la qualité scientifique de mon travail grâce à son expérience et à sa rigueur. En me laissant une très grande autonomie, il m'a aussi poussé à avoir un investissement total dans mon projet. En plus d'apprendre à diriger un projet, ceci m'a permis de développer ma confiance en moi.

Je voudrais remercier très amicalement Christophe Gourdel (*Ernesto, el ché*) et Alexandre Barthelemy (*Rodrigo*), qui en plus de m'avoir toujours aidé dans la compréhension scientifique des problèmes qui se sont présenté à moi, sont devenu de vrais amis au cours de ces trois dernières années. En plus, Christophe m'a entrainé à la découverte des plus beaux sommets que j'ai pu rencontrer jusqu'à là. Merci les cuculés !

Merci à Etienne Navarro d'avoir partagé avec moi les moments de détente ainsi que les galères et d'avoir été toujours disponible pour un conseil, une séance d'escalade ou tout simplement pour aller boire une bière en terrasse et discuter de nos thèses respectives.

Je tiens à remercier Didier Landru, qui en plus d'amener toujours de la bonne humeur au service de R&D, m'a fait découvrir le canyoning. Grâce à lui j'ai peut-être été le premier latino-américain à avoir enchainé 5 canyons corses en 4 jours!

Merci à Ionut R., Christophe F., Fabrice L., Grégory R., Yves-Mathieu L., William V., Laurent G., Daniel D. ainsi que toutes les personnes faisant partie du service R&D de Soitec. Merci également à Raphaël Meyer et Guillaume Besnard pour leur bonne humeur et pour avoir été toujours disponibles pour me dépanner avec des articles, je vous souhaite beaucoup de réussite et bon courage pour la suite. J'ai passé trois agréables années à travailler à vos cotés.

Je suis aussi très reconnaissant envers tous ceux qui ont contribué au bon déroulement de mes manips... Merci à Sébastien Mougel, Elodie Douguet, Cécile Moulin, Christelle Bertrand, Alexandre Chibko et toutes les autres personnes de Soitec qui m'ont aidé à la préparation de plaques !! Merci également à Catherine Euvrard-colnat, Maurice Rivoire et Aurelien Seignard du CEA-LETI, d'avoir voulu étudier avec moi l'impact de la *CMP* sur un bon nombre de plaques.

Je voudrais aussi remercier chaleureusement Nikolay Cherkashin, Grégory Seine, Robin Cours, Catherine Crestou, Dominique Lamirault, Jesse Groenen et toutes les autres personnes avec qui j'ai pu travailler pendant mes déplacements au CEMES pour leur aide, leur accueilli et leur soutien.

Je suis profondément reconnaissant à Laetitia Zavattoni, tu m'as accompagné et supporté pendant les moments difficiles de la rédaction. Tes innombrables relectures et tes bons conseilles pour rendre le texte et la présentation plus clairs ont été d'une grande aide. Merci!

Finalement, je voudrais remercier ma famille. Ivonne, gracias por tu apoyo y tus consejos, gracias también por mostrarme el camino, seguir tus pasos ha sido siempre una fuente de inspiración y de orgullo. Sin el apoyo incondicional de mi familia jamás habría podido emprender nuevos retos como el de esta tesis. Gracias a mi mama, a mis hermanas y a Laeti, por su ayuda en los últimos momentos antes de la defensa, las ultimas repeticiones, los preparativos y sobretodo regular mi estado de ánimo!

Contents

Introduction

The eagerness for improvement of performance in the microelectronic industry through miniaturization of components, has considerably encouraged extensive research in the field of manufacturing techniques. Nowadays, Fully-Depleted Silicon-On-Insulator (FD-SOI) wafers provide a very promising path for the next generations of *CMOS* architecture. A FD-SOI wafer consists of an ultrathin ($\sim 10\,nm$) silicon layer sitting on top of a buried oxide layer itself on a thick ($\sim 750\,\mu m$) silicon «*handle*» wafer. Physical characteristics of FD-SOI provide important benefits for low power consumption and high performance applications. Indeed, transistors processed on extremely thin SOI substrates demonstrate several advantages compared to those fabricated by the classical «bulk technology». Furthermore, devices can continue to be scaled without radically changing the transistor architecture [1,2]. Besides, they are not subjected to random dopant fluctuation in the channel which has historically been the major contributor to the threshold voltage variability.

However, the thickness variations of the top silicon layer can introduce additional variability of the threshold voltage of a single transistor. Additionally, the matching of this voltage for different transistors on the wafer depends on the thickness uniformity of the silicon film across the wafer as well as on the transistors spacing and size [3,4]. Thus, the capability to control and improve the thickness uniformity of the top silicon layer and its characterization over a wide spatial bandwidth, from single transistor to the whole wafer scales [$10\,nm$ - $300\,mm$] are major issues for the future of FD-SOI technology.

The purpose of this thesis is twofold, on the one hand, we seek to develop the metrological machinery allowing the multi-scale surface characterization over the whole spatial bandwidth of interest and, on the other hand, we apply the developed methodology to investigate the impact on the thickness uniformity of the technological steps involved in the SOI manufacturing.

Among the SOI fabrication techniques, the most mature and the widest used is the Smart Cut™ technology. Actually, this process can be used for the transfer of a thin crystalline layer of few tens of nanometers up to few micrometers from a «*donor*» wafer onto a new *handle* substrate. This is particularly advantageous when a thin monocrystalline layer is required onto a substrate which does not allow epitaxy of this layer.

The Smart Cut™ process can be seen as the combination of several technological steps as described hereafter. In general, the silicon *donor* wafer is thermally oxidized so as to provide the future buried oxide layer. Then, light ions are implanted on the *donor* wafer through the oxide layer already grown on the wafer. Ion implantation induces the formation of an in-depth weakened layer. Afterwards, the *donor* and the *handle* wafers are cleaned and bonded together by direct wafer bonding. Once the wafers are bonded together, a thermal annealing is performed. The thermal evolution of the implantation induced defects results in the fracture of the *donor* wafer allowing the effective transfer of the thin layer on the insulating layer (buried oxide). The thickness of the transferred layer is then adjusted by a sacrificial oxidation followed by the dissolution of the grown oxide layer. Finally, the surface topography of the transferred layer is improved by thermal treatment or by polishing the surface. Figure 1 shows a schematic illustration of the basic process flow composing the Smart Cut™ technology.

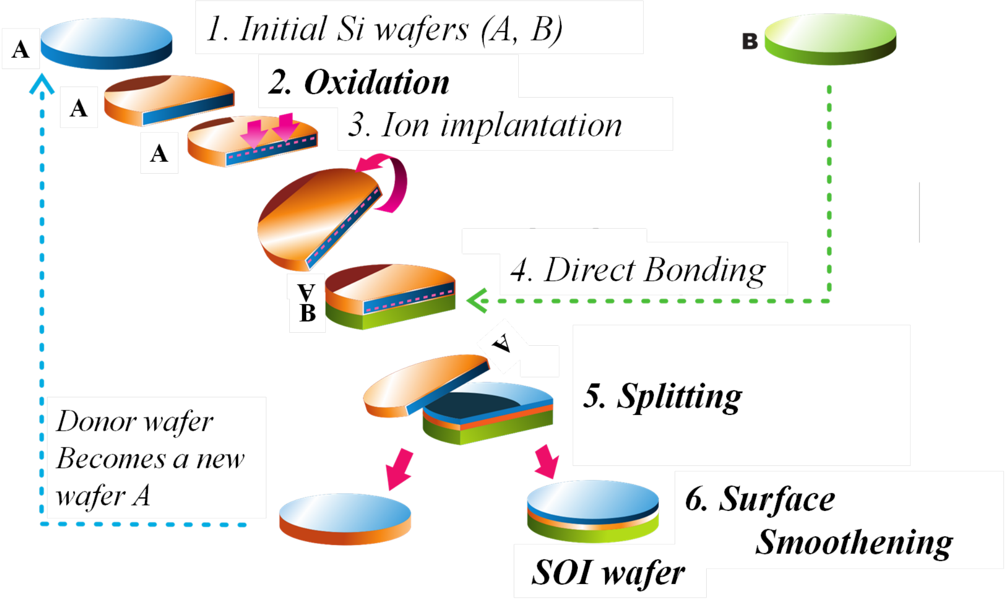

Fig. 1: Basic processing flow of the Smart Cut™ technology.

In chapter 1, we firstly discuss the origin of thickness variations and its relation with the topography of the boundary interfaces which delimit the top silicon layer. After an overview of different metrology techniques allowing the characterization of thickness and roughness, we present a new data processing method, based on the use of the Power Spectral Density (PSD) function, to describe both roughness and thickness variations over a wide spatial bandwidth. Then, we describe some improvements performed to complement the panoply of the metrology techniques.

Then, based on the characterization techniques presented in this first chapter, we investigate the impact, on the thickness uniformity, of the principal technological steps involved in the SOI manufacturing by Smart Cut™ process.

In chapter 2, we review the state of the art of the fundamental understanding of the splitting process. We tend to present the principal proposed scenarii, based on fundamental physics, describing the thermal evolution of the implantation induced defects. From the generation of ion implantation induced defects at room temperature to the fracture propagation leading to the splitting. Then, we study the impact of the implantation conditions on the topography of post-splitting surfaces. We will focus on the relationship between the post-splitting topography and the thermal evolution of implantation induced defects.

In chapter 3, we investigate the surface smoothening through high temperature annealing. In this aim, the atomic-scale mechanisms driving thermally activated self-surface diffusion are examined. Indeed, the spectral evolution of surface topography is characterized by AFM and quantified by means of the *PSD* functions. We propose a predictive model describing the evolution of the surface topography of silicon during thermal annealing as a function of time and temperature. Finally, after discussing the limitations of this smoothening technique, we presented a simulation code allowing to predict the surface evolution for any thermal budget.

In chapter 4 we investigate the evolution of the thickness uniformity and the surface roughness during thermal oxidation. We present experimental results on dry and wet oxidations. We also consider the impact of the initial morphology of the oxidized surface on the oxidation process.

Finally, in chapter 5 we consider the impact of chemical-mechanical polishing on the thickness uniformity and on the surface roughness. We study experimental parameters, such as the nature of the slurry and the initial surface topography. We also consider the impact of the presence of the implantation induced damage zone on the polishing kinetics.

Bibliography

[1] G. K. Celler and S. Cristoloveanu, “Frontiers of silicon-on-insulator,” *Journal of Applied Physics*, vol. 93, no. 9, pp. 4955–4978, 2003. (cited in pages 1 and 5)

[2] O. Faynot, F. Andrieu, O. Weber, C. Fenouillet-Beranger, *et al.*, “Planar fully depleted soi technology: A powerful architecture for the 20 nm node and beyond,” in *Electron Devices Meeting (IEDM), 2010 IEEE International*, pp. 321–324, 2010. (cited in pages 1 and 5)

[3] O. Weber, O. Faynot, F. Andrieu, C. Buj-Dufournet, *et al.*, “High immunity to threshold voltage variability in undoped ultra-thin FDSOI MOSFETs and its physical understanding,” in *Electron Devices Meeting, 2008. IEDM 2008. IEEE International*, pp. 1–4, 2008. (cited in pages 1 and 5)

[4] T. Hook, M. Vinet, R. Murphy, S. Ponoth, and L. Grenouillet, “Transistor matching and silicon thickness variation in ETSOI technology,” in *Electron Devices Meeting (IEDM), 2011 IEEE International*, pp. 571–574, 2011. (cited in pages 1 and 5)

1 | On the Multi-scale Characterization of Thin Films

Contents

Transistors processed on extremely thin SOI substrates demonstrate several advantages compared to those fabricated by the classical «bulk technology» [1,2]. Besides, they are not subject to random dopant fluctuation in the channel which has historically been the major contributor to the threshold voltage (V_{th}) variability. However, the non-uniformity of the SOI film thickness can introduce additional V_{th} transistor variability depending on transistor sizes and distances between them [3,4]. Thus, the characterization of thickness variations of the top silicon layer over a wide spatial bandwidth [$10\,nm$ - $300\,mm$] is a key issue for the future of FD-SOI technology.

The thickness of a layer is equal to the distance separating the two interfaces which define the boundaries of a layer. In general, thickness variations of the layer can be described by the surface topography of only one of its boundary interfaces if one of them is much rougher than the other. The roughness of a surface is most commonly quantified through its Root-Mean-Square (RMS) value. This value describes the surface variations regardless of the surface area and the sampling frequency [5–7]. Besides, the Power Spectral Density function (PSD) provides a complete statistical description of the surface since it represents a frequency decomposition of the power of a signal [8–11]. Thus, it is more suitable for multi-scale characterization by different measurement techniques. In the past, Samyn *et* *al.* [9] compared non-contact profilometry (NCP) and Atomic Force Microscopy (AFM) measurements to evaluate the roughness of paper coatings in the $[1\,nm$ - $1\,mm]$ spatial bandwidth. Yoshinobu *et al.* [10] studied the scaling behavior of the Si/SiO_2 interface roughness while Kaznatcheev *et al.* [11] characterized the roughness of optical surfaces from the macroscopic to the microscopic scales using optical interferometry at visible wavelengths and AFM measurements. The formalism of the PSD function is a mathematical tool which is not restricted to the assessment of roughness. However, the application of the PSD function formalism to the multi-scale characterization of the thickness of thin layers has not been reported up to now.

In this chapter we will firstly define thickness characteristics from the topography of the boundary interfaces which delimit the top silicon layer. We will review the different metrology techniques which permit the characterization of thickness and roughness. After that, we will propose a new data processing method able to describe both roughness and thickness variations of thin layers over a wide spatial bandwidth. Then, some metrology improvements developed during this thesis will be described. Finally, this characterization methodology will be applied to the study of the topography and thickness variations of SOI wafers fabricated using the Smart Cut™ process.

1.1 | Introduction

1.1.1 | Definitions of thickness and topography

In the case of SOI wafers, the thickness of the top silicon layer is defined by the distance between the top surface (Si/air interface) and the buried oxide (BOx) surface (Si/SiO_2 interface) (see Fig. 1.1).

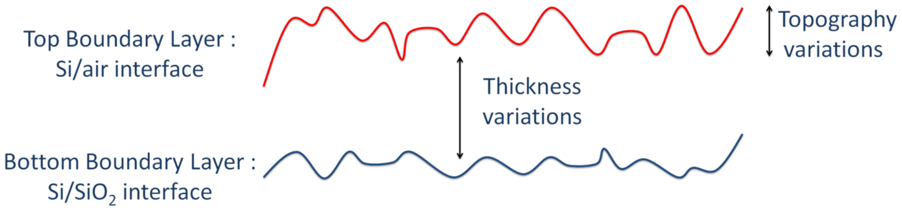

Fig. 1.1: Schematic illustration describing the definition of the thickness of a thin layer.

Hence, in order to measure the thickness of a layer, one can follow two different approaches; the first one consists in directly measuring the distance between the two interfaces while the second one consists in measuring the topological variations of each interface and then make the subtraction. When the roughness of the top interface is much higher than that of the bottom one, thickness variations of a layer reduces to topological variations. However, when the roughnesses of the two interfaces are of the same order of magnitude, the independent description of the topography of the interfaces is not sufficient and direct thickness measurements are required. (see Fig. 1.2 (b)).

One can then point out two additional cases, i) when the two interfaces are well-correlated and thus thickness variations are significantly smaller than topological variations (see Fig. 1.2 (a)) and ii) when the interfaces are completely uncorrelated and thus topological variations are smaller than thickness variations (see Fig. 1.2 (c)). Whether thickness variations can be investigated through topography measurements or not, thus depends on the correlation between the boundary interfaces of the layer.

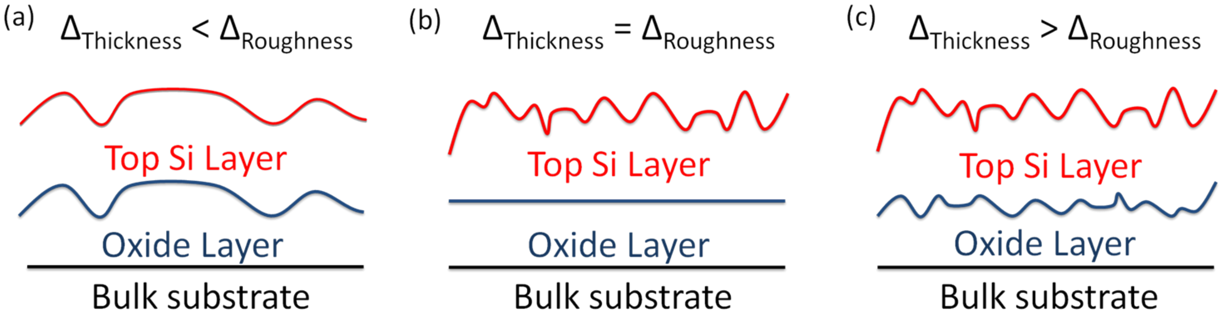

Fig. 1.2: Dependence of the correlation between top and bottom interfaces of silicon layer on the observation scale.

Furthermore, this correlation must be investigated through a large spatial frequency bandwidth, what may not be accessible using only one single experimental technique. In the following, we will define the different concepts necessary to quantify topographic variations of a surface.

1.1.2 | Mathematical background

Topographical variations refer to the deviations of the surface from planarity. Depending on their spatial frequency, these deviations can be arbitrarily classified into roughness, waviness, and form [12]. Waviness is generally associated to variations with horizontal spacings of the order of $1\,mm$ to $10\,mm$. Surface deviations with smaller spacings are attributed to roughness, while form is used to describe surface height variations on much larger lateral scales (see Fig.1.3).

In this work, the term roughness will refer to all these topographical variations. In general, roughness is quantified through a statistical approach using parameters such as, the average height variations of the surface (Ra), the equivalent root-mean-square (RMS) and the skewness (Sk). Nevertheless, these parameters only refer to the vertical variations and thus horizontal information relevant of spatial positions lacks. In order to analyze surface features from a multi-scale point of view, it is necessary to include position, *i.e.*, horizontal

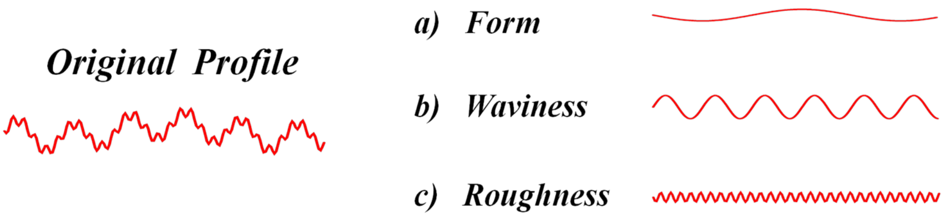

Fig. 1.3: Definition of roughness, waviness and form of a surface.

information. Two different approaches can be used. On the one hand, the spectral approach which uses the *PSD* function, and thus characterizes the roughness through its spatial wavelength components and its auto-correlation function. On the other hand, the fractal approach which characterizes the «geometric irregularity» of surfaces. Let us now present the mathematical machinery used to describe roughness characteristics along these three approaches.

1.1.2.1 The statistical approach

A surface can be described by a height function $(h(x, y))$ which represents the height deviations with respect to the surface mean line at every (x, y) point. This function can be recorded in a continuous $(h_c(x, y))$ or discretized $(h_d(x, y))$ way. From this function we can define several parameters.

Average deviation ($\boldsymbol{Ra}$): For continuous profiles, *Ra* is given by the following equation,

$$Ra = \frac{1}{L_x L_y} \int\limits_{-L_x/2}^{L_x/2} \int\limits_{-L_y/2}^{L_y/2} |h_c(x, y)| \, dx \, dy \tag{1.1}$$

where L_x and L_y are the transverse lengths over two horizontal directions. If the profile is discrete, (Eq. 1.1) rewrites,

$$Ra = \frac{1}{N_x N_y} \sum_{i=1}^{N_x} \sum_{j=1}^{N_y} |(h_d)_{ij}| \tag{1.2}$$

where, N_x and N_y now represent the number of points in the profile (one dimensional case) or in the area (two dimensional case), and h_{ij} is the height deviation at the surface point (i, j) with respect to surface mean *line* .

Root-Mean Square ($\boldsymbol{RMS}$): The *RMS* surface roughness describes the fluctuations of the surface heights around an average surface height and for a continuous profile is defined as,

$$RMS = \sqrt{\int\limits_{-L_x/2}^{L_x/2} \int\limits_{-L_y/2}^{L_y/2} \left|h_c^2(x,y)\right| \, dx \, dy} \tag{1.3}$$

The *RMS* can also be defined as the standard deviation of a discretized height function regardless of the spatial distribution of variations and of the sampling frequency. For a discrete profile (Eq. 1.3) rewrites,

$$RMS = \sqrt{\frac{1}{N_x N_y} \sum_{i=1}^{N_x} \sum_{j=1}^{N_y} \left|(h_d)_{ij}^2\right|} \tag{1.4}$$

Despite the usefulness of the information provided by these two parameters, one must realize that two very different surfaces can have the same *Ra* and *RMS* couple. Further refined quantification are thus required, and it may be improved by using the skewness of the distribution.

Skewness (*Sk*): The *Sk* is classically used to describe the «asymmetry» of a function. Here, on a surface positive values of skewness indicate smooth surfaces dominated by hills, whereas negative values generally account for a majority of holes. The skewness is defined by,

$$Sk = \sqrt{\int\limits_{-L_x/2}^{L_x/2} \int\limits_{-L_y/2}^{L_y/2} \left|h_c^3(x,y)\right| \, dx \, dy} \tag{1.5}$$

which again, for a discrete function rewrites,

$$Sk = \frac{1}{RMS^3} \frac{1}{N_x N_y} \sum_{i=1}^{N_x} \sum_{j=1}^{N_y} \left|(h_d)_{ij}^3\right| \tag{1.6}$$

More parameters may be used to refine the description of $h(x,y)$ but will not be reviewed in this work.

1.1.2.2 The spectral approach

Two functions are important to characterize the surface while keeping the information on the position of height variations: the auto-correlation and the power spectral density functions.

Auto-correlation function (*ACF*): The *ACF* function describes how accurately one can deduce the height of a point from the knowledge of this height at a first point. It is clear that for non-periodic surfaces, the correlation between two points decreases as the distance between them increases. The correlation length is usually defined as the distance at which the *ACF* reaches an arbitrary fraction of its maximal value (often $1/e$), and is representative of the variations of the surface profile as a function of its position. The *ACF* can be calculated by the following expression [13]:

$$ACF(f) = \frac{1}{x-l}\int_{0}^{x-l} h_r(x)h_r(x+l)\,dx \tag{1.7}$$

In the discrete case, the AFC can be estimated through:

$$AFC(i\Delta_x, j\Delta_y) = \frac{1}{N_x N_y}\sum_{m=1}^{N_x-i}\sum_{n=1}^{N_y-j}(h_d)_{m,n}\times(h_d)_{m+i,n+j} \tag{1.8}$$

where Δ represents the sampling period and N the number of points sampling the height function.

Power spectral density function (*PSD*): The *PSD* function of a two dimensional signal $h(x,y)$ can be expressed by the average of the Fourier Transform magnitude squared, over a large spectral interval (see Eq. 1.9). The *PSD* function may also be calculated as the Fourier Transform of the auto-correlation function.

$$PSD_{2D}(f_x,f_y) = \lim_{L\to\infty}\frac{1}{L_xL_y}\left|\int_{-L_x/2}^{L_x/2}\int_{-L_y/2}^{L_y/2} h(x,y)\exp[-2\pi i(xf_x+yf_y)]\,dx\,dy\right|^2 \tag{1.9}$$

In the discrete case, the *PSD* function can be estimated by the following expression:

$$PSD_{2D}(\frac{i_x}{N_x\Delta_x},\frac{j_y}{N_y\Delta_y}) = \frac{\Delta_x}{N_x}\frac{\Delta_y}{N_y}\left|\sum_{m=1}^{N_x}\sum_{n=1}^{N_y}(z_d)_{m,n}exp\left[2\pi i\left(i_x\frac{m}{N_x}+j_y\frac{n}{N_y}\right)\right]\right|^2 \tag{1.10}$$

The *PSD* function provides a complete statistical description of the surface since it represents a frequency decomposition of the power of a signal [8, 11]. Because of the spectral decomposition of the signal, the *PSD* function is more suitable for multi-scale characterization through the use of different measurement techniques.

Since *PSD* function provides a complete description of the surface, the *RMS* value can be calculated from the *PSD* function by,

$$RMS^2 = \frac{1}{L_xL_y}\sum_{m=1}^{N_x}\sum_{n=1}^{N_y}PSD_{2D}(\frac{i_x}{N_x\Delta_x},\frac{j_y}{N_y\Delta_y}) \tag{1.11}$$

This formula can be used as a cross-check asserting the validity of the *PSD* function calculation by comparing the *RMS* value calculated from equation 1.11 with the value computed directly from the raw height data using the equation 1.4.

1.1.2.3 Fractal characterization and Dynamic scaling

The term «fractal» was introduced by Benoit Mandelbrot in the 70's [14]. It comes from the Latin *fractus*, meaning «broken» or «fractured». The notion of fractal permits to take into account the degree of regularity of the organizational structure related to the characteristics of a physical system [15, 16]. A fundamental characteristic of fractal objects is that their measured metric properties, such as length or area, are related to the scale of measurement. A classical example to illustrate this property is the «length» of a coastline [15, 17].

The principal interest of fractal geometry lies in its ability to describe the irregular or fragmented shape of natural features as well as other complex objects that traditional Euclidean geometry fails to analyze. This characteristic is often expressed by spatial-domain statistical scaling laws and is mainly characterized by the power-law behavior of physical systems. The fractal approach is widely used to analyze surface roughness to study physical phenomena such as: hydrophobicity [18], fracture [19, 20] or growth [21–23].

Scaling exponents: In the case of a ballistic deposition growth process, the value of *Ra* (defined above) increases linearly with time if the deposition rate is constant [23]. A typical plot of the *RMS* value during such a process is shown in figure 1.4.

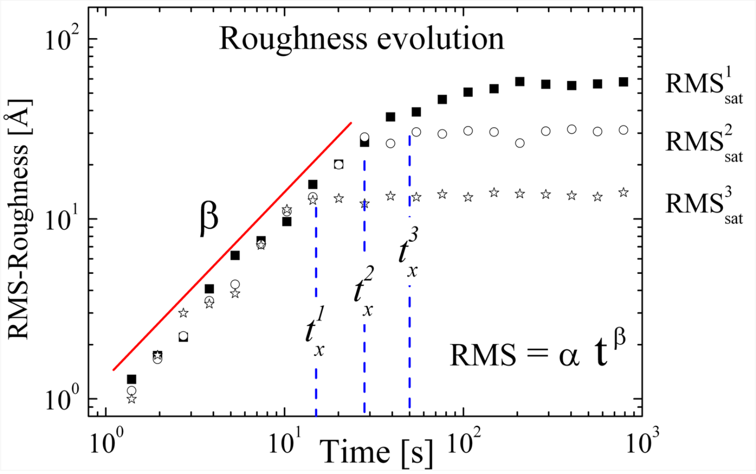

Fig. 1.4: Evolution of the *RMS* value with time in the case of ballistic growth of a interface. One observe two regimes: (a) increase following a power law (straight line in log-log plot) and (b) a saturation after t_x^i.

On the beginning, the *RMS* value increases following the relation,

$$RMS(L,t) \sim t^{\beta} \tag{1.12}$$

The exponent β is named the *growth exponent* and characterizes the time-dependent dynamics of the roughening process during the first stage. This increase of the *RMS* is followed by a saturation regime, which value RMS_{sat} depends on the size of the system [23],

$$RMS_{sat}(L) \sim L^{\alpha} \tag{1.13}$$

where the exponent α is named the *roughness exponent*. Furthermore, the value of t_x, at which the RMS saturates depends on the system size (L) as,

$$t_x(L) \sim L^{z} \tag{1.14}$$

where z is the *dynamic exponent*. From the previous equations, one obtains the *Familiy-Vicsek* scaling relation [23, 24],

$$RMS(L,t) \sim L^{\alpha} f\left(\frac{t^{\beta}}{L^{\alpha}}\right) \tag{1.15}$$

where $f(\frac{t^{\beta}}{L^{\alpha}})$ is called the scaling function and $f(\upsilon) = \upsilon$ when $(t << t_x)$ and $f(\upsilon) = constant$ (when $t >> t_x$). Finally, the continuity of the RMS value implies that $t_x^{\beta} \sim L^{\alpha}$, hence we have,

$$z = \frac{\alpha}{\beta} \tag{1.16}$$

this relation, which links the three scaling exponents, is valid for any growth process that obeys the *Family-Vicsek* scaling relation. These exponents permit the classification of the physical processes which influence the surface evolution through the study of continuum equations. To go further, we recommend reading of the book *Fractal concepts in surface growth* by Barabási *et al.* [23].

Fractal objects can present two principal characteristics: *self-similarity* and *self-affinity*. Self-similar fractals are invariant under isotropic scale transformation, whereas self-affine fractals are invariant under anisotropic transformations. Real surfaces generally belong to the second class of fractals.

Fractal dimension: In order to quantify the fractal character of an object, we have to define its volume. Lets d_E be the smallest Euclidean dimension of the space containing the object. The volume of the object can be defined by $V(l) = N(l)l^{d_E}$, where l^{d_E} is the elementary volume in the d_E-dimensional space. It means that $N(l)$ elementary volumes are needed to cover the considered object. The fractal dimension (d_f) is defined as,

$$d_f = \lim_{l \to 0} \frac{\ln N(l)}{\ln(1/l)} \tag{1.17}$$

d_f can be seen as the quantity which describes the space-filling capacity of an object.

For example, we can consider the *Sierpinski* triangle which is a self-similar fractal. It is built by successive iterations. Lets k be the iteration number. Increasing the size of the dotted box (see Fig. 1.5 ($k = 4$)) by a factor of two, leads to the triangle with $k = 3$. Then, the triangle of generation k can be covered by $N(l) = 3^k$ triangles of linear size $l = (1/2)^k$. Thus, the fractal dimension of the *Sierpinski* triangle is $d_f = \ln(3)/\ln(2) = 1.58$, what is smaller than the Euclidean dimension $d_E = 2$.

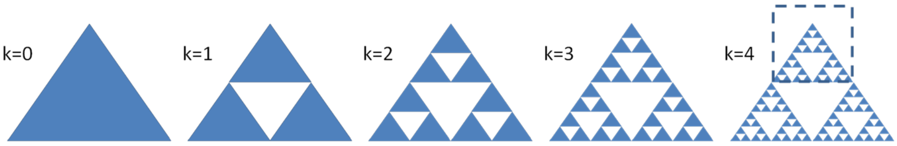

Fig. 1.5: Sierpinski gasket. (k=0) the object construction starts with a filled triangle, (k=1) a triangle whose area is one fourth of the total is removed, (k=2) the procedure is reproduced for the remaining filled triangles, then the procedure is repeated indefinitely.

The scale transformation we described for the *Sierpinski* triangle is isotropic. Real fractal objects must often be rescaled using some anisotropic transformation. The scaling relation of anisotropic fractals is described by single-valued functions called self-affine functions, given by,

$$h(x) \sim b^{-\alpha} h(bx) \tag{1.18}$$

where α is named the self-affine exponent (also called the roughness exponent) and characterizes the «roughness» of the function $h(x)$. Actually, relation 1.18 gives the formal expression of the difference between the horizontal and vertical rescaling of the function. A part of a self-affine object must be expanded vertically by a factor b_v and horizontally by a factor b_h in order to overlap with the entire object. It is thus possible to define the roughness exponent as:

$$\alpha = \frac{b_v}{b_h} \tag{1.19}$$

Let us consider a surface having a fractal dimension of $d_f = 2.5$ (see Fig.1.6 (a)). If we randomly extract a profile from this surface, we obtain a profile with the same fractal properties and a fractal dimension of $d_f = 1.5$. Figure 1.6 (b) shows that by expanding the horizontal and the vertical scales by a factor of 2 and 1 respectively, we obtain a new profile (see inset in the figure 1.6 (b)) similar to the initial profile. Hence, using Eq. 1.19, it is possible to calculate the roughness exponent and one obtains $\alpha = 0.5$. Indeed, Euclidean and fractal dimensions are related by $d_f = d_E - \alpha$.

In case of fractal surfaces, the roughness exponent can also be estimated through the *PSD* function. Indeed, the *PSD* function of a fractal surface can be approximated by a power law given by [23]:

$$PSD_{D_T}(f) = f^{-(2\alpha + D_T)} \tag{1.20}$$

where D_T is the topological dimension, *i.e.*, 1 in case of lines (profiles) and to 2 in case

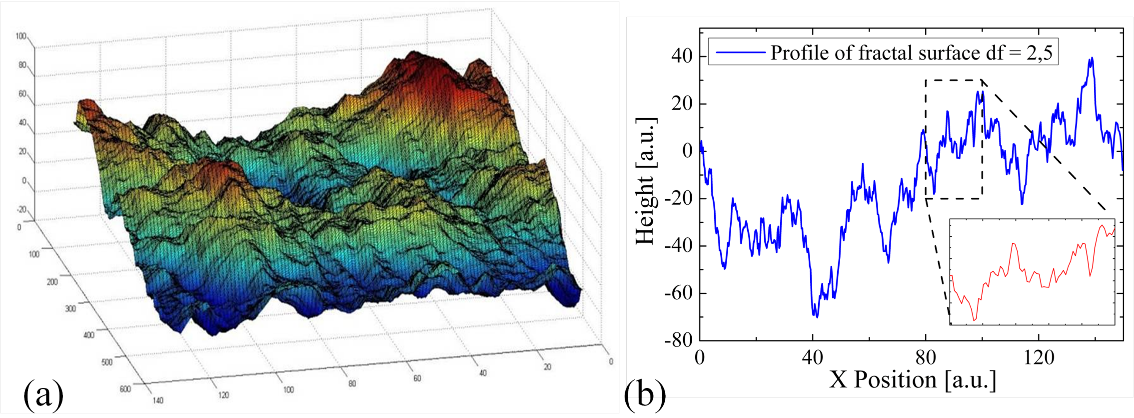

Fig. 1.6: (a) $3D$ representation of a fractal surface of dimension $d_f = 2.5$. (b) Profile extracted from this fractal surface. (inset) Rescaling of the profile using vertically a factor b_v and horizontally a factor b_h.

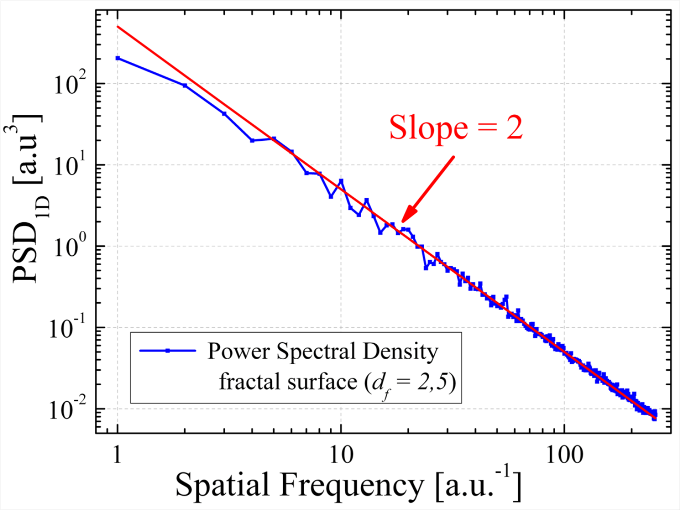

Fig. 1.7: *PSD* function describing the topographic variations of the simulated fractal surface presented in figure 1.6.

of surfaces. If we calculate the *one-dimensional PSD* of $1D$ profiles, the curve one obtains, shown in figure 1.7, can be fitted by a straight line corresponding to equation 1.20 in a log-log plot. In this example, the slope obtained by fitting is $S = -2$. The value of the roughness exponent is $\alpha = 0.5$. In conclusion, the fractal analysis of a surface may be done through the *PSD* function.

1.1.3 | Metrology

Hereafter, we introduce the metrology techniques which we have used to characterize thickness and topological variations of thin silicon layers.

1.1.3.1 Topography measurements

Atomic Force Microscopy (AFM): AFM operates by measuring the force between a probe and the sample [25, 26]. The instrument is composed of a cantilever fixed on one side (fixed end), and with a sharp tip allowing to scan the topography of the surface on the other side (free end). The cantilever is usually made of silicon, silicon oxide or silicon nitride and is typically 100 μm long, 20 μm wide, and 1 μm thick (see Fig. 1.8). The vertical sensitivity depends on the cantilever length. For topographic imaging, the tip is brought into continuous or intermittent contact with the sample and scanned across the sample surface. Depending on the microscope design, piezoelectric scanners translate either the sample under the cantilever or the cantilever over the sample.

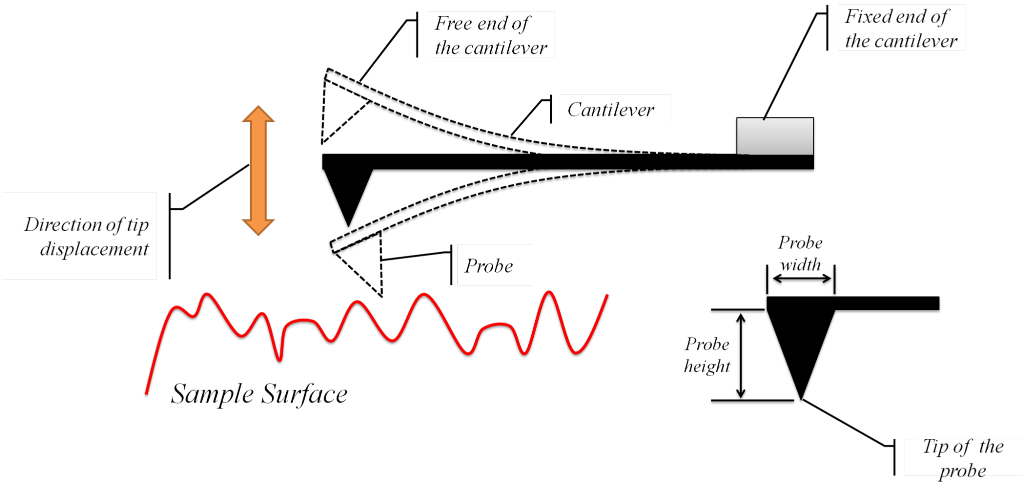

Fig. 1.8: Schematic of the atomic force microscopy.

In this work, only the intermittent contact mode, also called tapping mode, was used. Tapping mode imaging is useful for soft, adhesive, or fragile samples. The cantilever oscillates at, or near to its resonant frequency using a piezoelectric crystal. The oscillating cantilever lightly touches the surface intermittently. By measuring the amplitude reduction due to the tip contacting the surface, it is then possible to identify and measure surface features. The oscillation amplitude of the tip is measured and the feedback loop adjusts the tip-sample distance maintaining a constant amplitude and force on the sample. For a more detailed description of AFM, we suggest to read *Non-Contact Atomic Force Microscopy* by S. Morita [27] and/or the review by F. Giessibl [28].

AFM permits imaging the surface topography of silicon wafers at the micrometric scale with a spatial resolution on the (x, y) plane of few nanometers. Thus, it is possible to characterize the surface topography over areas from few nanometers up to few tens of micrometers. In order to cover a spatial bandwidth as large as possible using standard AFM platforms, we record images with different scan sizes but always with an identical number of points (512×512 pixels). Figure 1.9 shows typical images obtained by AFM on standard SOI wafers.

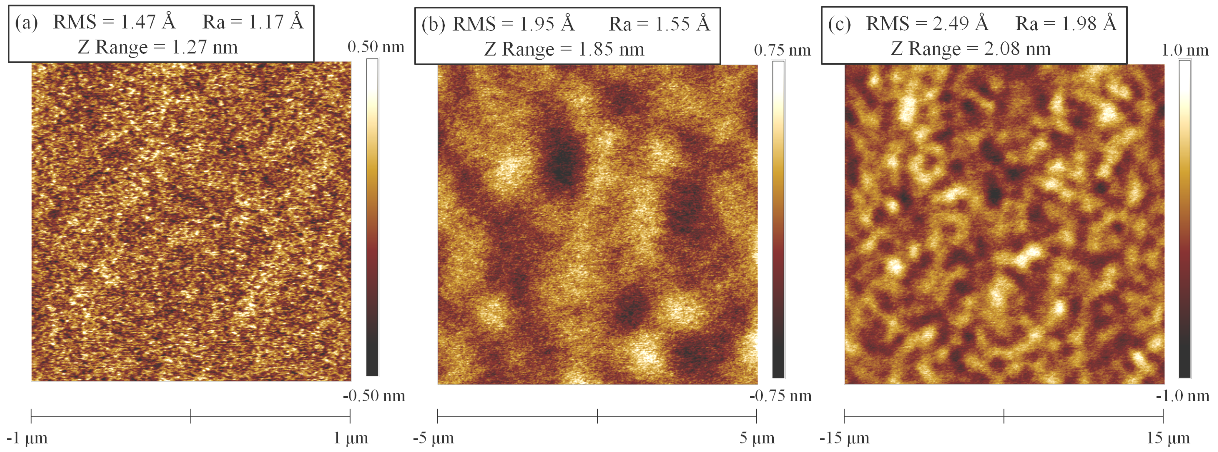

Fig. 1.9: Surface topography recorded by AFM (512×512 pixels). Three different scan sizes are recorded (a)$S_1 = 2 \times 2\,\mu m^2$, (b)$S_2 = 10 \times 10\,\mu m^2$ and (c) $S_3 = 30 \times 30\,\mu m^2$.

According to the Nyquist sampling theorem [29], the spectral bandwidth that can be characterized by AFM is limited by the number of recorded points (N^2) and by the scan size of the image (S) (N is the number of measured points by recorded profile). These spectral limits can be written,

$$f_{min} = \left(\frac{2}{S}\right) \qquad and \qquad f_{max} = \left(\frac{N}{2 \times S}\right) = f_{min}\frac{N}{4} \tag{1.21}$$

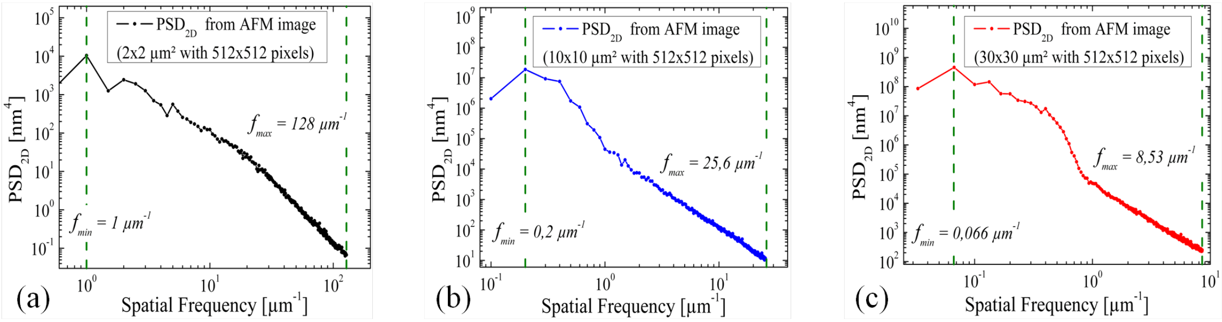

Fig. 1.10: PSD_{2D} functions obtained from AFM images. Three different scan sizes are recorded (a) $S_1 = 2 \times 2\,\mu m^2$, (b) $S_2 = 10 \times 10\,\mu m^2$ and (c) $S_3 = 30 \times 30\,\mu m^2$. Relevant bandwidths are delimited by the vertical dashed lines.

From the recorded AFM images, we can calculate the *PSD* functions corresponding to the spatial bandwidth covered by the images. We have plotted in figure 1.10 the *PSD* functions obtained from the images shown in figure 1.9. The pertinent bandwidth is delimited by the vertical green dashed lines representing f_{min} and f_{max}.

Scanning White Light Interferometry (SWLI): *SWLI* is a contacless technique where quantitative vertical variations of the surface are detected using Phase-Shit Interferometry (PSI). SWLI methods are largely used in the semiconductor industry for measuring engineering surfaces [30].

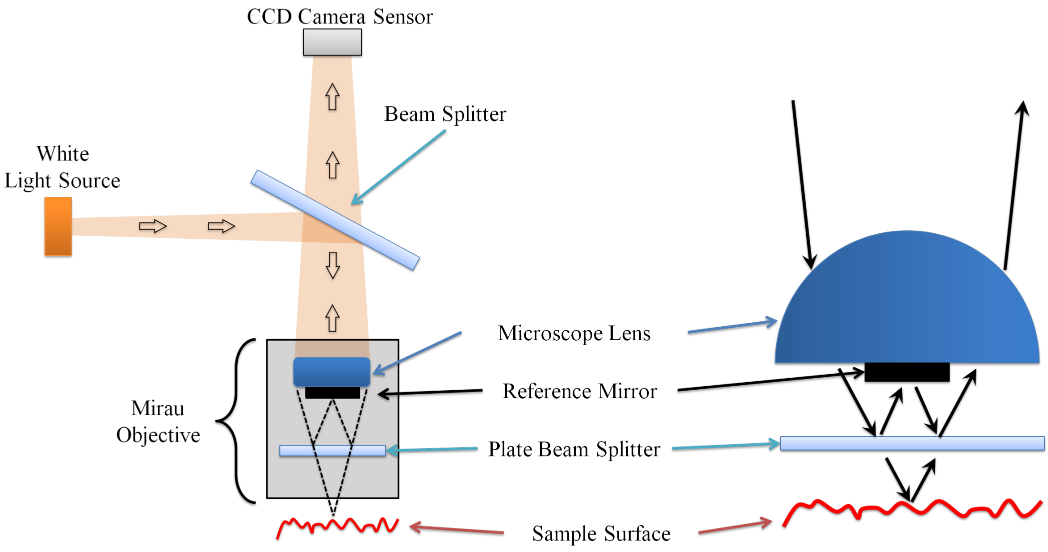

Fig. 1.11: Schematic representation of a Mirau interference microscope.

Interferometric microscopy can be implemented in several ways, one of these is used in the Mirau interference microscope schematically illustrated in figure 1.11. The incident light is splitted in the microscope objective into two different beams. One is transmitted towards the sample surface, and the other one is reflected towards a reference mirror surface. Beams reflected by the sample and the mirror surfaces are combined at the plate beam splitter and interfere. The interferogram resulting from the interaction of these two beams consists of light and dark fringes. These fringes results from the phase shift due to the difference between optical paths of the beam coming from the sample surface and that coming from the reference mirror. The reference mirror, the objective lens, and the beam splitter are attached to a piezoelectric transducer (PZT) translating the reference surface to vary the phase of the reference beam [31]. Phase modulation techniques allow one to analyze the fringes and deduce the height variations of the sample surface. In order to unambiguously determine the height of the sample surface, one combines the results obtained using several wavelengths. Typically, the sample is imaged using a microscope, thus giving a maximum lateral resolution, *i.e.* x and y, of $\sim 0.5\lambda/NA$, where λ is the incident wavelength, and NA is the numerical aperture of the objective. The z resolution, however, is determined by the ability to «interpret» fringes using phase modulation techniques. The vertical resolution is around $1\,nm$ but can be as good as $0.1\,nm$. For further discussion on interference microscopy we recommend reading of the book *Optical Shop Testing* by Malacara [30].

In order to cover a spectral bandwidth as large as possible, the objective is used at

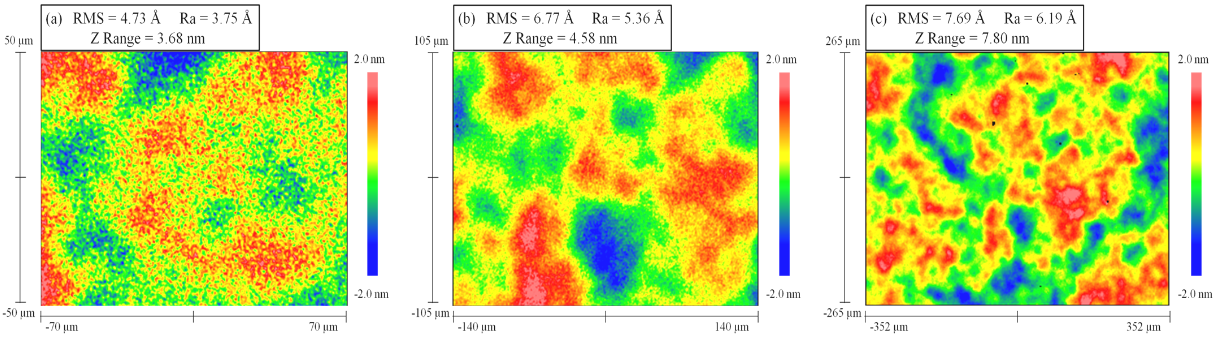

Fig. 1.12: Surface topographies recorded by SWLI (640×480 pixels). Three different magnifications are used (a) $20\times$ corresponding to a image size of $S_1 \sim 700 \times 530\,\mu m^2$, (b) $50\times$ corresponding to a image size of $S_2 \sim 280{\times}210\,\mu m^2$ and (c) $100\times$ corresponding to a image size of $S_3 \sim 140 \times 100\,\mu m^2$.

magnifications of $20\times$, $50\times$ and $100\times$. Typical surface images are shown in figure 1.12. As for AFM measurements, one can calculate the *PSD* functions corresponding to these images using Eq. 1.10. Figure 1.13 shows the one dimensional *PSD* functions obtained from the images shown in figure 1.12.

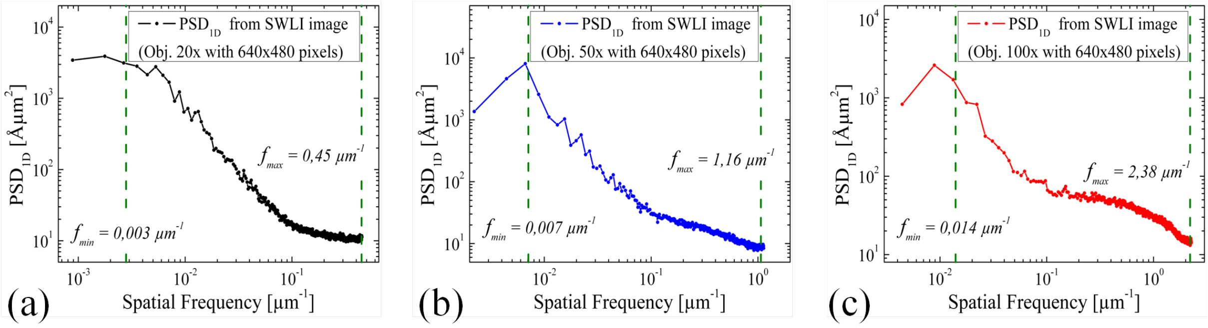

Fig. 1.13: PSD_{1D} functions obtained from SWLI images. PSD_{1D} functions are calculated from images with different sizes (a) $S_1 \sim 700 \times 530\,\mu m^2$, (b) $S_2 \sim 280 \times 210\,\mu m^2$ and (c) $S_3 \sim 140 \times 100\,\mu m^2$. Relevant bandwidths are limited by vertical dashed lines.

However, *SWLI* microscopy presents some limitations. The optical properties of the sample must be known since the interferogram directly depends on the optical thickness of the sample. For example, when very thin or transparent samples are examined, the reflected light used to obtain the interference fringes may comes from the bottom interface of the sample. In the case of SOI wafers, the top silicon layer should be thicker than few hundreds of nanometers. However, coating the surface sample with a reflective material eliminates this problem.

1.1.3.2 Thickness measurements

Spectroscopic Ellipsometry (SE): *SE* is a contact-less, non-invasive technique measuring changes in the polarization state of the light reflected from a surface. It is principally used to deduce the thickness of thin dielectric films on absorbing substrates, their line width, and the optical characteristics of films and substrates [32]. Rather than directly measuring the thickness of films, it measures several optical characteristics from which the thickness and other parameters can be extracted. *SE* measurements have extended the field of application of ellipsometry by using more than one wavelength [33]. Furthermore, it is possible to vary not only the wavelength but also the angle of incidence (φ). This allows non-invasive and real-time process measurements such as layer growth monitoring during MBE [34], and *in situ* diagnostic and process control [35]. *SE* is sensitive to thickness changes of the order of a monolayer. For a more detailed description of this measurement technique we recommend the reading of the book *Ellipsometry and Polarized Light* by Azzam and Bashara [32]. Here, we will limit the discussion to the description of how to use *SE* in order to cover the maximum achievable spatial bandwidth when measuring the thickness of a thin *Si* layer.

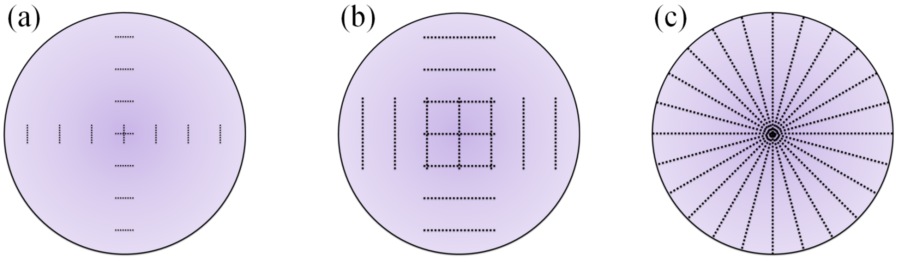

Fig. 1.14: Schematic illustrations showing the location, across the wafer, of points composing profiles for thickness measurements using three different sampling periods (a) $\Delta x_1 = 30\,\mu m$, (b) $\Delta x_2 = 300\,\mu m$ and (c) $\Delta x_3 = 2420\,\mu m$.

In this work, *SE* measurements are carried out using an Aleris™ Rotating Analyzer Ellipsometer (RAE) from KLA-Tencor. The measurement spot size is approximately $30\,\mu m^2$. Then, according to Eq. 1.21 the highest spatial frequency for which thickness variations can be measured by *SE* is $f_{max} \sim 0.015 \mu m^{-1}$. Otherwise, the lowest spatial frequency depends on the number of measured points. It is thus possible to characterize thickness variations over a whole $300\,mm$-in-diameter wafer using a very large number of points. Indeed, to measure the thickness variations of the top silicon layer over a diameter of the SOI wafer, 10000 points separated by $30\,\mu m$ are required. In order to characterize the thickness of the layer over the whole wafer, several profiles along different diameters are required. This approach is thus extremely time consuming.

Actually, to cover a quite similar spatial bandwidth using much less measurement points, we can characterize the thickness variations through profiles using different sampling periods.

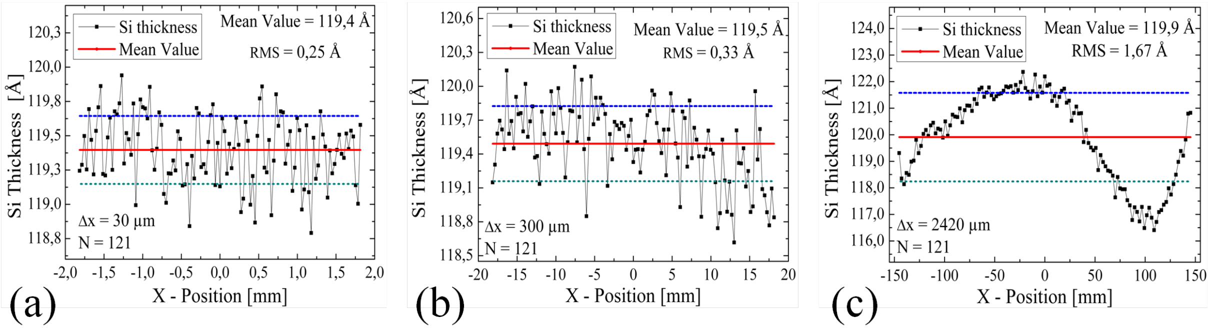

Fig. 1.15: Thickness profiles (composed of $N = 121$ measurement points) measured by *SE* using three different sampling periods: (a) $\Delta x_1 = 30\,\mu m$, (b) $\Delta x_2 = 300\,\mu m$ and (c) $\Delta x_3 = 2420\,\mu m$. The size of the measurement spot is approximately $30 \times 50\,\mu m^2$.

We have set three sampling periods at, $\Delta x_1 = 30\,\mu m$, $\Delta x_2 = 300\,\mu m$ and $\Delta x_3 = 2420\,\mu m$. The number of measurement points per profile has been arbitrary fixed to $N = 121$. To fully describe the thickness variations over $300\,mm$-in-diameter SOI wafers, 14 profiles are recorded for each sampling period (see Fig. 1.14).

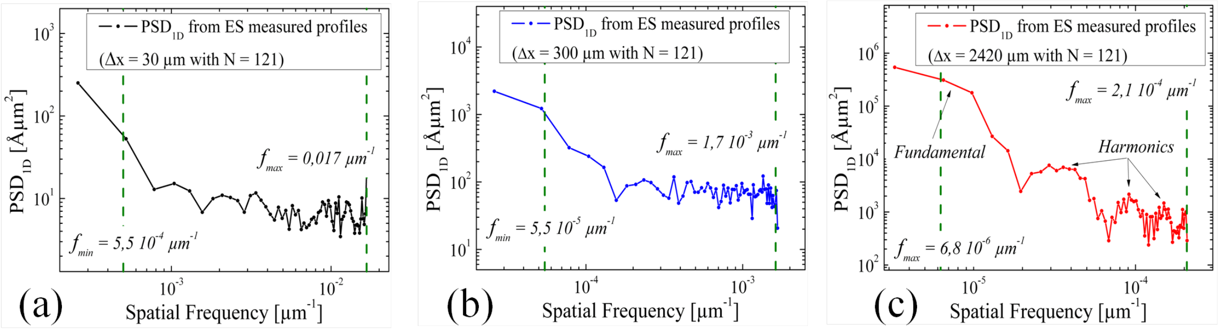

Fig. 1.16: PSD_{1D} functions describing thickness variations of the silicon top layer of a SOI wafer measured by SE. Three different sampling periods are used: (a) $\Delta x_1 = 30\,\mu m$, (b) $\Delta x_2 = 300\,\mu m$ and (c) $\Delta x_3 = 2420\,\mu m$.

Typical experimental profiles obtained by this method, are shown in figure 1.15. Furthermore, we can calculate the *PSD* functions corresponding to each sampling period. Then, the 14 *PSD* functions can be averaged in order to decrease the noise. Figure 1.16 shows the typical *PSD* functions we have obtained on standard SOI wafers. On figure 1.16 (c) we can note three peaks corresponding to harmonics of the fundamental peak located at approximately $7 \times 10^{-6}\,\mu m^{-1}$. These peaks are artifacts introduced by the calculation.

It can be observed in figure 1.17 that *SE* measurements may cover a large spectral bandwidth. The experimental results are consistent with those obtained using a fixed sampling period and a very large number of points. Nevertheless, an offset between the *PSD* functions corresponding to different sampling periods is observed. This offset, is due to differences of sampling periods and the fixed spot size used to make the measurements.

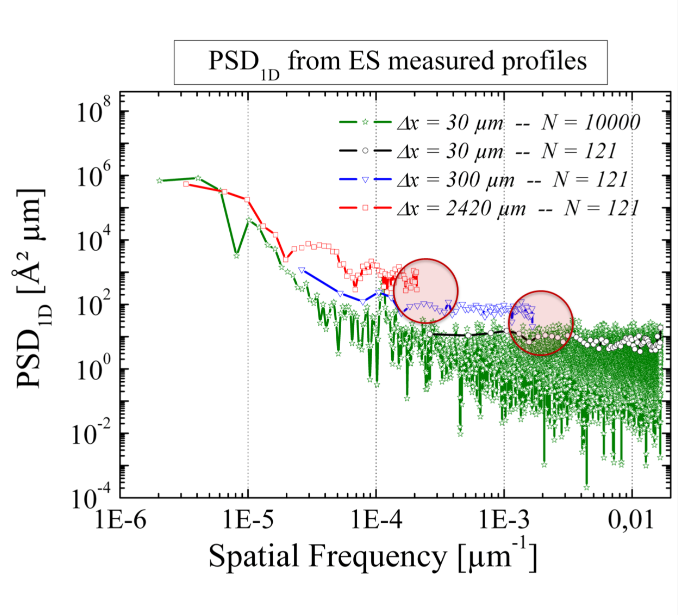

Fig. 1.17: Comparison between PSD_{1D} functions obtained from: *SE* measurement with a fixed sampling period ($\Delta x_1 = 30\,\mu m$) (green line) and using different sampling periods: $\Delta x_3 = 2420\,\mu m$ (red line), $\Delta x_2 = 300\,\mu m$ (blue line) and $\Delta x_1 = 30\,\mu m$ (black line).

Indeed, changing these parameters results in changing the transfer function of the apparatus. In the next section, we will discuss this issue.

1.1.4 | Data processing

The main goal of this section is to introduce a data processing method based on the use of the *PSD* function, allowing the comparison of results obtained from different characterization techniques, each one using different spot sizes and different sampling periods.

In the case of SOI wafers fabricated by Smart Cut™ technology, we can assume that the roughness and thickness variations of the Si top layer are homogeneous and isotropic through the wafers, due to the isotropic nature of involved processes. Hence, surface variations can be characterized by one-dimensional *PSD* (PSD_{1D}) functions. Therefore, we intentionally restrict the following discussion to the calculation of PSD_{1D} from surface profile measurements.

Figure 1.18 shows the case of measurements carried out with the same spot size (S) and different sampling periods (Δx_1 and Δx_2). Note that, in this example, both signals are not continuous since the sampling period is larger than the resolution ($\Delta x > S$).The measured signal, $z_m(k)$, where $k = \Delta x n$ and $n = 1 \ldots N$, can be described by

$$z_m(k) = z_r(x) \otimes \Pi_S \times \Psi_{\Delta x}^{L} \tag{1.22}$$

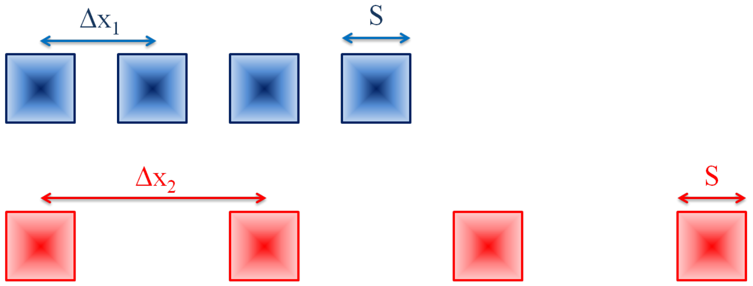

Fig. 1.18: Illustration of two different measurements, where the spot size is fixed to S while the sampling period is different for each measurement ($\Delta x_1 < \Delta x_2$).

where $z_r(x)$ is the real signal, the transfer function can be approximated by Π_S which is a rectangular function whose width has the size of the measurement spot (see Eq. 1.23), $\Psi^L_{\Delta x}$ is a sampling function constructed from Dirac delta functions and whose length is $L = N \times \Delta x$ (N is the number of measured points).

$$\Pi_S = \begin{cases} 0 \, for \, |x| > S/2 \\ \frac{1}{2} \, for \, |x| = S/2 \\ 1 \, for \, |x| < S/2 \end{cases} \tag{1.23}$$

$$\Psi^L_{\Delta x} = \sum_{n=-\frac{N}{2}}^{\frac{N}{2}} \delta_{\Delta x} \tag{1.24}$$

Any other Π_S and $\Psi^L_{\Delta x}$ couples can be considered since they describe the transfer function of the measurement. The PSD_{1D} function is defined by the following expression [36], which corresponds to Eq. 1.9 but for the one-dimensional case,

$$PSD_{1D}(f) = \lim_{L \to \infty} \frac{1}{L} \left| \int_{-L/2}^{L/2} z_r(x) e^{2\pi i f x} \, dx \right|^2 \tag{1.25}$$

Nevertheless, experimental data are generally sampled. In such a case, considering N values of $z_r(x)$ and a sampling period $\Delta x > S$, the PSD_{1D} function can be estimated by Equation 1.26 , where $f_j = j\Delta f$ is the discrete spatial frequency and $j \epsilon N^*, 1 \leq j \leq N/2$.

$$PSD_{1D}(f_j) = \frac{2 \times \Delta x}{N} \left| \sum_{n=1}^{N} z_m(n\Delta x) e^{(2i\pi)jn/N} \right|^2 \tag{1.26}$$

The values of the PSD_{1D} function for negative spatial frequencies are equal to their corresponding values of positive frequencies and do not provide any additional information. Thus, we can doubled the values of the PSD_{1D} function of positive frequencies in Eq. 1.26 to take into account the values corresponding to the negatives frequencies. Moreover, PSD_{1D} is defined over a limited spatial frequency bandwidth given by: $f_{min=2/L}$ and $f_{max=1/(2S)}$. The PSD_{1D} function can be calculated using a standard Fast Fourier Transform (FFT) algorithm, using the following equation,

$$PSD_{1D}(f_j) \sim \frac{\Delta x}{N} \left| FFT(z_{con}(x_k)) \right|^2 \tag{1.27}$$

As explained above, *PSD* function contains all the statistical information of the signal, it can then be related to the *RMS*-Roughness value through,

$$\sigma_{1D}^2 \sim \frac{1}{N} \sum_{n=1}^{N} (z_m(n\Delta x))^2 \tag{1.28}$$

The *RMS*-Roughness value obtained in this way is commonly named the one-dimensional *RMS*-Roughness (σ_{1D}). In order to directly compare *PSD* functions obtained from different signals, it is necessary to built a continuous signal ($z_{cor}(x_k)$) that can be obtained from a discontinuous one by convolution with a rectangular function whose width corresponds to the sampling period,

$$z_{cor}(x_k) = z_m(x_{nk}) \otimes \Pi_{\Delta x}(x_{nk}) \tag{1.29}$$

Which can be rewritten as,

$$Z_{cor}(x_k) = Z_m(x_{nk}) \times FFT\left(\Pi_{\Delta x}(x_{nk})\right) \tag{1.30}$$

and thus,

$$PSD_{1D}^{cor}(f_k) = PSD_{1D}^{m}(f_{nk}) \times \left[sinC(\pi \Delta x\, (f_{nk}))\right]^2 \tag{1.31}$$

Thus, from the PSD_{1D}^{m} function calculated from a discontinuous signal one can calculate a «corrected» PSD_{1D}^{cor} function describing the «equivalent» continuous signal. Actually, the use of different sampling periods allows covering the same spectral bandwidth using a reduced number of data points without losing information (see section 1.1.3).

Figure 1.19 shows the comparison between a PSD_{1D} function obtained from a continuous signal and the corrected PSD_{1D}^{cor} obtained from a discontinuous signal. Again, the bumps between $4\times10^{-5}\,\mu m^{-1}$ and $2\times10^{-4}\,\mu m^{-1}$ on the red curve, are artifacts which should not be taken into account. We can observe that the obtained PSD_{1D} functions overlap and show a good continuity over the whole spectral bandwidth.

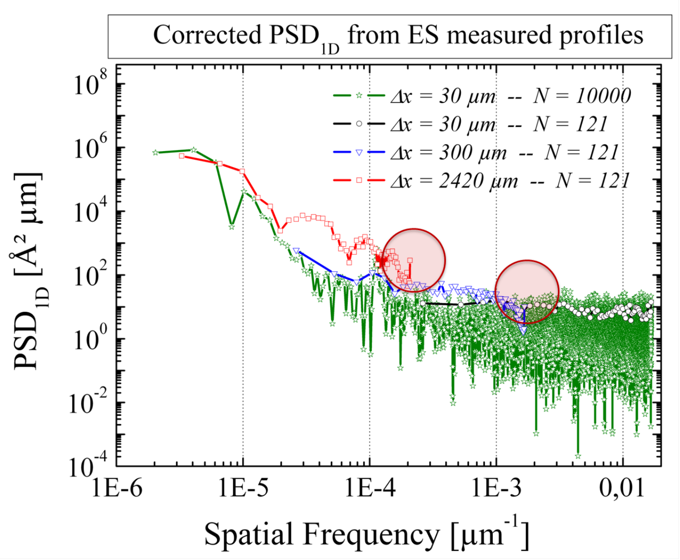

Fig. 1.19: Comparison of raw and corrected *PSD* functions describing SOI film thickness variations measured by ellipsometry. Raw *PSD* is obtained from a continuous signal with 10000 data points (green line). Corrected *PSD* are obtained from a discontinuous signal with 121 data points with a sampling period $\Delta x = 2420\,\mu m$ (red line), $\Delta x = 300\,\mu m$ and (blue line) and $\Delta x = 30\,\mu m$ (black line). The measurement spot size is $S = 30\,\mu m$ for all measures.

1.2 | Experimental methods

1.2.1 | Topography

The roughness of 5 rough SOI wafers was measured using the metrology techniques presented in section 1.1.3. Figure 1.20 shows the *PSD* functions obtained from these measurements.

The overlapping of the *PSD* functions obtained by AFM and SWLI shows the consistency of the experimental results. We can also observe that there is a region in the low spatial frequencies domain [from 7×10^{-6} up to $3\times10^{-2}\mu m^{-1}$] not covered by these techniques. Metrology techniques able, in principle, to cover this spectral domain, such as for example mechanical profilers do not have the required accuracy needed to investigate sub-nanometer variations at this scale.

1.2.2 | Thickness

Thickness variations of the top silicon layer of 5 standard SOI wafers was measured using the *SE* technique (see section 1.1.3).

Typical *PSD* functions describing the thickness variations of the top silicon layers are shown in figure 1.21. Even if this method allows to characterize the thickness over a large spatial bandwidth [from 7×10^{-6} up to $2\times10^{-2}\,\mu m^{-1}$], we can note that the high frequency

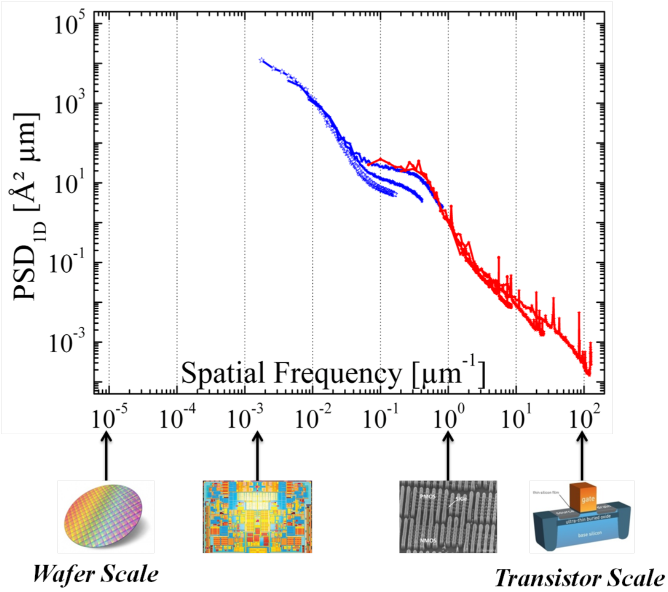

Fig. 1.20: PSD_{1D} functions describing surface topological variations of a SOI wafer which are measured by AFM (red lines) and by SWLI (blue lines). AFM images are recorded with different sizes: $S_1 = 2 \times 2\, \mu m^2$, $S_2 = 10 \times 10\, \mu m^2$ and $S_3 = 30 \times 30\, \mu m^2$. *SWLI* measurement are done using three magnifications: $20\times$, $50\times$ and $100\times$.

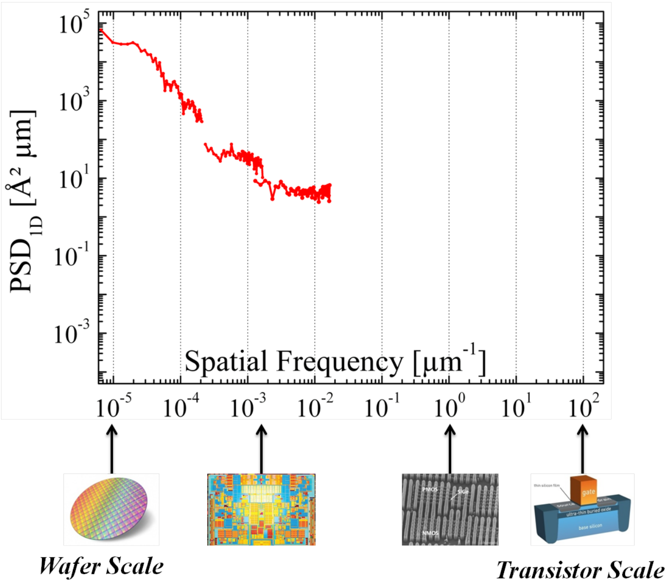

Fig. 1.21: Corrected PSD_{1D} functions describing thickness variation of the silicon top layer of a SOI wafer measured by *SE*. Sampling period used for these measurement are $\Delta x_1 = 30\, \mu m$, $\Delta x_2 = 300\, \mu m$ and $\Delta x_3 = 2420\, \mu m$.

domain is not covered because the spot size of the employed equipment is too large. Actually, the use of *SE* for the thickness characterization is limited by the measurement spot size. In order to describe thickness variations over the high spatial frequency domain, we thus need a technique with higher spatial resolution.

1.2.3 | Metrology developments

It has been demonstrated that conventional metrology techniques do not permit the thickness characterization for spatial frequencies higher than $2\times10^{-2}\,\mu m^{-1}$. Hereafter, we will introduce metrology techniques developed during this work in order to overcome the limitations of the metrology techniques presented above.

1.2.3.1 Thickness measurement by AFM

To study the thickness variations of the top silicon layer in the high spatial frequency domain [from 5×10^{-2} up to $1\times10^{2}\mu m^{-1}$], we have developed a characterization method combining AFM measurements and selective chemical etching. This technique consists in recording AFM images of the topography of the top and the bottom boundary interfaces of the layer and then to extract its thickness variations (see section 1.1) from the height differences.

Actually, after recording an AFM image of the top interface, the silicon layer is removed using a selective chemical etching and then the topography of the bottom interface of the layer is captured by AFM. The silicon film is selectively etched using a potassium hydroxide (KOH) solution (20% concentration) at 60°C. Using these experimental conditions, less than 2 seconds are needed to dissolve the $12\,nm$-thick silicon layer [37,38]. Despite the high selectivity between Si and SiO_2 of the KOH etching (~ 500), it is necessary to verify that this chemical etching does not modify the roughness of the bottom interface of the silicon layer (Si/SiO_2 interface). In other words, it must be verified that SiO_2 is not etched by KOH solution in our experimental conditions. In this aim, an oxidized silicon wafer was put in an etching bath. AFM images of the surface were recorded before and after few seconds of chemical treatment. The PSD functions corresponding to the SiO_2 surface topography before and after the KOH treatment were extracted from these AFM images.

It can be observed in figure 1.22 that the PSD function is not modified by the etching process up to a spatial frequency of approximately $30\,\mu m^{-1}$ meaning that the SiO_2 surface perfectly reflects the roughness of the Si/SiO_2 interface for spatial frequencies lower than that.

In order to accurately estimate the thickness variations of the top silicon layer, it is important to record the AFM images (top et bottom interfaces) of exactly the same area. The alignment of the two images is made with the help of focused ion beam (FIB) marks ($0.2\,\mu m$-wide and $1\,\mu m$-deep holes). Figure 1.23 shows typical images obtained by this method. We can note that FIB marks are not located at the same position in the images.

We have thus developed an image processing code using MatLab®, allowing us to resize and replace the images until they superimpose. The precision of alignment is approximately $0.1\,\mu m$, implying that thickness variations can be correctly estimated for spatial frequencies

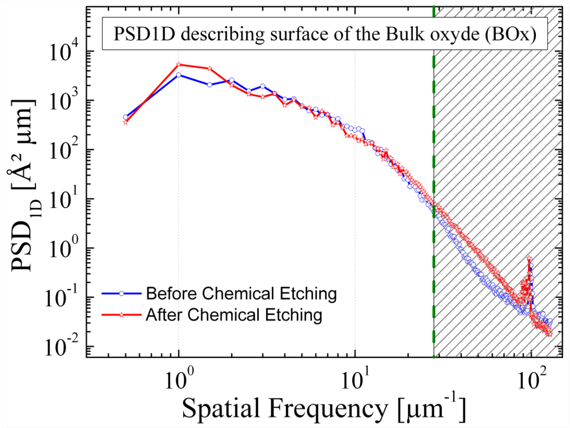

Fig. 1.22: PSD_{1D} functions describing the roughness of the BOx surface before (blue line) and after (red line) KOH etching. Some difference is observed up to a spatial frequency of $28\,\mu m^{-1}$.

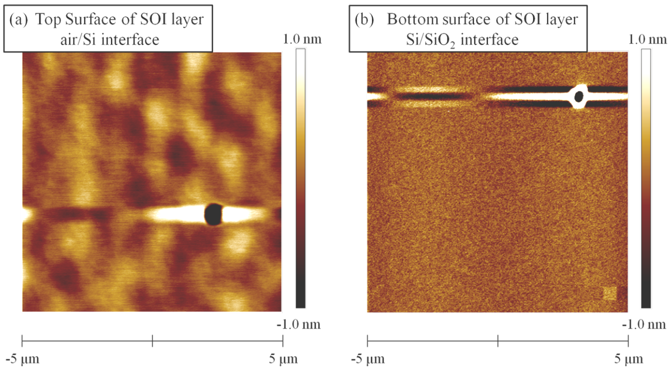

Fig. 1.23: AFM images of (a) top surface of the layer (Si/air interface) and (b) bottom interface of the layer (Si/SiO_2 interface).

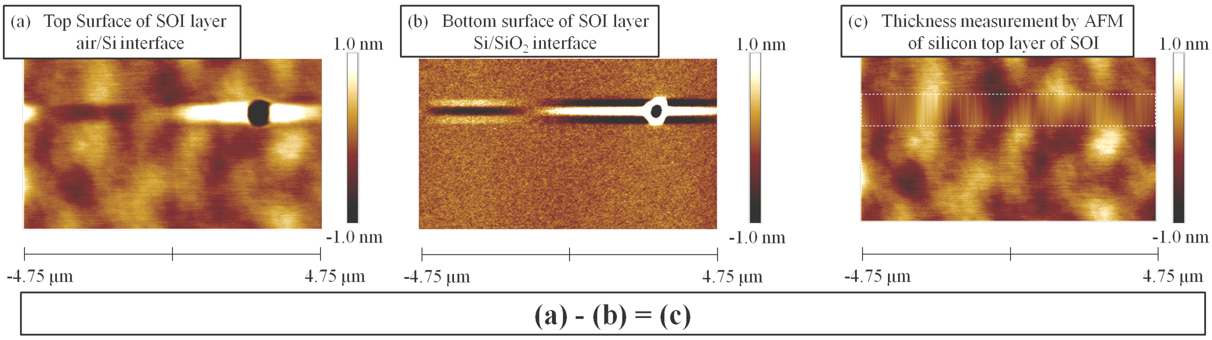

Fig. 1.24: AFM images obtained after resizing and centring of interfaces of the top silicon layer: (a) top and (b) bottom interface. (c) thickness variations image obtained by subtraction of height values.

lower than $10\,\mu m^{-1}$. Values obtained at lower frequencies are considered as noise introduced by the method and must not be taken into account in the analysis. Figure 1.24 shows the images of the top (a) and bottom (b) interfaces after alignment. Thickness variations of the top silicon layer are then extracted by subtracting the height values corresponding to the two images (see Fig. 1.24 (c)).

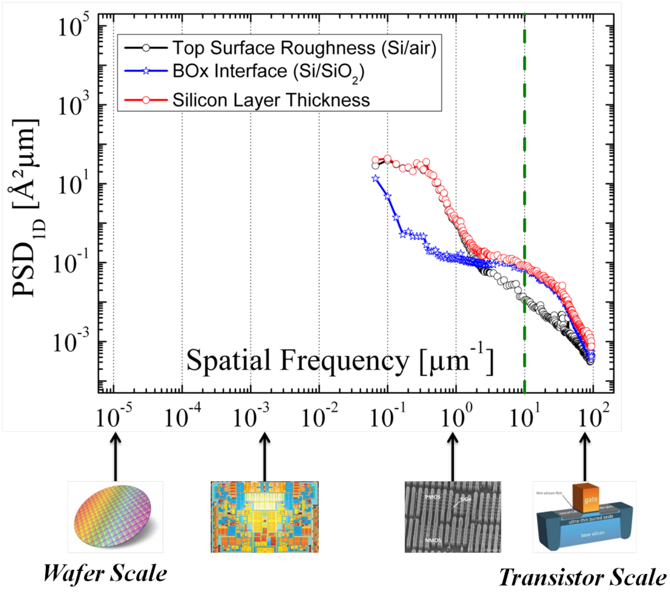

Fig. 1.25: Superimposition of the *PSD* functions describing topological variations of the Si surface (black line) and the Si/SiO_2 interface (blue line) and of the resulting thickness variations measured by AFM (red line).

Finally, the *PSD* function describing the thickness variations over the high spatial frequency domain [from 5×10^{-2} up to 1×10^2 μm^{-1}] can be calculated and is shown in figure 1.25 along with the topological variations of both the top and the bottom interfaces.

1.2.3.2 Differential Reflectance Microscopy

Differential Reflectance Microscopy (DRM) is based on the dependence of the optical reflectivity of a layer on its thickness. This dependence can be calculated using the transfer matrix formalism [39–41]. This method permits thickness measurements with high spatial resolutions [down to $0.5\,\mu m$] corresponding to a standard optical microscope.

In the case of SOI wafers, the situation is not trivial because the reflectivity of the wafer also depends on the thickness of the BOx layer. The transfer matrix formalism must thus handle a two layers stack.

Figure 1.26 (a) shows the reflectivity spectrum of SOI wafers for four different top silicon layer thicknesses (from $11\,nm$ to $14\,nm$) and the same the BOx thickness of $12\,nm$. We note that, for these particular stacks, the sensitivity of the technique is the highest for a wavelength around $500\,nm$. The optimum wavelength of about $515\,nm$ insures that the signals contain information only related to the variations of the thickness of top Si layer (see Fig. 1.26 (b)). Hence, one can obtain a thickness map of the top Si layer by recording a bright field image of the surface of a SOI wafer using an optical microscope equipped with an appropriate interferometric filter.

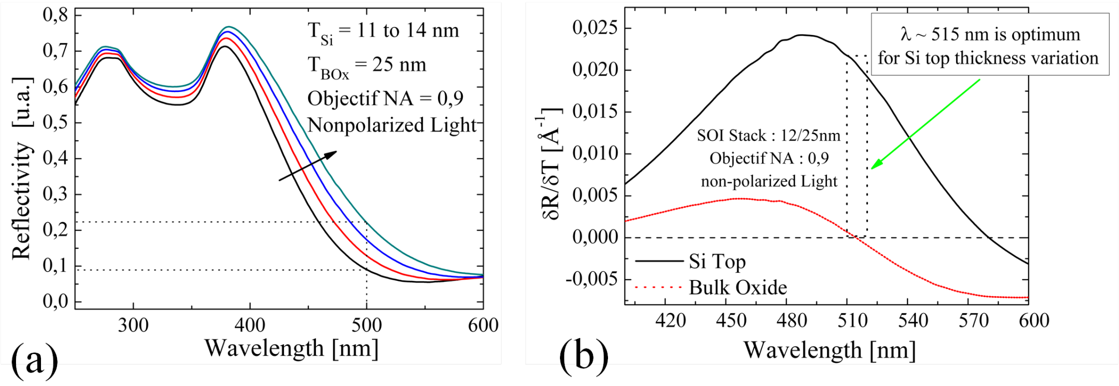

Fig. 1.26: (a) Reflectivity variations for different top silicon layer thicknesses. (b) Sensitivity values obtained for a thickness variation of 1 Å of the top silicon layer (black line) and of the BOx.

The experimental setup used to implement this method consists in a *Zeiss Axiotron 2* optical microscope equipped with a 100× objective ($NA = 0.9$) and with a normal halogen illumination which provides a non-polarized white light. The surface sample is illuminated through an interferometric filter which nominal wavelength is $\lambda = 515 \pm 5\, nm$.

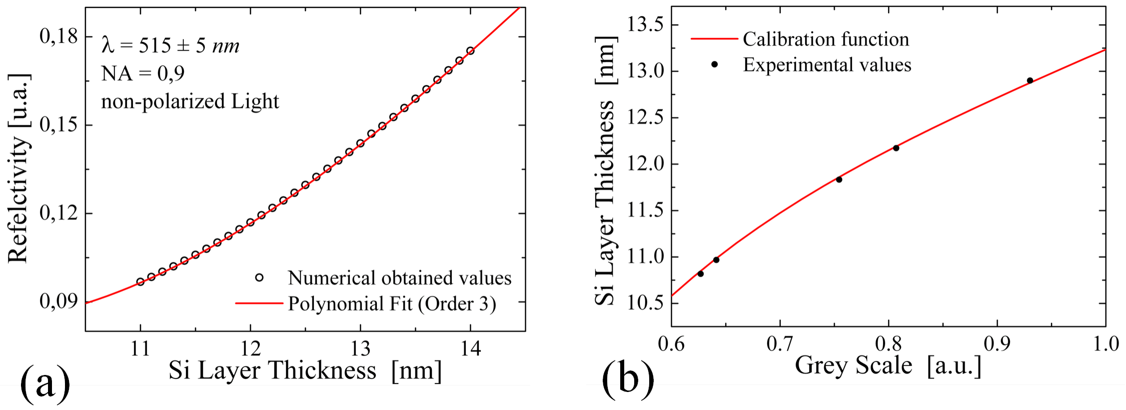

Fig. 1.27: (a) Reflectivity coefficient evolution as a function of the top silicon layer thickness using the optimal wavelength. (b) Calibration curve (red line) obtained from experimental values of 5 SOI wafers (Si layer thickness measured by *SE*. Grey scale obtained by DRM).

Figure 1.27 (a) shows the variation of the reflectivity coefficient as a function of the top silicon layer thickness. Actually, DRM measures light intensities, thus, in order to calibrate the conversion from intensities into thickness values, we have fabricated SOI wafers with incremental top layer thicknesses and covering the thickness range of interest. Several DRM images of each wafer were recorded and averaged. The intensity values plotted as a function of the thickness of the top *Si* layer measured by *SE*. Finally, it is possible to calibrate the intensity of DRM images (grey level) against the thickness of the silicon top layer using some fitting (see Fig 1.27 (b)).

The spatial bandwidth covered by this technique is defined by the field of view and the optical resolution offered by objectives lens. Different magnifications can be used with the microscope (100×, 20× and 5×) but optical deformations induced by the 5× objective are too important to allow precise measurements.

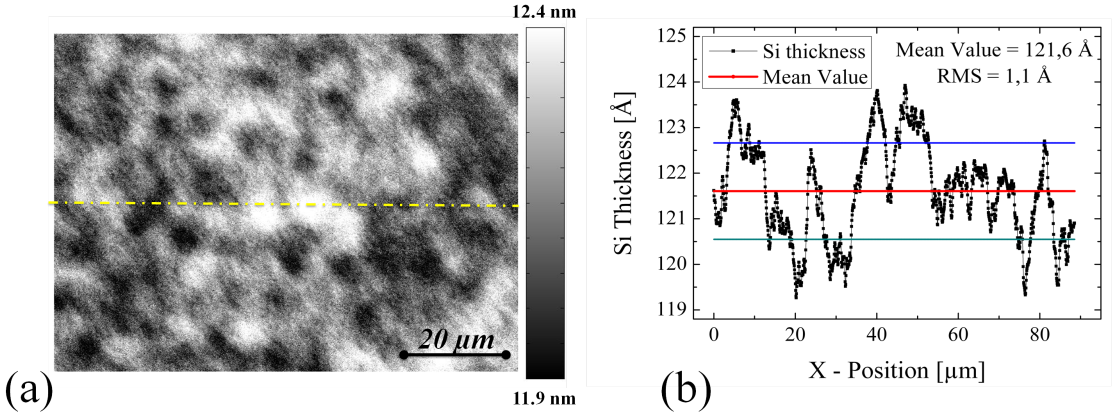

Fig. 1.28: DRM image obtained with a *Zeiss Axiotron 2* microscope with a 100× magnification objective ($NA = 0.9$), using a green interferometric filter ($515\,nm$) and a CCD camera (1292×968 pixels). (a) $88.6\times66.6\,\mu m^2$ image where the grey level of each pixel represents the thickness of the top silicon layer. (b) Thickness profile obtained from the image shown in a).

Figure 1.28 shows a typical image and an extracted thickness profile obtained with a 100× objective. The repeatability of the measurements and the noise level have been analyzed by conventional methods, for example recording several images from a test sample in order to evaluate the noise amplitude. The noise level of the DRM technique is estimated to be smaller than 1.5 Å. This compares well to the noise level of a high performance AFM (~ 3.0 Å). Moreover, it is worth noting that the stability of the light source has a considerable influence on the repeatability of the measurement. Then, it is suitable to repeat the calibration procedure before each series of measurements.

Figure 1.29 shows the *PSD* function obtained from the thickness image shown in figure 1.28. The *PSD* function corresponding to a DRM measurement using a 20× objective is superimposed.

In conclusion, DRM permits the characterization of thickness variations over a spatial bandwidth [from 2×10^{-3} up to $2\,\mu m^{-1}$] which was inaccessible by other techniques.

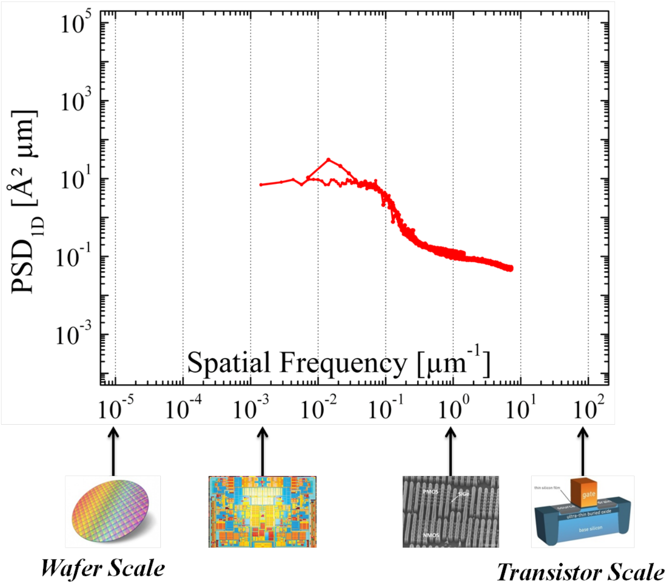

Fig. 1.29: Superposition of *PSD* functions corresponding to DRM measurements using a 100× and a 20× objectives. Images are recorded using the same sample than that shown in figure 1.28.

1.2.3.3 Thickness measurement by Off-axis Holography

Transmission electron microscopy is widely used for the characterization of the micro and nano structure of materials. There are several imaging techniques, but most of them does not give access to the information transported by the phase shift of the high energy electron waves. Electron holography was introduced by Dennis Garbor [42], and is able to image the magnetic and electric fields in materials with very high spatial resolution (nanometer scale), using phase shift information [43]. Off-axis electron holography is based on the interference between electron waves that have passed through the vacuum and through an object, forming the resulting interference pattern (hologram). Figure 1.30 (a) shows a schematic illustration of the off-axis electron holography technique.

An hologram contains two parts. The first, reference part, is formed as a result of the interference between waves both passed through vacuum. The second part is generated by the interference between a wave passed though vacuum and the one that has been phase shifted due to its interaction with an object. The analysis of the hologram fringe distances with respect to the reference ones allows the local phase shift of the electron beam to be recovered [43]. In a nonmagnetic sample, the phase shift ($\phi(x, y)$) of the electron wave is proportional to the local changes of the electrostatic potential projected along the electron pass. For a Si film, the electrostatic contribution to the phase shift is associated solely with the mean inner potential (MIP) of the matrix, *i.e.* the local composition, and thickness of

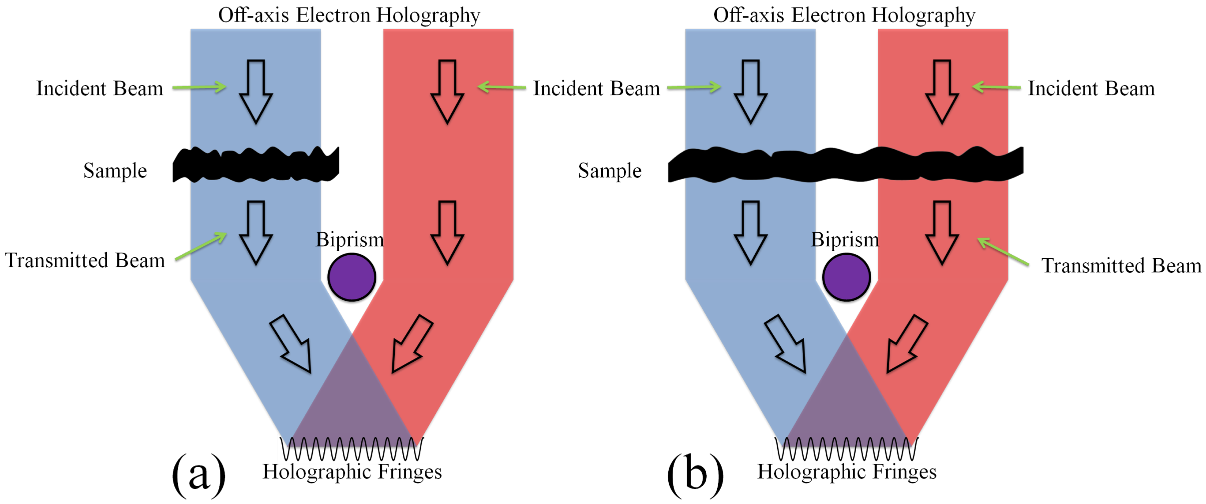

Fig. 1.30: Schematic illustration of the standard setup for off-axis electron holography using: (a) vacuum as zero phase-shift reference and (b) the mean phase-shift as reference.

the sample, $t(x,y)$ and is given by the expression,

$$\phi(x,y) = C_E V_0 t(x,y) \tag{1.32}$$

where (x,y) lie in the plane of the sample, $C_E = \frac{2\pi}{\lambda}\frac{E+E_0}{E(E+2E_0)}$ is a wavelength-dependent constant [44] ($C_E = 6.5\times10^6\,radV^{-1}m^{-1}$ at $300\,kV$) and V_0 is the mean electrostatic potential of crystalline Si equal to $12.1\pm1.3\,V$. Thus, an absolute value of the local sample thickness can be extracted from the measurement of the local phase shift of the electron beam with respect to vacuum with a very high spatial resolution (few nanometers).

As it follows from the previous description, the necessary condition to obtain absolute sample thickness measurement is the presence of vacuum near the edge of the sample. However, if the hologram is formed by the interference between electron waves that have both passed through an object (see Fig.1.30 (b)), the absolute zero reference is not present in the hologram but the mean phase can be taken as a zero reference. In this case, the phase variations are directly related to the local sample thickness variations around the unknown mean sample thickness value.

Our contribution to the development of this method is essentially focused on the sample preparation. Indeed, the experimental procedure for recording holograms as well as the theoretical analysis of the recorded images were carried out by Nikiolay Cherkashin at *Centre d'Elaboration de Matériaux et d'Etudes Structurales* (CEMES, Toulouse).

The main objective of the sample preparation procedure I had to set up is to extract the top silicon layer from a FD-SOI wafer while its nominal thickness is about $12\,nm$. Actually, in the Smart Cut™ technology the final thickness of the top silicon layer is adjusted through oxidation/etching steps. In this work, we do not dissolve the superficial SiO_2 layer to use it to protect the Si surface from chemical etching (see Fig. 1.31 (a)). Then, the sample preparation consists in the following steps (see Fig. 1.31). Firstly, the bulk silicon substrate is mechanically thinned using a disc grinder which produces good quality parallel-sided thin sample (approximately $50\,\mu m$ thick). Then, a dimple grinder is used to generate a large and thin area (approximately $3\,\mu m$ thick) in the center of sample surrounded by thick rims (see Fig. 1.31 (b)). After that, the sample is soaked in a KOH bath. This chemical etching selectively etch Si and is then stopped by the BOx layer (see Fig. 1.31 (c)). Finally, both SiO_2 layers are dissolved by a wet HF bath (see Fig. 1.31 (d)).

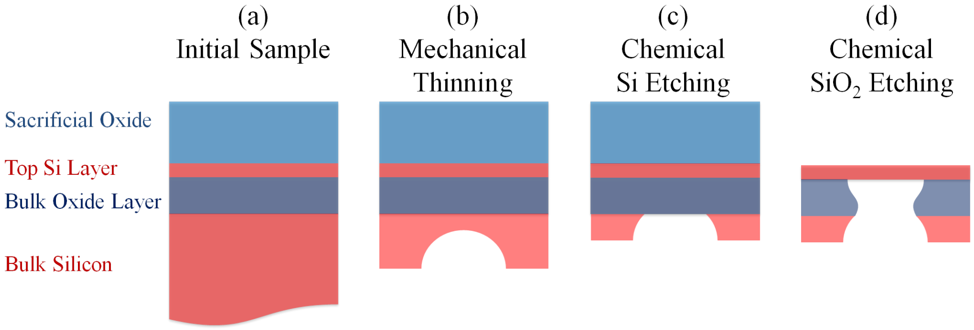

Fig. 1.31: Schematic illustration of different steps involved the preparation of a free film for thickness measurements by electronic holography.

As explained before, off-axis electron holography measurements require a reference electron wave propagating in the vacuum to obtain absolute sample thickness value. Thus, FIB is used to create holes through the sample. However, this sample preparation procedure is very delicate and most of films are broken at the last steps of the preparation and/or contaminated during the fabrication of holes by FIB.

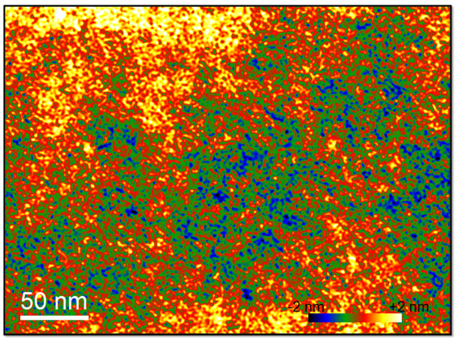

Fig. 1.32: Image obtained by off-axis electronic holography for thickness measurement using the mean phase as zero reference.

Off-axis electron holography experiments were carried out on the Hitachi I2TEM-Toulouse (in situ interferometry TEM), an HF3300 equipped with CFEG, double stage for

Lorentz microscopy, imaging aberration corrector (CEOS Aplanator) and multiple biprisms. The second specimen stage is located just above the objective lens that can serve as a powerful Lorentz lens coupled to the state-of-the-art aberration corrector. Holograms were obtained with a resolution of $2\,nm$. The multiple biprisms allow more flexibility in choosing holographic fringe spaces and field of view, and Fresnel fringes can be eliminated [45]. Any additional phase shifts of the beam due to the effect of the microscope optic elements are removed acquiring a reference hologram and subtracting it following the method described, for instance, in [46, 47]. The holograms have been recorded in the mode corresponding to figure 1.30 (b). Off-Bragg conditions have been carefully maintained during hologram acquiring to avoid dynamical effects of the electron beam-object interaction [43]. Figure 1.32 shows an image of local thickness variations of a typical silicon top layer extracted from holography measurement.

Figure 1.33 shows the *PSD* function obtained from the off-axis holography image shown in figure 1.32. In conclusion, off-axis holography allows characterizing the thickness variations over a spatial bandwidth [from $6\,\mu m^{-1}$ up to $200\,\mu m^{-1}$] which was inaccessible by other techniques. However, to render the technique a «routine», considerable effort should be put on improving the sample preparation procedure.

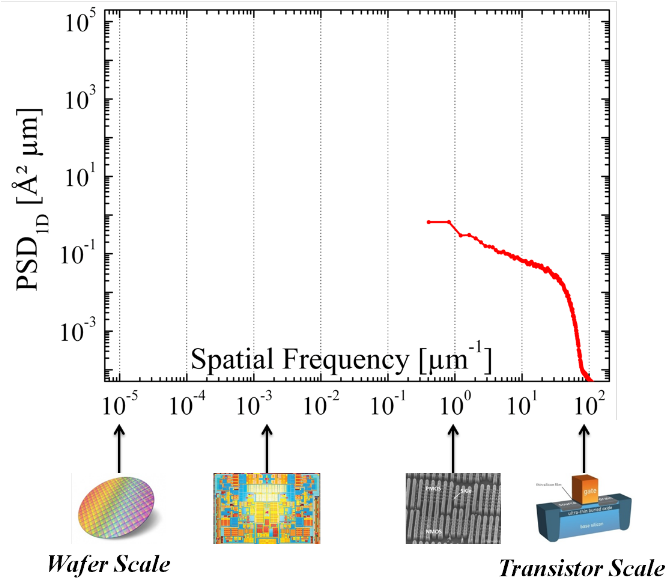

Fig. 1.33: *PSD* function corresponding to off-axis holography thickness measurements.

To summarize, we have now in hands new characterization techniques allowing us to investigate thickness variations over the whole spatial bandwidth of interest, from the single transistor scale to the whole wafer scale [from $3 \times 10^{-6}\,\mu m^{-1}$ up to $1 \times 10^2\,\mu m^{-1}$]. In the next section, we present principal results on the thickness and roughness multi-scale characterization of SOI wafers.

1.3 | Experimental results

Combining the techniques introduced in the previous paragraphs, we are now able to characterize thickness variations over a very large spatial bandwidth. In this section, we will study the correlation between thickness and roughness variations of standard SOI wafers. Then, we will analyze thickness variations in the new generation SOI wafers and will evidence the impact of some of the technical steps involved in Smart Cut™ technology onto the final characteristics.

1.3.1 | Thickness - Roughness

Several SOI wafers with a top silicon layer thickness of 88 nm and BOx thickness of 145 nm have been characterized using the techniques presented in the previous sections. Cumulating these results, figure 1.34 shows the typical PSD functions describing the thickness and roughness variations of the top silicon layer of these SOI wafers.

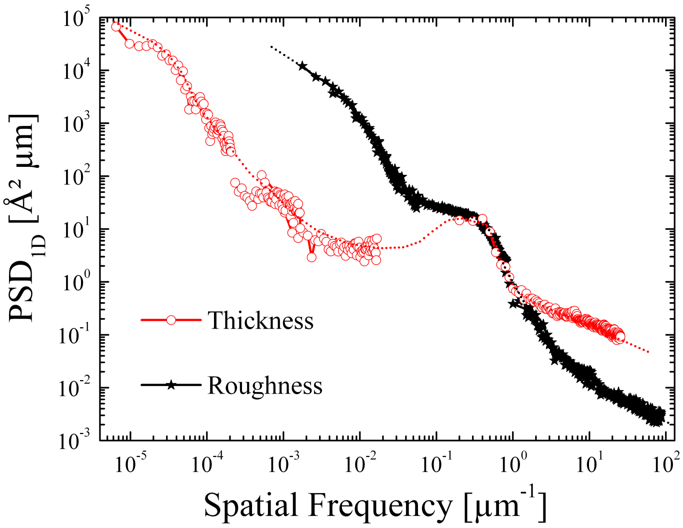

Fig. 1.34: PSD_{1D} functions describing thickness (red open-circles) and roughness (black points) variations of a top silicon layer. Three spectral domains are observed, (a) low-frequencies [from $1\times10^{-3}\,\mu m^{-1}$ to $0.1^{-1}\,\mu m^{-1}$] roughness larger than thickness variations, (b) middle-frequencies [from $0.1\,\mu m^{-1}$ to $1\,\mu m^{-1}$] roughness and thickness variations are similar and (c) high-frequencies [from $1\,\mu m^{-1}$ to $30\,\mu m^{-1}$] thickness variations larger than roughness variations.

It can be observed that there are three different spectral domains. At low-frequencies [from $1\times10^{-3}\,\mu m^{-1}$ up to $1\times10^{-1}\,\mu m^{-1}$], roughness variations are larger than thickness variations. The top silicon film conformably follows the BOx roughness; thereby the two surfaces are correlated in this frequency domain. In the intermediate frequencies region [from $1{\times}10^{-1}\,\mu m^{-1}$ up to $1\,\mu m^{-1}$], roughness and thickness variations are similar, indicating that the top surface roughness variations are much larger than the bottom interface ones.

In this case, thickness variations can be estimated by measuring only the roughness of the top surface. Finally, at high-frequencies [from $1\,\mu m^{-1}$ up to $30\,\mu m^{-1}$] thickness variations are larger than roughness variations. The top and the bottom interfaces are not correlated and the roughness variations of the bottom interface are, at least, of the same order of magnitude than the roughness variations of the top surface.

Frequency Band [μm^{-1}]	*Spatial Band [μm]*	*Roughness RMS [Å]*	*Thickness RMS [Å]*
1 - 100	0.01- 1	1.01	1.62
0.1 - 1	1 - 10	2.95	2.95
1×10^{-3} - 0.1	10 - 1000	7.3	2.94
1×10^{-3} - 1×10^{-5}	1×10^{3} - 1×10^{5}	–	1.32

Tab. 1.1: Summary of the statistical parameters describing roughness and thickness variations.

The equivalent *RMS* of thickness and roughness variations can be estimated from the PSD_{1D} function for each frequency bandwidth (see Eq. 1.28). The obtained *RMS* values, describing the amplitude of thickness and roughness variations, are in agreement with the observations reported above. The results are summarized in Table 1.1

1.3.2 | Smart Cut™ and thickness variations

Hereafter, we will analyze thickness variations of silicon layers of SOI wafers over a very large spatial bandwidth [from $6.8\times10^{-6}\,\mu m^{-1}$ up to $1\times10^{2}\,\mu m^{-1}$]. Figure 1.35 shows the PSD_{1D} function characteristic of the thickness of the top silicon layer of the new generation of SOI wafers. It is obtained by averaging the thickness spectra from five representative wafers.

We can observe different behaviors on the *PSD* function. In region I, corresponding to the lower frequency part of the spectrum [from $3\times10^{-6}\,\mu m^{-1}$ to $2\times10^{-3}\mu m^{-1}$], the PSD_{1D} describing the thickness variations decreases as a power-law (linear on a log-log scale), what is characteristic of fractal surfaces. In fact, this PSD_{1D} exhibits a fractal behavior with a scaling exponent equal to 0.3 ± 0.1 (obtained from the slope of the PSD_{1D} function, see section 1.1). This exponent is much smaller than the typical values $(0.5 - 0.8)$ obtained in the case of fractured surfaces [48, 49]. Indeed, over this frequency range, thickness variations result from fracture propagation in silicon single crystal along weak path predefined by the micro-cracks involved in the ion cut process. As the depth-distribution of *micro-cracks* is very tight (few nanometers) therefore, the low frequency thickness variations we evidence may result from some «non-uniformity» of the implantation used for SOI manufacturing and thus do not show the classical fractal characteristic of fractured surfaces. In region II [from $2\times10^{-3}\,\mu m^{-1}$ to $2\times10^{-2}\,\mu m^{-1}$], the amplitude of the PSD_{1D} remains constant, meaning that the thickness varies randomly over this frequency range. The bump visible in the region

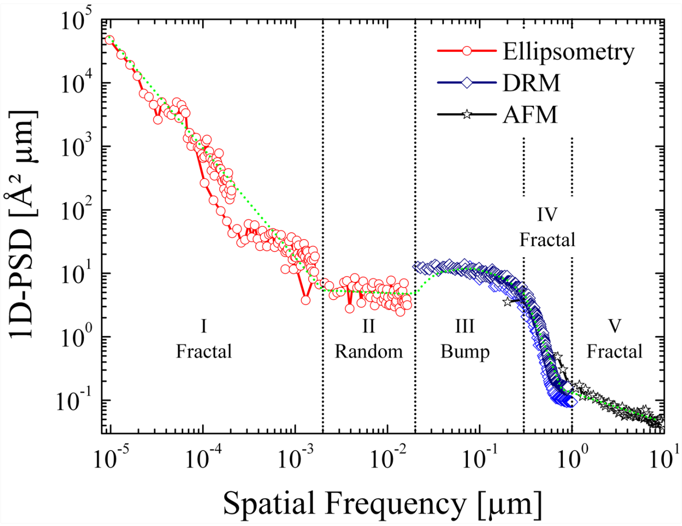

Fig. 1.35: PSD_{1D} function representing the top silicon layer thickness variations, measured by: (left) Ellipsometry (three different sampling periods: $\Delta x_1 = 30\,\mu m$, $\Delta x_2 = 300\,\mu m$ and $\Delta x_3 = 2420\,\mu m$. (center) Differential Reflectivity Microscopy (image size: $66.6{\times}88.6\,\mu m^2$) and (right) AFM (scan-size: $30{\times}30\,\mu m^2$ and $10{\times}10\,\mu m^2$).

III [from $2\times10^{-2}\,\mu m^{-1}$ to $0.3\,\mu m^{-1}$] corresponds to the size of the micro-cracks formed by hydrogen precipitation just before the catastrophic splitting. Their size-distribution depends on the implantation conditions (dose, energy) and thermal budget used for wafer splitting [50].

The higher frequency part of the spectrum exhibits two different fractal behaviors. In region IV [from $0.3\,\mu m^{-1}$ to $0.1\,\mu m^{-1}$], the observed scaling exponent is equal to 1.2 ± 0.1 which agrees well with the surface diffusion phenomenon described by the Mullins-Herring equation [51]. In region V [from $1\,\mu m^{-1}$ to $10\,\mu m^{-1}$] the value of the scaling exponent 0.2 ± 0.1 suggest that this roughness originates from silicon oxidation. Indeed, two different models have been proposed in the literature to describe the roughness evolution of the Si/SiO_2 interface during oxidation. The first is based on the *Kardar-Parisi-Zhang* equation, whose typical values of scaling exponent are between 0.2 and 0.3 [52, 53]. The second states that silicon oxidation can be described by the *Edward-Wilkinson* growth model, with a scaling exponent equal to 0 [54, 55]. The limited accuracy of our data does not allow us to discriminate between these two models. Thus, in this very high frequency range, thickness variations are impacted by the topography of the two Si/SiO_2 interfaces, the BOX/top silicon interface resulting from thermal oxidation and the top silicon surface which results from the removing of the sacrificial SiO_2 layer used as the finishing step in the SOI manufacturing process.

Conclusions

In this chapter, we have explained why a multi-scale characterization of thin films is required over a very large spatial bandwidth [from $7{\times}10^{-6}\,\mu m^{-1}$ up to $1{\times}10^{2}\,\mu m^{-1}$]. Some standard metrology techniques, such as AFM, SWLI and SE, commonly used for the characterization of films are introduced. We have also discussed the analysis methods and their limitations in terms of spatial resolution. It shows that thickness characterization over the whole spatial bandwidth of interest is not possible using only these techniques. We have thus introduced new characterization techniques allowing to overcome these limitations. We have also studied the correlation between thickness and roughness on standard SOI wafers. Finally, we have discussed the origin of thickness variations. Indeed, the analysis of the thickness variations permits the identification of the frequency bands over which thickness is not uniform. Then, we have determined the spectral foot-prints of the principal technological steps involved in the Smart Cut™ technology influencing the thickness uniformity of the top silicon layer of SOI wafers.

Bibliography

[1] G. K. Celler and S. Cristoloveanu, “Frontiers of silicon-on-insulator,” *Journal of Applied Physics*, vol. 93, no. 9, pp. 4955–4978, 2003. (cited in pages 1 and 5)

[2] O. Faynot, F. Andrieu, O. Weber, C. Fenouillet-Beranger, *et al.*, “Planar fully depleted soi technology: A powerful architecture for the 20 nm node and beyond,” in *Electron Devices Meeting (IEDM), 2010 IEEE International*, pp. 321–324, 2010. (cited in pages 1 and 5)

[3] O. Weber, O. Faynot, F. Andrieu, C. Buj-Dufournet, *et al.*, “High immunity to threshold voltage variability in undoped ultra-thin FDSOI MOSFETs and its physical understanding,” in *Electron Devices Meeting, 2008. IEDM 2008. IEEE International*, pp. 1–4, 2008. (cited in pages 1 and 5)

[4] T. Hook, M. Vinet, R. Murphy, S. Ponoth, and L. Grenouillet, “Transistor matching and silicon thickness variation in ETSOI technology,” in *Electron Devices Meeting (IEDM), 2011 IEEE International*, pp. 571–574, 2011. (cited in pages 1 and 5)

[5] S. J. Fang, S. Haplepete, W. Chen, C. R. Helms, and H. Edwards, “Analyzing atomic force microscopy images using spectral methods,” *Journal of Applied Physics*, vol. 82, no. 12, 1997. (cited in page 5)

[6] J. M. Elson and J. M. Bennett, “Calculation of the power spectral density from surface profile data,” *Appl. Opt.*, vol. 34, pp. 201–208, Jan 1995. (cited in page 5)

[7] S. G. Alcock, G. D. Ludbrook, T. Owen, and R. Dockree, “Using the power spectral density method to characterise the surface topography of optical surfaces,” in *Advances in Metrology for X-Ray and EUV Optics III*, p. 8, August 2010. (cited in page 5)

[8] R. Gravila, A. Dinescu, and D. Mardare, “A power spectral density study of thin films morphology based on AFM profiling,” *Romanian journal of information science and technology*, vol. 10, no. 3, pp. 291–300, 2007. (cited in pages 5 and 10)

[9] P. Samyn, J. V. Erps, H. Thienpont, and G. Schoukens, “Paper coating with multi-scale roughness evaluated at different sampling sizes,” *Applied Surface Science*, vol. 257, no. 1, pp. 5613–5625, 2011. (cited in pages 5 and 6)

[10] T. Yoshinobu, A. Iwamoto, K. Sudoh, and H. Iwasaki, “Scaling of Si/SiO_2 interface roughness,” *Journal of Vacuum Science Technology B: Microelectronics and Nanometer Structures*, vol. 13, no. 4, pp. 1630–1634, 1995. (cited in pages 5 and 6)

[11] K. Kaznatcheev and P. Z. Takacs, “Optical metrology at the NSLS-II,” *Nuclear Instruments and Methods in Physics Research A*, vol. 649, no. 1, pp. 144–146, 2011. (cited in pages 5, 6 and 10)

[12] J. D. Briers, *Surface Roughness Evaluation.* 1993. (cited in page 7)

[13] T. V. Vorburger and E. Marx, “Direct and inverse problems for light scattered by rough surfaces,” *Applied Optics*, 1990. (cited in page 10)

[14] B. Mandelbrot, *Fractals : form, change and dimension.* Wageningen UR Library: W.H. Freeman, 1977. (cited in page 11)

[15] B. B. Mandelbrot, “How long is the coast of britain,” *Science*, vol. 156, no. 3775, pp. 636–638, 1967. (cited in page 11)

[16] B. B. Mandelbrot, *The fractal geometry of nature*. W.H. Freeman, 1 ed., Aug. 1982. (cited in page 11)

[17] R. Lopes and N. Betrouni, “Fractal and multifractal analysis: A review,” *Medical Image Analysis*, vol. 13, no. 4, pp. 634 – 649, 2009. (cited in page 11)

[18] F. Gentile, E. Battista, A. Accardo, M. Coluccio, *et al.*, “Fractal structure can explain the increased hydrophobicity of nanoporous silicon films,” *Microelectronic Engineering*, vol. 88, no. 8, pp. 2537 – 2540, 2011. (cited in page 11)

[19] B. B. Mandelbrot, D. E. Passoja, and A. J. Paullay, “Fractal character of fracture surfaces of metals,” *Nature*, vol. 308, pp. 721–722, 1984. (cited in page 11)

[20] S. Erdem and M. A. Blankson, “Fractal–fracture analysis and characterization of impact-fractured surfaces in different types of concrete using digital image analysis and 3D nanomap laser profilometery,” *Construction and Building Materials*, vol. 40, 2013. (cited in page 11)

[21] T. A. Witten and L. M. Sander, “Diffusion-limited aggregation,” *Phys. Rev. B*, vol. 27, pp. 5686–5697, May 1983. (cited in page 11)

[22] A. Majumdar and C. Tien, “Fractal characterization and simulation of rough surfaces,” *Wear*, vol. 136, no. 2, pp. 313 – 327, 1990. (cited in page 11)

[23] A. L. Barabasi and H. E. Stanley, *Fractal Concepts In Surface Growth*. Cambridge Press, 1995. (cited in pages 11, 12, 13, 78, 79, 80, 84, 85, 88, 89, 109, 117 and 118)

[24] F. Family and T. Vicsek, “Scaling of the active zone in the eden process on percolation networks and the ballistic deposition model,” *Journal of Physics A: Mathematical and General*, vol. 18, no. 2, p. L75, 1985. (cited in pages 12 and 109)

[25] G. Binnig, C. F. Quate, and C. Gerber, “Atomic force microscope,” *Phys. Rev. Lett.*, vol. 56, pp. 930–933, Mar 1986. (cited in page 15)

[26] B. Cappella and G. Dietler, “Force-distance curves by atomic force microscopy,” *Surface Science Reports*, vol. 34, no. 1–3, pp. 1 – 104, 1999. (cited in page 15)

[27] S. Morita, E. Meyer, and R. Wiesendanger, *Non-Contact Atomic Force Microscopy*, vol. I. Springer, 2002. (cited in page 15)

[28] F. J. Giessibl, “Advances in atomic force microscopy,” *Rev. Mod. Phys.*, vol. 75, pp. 949–983, Jul 2003. (cited in page 15)

[29] C. Shannon, “Communication in the presence of noise,” *Proceedings of the IEEE*, vol. 86, no. 2, pp. 447–457, 1998. (cited in page 16)

[30] D. Malacara, *Optical Shop Testing*. John Wiley and Sons, Inc., 3 ed., 2007. (cited in page 17)

[31] B. Bhushan, J. C. Wyant, and C. L. Koliopoulos, "Measurement of surface topography of magnetic tapes by mirau interferometry," *Appl. Opt.*, vol. 24, pp. 1489–1497, May 1985. (cited in page 17)

[32] R. Azzam and N. Bashara, *Ellipsometry and Polarized Light.* Elsevier, North-Holland, Amsterdam, 1989. (cited in page 19)

[33] D. Aspnes, "New developments in spectroellipsometry: the challenge of surfaces," *Thin Solid Films*, vol. 233, no. 1–2, pp. 1 – 8, 1993. (cited in page 19)

[34] D. Aspnes, R. Bhat, C. Caneau, E. Colas, *et al.*, "Optically monitoring and controlling epitaxial growth," *Journal of Crystal Growth*, vol. 120, no. 1–4, pp. 71 – 77, 1992. (cited in page 19)

[35] W. M. Duncan, S. A. Henck, and L. M. Loewenstein, "Spectral ellipsometry for in situ real-time measurement and control," in *Wafer Level Reliability Workshop, 1992. Final Report., 1992 International*, pp. 117–121, 1992. (cited in page 19)

[36] E. Sidick, "Power spectral density specification and analysis of large optical surfaces," *Proc. SPIE Modeling Aspects in Optical Metrology II*, vol. 7390, 2009. (cited in page 22)

[37] M. Gosalvez, I. Zubel, and E. Viinikka, "Chapter twenty four - wet etching of silicon," in *Handbook of Silicon Based MEMS Materials and Technologies* (V. Lindroos, M. Tilli, A. Lehto, and T. Motooka, eds.), Micro and Nano Technologies, pp. 375 – 407, Boston: William Andrew Publishing, 2010. (cited in page 26)

[38] K. Sato and M. Shikida, "1.07 - wet etching," in *Comprehensive Microsystems* (Y. B. Gianchandani, O. Tabata, and H. Zappe, eds.), pp. 183 – 215, Oxford: Elsevier, 2008. (cited in page 26)

[39] L. A. A. Pettersson, L. S. Roman, and O. Inganäs, "Modeling photocurrent action spectra of photovoltaic devices based on organic thin films," *Journal of Applied Physics*, vol. 86, no. 1, 1999. (cited in page 28)

[40] E. Centurioni, "Generalized matrix method for calculation of internal light energy flux in mixed coherent and incoherent multilayers," *Appl. Opt.*, vol. 44, Dec 2005. (cited in page 28)

[41] C. C. Katsidis and D. I. Siapkas, "General transfer-matrix method for optical multilayer systems with coherent, partially coherent, and incoherent interference," *Appl. Opt.*, vol. 41, pp. 3978–3987, Jul 2002. (cited in page 28)

[42] D. Gabor, "A new microscopic principle," *Nature*, vol. 161, pp. 777–778, 1948. (cited in page 31)

[43] R. E. Dunin-Borkowski, M. R. McCartney, and D. J. Smith, *Electron Holography of nanostructured materials.* American Scientific Publisher, 2003. (cited in pages 31 and 34)

[44] L. Reimer, *Transmission Electron Microscopy.* Springer-Verlag, Berlin, 1991. (cited in page 32)

[45] K. Harada, A. Tonomura, Y. Togawa, T. Akashi, and T. Matsuda, "Double-biprism electron interferometry," *Applied Physics Letters*, vol. 84, no. 17, 2004. (cited in page 34)

[46] H. Lichte, "Electron holography: optimum position of the biprism in the electron microscope," *Ultramicroscopy*, vol. 64, no. 1–4, pp. 79 – 86, 1996. 1 Å Exit Wave Reconstruction. (cited in page 34)

[47] H. Lichte, D. Geiger, A. Harscher, E. Heindl, M. Lehmann, D. Malamidis, A. Orchowski, and W.-D. Rau, "Artefacts in electron holography," *Ultramicroscopy*, vol. 64, no. 1–4, pp. 67 – 77, 1996. 1 Å Exit Wave Reconstruction. (cited in page 34)

[48] C. Lu, D. Vere-Jones, and H. Takayasu, "Avalanche behavior and statistical properties in a microcrack coalescence process," *Phys. Rev. Lett.*, vol. 82, pp. 347–350, Jan 1999. (cited in pages 36 and 65)

[49] J. Schmittbuhl and K. J. Måløy, "Direct observation of a self-affine crack propagation," *Phys. Rev. Lett.*, vol. 78, pp. 3888–3891, May 1997. (cited in pages 36 and 65)

[50] S. Personnic, K. K. Bourdelle, F. Letertre, A. Tauzin, *et al.*, "Impact of the transient formation of molecular hydrogen on the microcrack nucleation and evolution in h-implanted si (001)," *Journal of Applied Physics*, vol. 103, no. 2, 2008. (cited in pages 37, 48, 49, 50, 51, 52, 53, 54, 55, 56 and 57)

[51] E. Darvish and A. A. Masoudi, "Kinetic surface roughening for the mullins–herring equation," *Journal of Mathematical Physics*, vol. 50, no. 1, pp. –, 2009. (cited in pages 37, 85 and 88)

[52] M. Lütt, J. P. Schlomka, M. Tolan, J. Stettner, O. H. Seeck, and W. Press, "Kardar-Parisi-Zhang growth of amorphous silicon on Si/SiO_2," *Phys. Rev. B*, vol. 56, pp. 4085–4091, Aug 1997. (cited in page 37)

[53] H. Omi, H. Kageshima, and M. Uematsu, "Scaling and universality of roughening in thermal oxidation of Si(001)," *Phys. Rev. Lett.*, vol. 97, p. 016102, Jul 2006. (cited in page 37)

[54] J. T. Drotar, Y.-P. Zhao, T.-M. Lu, and G.-C. Wang, "Surface roughening in low-pressure chemical vapor deposition," *Phys. Rev. B*, vol. 64, p. 125411, Sep 2001. (cited in page 37)

[55] J. Farjas and P. Roura, "Oxidation of silicon: Further tests for the interfacial silicon emission model," *Journal of Applied Physics*, vol. 102, no. 5, 2007. (cited in page 37)

2 | Fracture Induced by Ion-Implantation

Contents

The Smart Cut™ process, aimed at fabricating SOI wafers, is essentially based on the combination of ion implantation, direct wafer bonding and layer splitting processes applied to the transfer of a thin single crystalline Si layer from a «*donor*» wafer onto a new «*handle*» Si substrate. In general, the silicon *donor* is thermally oxidized in order to provide the future buried oxide layer. It is implanted with H^+ ions at room temperature and then bonded onto the *handle* substrate. Then, a thermal annealing leads to the splitting of the *donor* wafer. Splitting is one of the macroscopic results of the thermal evolution of microscopic lattice defects resulting from the H^+ implantation. Specifically, high dose ion implantation of hydrogen and/or helium in Si (which are hardly soluble in most materials) leads, after a brief thermal treatment, to the formation of disk-shaped structures in the bulk substrate (*platelets* and/or *micro-cracks*). Further annealing favors the lateral expansion of these crack-like structures through the increase of gas pressure within these structures and generates stress in the implanted region. This stress plays a crucial role, at different length scales, on the thermal evolution of the micro-structure [1–7].

At this point, the material response depends on the presence or not of a stiffener (*handle* wafer). Actually, when there is no stiffener and since the implantation depth is typically less than $1\,\mu m$, elastic stress relaxation at the «free-to-move» implanted surface leads to blistering (see Fig. 2.1 (a)). It is worth noting that blistering is a threshold phenomenon, the on-set of surface blistering depending on the implantation conditions (*i.e.*, dose and energy) [8]. It has been reported that there are lower and higher limit doses (approximately $1 \times 10^{16}\ cm^{-2}$ and $1 \times 10^{17}\ cm^{-2}$ respectively) giving rise to blisters depending on ion energies [9].

Besides, the presence of a rigid stiffener above the implanted region blocks the vertical relaxation of the stress and favors its propagation parallel to the wafer surface leading to the exfoliation of a large area (see Fig. 2.1 (b)). It is then possible to induce the fracture of implanted layer across the whole wafer and finally to transfer thin crystal layers onto a *handle* substrate [10].

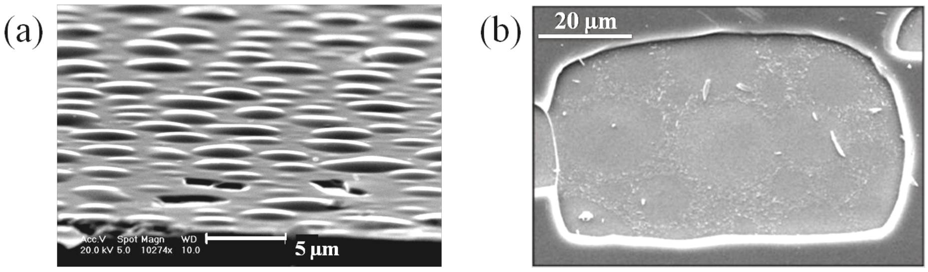

Fig. 2.1: SEM top view images of implanted and annealed silicon wafers. (a) Dome shaped blisters (adapted from [1]). (b) exfoliated region (adapted from [11]). Annealing at 350 °C was performed.

In this chapter, we will firstly review the current state of understanding of the splitting process. Understanding splitting means establishing a scenario, based on fundamental physics, able to describe the thermal evolution of the implantation induced defects leading to the fracture. It involves a number of successive steps: the generation of ion implantation induced defects at room temperature, their thermal evolution (transformation), the crack initiation and finally its propagation during annealing. Secondly, we will use the characterization techniques presented in chapter 1 to study the impact of the implantation conditions on the topography of post-fracture surfaces.

2.1 | Fracture in Smart Cut™ technology

Since the first publication *Silicon on insulator material technology* [10] and despite the publication of many papers in the field, a complete picture of the underlying physical mechanisms involved in the splitting process is still lacking. Ion implantation induced defects evolves during annealing through different length scales (from few Å to several mm). Figure 2.2 shows the different defects involved in this process [1]. Actually, it is a great challenge to identify all physical mechanisms and phenomena playing a role during this multi-scale transformation.

2.1.1 | Ion-induced defects: As-implanted Si wafers

After H^+ implantation, using doses in the range of a few 10^{16} to 10^{17} H^+cm^{-2} and energies from few keV up to tens of keV, a heavily damaged and strained zone around

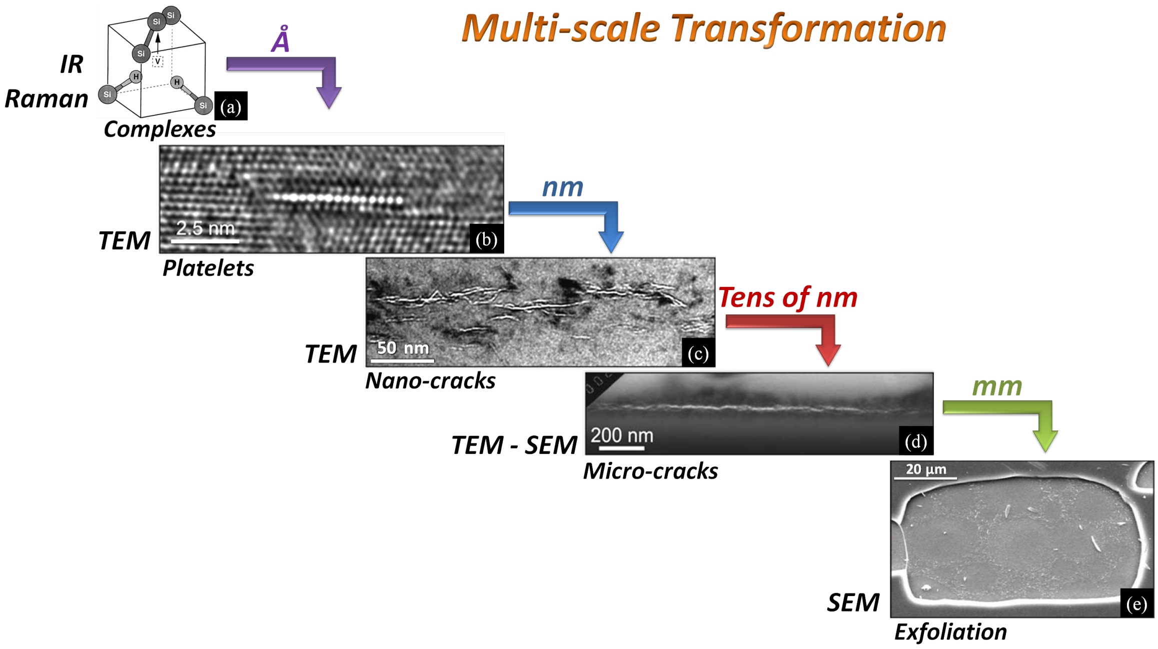

Fig. 2.2: Scheme illustrating the thermal evolution of ion implantation induced defects at different stages on the splitting process: (a) gas filled *platelets*, (b) *nano-cracks*, (c) *micro-cracks*, and (d) exfoliated surface resulting from cleavage assisted *micro-cracks* coalescence. (adapted from [1]).

the ion projected range (Rp) whose depth is defined by the ion acceleration energy, is observed [10, 12]. This damaged zone, largely supersaturated with hydrogen atoms, has been studied by different techniques (TEM, X-ray scattering, etc.) [5, 7, 13]. In this region, several hydrogenated complex defects are produced in large concentrations. Indeed, H^+ implantation generates self-interstitials (I_S), and vacancies (V_S) (Frenkel pairs) which diffuse at room temperature and recombine with the implanted H atoms. These reactions result in different types of hydrogen-vacancy and hydrogen-interstitial complexes.

Figure 2.3 shows the typical spectra obtained by Fourier Transform Infra Red - Multiple Internal Reflection (*FTIR-MIR*) and *Raman* spectroscopies, from H^+ as-implanted silicon at room temperature. Both of them evidence the contribution of stretching modes corresponding to H-related complexes.

Indeed, wavenumbers between $1880\,cm^{-1}$ and $2050\,cm^{-1}$ correspond to multi-vacancy complexes (V_nH_m) while higher wavenumbers ($\geq 2100\,cm^{-1}$) correspond to mono-vacancy complexes (VH_n). In other words, the *FTIR-MIR* spectrum is dominated by stretching modes associated to V_2H_2 and Si-H while modes related to V_2H_2 and VH_3 are evidenced in the *Raman* spectrum. For a more detailed description of the H-related complexes formed in Si, we recommend reading the Ph.D. theses of Personnic [16] and Daix [15] and the review paper by Terreault [9].

A direct effect of the introduction of H-related complexes, is the appearance of an

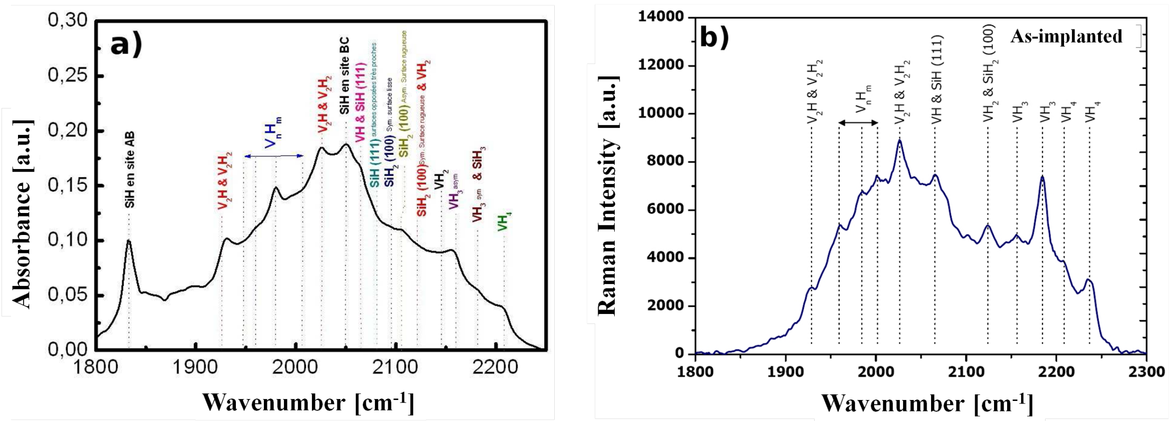

Fig. 2.3: *FTIR-MIR* (a) and *Raman* (b) spectra of the Si-H stretching modes in H-implanted Si before thermal annealing. (adapted from [14] and [15]).

in-plane stress and an out-of-plane strain in the implanted region. This strain can be characterized by X-ray diffraction (XRD) analysis [6, 7]. Figure 2.4 shows typical curves obtained on H^+ as-implanted Si at room temperature. All of them show a main diffraction peak corresponding to the (004) reflection of Si (at $2\theta_B = 69.14\,°$). For the implanted samples, the interference structure on the left-hand side of the peak allows the determination of the strain profile. The measured interference fringe pattern is characteristic of a tensile strain gradient of Gaussian-like shape [17]. It suggests that the vertical strain distribution in as-implanted Si is intimately linked to the implanted ion depth profiles.

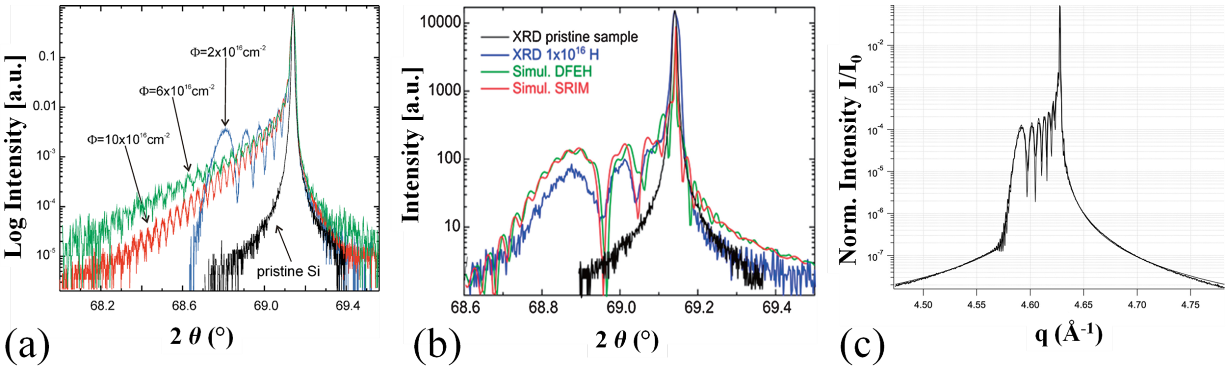

Fig. 2.4: $\theta/2\theta$ *XRD* scans close to the (004) reflection of Si obtained from: (a) samples implanted at fluences $\Phi_T = 2, 6$ and $10\times10^{16}\,cm^{-2}$ (adapted from [7]) and (b) $\Phi_T = 1\times10^{16}\,cm^{-2}$, the simulated curves are obtained assuming that the strain distribution is related to the H depth distribution, or, using depth distribution of strain measured by *DFEH* (adapted from [5]). Both with a reference curve from a pristine sample. (c) High resolution X-ray scattering intensity around (004) Bragg peak, sample implanted at fluence $\Phi_T = 3\times10^{16}\,cm^{-2}$. (adapted from [6]).

More recently, Cherkashin *et al.* [5] have studied in detail the mechanical strain within H^+ as-implanted Si. They used the dark-field electron holography ($DFEH$) technique to observe two-dimensional ($2D$) direct information on the in-plane and out-of-plane components of strain field in the damaged region [18, 19].

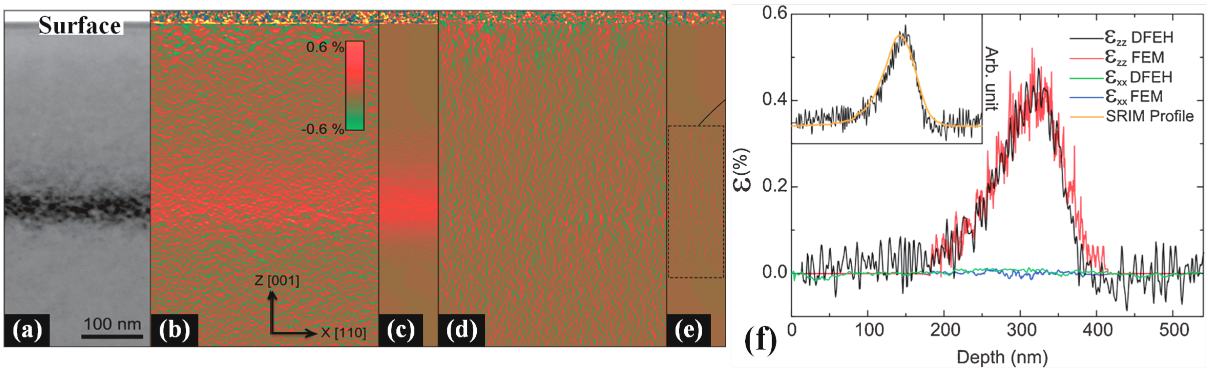

Fig. 2.5: Dark-field electron holography of a (001) Si crystal implanted at $10^{16}\ H^{+}cm^{-2}$. (a) Conventional bright-field *TEM* image under two-beam condition for the (111) diffracted beam; (b) out-of-plane ε_{zz} and (d) in-plane ε_{xx} strain maps obtained by *DFEH*; (c) and (e) the corresponding strain components calculated from a FEM model. (f) Vertical strain profiles of the two components of ε_{zz} and ε_{xx}, extracted from the experimental and simulated images. Zero depth corresponds to the surface of the sample. The inset compares the H depth distribution (by SRIM) and the strain profile (by *DFEH*). (adapted from [5]).

Figure 2.5 (a) shows a conventional bright-field *TEM* micrograph where the dark contrast region corresponds to the damage produced by H^{+} implantation in the Si crystal. The width of the damage region is about $100\,nm$. Figures 2.5 (b) and (d) show the *DFEH* maps of the out-of-plane (normal to the surface, ε_{zz}) and in-plane (parallel to the surface, ε_{xx}) strain components. Figures 2.5 (c) and (e) present out-of-plane and in-plane strains obtained by simulation. The vertical profiles ($depth = 0$ at the surface) extracted from the experimental and simulated images of ε_{zz} and ε_{xx} are compared in figure 2.5 (f). The maximum out-of-plane strain is $\varepsilon_{zz} \sim 0.4\,\%$ at a depth corresponding to Rp (in their experimental conditions $Rp \sim 300\,nm$). The in-plane strain ε_{xx} oscillates around zero with amplitude of about 10^{-4} [5]. The inset on the figure 2.5 (f) shows the proportionality between the H^{+} depth distribution calculated by Stopping and Range of Ions in Matter ($SRIM$) code [20] and the measured strain profile [5].

At this point, we note that most of authors agree that H-related complexes, induced by ion implantation at room temperature, give rise to an in-plane stress and an out-of-plane strain in the implanted region of Si.

Nevertheless, the origin of mechanical strain in H-implanted Si is still matter of discussion. Recently, two different models have been proposed to physically describe it. On the one hand, Cherkashin *et al.* [5] found that strain fields measured by *DFEH* can be correctly simulated by modelling the overlapping and averaging of discrete fields generated by sub-nanometric H-related structures, such as mono-hydride multi-vacancies and H_2^*-

complexes. These defects define of gas-vacancy clusters. On the other hand, Rieutord *et al.* [6] claim that the level of expansion of the lattice spacing is inconsistent with any kind of direct mechanical action (*e.g.*, of the hydrogen gas) on the silicon because they found that the corresponding volume increase per H^+ would be $5\,\text{Å}^3$. Instead, this expansion value can be attributed to a variety of H species which have been observed using IR spectroscopy such as H^0_{BC}, $H^+_2.{}_{BCAB}$, and $H^0_2.{}_{BCAB}$ [2].

All these configurations share a bond center location for one hydrogen, possibly associated to a hydrogen in anti-bonding position forming the H^*_2-complex. Then, they suggest that the effect of one or two charged H^+ hydrogen in BC site inducing higher volume expansion may be consistent with the observed slope increase.

In conclusion, H^+-implantation produces a micro-structural modification of the Si matrix. This modification is associated to the introduction of H-related defects, essentially represented by hydrogenated species such as V_2H_2, VH_3, and Si-H complexes. Most of authors agree that, during the implantation or at low temperature/very short times annealing, implanted Si can be described as a two phases material (Si:H), where the second phase, dipped in the Si matrix, is composed of plate-like cavities named *platelets* [5, 6].

2.1.2 | Platelets nucleation

Many authors have observed *platelets* in the implant-induced damage zone [2–4, 21, 22]. Figure 2.6 (a-b) shows typical images obtained by *TEM*, under *Fresnel* contrast, of (001) *platelets*. Typical *platelets* sizes are around few tens of nanometers in diameter and few nanometers thick [3, 13].

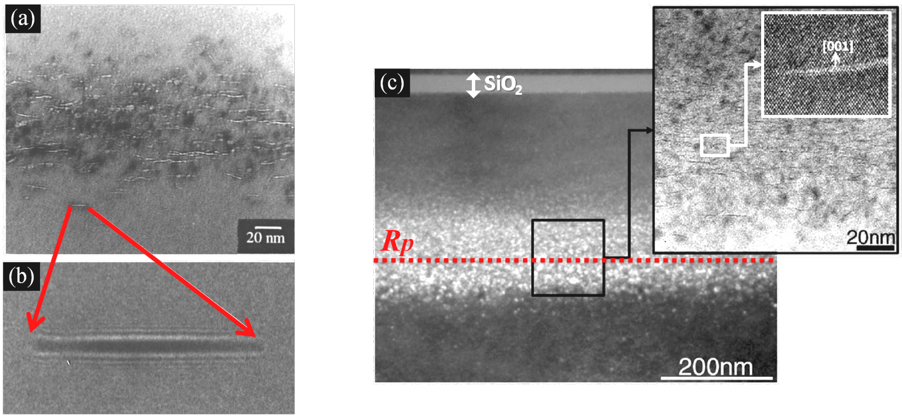

Fig. 2.6: Cross section *TEM* image in «out-of-Bragg» conditions of *platelets* [2, 23]. Typical sizes are around few tens of nanometers in diameter and few nanometers thick. (adapted from [3]).

It can be noted that atomic planes of the crystal are interrupted in the vicinity of *platelets* and therefore it is not a pure interstitial defect. *Platelets* result from the co-precipitation of vacancies and hydrogen atoms (see also Fig. 1 in Ref. [3] and [24]).

It has been also experimentally shown that (001) *platelets* are dominant in implanted (001) *Si* [4,9,21]. As implied by its notation (001), not {100}, dominant *platelets* are located in a plane parallel to the surface. Same behavior has been observed in case of implanted (111) *Si* where (111) *platelets* unsurprisingly dominate [25]. Indeed, spatial orientation of *platelets* is the major result of the strain, on their nucleation [4,9,11].

Moreover, Personnic *et al.* [23] investigated the evolution of the H depth distribution during the first stages of the annealing by secondary ion mass spectrometry (*SIMS*). They observed a reduction of the wideness of the concentration plateau around Rp region (see Fig. 2.7 (a)). In a previous work [14], they also proved that the decrease of the SIMS signal amplitude seen in figure 2.7 (a) is not due to the out-diffusion of H from the implanted region but to some rearrangement of the H atoms in a form not detectable by SIMS, *e.g.*, molecular H_2.

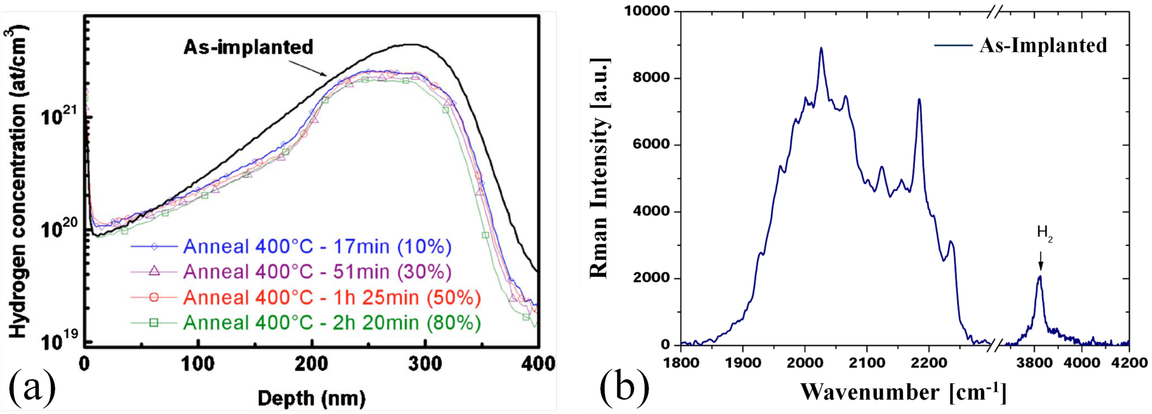

Fig. 2.7: (a) Hydrogen SIMS profiles before and after isothermal annealing (400 °C) [23]. (b) *FTIR* spectra of the *Si-H* stretching modes in H implanted Si before and after isothermal annealing at 450 °C [14].

More recently, N. Daix has observed the *Raman* spectrum of a as-implanted *Si* [15]. It has been unambiguously observed peak at a frequency of $3825\,cm^{-1}$, evidencing that there is molecular H_2 trapped within *platelets*. These experimental observations are consistent a rapid transformation of hydrogen complexes into molecular H_2 [2,23].

Let us now present the principal theoretical models proposed to describe the nucleation of *platelets*.

2.1.2.1 VH_n aggregation mechanism

According to several authors, the VH_n defects are supposed to be the precursors of *platelets* [2,26]. The increasing contribution of VH_n in the *FTIR* spectra and the *platelet* volume fraction measured by *TEM* are additional evidences that tend to confirm the VH_n

precursors theory [23]. The signature of this nucleation can be seen in the *FTIR* modes assigned to hydrogenated mono-vacancy defects (VH_n) (see Fig. 2.7 (b)).

Reboredo *et al.* [26] proposed a model of *platelet* nucleation based on calculations of configuration energies using the density functional theory. Assuming that the *pre-platelet* species are the highly stable VH_4 and mobile H_2, they show that *platelets* can grow progressively through chemical reactions giving rise to hydrogenated internal surfaces. Controversial issues of this model are the high activation energy (2.5 eV) required by some of these reactions as well as the limited mobility of H_2. Indeed, it is difficult to explain the presence of *platelets* at room temperature [26], unless we consider that local heating occurs during the implantation process.

2.1.2.2 Stress induced *platelets* nucleation

Swadener et al. [27] studied the effect of strain on vacancy clusters and *platelet* formation through molecular dynamics (the strain was simulated by applying a 1% in-plane compressive strain and allowing the structure to relax). They have compared the nucleation energies of planar (100) *platelets* to those of (111) and spherical cavities, with and without strain. Figure 2.8 shows the difference in energy between (100) planar and spherical clusters, with strain present.

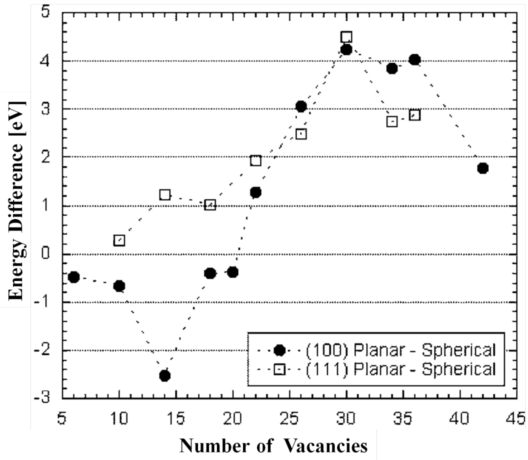

Fig. 2.8: Differences in total energy of formation between (100) planar and spherical vacancy clusters (full circles), and between (111) planar and spherical vacancy clusters (open squares) under bi-axial compression in the (100) plane (adapted from [27]).

It can be noted that, for cavities with 20 vacancies or less, planar (100)-oriented cavities are favored. Assuming that planar vacancies are stable only for small sizes, they proposed that hydrogen *platelets* are formed by a multi-step process. Firstly, the vacancies aggregate into small planar clusters. The clusters could be oriented in (100) or (111) planes depending on the stress state. Secondly, H atoms diffuse to the vacancy clusters and satisfy the dangling bonds on the cluster internal surfaces. Then, the driving force for larger clusters to take a spherical shape would be eliminated. The *platelets* can then grow by *Ostwald* ripening, *i.e.* by the addition of free vacancies and hydrogen [3, 23, 27].

The stress-induced vacancy *platelet* model correctly accounts for some experimental observations. For example, in (100) *Si* wafers, which induces a state of bi-axial stress in the (100) plane, (100) *platelets* are formed in the region of highest strain around *Rp*, while (111) *platelets* are nucleated in lower strain regions in the wafer [4, 5, 28, 29] . In implanted (110) Si wafers, where strain is induced in the (110) plane, both (100) and (111) *platelets* are observed in the high stress region [5, 30, 31] in agreement with this model. Nevertheless, an objection to this model is that experimental observations show *platelets* with much more vacancies ($\sim$ 100 vacancies).

2.1.2.3 Vacancy-less formation of hydrogenated internal surfaces

Martsinovich et al. [32] investigated possible structures of (100) *platelets* by analyzing the energies of well-developed *platelets*. They compare the stabilities of (100) *platelet* structures with the energies of (111) *platelets* presented in their previous work [33]. There is some experimental evidence for the 2×1 and 1×1 internal surface structures in (100) *platelets* induced by H^+ implantation in silicon. Indeed, infrared spectra of *platelets* during annealing at temperatures above 450 °C indicate vibrational modes with frequencies assigned to atomically rough and atomically smooth dihydride-terminated (100) *Si* internal surfaces [34].

Martsinovich et al. [32] propose that hydrogen passivated (100) *platelets* do not require vacancies or stress to nucleate. Using density functional total energy calculations, they show that (100) *platelets* are as stable as the (111) *platelets*. The basic structure consists of Si–H or Si–H_2 decorated (100) planes that are separated by a dilation of the crystalline network. Their formation requires the breaking of Si–Si bonds by H insertion. In implanted material, many broken bonds are already present, thus minimizing the apparent activation energy. More important, these calculations show that these *platelets* can accommodate H_2 molecules exothermally in the interstices. Figure 2.9 shows the formation energies obtained by their calculations for the monohydride ($Si - H$) and for symmetric and canted (not straight) dihydride ($Si - H_2$) structures [32].

It can be observed that, with an optimal dilation of around 2.7 Å, stable structures are obtained (the most stable being the dihydride structure). One can also note that H_2 molecules can be absorbed in all three structures without destabilizing them. Finally, concerning the vacancy models, these calculations show that they have energies very similar to those of the optimized vacancy-less structures. They also show that a canted structure (not considered by Reboredo *et al.*) has the lowest energy.

In terms of stability, one cannot select vacancy or vacancy-less models. However, the latter have the great advantage of not requiring the high activation energies implied by

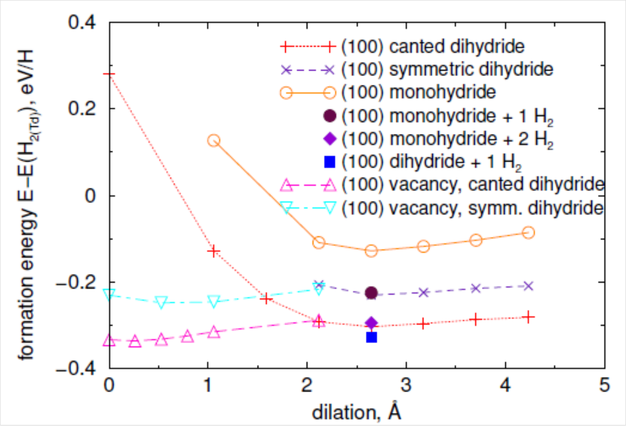

Fig. 2.9: Energies of hydrogenated Si(100) internal surfaces as a function of dilatation with the monohydride ($Si-H$) and symmetric and canted dihydride ($Si-H_2$) structures. (adapted from [32]).

chemical reactions. Nevertheless, *TEM* studies show the presence of vacancies. Both types of models also result in *platelet* thicknesses $\leq 0.41\,nm$, compared to a measured value of $\sim 1\,nm$. In the following, we review proposed models to explain physical phenomena leading to the *platelets* growth.

2.1.3 | Platelets evolution

It has been widely observed that once *platelets* are formed, they develop and grow during annealing. Annealing at 350 - 500 °C results in the growth of these *platelets* yielding to the formation of micron-sized cracks roughly parallel to the surface [3, 21].

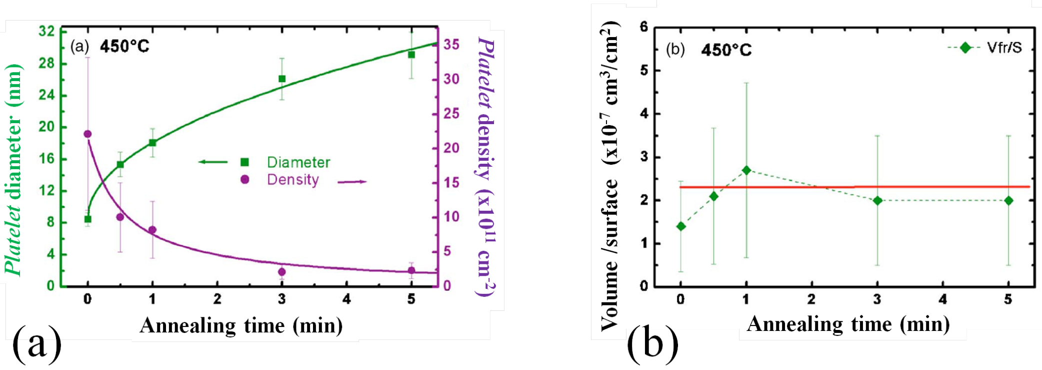

Fig. 2.10: (a) Evolution of mean diameter and surface density of (100) *platelets* as a function of the time for $T_{an} = 450\,°C$ annealing, the implantation dose was of few $10^{16}\,cm^{-1}$. (b) Variation of *platelet* volume fraction per unit area with annealing time. (adapted from [23]).

N. Cherkashin have performed detailed observations of the *platelets* thermal evolution, this work having been reported by Personnic *et al.* [23]. Beyond diameter and density evolutions, they studied the evolution of the volume and the surface fractions occupied by the *platelet* populations. They observed that this surface fraction increases during the first stages of the annealing (less than 1 min) while the *platelets* density does not increase, meaning that, under their experimental conditions, the nucleation stage of the *platelets* is already completed after implantation. Hence, *platelets* are involved in a «pure growth» regime during which the existing *platelets* grow by «pumping» H from other less stable defects in the matrix, invisible by TEM. This model of *platelet* evolution is consistent with the $FTIR$ and $SIMS$ results showing an important decrease of the signal intensities during the same transient stage [14, 23]. Only the IR band corresponding to the mono-vacancies defects $VH_{3,4}$ increases with time. They estimated that 3% of the implanted dose is used for formation of new platelets during the transient stage of annealing.

For longer annealing, *platelets* can undergo a conservative *Ostwald* ripening process during which the *platelets* interchange the species they are composed of (hydrogen atoms and vacancies) [3]. Other observations tend to confirm the evolution of *platelets* by an *Ostwald* ripening process [23]. Aspar *et al.* [22] studied the case of 6×10^{16} H^+/cm^2 implantation at around 70 keV and they showed that the firsts steps of thermal treatment lead to the growth of *platelets* while their density decreases, as expected for a conservative *Ostwald* ripening type growth mechanism (see Fig. 2.10). It can be inferred that the H_2 molecules are produced mostly following the dissociation of hydrogenated point defects and the migration of H toward the *platelets* during a transient period. As the *platelets* grow by the injection of H from other less stable defects, the internal pressure quickly increases leading to their lateral propagation. Then, the average diameter of the *platelets* still increases and their density decreases in such a manner that the surface and volume fractions per unit area remain nearly constant (see Fig. 2.10 (b)). These observations are consistent with the model of a conservative *Ostwald* ripening mechanism.

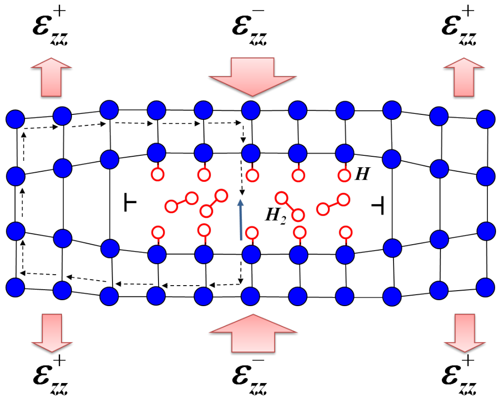

Fig. 2.11: Schematic representation of the lattice distortion resulting from a H-terminated Si atoms of a *platelet*. The cavity is filled with H_2 molecules and the internal surfaces are decorated with H atoms captured by dangling bonds. (adapted from [35]).

The most accepted model of *platelets* growth explains that the post-implant annealing cause the hydrogen diffusion in the vicinity of the *platelets* and then H is trapped and accumulates within them (see Fig. 2.11). This occurs at first stage of the annealing and is correlated to a abrupt decrease of hydrogen (shown by SIMS analysis in previous section). *Platelets* minimize their energy by forming a circular shape. These nanometric crack-like cavities contain pressurized H_2 gas [3, 22, 23, 35]. As a result of thermal annealing, pressure build-up and chemical action of H atoms at the crack tips may cause their lateral expansion.

An alternative scenario of *platelets* growth is given by Moras *et al.* [36]. Using molecular dynamics (MD), they simulate the thermal evolution of a realistically sized (100) *platelets*. Based on a dynamical «quantum-classical embedding» technique [36, 37], they model the growth of $10\,nm$-wide and $1\,nm$-thick *platelets* composed of two dihydride-terminated internal facing. Each *platelet* is embedded in a bulk silicon matrix, leading to model system sizes of up to 35000 atoms (see Fig. 2.12 (a) and (b)).

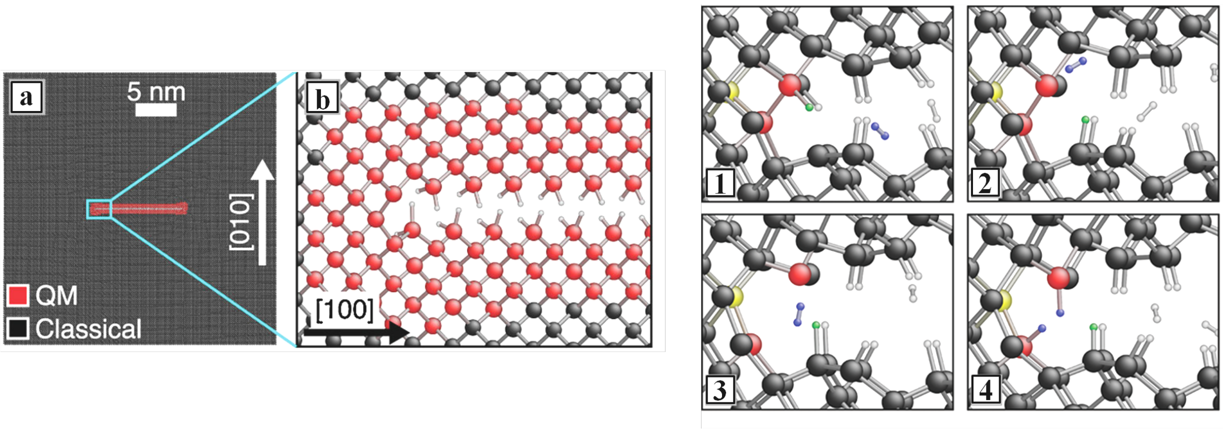

Fig. 2.12: Left : (a) Atomistic model of a (100) *platelets* at the center of a $35{\times}35\,nm^2$ bulk Si model system using periodic boundary conditions. The «quantum-classical embedding» region contain the Si atoms depicted in red and all H atoms. (b) Enlarged picture of a *platelet* left edge [36]. Right : Stress-corrosion mechanism for the *platelets* growth. (1)-(4) Snapshots of the bond-breaking reaction from an $800\,K$ hybrid quantum/classical molecular dynamics simulation. (adapted from [36]).

The MD simulations at $800\,K$ show that the presence of unsaturated dangling Si bonds triggers a dihydride-to-monohydride reconstruction of the internal surfaces, accompanied by the formation of H_2 molecules inside the *platelets*. It suggests that H_2 formation occurs spontaneously, sustained by H diffusion into the *platelet* from the surrounding H-supersaturated Si matrix. They argue that pressure-induced supercritical growth does not take place for *platelet* diameters smaller than approximately 1 µm. Further simulations show that some of the H_2 molecules reach the *platelet* edges. Then, one of the strained Si-Si bonds (connecting the red atoms in Fig. 2.12 (1)-(4)) breaks, while a H_2 molecule diffuses close to the two Si atoms (blue in Fig. 2.12 (1)-(3)). The molecule eventually dissociates irreversibly saturating the newly formed *Si* dangling bonds (Fig. 2.12 (4)). This model, based on a stress-corrosion mechanism, is consistent with the remarkably slow *platelet* growth observed experimentally [3, 21].

Nevertheless, an objection to this model is that, in contrast with the model presented previously, the irreversible character of the stress-corrosion model is not consistent with a conservative *Ostwald* ripening mechanism experimentally observed by Grisolia *et al.* [3] and more recently by Cherkashin *et al.* [38].

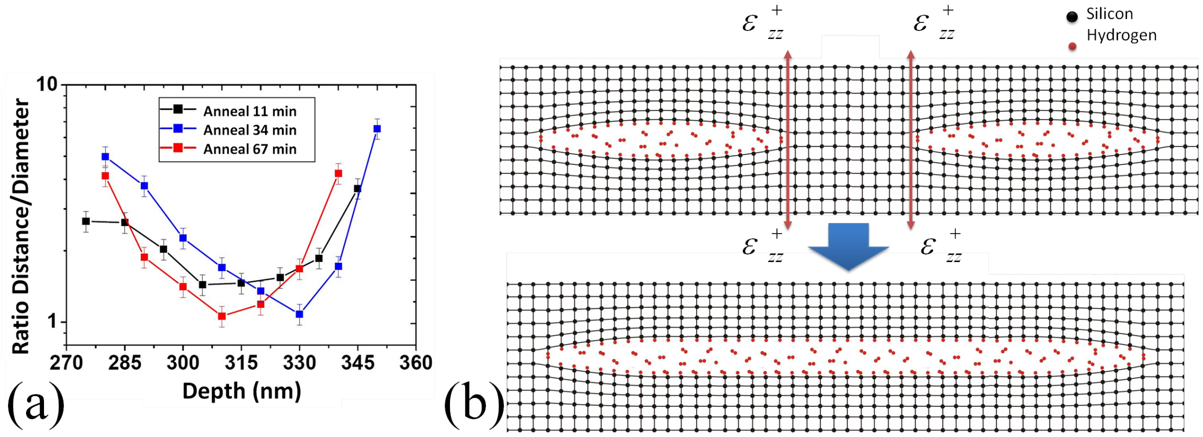

Fig. 2.13: (a) Ratio of edge to edge distance and *platelets* size as a function of the depth for different annealing duration at $T_{an} = 360\,°\mathrm{C}$. (b) Schematic of the *platelets* growth by coalescence process. (adapted from [24]).

Besides, it has been observed that larger micrometer-size *micro-cracks* appear at some stage in the *platelet* assembly. N. Daix has clearly demonstrated that this *micro-cracks* cannot be obtained by the extrapolation of the growth laws of *platelets* [15]. Moreover, it has been shown that the probability of interaction between neighboring *platelets* takes a maximum value when the distance separating two *platelets* is approximately equal to their diameter (see Fig. 2.13). It has then be suggested that *micro-cracks* spontaneously nucleate in *platelet*-rich regions by a coalescence process when the ratio distance/diameter is about 1 [15, 23]. This result is in agreement with mechanical simulations [39].

Furthermore, plan view *TEM* observations (see Fig. 2.14) [15, 24] show unambiguously that there is no *platelets* visible within *micro-cracks*, confirming that *micro-cracks* result from the collective mechanical interaction of a population of *platelets*. The driving force of this phenomenon would then be the minimization of the elastic energy of the system, obtained by forming a single extended defect from several *platelets* [15, 40].

The suggested scenario explains that *platelets* which are close to the maximum hydrogen concentration undergoes a very fast growth because of the «pumping» of molecular hydrogen combined to the geometric coalescence.

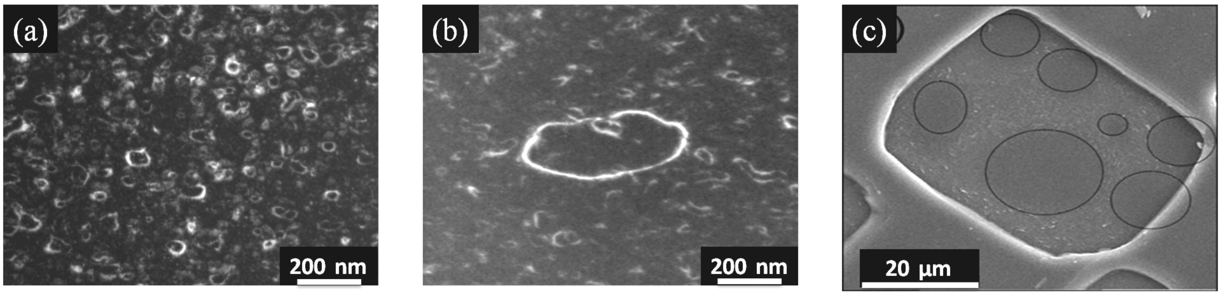

Fig. 2.14: Plane view *TEM* images of implanted and annealed Si samples at $360\,°C$ during (a) $11\,min$ where only *platelets* can be observed, and (b) $67\,min$ showing a *micro-crack* [24]. (c) High-magnification SEM micrographs showing the exfoliation morphologies for implanted and annealed Si samples (the dashed circles highlight the circular feature observed in the bottom of the exfoliated region. (adapted from [40]).

2.1.4 | Micro-cracks evolution

After longer annealing *micro-cracks* with sizes ranging from a few to several micrometers have been clearly evidenced by optical profilometry [23]. The evolution of this micrometer-size defects during the thermal annealing leading to the layer splitting is still matter of controversy. On the one hand, Personnic *et al.* [23] observed an almost conservative growth process based on *Ostwald* ripening mechanism until coalescence process takes place. On the other hand, Penot *et al.* [41] point out a non-conservative growth process supposedly driven by the vertical collection of the available gas from small *platelets*.

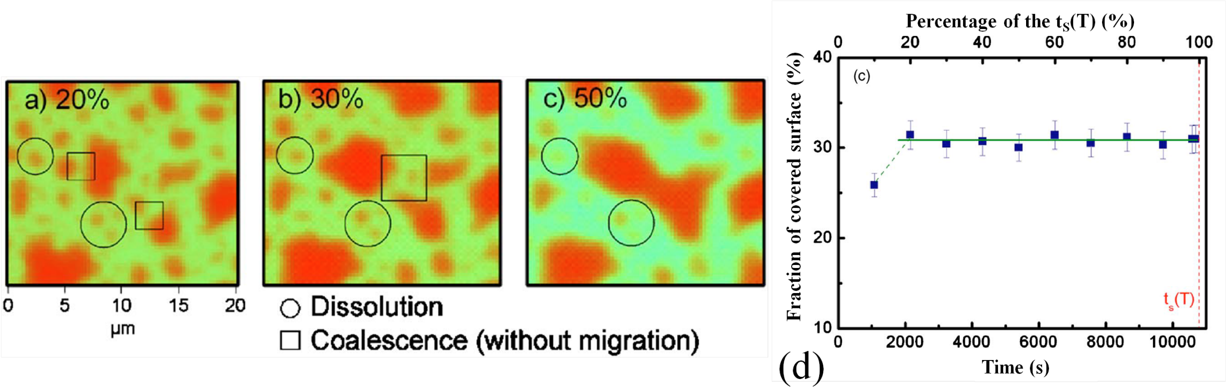

Fig. 2.15: Optical microscope images of buried *micro-cracks* after an annealing at $350\,°C$ for 20% (a), 30% (b), and 50% (c) of $t_s(T)$. The images illustrate the *Ostwald* ripening and the coalescence mechanisms. (d) Time dependence of the fraction of surface covered by *micro-cracks* [23].

Actually, Personnic *et al.* [23] investigated the thermal evolution of the *micro-cracks* at $350\,°C$ through optical interferometry (see Fig. 2.15 (a)-(c)). They have observed two distinct phenomena. First, small *micro-cracks* dissolve, while larger ones grow (circles in Fig. 2.15). This behavior suggests that *micro-cracks* are also involved in *Ostwald* ripening, *i.e.*, interchange the vacancies and hydrogen atoms they are composed of. However, it can be observed that the growth of the largest *micro-cracks* also occurs through the coalescence between neighboring, already large, *micro-cracks* (squares in Fig. 2.15). This phenomenon does not involve the motion of these defects but instead appears as the result of the sudden overlapping of their strain fields as they grow by the regular *Ostwald* ripening mechanism. Such a geometric coalescence leads to the random formation of large *micro-cracks* with the size up to tens of micrometers after annealing for 50% of $t_s(T)$. This growth mechanism gives rise to the formation of *micro-cracks* of irregular shapes, in contrast with the circular shape of the platelets. The study of the size distributions of the *micro-cracks* for different isothermal annealings, shows that the distribution becomes bimodal indicating the contribution of mechanical coalescence to the overall growth of the *micro-cracks* at the end of the annealing, just before fracture. Experimental observations by N. Daix [15], on other samples and using optical microscopy, confirms this behavior.

The most important conclusion from this analysis is that *micro-crack* coalescence occurs after and in parallel to their «regular» growth by *Ostwald* ripening and so that this coalescence process is almost conservative until fracture occurs.

More recently, Penot *et al.* [41] investigated *micro-cracks* using optical microscopy techniques (standard and near infra-red radiation). They observed that the mean diameter of *micro-cracks* increases while their density decreases, which is in agreement with the previous observations [23]. Additionally, the dispersion of sizes is quite large suggesting that coalescence between *micro-cracks* is dominant in the growth process. A typical example *micro-crack* development is shown in figure 2.16.

A quantification of the surface area covered by *micro-cracks* is made from the optical images (see Fig. 2.16 (a)). It shows an increase of the surface area with time in contrast with Personnic's observations. They also consider the absolute measurements of the interfacial gas released when propagating a crack through the *micro-cracks* (see Fig. 2.16 (b)). It can be noted that the amount of gas released increases with annealing time, in apparent contradiction with conservative mechanisms.

The proposed interpretation is that *micro-cracks* do not grow by *Ostwald* ripening, *i.e.*, interchanging vacancies and hydrogen atoms between *micro-cracks* but grow through vertical diffusion of hydrogen from small size high pressure *platelets* to larger size lower pressure *micro-cracks*. Indeed, when a large *micro-crack* is close to a highly pressurized small size *platelet*, there will be flux of hydrogen due to the large gradient of chemical potential between these two objects. As the depth distribution of hydrogen is concentrated around *Rp*, only vertical diffusion from *platelets* to *micro-cracks* is to be taken into account. The amount of hydrogen present in a *micro-crack* is proportional to the area that it cover. Hence, it is proposed that *micro-cracks* «pump» all the available hydrogen in *platelets* below and above the *micro-crack* plane. Actually, this model does not explain that small

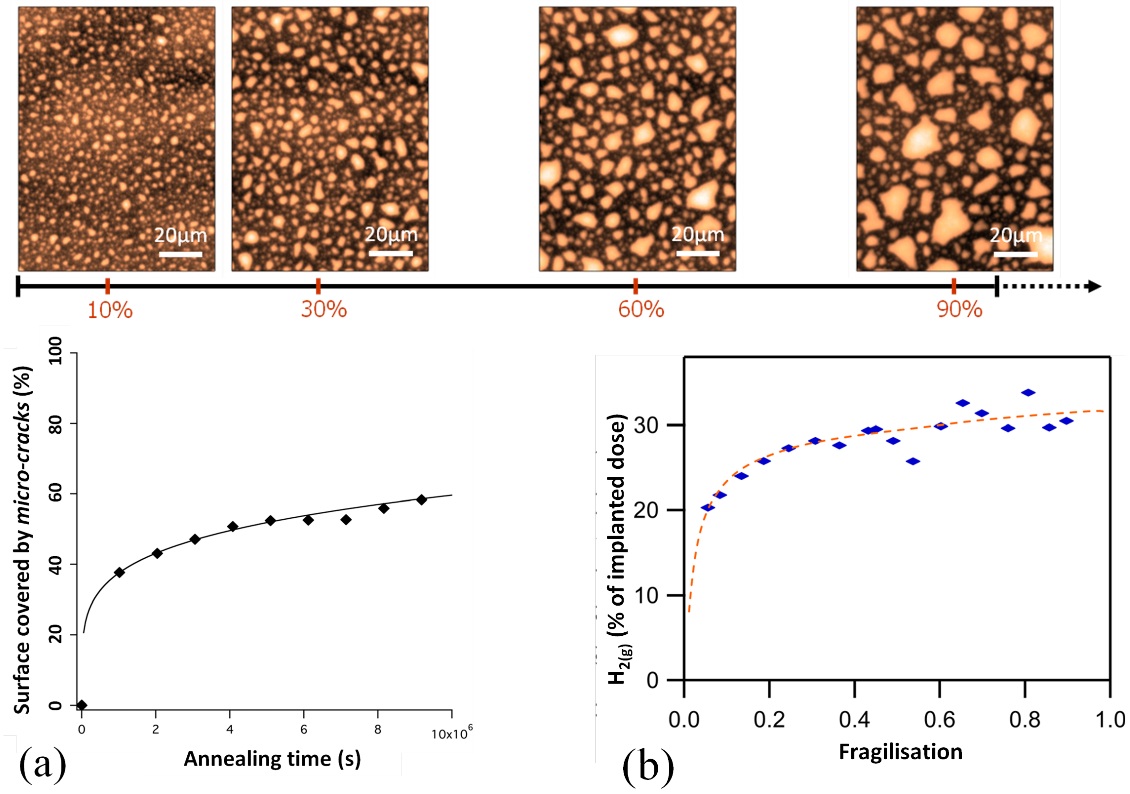

Fig. 2.16: Top: Typical evolution of *micro-cracks* as a function of annealing time observed by optical microscopy. Bottom: (a) Fraction of surface covered by *micro-cracks*. (b) Amount of hydrogen released from the interface opening. (adapted from [41]).

micro-cracks «disappear» during annealing.

Although different models are proposed to explain the thermal evolution of *micro-cracks*, most of authors agree that in the last stage of annealing, the larger *micro-cracks* under high hydrogen gas pressure strongly interact through the overlapping of their strain fields leading to some sudden coalescence process. This «catastrophic» behavior results in the fracture propagation across the *micro-cracks* plane and hence the splitting of the implanted layers allowing the full layer transfer of Si.

2.1.5 | Splitting and topography

Splitting induced by H^+ implantation followed by annealing leads to the formation of two new surfaces through the mechanisms described above. The morphology of these surfaces has been much less reported in the literature than the fundamental mechanisms involved in the splitting process. Chabal *et al.* [34] investigated post-splitting surfaces by AFM and observed that the RMS value is typically of about 5-10 nm.

Even if this layer is transferred by implantation induced splitting is suitable for wide-scale production, the improvement of the post-splitting roughness is required for the optimization of the process. Some approaches have been proposed to obtain a better selectivity of the «fracture propagation paths», through *micro-cracks* and/or *platelets*, in order to reduce the post-splitting roughness. The tight control of the H-implanted dose, the co-implantation of H^+ and He^+ and the spatial confinement of fracture by boron doping, are among the principal solutions investigated for this propose.

2.1.5.1 H^+ implantation dose

Chabal *et al.* [34] observed that the roughness of the post-splitting surfaces decreases as the implanted dose increases. Indeed, for $5\times10^{16}H^+/cm^2$ the obtained RMS value is equal to $11\,nm$ while it is only $5\,nm$ after $1\times10^{17}H^+/cm^2$. These observations are in agreement with those from Aspar *et al.* [22]. Bourdelle *et al.* [30] have shown that the orientation of the implanted wafer does not have any influence on the roughness or on the morphology of post-splitting surfaces. In all cases, these small values of roughness evidence that the fracture front propagates through *micro-cracks* located at approximately the same depth. We thus infer that the roughness of the post-splitting surfaces is related to the depth distribution of the *micro-cracks*.

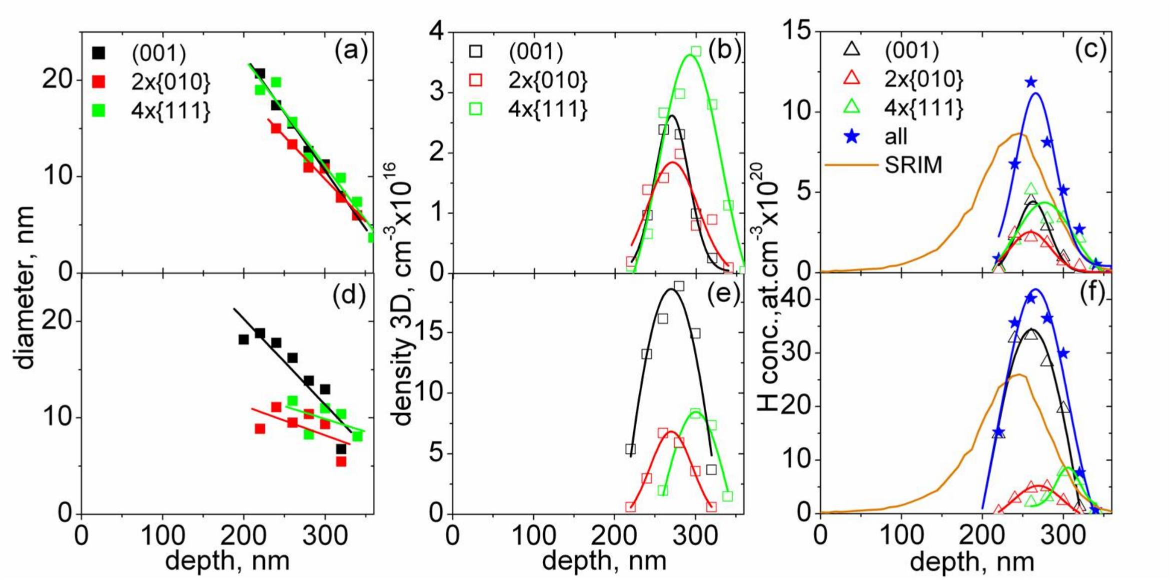

Fig. 2.17: Depth-distribution of diameter (a-d), densities (b-e) and H concentrations (c-f) for *platelets* with different orientations ((001), 010 and 111). Two different implanted fluence are investigated (1×10^{16} top and 3×10^{16} bottom). In (c) and (f), the H profiles predicted by *SRIM* are superimposed. (adapted from [42]).

Cherkashin *et al.* have investigated the depth-distribution of platelets formed in a (100) Si wafer [42]. Figure 2.17 shows an example of the analysis that they have performed. It can be noted that *platelets* size decreases linearly from the surface toward the substrate for any type of *platelet*.

Increasing the implanted dose favors the nucleation of (100)-*platelets* against the nucleation of (111)-*platelets*. Since (100)-*platelets* show a narrower depth-distribution than other types of *platelets*, the *micro-cracks* nucleate with a smaller vertical dispersion when the dose increases. Hence, the resulting post-splitting roughness tends to be lower when the implantation dose increases [17, 21]. It can then be suggested that roughness differences are intimately related to the depth-distributions of the *micro-cracks* which depends on the initial depth-distributions of the *platelets*.

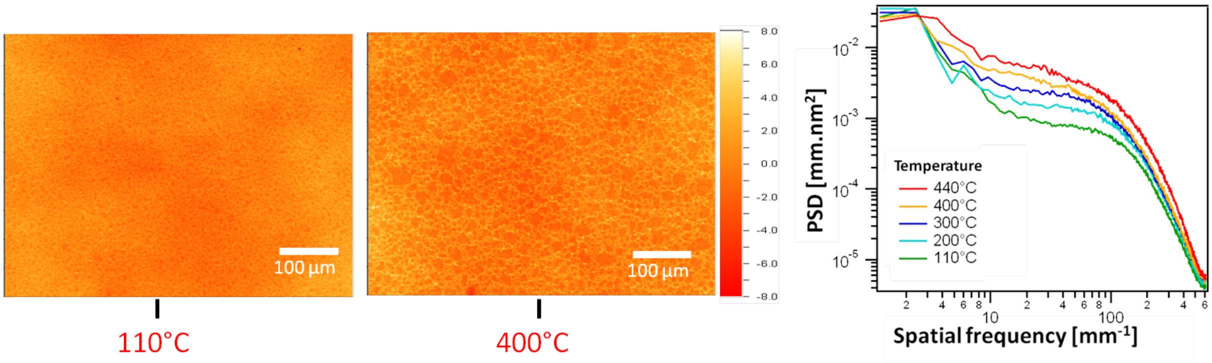

Fig. 2.18: Left: Surface topography recorded by optical interferometry of post-splitting surfaces fabricated using different temperatures. Right: *PSD* functions describing the topographic variations of these post-splitting surfaces. (adapted from [43]).

Besides, it has been demonstrated that the post-splitting roughness also depends on the annealing temperature [43]. Figure 2.18 shows images obtained by optical interferometry of post-splitting surfaces using different annealing temperatures. The corresponding *PSD* functions are also plotted in the same figure. It can be observed that, for spatial frequencies between $10\,mm^{-1}$ and $100\,mm^{-1}$, the amplitude of the *PSD* functions decreases with the annealing temperature. This suggests that the lateral size of *micro-cracks* just before splitting does not depend too much on the temperature while their depth-distribution increases with increasing temperature [43].

2.1.5.2 *H*-*He* Co-implantation

Agarwal *et al.* [44] have observed that H and He co-implantation produces splitting for much smaller total doses than any of the individual elements alone (see Fig. 2.19). Under their specific experimental conditions, the best results, in terms of splitting kinetics, were obtained by implanting H first, then He [44, 45]. However, there are controversial reports about the role and benefit of the implantation order and we recommend reading the Ph.D. thesis by Reboh [11] and Daix [15] for further information concerning splitting kinetics in the co-implantation case. Today, best results are obtained by using He first.

In terms of roughness, it has been observed that it is possible to obtain post-splitting surfaces with *RMS* values down to 5-8 nm after using co-implantation [15] . Figure 2.19 shows the *RMS* values obtained from AFM measurements of surfaces after splitting using

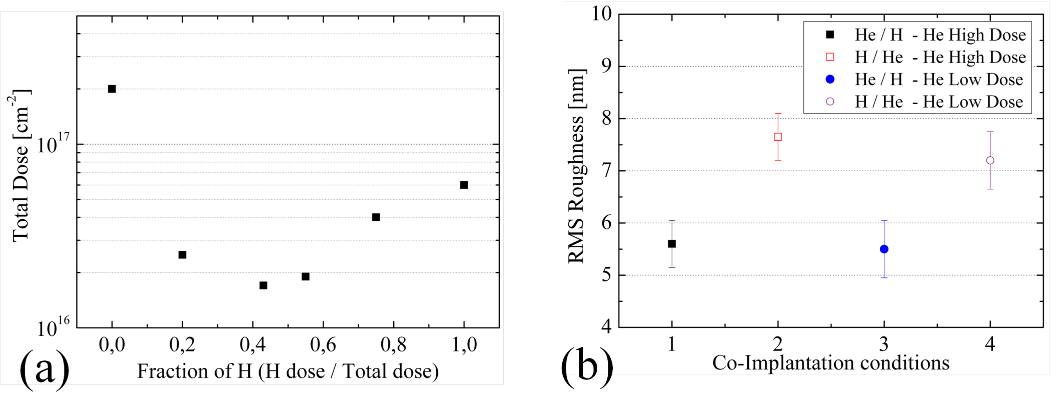

Fig. 2.19: (a) Total ($H + He$) implantation dose necessary for blistering vs. fraction of H (adapted from [44]). (b) *RMS* value extracted from AFM images of post-splitting surfaces as a function of the implantation conditions. (adapted from [15]).

different co-implant conditions. When He is implanted first, the post-splitting roughness is considerably reduced comparing with that obtained when H is implanted first.

Hence, appropriate co-implantation conditions can lead both to the reduction of the total implanted dose needed to split the implanted layer [44, 46], and to an improvement in the roughness of the transferred Si layers.

2.1.5.3 Buried Boron Layer

Tong *et al.* [47] have investigated the splitting kinetics of Si wafers which have been first implanted by B^+ and then implanted by H^+. They have found that the splitting temperature for B-H co-implanted wafers is significantly reduced compared to the H-only implanted ones. Figure 2.20 (a) shows the changes of the blistering temperature as a function of the B dose when the annealing time is fixed to 1 min. Sequential implantation of B and H ions into Si favor the growth of (100) *platelets* against the growth of (111) *platelets* during annealing (see Fig.2.20 (b)-(c)) [47, 48].

It has also been observed that the roughness of the post-splitting surfaces obtained by B-H co-implantation is much smaller than those obtained after a standard H-only implantation (see Fig.2.21). Since the B depth distribution is narrower than that of H, and because it is though that defects induced by B implantation can adsorb the H ions, so the latter is concentrated in a limited depth range and splitting is confined into this band contributing to the decrease of the roughness of the obtained surfaces.

It is also possible to use buried layers, heavily doped with B grown by CVD, to decrease even more the post-splitting roughness. Kilanov *et al.* [50] have investigated the effect of a very narrow B layer (1-2 monolayers-thick) buried at 500 nm from the surface on the exfoliation of Si layer after H implant. They observed that the composition of H-induced defects, after annealing, is not affected by the presence of the B buried layer. They also

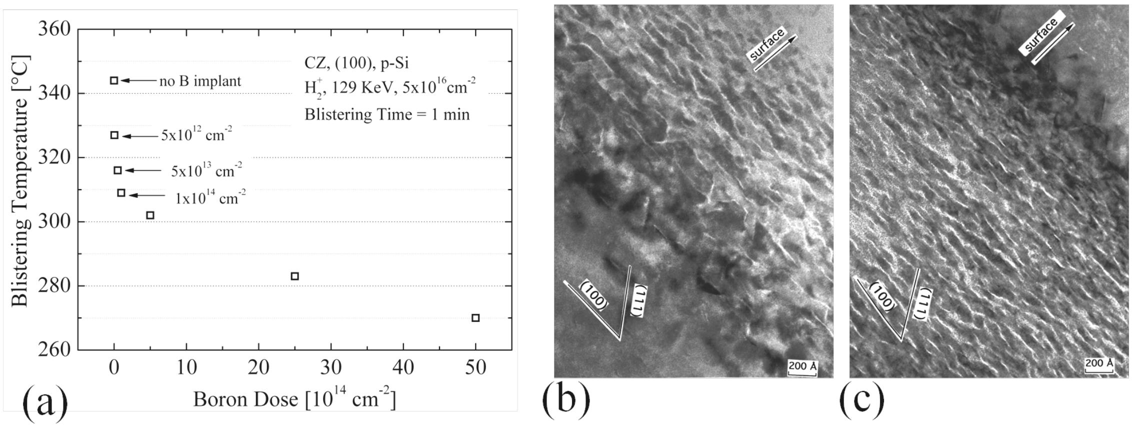

Fig. 2.20: (a) Required temperature to form optically detectable surface blisters in H-implanted Si for a fixed annealing time as a function of the dose of boron ions implanted. Cross-sectional *HRTEM* images of (b) H-only implanted and (c) B-H co-implanted Si wafers. (adapted from [47]).

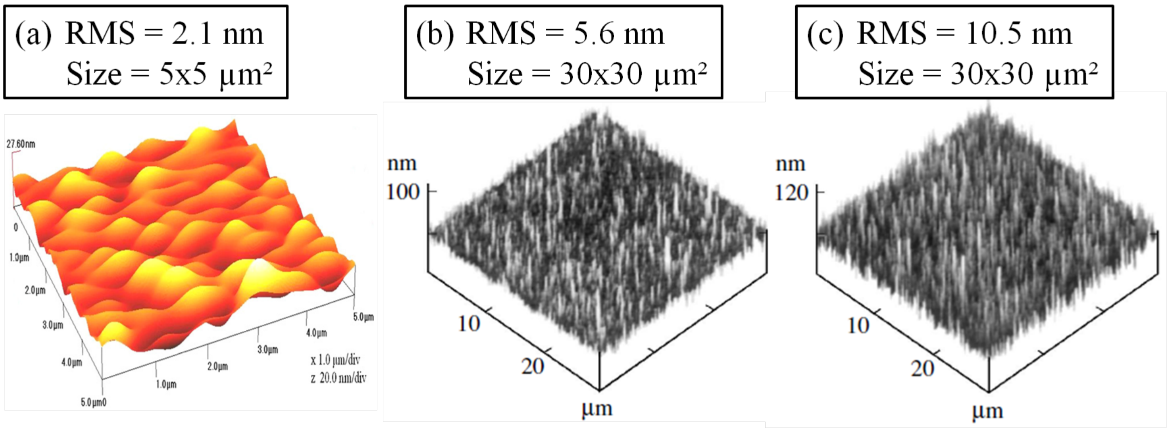

Fig. 2.21: AFM images of post-splitting surfaces obtained from: (a) post-splitting wafer with B-H co-implantation (adapted from [49]). (b) from a wafer containing a buried doped layer and (c) from a wafer without buried layer. (adapted from [50])

note that *micro-cracks* are formed in a region close to the buried layer. As shown in figures 2.21 (b)-(c) roughness obtained using this kind of buried layer is reduced by a factor of 2.

The approaches presented above may be considered as candidates to improve the Smart Cut™ technology, providing both reduced implantation doses and smaller roughnesses than those obtained by H-only implantation.

2.2 | Experimental results

Hereafter, we will study the influence of the total dose, in both the H-implantation and H-He co-implantation, on the surface topography after splitting. The experiment consists in recording AFM images of post-splitting surfaces and then analyzing their roughness, in terms of amplitude variations (RMS values) and in terms of spectral «foot-prints» through their PSD functions.

2.2.1 | Sample preparation

(100)-oriented Czochralski (Cz) grown p-type $300\,mm$-in-diameter Si wafers with high surface and warpage qualities were used. A $145\,nm$-thick oxide was formed by thermal oxidation and then the Si wafers were implanted through the oxide layer using two different protocols. The first one, consists in implanting H^+ ions with an energy such that $Rp \sim 300\,nm$ (few tens of keV) at doses of 5.5, 6, 8 and $10 \times 10^{16}\,cm^2$. The second one, consists in co-implanting H and He ions, in order to study the impact of the He implanted dose and of the order of implantation. Implantation order and doses used in this experiment are summarized in table 2.1. H^+ ions were always implanted with an energy of few tens of keV while the He^+ ions were implanted with energies such that the corresponding Rp is located slightly deeper than that of H^+ (LE = low energy). In order to test the influence of the implantation energy, an additional sample was prepared using an energy of about $10\,keV$ higher (HE = high energy), *i.e.*, implanted even deeper. Note that He^+ is always implanted deeper than H^+ in our experimental conditions.

Sample	***Co-imp 1***	***Co-imp 2***	***Co-imp 3***	***Co-imp 4***
Fisrt Implant($\times 10^{16}\,cm^{-2}$)	$H : 1.0$	$H : 1.0$	$He : 1.5$; LE	$He : 1.5$; HE
Second Implant($\times 10^{16}\,cm^{-2}$)	$He : 1.5$; LE	$He : 1.5$; HE	$H : 1.0$	$H : 1.0$

Tab. 2.1: Summary of the implantation doses and energies of H-He co-implantation experiment (LE = low energy ; HE = high energy).

After implantation, the wafers were cleaned by standard RCA process and then bonded with Si wafers by hydrophilic direct wafer bonding. Then, thermal treatments were performed in the temperature range $T_{an} = 400 - 500\,°C$ during several tens of minutes (enough for splitting). Finally, the roughness of the post-splitting surfaces were measured by AFM.

2.2.2 | H^+-implantation

Images with different sizes have been recorded in order to investigate the topographic variations of the surface at different scales. Figure 2.22 shows typical $2{\times}2\,\mu m^2$ AFM images of the topography of the post-splitting Si surfaces for increasing implanted doses (H^+ implant only).

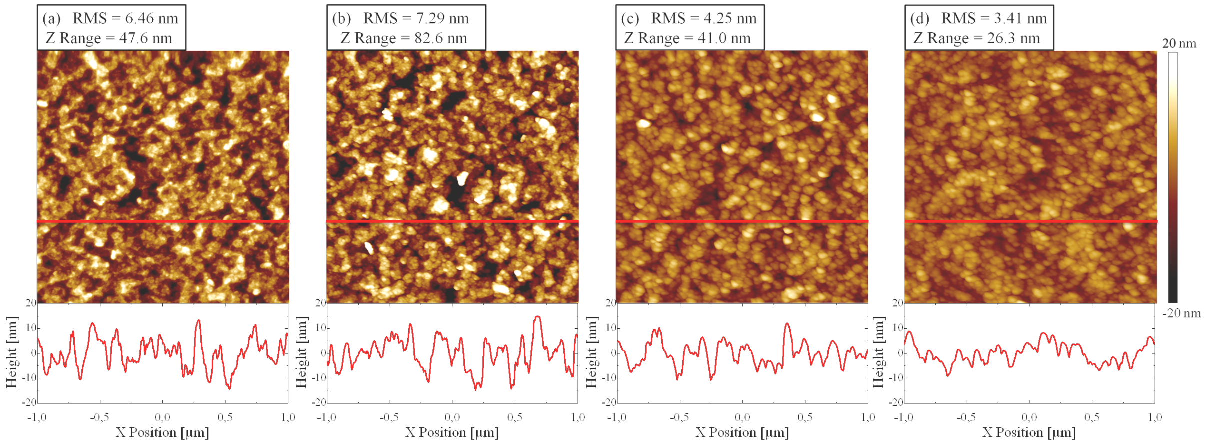

Fig. 2.22: Surface topography of post-splitting surfaces recorded by AFM (Scan size: $2{\times}2\,\mu m^2$; $512{\times}512$ pixels). Corresponding implanted doses are: (a) $5.5{\times}10^{16}\,cm^{-2}$, (b) $6{\times}10^{16}\,cm^{-2}$, (c) $8{\times}10^{16}\,cm^{-2}$ and (d) $10{\times}10^{16}\,cm^{-2}$. The bottom insets show height profiles for each image.

Figure 2.23 shows the RMS values obtained from $2{\times}2\,\mu m^2$ and $10{\times}10\,\mu m^2$ AFM images of the post-splitting surfaces. The RMS values continuously decrease as the implanted dose increases. Indeed, increasing the implanted dose favors the nucleation of (100)-*platelets* and thus the nucleated *micro-cracks* are better confined (see section 2.1.5). It is worth noting that roughnesses lower than $4\,nm$ are not attainable because higher doses do not lead to splitting [9].

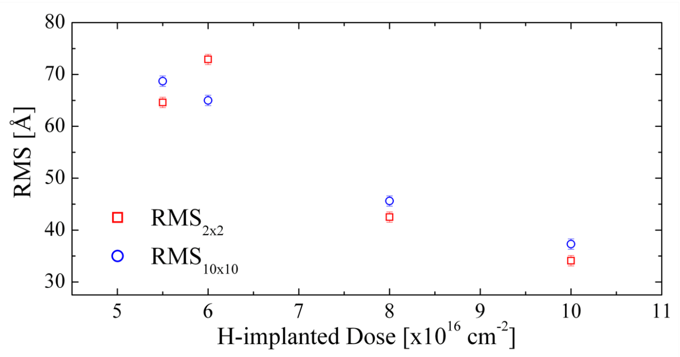

Fig. 2.23: *RMS* values calculated from recorded AFM images of post-splitting surfaces.

From the recorded AFM images, one can calculate either the one-dimensional *PSD* function (PSD_{1D}) or the two-dimensional function (PSD_{2D}). Since the post-splitting surface is considered as isotropic, both of them give similar results. Figure 2.24 shows the PSD_{1D} functions calculated from the AFM images shown in figure 2.22 superimposed with PSD_{1D} functions calculated from the $10\times10\,\mu m^2$ AFM images of the same samples. The PSD functions obtained from $10\times10\,\mu m^2$ images well overlaps those obtained from $2\times2\,\mu m^2$ images evidencing the consistency of the measurements.

We can distinguish two different behaviors. On the one hand, for spatial frequencies higher than $10\,\mu m^{-1}$, the amplitude of the PSD functions decreases as a power-law of the spatial frequency. This is a typical behavior of self-affine fractal surfaces (see section 1.1.2). The scaling exponent is found to be $\alpha = 0.85 \pm 0.10$ close to the value predicted for brittle fracture surfaces (around $\alpha = 0.8$) [51–53] and to that obtained for a fracture resulting from the coalescence of numerous *micro-cracks* described by an «avalanche behavior» (around $\alpha = 0.7$) [54, 55]. On the other hand, for spatial frequencies lower than $2\,\mu m^{-1}$, the amplitude of the PSD functions remains almost constant. This means that each spatial frequency equally contributes to the total height variations, what is typical of a random phenomenon.

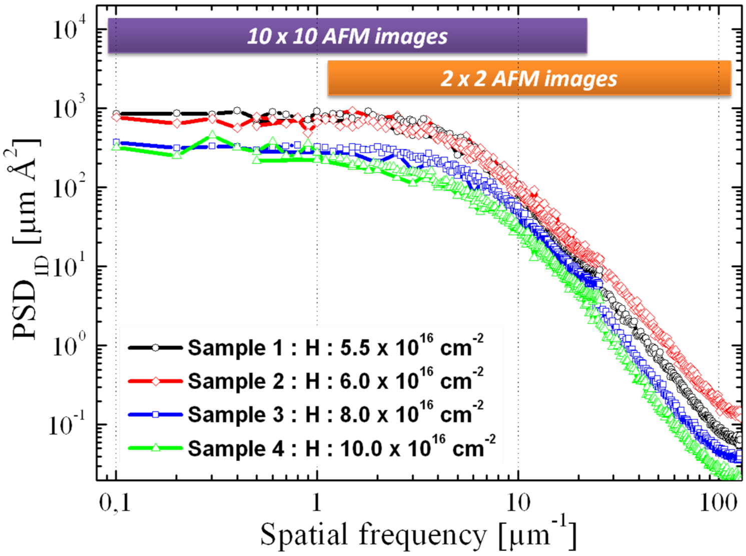

Fig. 2.24: PSD_{1D} functions (obtained from 2×2 and $10\times10\,\mu m^2$ AFM images) describing roughness variations of post-splitting silicon layers after H-implantation with different doses. Two spectral domains are observed, (a) low-frequencies [lower than $2\,\mu m^{-1}$] where the amplitude remains constant and (b) high-frequencies [higher than $10\,\mu m^{-1}$] where amplitude decreases as a power function of the spatial frequency.

Besides, from such curves, we can extract the characteristic spatial frequency f_c which corresponds to the crossover length $\lambda = f_c^{-1}$ separating the two different characteristic regions describing the post-splitting surfaces (see Fig. 2.25). This characteristic length quantifies the larger lateral dimensions of the topographical features measured on the post-splitting surfaces which shows a fractal characteristic.

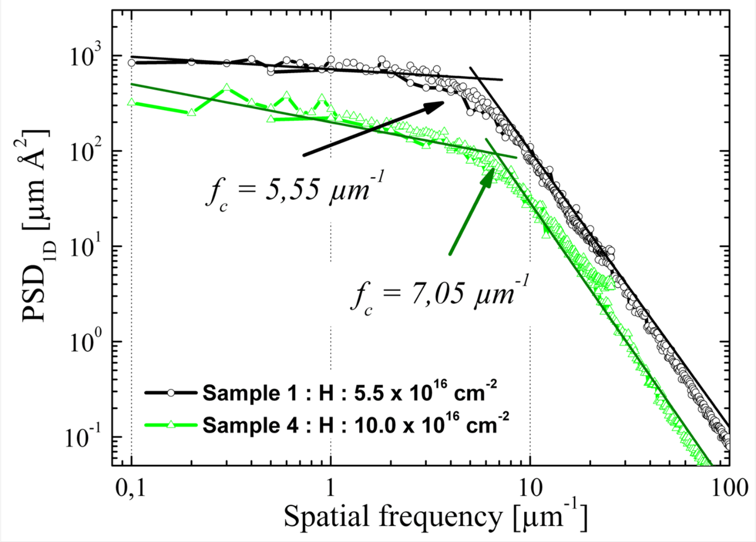

Fig. 2.25: PSD_{1D} functions corresponding to the higher and lower limit doses. For the low-frequencies [lower than $2\,\mu m^{-1}$] the amplitude oh the *PSD* function remains constant and for high-frequencies [higher than $10\,\mu m^{-1}$] the observed roughness exponent is $\alpha = 0.85 \pm 0.10$.

Figure 2.26 shows the evolution of this characteristic length as a function of the implanted dose. We observe that, whatever we use the PSD_{1D} or PSD_{2D} functions, the characteristic length decreases (from $180\,nm$ down to $140\,nm$) when the H-implanted dose increases (from 5.5×10^{16} to $10 \times 10^{16}\,cm^{-2}$).

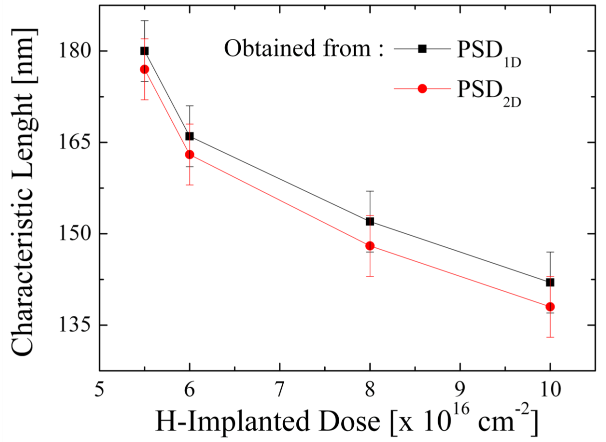

Fig. 2.26: Characteristic length estimated from *PSD* functions describing roughness of post-splitting surfaces

Indeed, the growth of the *platelets* results from a *Ostwald* ripening mechanism, which has been modeled by J. Grisolia [56] following the work by Bonafos *et al.* [57]. The extrapolation of this growth law ($3\,h$ annealing) leads to an average diameter equal to $140\,nm$, which is consistent with values obtained hereinabove. Thus, we can infer that the lateral dimensions of the topographical structures observed by AFM on the post-splitting surfaces, are intimately related to the diameter of the *platelets* when the splitting occurs. Since typical size of *micro-cracks*, after splitting, is about few tens of microns (see section 2.1.4), the AFM images performed in our experiments do not permit their characterization.

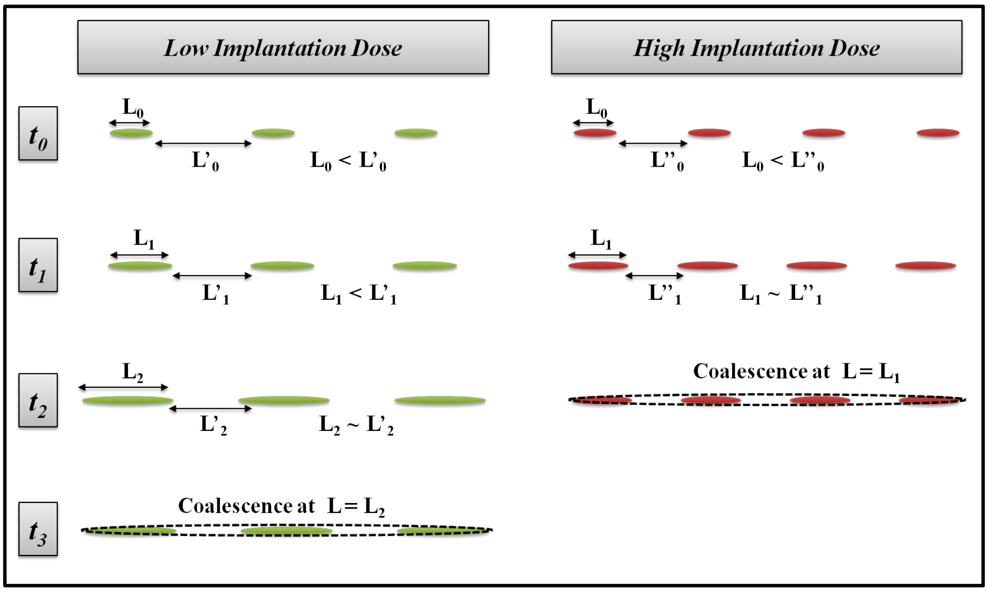

Fig. 2.27: Evolution of *platelets* during annealing using high and low implanted doses. L_0 represents the initial diameter of the *platelets* (just after nucleation). L'_0 and L''_0 are the initial edge to edge distances between *platelets* in the case of the low and high implanted doses respectively. According to the implantation dose, the coalescence criteria ($ratio\ distance/diameter \sim 1$) is reach at $L = L_2$ and $L = L_1$ respectively.

Figure 2.27 shows a schematic illustration of the evolution of *platelets* in the case of high and low implanted doses. Indeed, a higher implantation dose leads to an increase of the density of the nucleation sites for the *platelets* (see section 2.1.2). Because the *platelets* density is higher, the average distance between *platelets* is shorter for higher implanted doses (see L'_0 in Fig. 2.27). Since the *platelets* growth follows an *Ostwald* ripening mechanism, the initial supersaturation (given by the implanted dose) has no influence on the initial size of *platelets* or on the growth kinetics [38]. Thus, initial size of *platelets* is similar in both cases as observed experimentally and expected from the *Ostwald* ripening theory (see L_0 in Fig. 2.27). Then, *platelets* grow until they reach the critical size giving rise to their coalescence (ratio distance/diameter $\sim$ 1). We can thus suppose that the diameter of *platelets*, at the onset of the *micro-cracks* nucleation, is strongly related to the implanted dose (see L_1 vs. L_2 in Fig. 2.27).

In summary, we have observed that vertical height variations of the post-splitting surfaces decrease when the implanted dose increases, and this results both in a narrower depth distribution of *platelets* and *micro-cracks* and the decrease of the density of (111)-*platelets*. Besides, the mean diameter of the features observed on the surface also decreases when the implanted dose increases, this arises from the increase of the *platelets* density.

2.2.3 | He^{+}-H^{+} Co-implantation

Figure 2.28 shows typical AFM images of the post-splitting surfaces after He^{+}-H^{+} co-implantation.

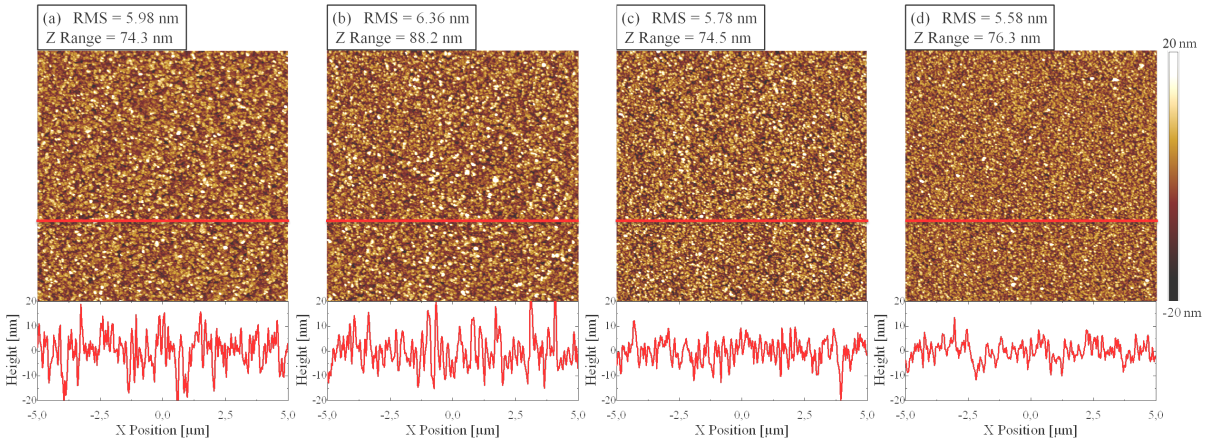

Fig. 2.28: Surface topography of post-splitting surfaces after co-implantation recorded by AFM (Scan size: $10 \times 10\,\mu m^2$; 512×512 pixels). Implanted doses were: H : $1.0 \times 10^{16}\,cm^{-2}$ and He : $1.5 \times 10^{16}\,cm^{-2}$. (a)-(b) Helium last-implanted with low (LE) and high (HE) energy respectively. (c)-(d) Helium first-implanted with LE and HE respectively.

Figure 2.29 shows the RMS values obtained from the AFM images presented above. It shows that the roughness obtained by first implanting He ions is significantly lower than that obtained by implanting H ions at first. We also note that the change of the He implantation energy does not impact the RMS value, in agreement with the literature [44–46].

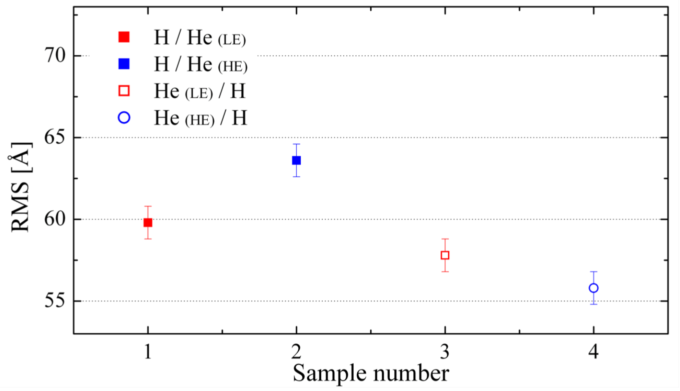

Fig. 2.29: *RMS* values calculated from AFM images shown in figure 2.28.

Figure 2.30 shows the PSD_{1D} functions characteristic of the post-splitting surfaces. We note that, as for H-only implantation, two domains are observed. However, the roughness exponent extracted from the slope of the PSD_{1D} functions over the high spatial frequencies domain, is slightly larger ($\alpha = 0.95 \pm 0.5$) than that obtained in the case of H-only implantation.

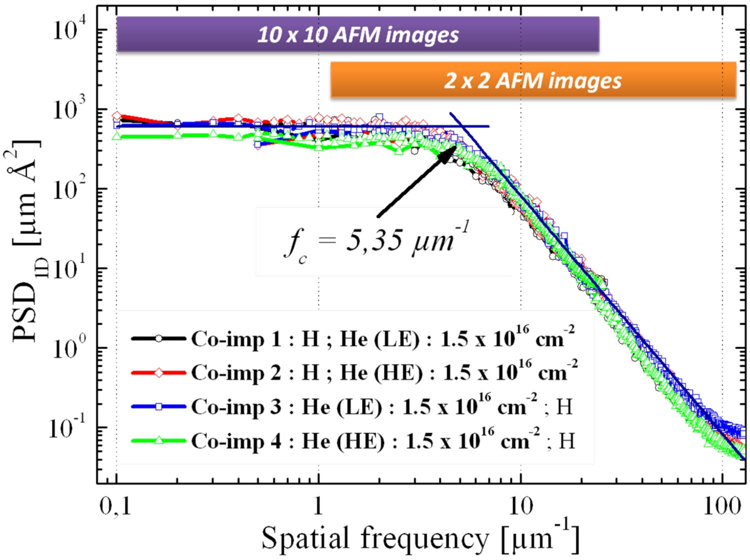

Fig. 2.30: PSD_{1D} functions (obtained from 2×2 and 10×10 μm^2 AFM images) describing roughness variations of post-splitting silicon layers after He^+-H^+ co-implantation with different conditions. Two spectral domains are observed, (a) low-frequencies [lower than $2\,\mu m^{-1}$] where the amplitude remains constant and (b) high-frequencies [higher than $10\,\mu m^{-1}$] where amplitude decreases as a power function of the spatial frequency with a roughness exponent $\alpha = 0.95 \pm 0.5$.

Furthermore, the crossover length extracted from the PSD functions is found to be approximately constant at $\lambda = 187\,nm$. Thus, this characteristic length is constant although the roughness changes (see Fig. 2.29). This implies that the final mean diameter of the *platelets*, is approximately independent on the co-implantation conditions.

Besides, the roughness of the post-splitting surfaces is significantly higher when H ions are implanted at first. It has been suggested that when He (which is implanted deeper) is implanted after H, the He implantation «breaks» the hydrogenated complexes (VH_n) which are the precursors of the *platelets*. Moreover, it has been shown that this interaction leads to a larger wideness of the nucleation sites depth-distribution [15]. Then, fracture propagation takes place over a larger depth distribution an this results in larger height variations (rougher surfaces). This hypothesis may explain that post-splitting surfaces obtained by first implanting H are rougher than those obtained by first implanting He.

Conclusions

In this chapter we have reviewed the principal physical mechanisms involved in the fracture process induced by light ion implantation and annealing. We have evidenced that fracture results from the multi-scale transformation of defects induced by implantation. Indeed, ion implantation produces point defects in the crystal matrix which transform into complexes at room temperature. Then, during annealing these defects precipitates leading to extended defects (*platelets* and/or *micro-cracks*) which grow during annealing. The interactions between these micrometric objects leads to their coalescence and finally to the splitting.

Besides, we have studied the influence of the implantation dose in the case of the H^+-implantation as well as the influence of the implantation order in the case of He^+-H^+ co-implantation, on the roughness of the post-splitting surfaces. For H-only implantation, we observed that the roughness of the post-splitting surfaces decreases when the implantation dose increases, because high doses favor the nucleation and growth of (100)-*platelets* in a narrow band, this ultimately resulting in a better confinement of the produced *micro-cracks*. Moreover, we have shown that a characteristic length, we have supposed to be related to the *platelets* mean diameter, decreases when the implantation dose increases. This suggests that the coalescence criterion is reached «earlier» for higher implanted dose. In the case of the He^+-H^+ co-implantation, the post-splitting surfaces are rougher when H is implanted at first. Since He^+ is implanted deeper than H^+, it is though that the increase of the roughness results from the interaction between H-induced defects (already formed) and the He implanted ions.

Bibliography

[1] S. Reboh, A. A. de Mattos, J. F. Barbot, A. Declemy, *et al.*, "Localized exfoliation versus delamination in H and He coimplanted (001) Si," *Journal of Applied Physics*, vol. 105, no. 9, 2009. (cited in pages 43, 44 and 45)

[2] M. K. Weldon, V. E. Marsico, Y. J. Chabal, A. Agarwal, *et al.*, "On the mechanism of the hydrogen-induced exfoliation of silicon," *Journal of Vacuum Science and Technology B*, vol. 15, no. 4, pp. 1065–1073, 1997. (cited in pages 43, 48 and 49)

[3] J. Grisolia, G. Ben Assayag, A. Claverie, B. Aspar, *et al.*, "A transmission electron microscopy quantitative study of the growth kinetics of H platelets in Si," *Applied Physics Letters*, vol. 76, no. 7, pp. 852–854, 2000. (cited in pages 43, 48, 49, 51, 52, 53, 54 and 55)

[4] T. Höchbauer, A. Misra, M. Nastasi, and J. W. Mayer, "Investigation of the cut location in hydrogen implantation induced silicon surface layer exfoliation," *Journal of Applied Physics*, vol. 89, no. 11, pp. 5980–5990, 2001. (cited in pages 43, 48, 49 and 51)

[5] N. Cherkashin, S. Reboh, A. Lubk, M. J. Hÿtch, and A. Claverie, "Strain in hydrogen-implanted Si investigated using dark-field electron holography," *Applied Physics Express*, vol. 6, no. 9, p. 091301, 2013. (cited in pages 43, 45, 46, 47, 48 and 51)

[6] F. Rieutord, F. Mazen, S. Reboh, J. D. Penot, *et al.*, "Lattice strain of hydrogen-implanted silicon: Correlation between x-ray scattering analysis and ab-initio simulations," *Journal of Applied Physics*, vol. 113, no. 15, p. 153511, 2013. (cited in pages 43, 46 and 48)

[7] S. Reboh, J. F. Barbot, M. F. Beaufort, and P. F. P. Fichtner, "H-induced subcritical crack propagation and interaction phenomena in (001) Si using He-cracks templates," *Applied Physics Letters*, vol. 96, no. 3, 2010. (cited in pages 43, 45 and 46)

[8] L.-J. Huang, Q.-Y. Tong, Y.-L. Chao, T.-H. Lee, T. Martini, and U. Gösele, "Onset of blistering in hydrogen-implanted silicon," *Applied Physics Letters*, vol. 74, no. 7, 1999. (cited in page 43)

[9] B. Terreault, "Hydrogen blistering of silicon: Progress in fundamental understanding," *physica status solidi (a)*, vol. 204, no. 7, pp. 2129–2184, 2007. (cited in pages 44, 45, 49 and 64)

[10] M. Bruel, "Silicon on insulator material technology," *Electronics Letters*, vol. 31, no. 14, pp. 1201–1202, 1995. (cited in pages 44 and 45)

[11] S. Reboh, *Defect engineering in H and He implanted Si.* PhD thesis, Universidade Federal do Rio Grande do Sul - Brasil and Université de Poitiers - France, 2008. (cited in pages 44, 49 and 60)

[12] N. M. p Johnson, F. A. Ponce, R. A. Street, and R. J. Nemanich, "Defects in single-crystal silicon induced by hydrogenation," *Phys. Rev. B*, vol. 35, pp. 4166–4169, Mar 1987. (cited in page 45)

[13] L. Capello, F. Rieutord, A. Tauzin, and F. Mazen, “Quantitative study of hydrogen-implantation-induced cavities in silicon by grazing incidence small angle x-ray scattering,” *Journal of Applied Physics*, vol. 102, no. 2, p. 026106, 2007. (cited in pages 45 and 48)

[14] S. Personnic, A. Tauzin, K. K. Bourdelle, F. Letertre, *et al.*, “Time dependence study of hydrogen induced defects in silicon during thermal anneals,” *AIP Conference Proceedings*, vol. 866, no. 1, pp. 65–68, 2006. (cited in pages 46, 49 and 53)

[15] N. Daix, *Mécanismes de base dans la co-implantation hélium / hydrogène du silicium.* PhD thesis, Université de Toulouse III - Paul Sabatier, 2009. (cited in pages 45, 46, 49, 55, 57, 60, 61 and 69)

[16] S. Personnic, *Etude des mécanismes de rupture du silicium induits par l’implantation ionique d’hydrogène dans le cadre de la technologie Smart Cut*^{TM}. PhD thesis, Ecole Nationale Supérieur des Mines, Saint-Etienne, 2007. (cited in page 45)

[17] N. Sousbie, L. Capello, J. Eymery, F. Rieutord, and C. Lagahe, “X-ray scattering study of hydrogen implantation in silicon,” *Journal of Applied Physics*, vol. 99, no. 10, p. 103509, 2006. (cited in pages 46 and 60)

[18] M. Hytch, F. Houdellier, F. Hue, and E. Snoeck, “Nanoscale holographic interferometry for strain measurements in electronic devices,” *Nature*, vol. 453, pp. 1086–1089, 2008. (cited in page 47)

[19] M. Hytch, N. Cherkashin, S. Reboh, F. Houdellier, and A. Claverie, “Strain mapping in layers and devices by electron holography,” *physica status solidi (a)*, vol. 208, no. 3, pp. 580–583, 2011. (cited in page 47)

[20] J. Biersack and J. Ziegler, “The stopping and range of ions in solids,” in *Ion Implantation Techniques* (H. Ryssel and H. Glawischnig, eds.), vol. 10 of *Springer Series in Electrophysics*, pp. 122–156, Springer Berlin Heidelberg, 1982. (cited in page 47)

[21] B. Aspar, M. Bruel, H. Moriceau, C. Maleville, *et al.*, “Basic mechanisms involved in the Smart-Cut process,” *Microelectronic Engineering*, vol. 36, no. 1–4, pp. 233 – 240, 1997. Proceedings of the biennial conference on Insulating Films on Semiconductors. (cited in pages 48, 49, 52, 55 and 60)

[22] B. Aspar, H. Moriceau, E. Jalaguier, C. Lagahe, *et al.*, “The generic nature of the smart-cut process for thin film transfer,” *Journal of Electronic Materials*, vol. 30, no. 7, pp. 834–840, 2001. (cited in pages 48, 53, 54 and 59)

[23] S. Personnic, K. K. Bourdelle, F. Letertre, A. Tauzin, *et al.*, “Impact of the transient formation of molecular hydrogen on the microcrack nucleation and evolution in H-implanted Si (001),” *Journal of Applied Physics*, vol. 103, no. 2, p. 023508, 2008. (cited in pages 37, 48, 49, 50, 51, 52, 53, 54, 55, 56 and 57)

[24] A. Claverie, N. Daix, F. Darras, S. Reboh, and N. Cherkashin, “Understanding the smart cut process: Evolution of defects during annealing of H^+ implanted silicon,” in *Surface Modification of Materials by Ion Beams*, vol. 13, 2013. (cited in pages 49, 55 and 56)

[25] K. K. Bourdelle, “Determining the mechanisms of fracture in group-IV materials,” in *Silicon-on-Insulator Technology and Devices XII, 2005: Proceedings Of The International Symposium*, vol. 2005, p. 167, The Electrochemical Society, 2005. (cited in page 49)

[26] F. A. Reboredo, M. Ferconi, and S. T. Pantelides, “Theory of the nucleation, growth, and structure of hydrogen-induced extended defects in silicon,” *Phys. Rev. Lett.*, vol. 82, pp. 4870–4873, Jun 1999. (cited in pages 49 and 50)

[27] J. G. Swadener, M. I. Baskes, and M. Nastasi, “Stress-induced platelet formation in silicon: A molecular dynamics study,” *Phys. Rev. B*, vol. 72, p. 201202, 2005. (cited in pages 50 and 51)

[28] M. Nastasi, T. Höchbauer, J.-K. Lee, A. Misra, *et al.*, “Nucleation and growth of platelets in hydrogen-ion-implanted silicon,” *Applied Physics Letters*, vol. 86, no. 15, p. 154102, 2005. (cited in page 51)

[29] A. Claverie, *Transmission Electron Microscopy in Micro-nanoelectronics.* Wiley Online Library, 2013. (cited in page 51)

[30] K. Bourdelle, T. Akatsu, N. Sousbie, F. Letertre, *et al.*, “Smart Cut^{TM}; transfer of 300 mm (110) and (100) Si layers for hybrid orientation technology,” in *SOI Conference, 2004. Proceedings. 2004 IEEE International*, pp. 98–99, 2004. (cited in pages 51 and 59)

[31] X. Hebras, P. Nguyen, K. Bourdelle, F. Letertre, N. Cherkashin, and A. Claverie, “Comparison of platelet formation in hydrogen and helium-implanted silicon,” *Nuclear Instruments and Methods in Physics Research Section B: Beam Interactions with Materials and Atoms*, vol. 262, no. 1, pp. 24 – 28, 2007. (cited in page 51)

[32] N. Martsinovich, I. Suárez Martínez, and M. I. Heggie, “First principles modelling of (100) H-induced platelets in silicon,” *physica status solidi (c)*, vol. 2, no. 6, pp. 1771–1780, 2005. (cited in pages 51 and 52)

[33] N. Martsinovich, M. Heggie, and C. Ewels, “First-principles calculations on the structure of hydrogen aggregates in silicon and diamond,” *Journal of Physics: Condensed Matter*, vol. 15, no. 39, p. S2815, 2003. (cited in page 51)

[34] Y. Chabal, M. Weldon, Y. Caudano, B. Stefanov, and K. Raghavachari, “Spectroscopic studies of h-decorated interstitials and vacancies in thin-film silicon exfoliation,” *Physica B: Condensed Matter*, vol. 273–274, no. 0, pp. 152 – 163, 1999. (cited in pages 51, 58 and 59)

[35] A. J. Pitera and E. A. Fitzgerald, “Hydrogen gettering and strain-induced platelet nucleation in tensilely strained $Si_{0.4}Ge_{0.6}/Ge$ for layer exfoliation applications,” *Journal of Applied Physics*, vol. 97, no. 10, p. 104511, 2005. (cited in pages 53 and 54)

[36] G. Moras, L. C. Ciacchi, C. Elsässer, P. Gumbsch, and A. De Vita, “Atomically smooth stress-corrosion cleavage of a hydrogen-implanted crystal,” *Phys. Rev. Lett.*, vol. 105, p. 075502, Aug 2010. (cited in page 54)

[37] G. Csányi, T. Albaret, M. C. Payne, and A. De Vita, ““learn on the fly”: A hybrid classical and quantum-mechanical molecular dynamics simulation,” *Phys. Rev. Lett.*, vol. 93, p. 175503, Oct 2004. (cited in page 54)

[38] N. A. Cherkashin, A. Claverie, C. Bonafos, V. V. Chaldyshev, *et al.*, "Influence of the initial supersaturation of solute atoms on the size of nanoparticles grown by an ostwald ripening mechanism," *Journal of Applied Physics*, vol. 102, no. 2, p. 023520, 2007. (cited in pages 55 and 67)

[39] R. Gers, *Fragilisation et rupture du silicium implanté dans le procédé Smart Cut^{TM}: Modélisation et simulation par éements finis.* PhD thesis, Institut National des Sciences Appliquées de Lyon,. (cited in page 55)

[40] S. Reboh, A. de Mattos, F. Schaurich, P. Fichtner, M. Beaufort, and J. Barbot, "The mechanisms of surface exfoliation in H and He implanted Si crystals," *Scripta Materialia*, vol. 65, no. 12, pp. 1045 – 1048, 2011. (cited in pages 55 and 56)

[41] J.-D. Penot, D. Massy, F. Rieutord, F. Mazen, *et al.*, "Development of microcracks in hydrogen-implanted silicon substrates," *Journal of Applied Physics*, vol. 114, no. 12, p. 123513, 2013. (cited in pages 56, 57 and 58)

[42] N. Cherkashin and A. Claverie, *Characterization of Process-Induced Defects, in Transmission Electron Microscopy in Micro-Nanoelectronics*, pp. 165–198. John Wiley and Sons, Inc., 2013. (cited in page 59)

[43] J.-D. Penot, *Fragilisation et dynamique de la rupture du silicium implanté.* PhD thesis, Université de Grenoble, 2010. (cited in page 60)

[44] A. Agarwal, T. E. Haynes, V. C. Venezia, O. W. Holland, and D. J. Eaglesham, "Efficient production of silicon-on-insulator films by co-implantation of He^+ with H^+," *Applied Physics Letters*, vol. 72, no. 9, 1998. (cited in pages 60, 61 and 68)

[45] X. Duo, W. Liu, M. Zhang, L. Wang, *et al.*, "Evolution of hydrogen and helium co-implanted single-crystal silicon during annealing," *Journal of Applied Physics*, vol. 90, no. 8, 2001. (cited in pages 60 and 68)

[46] F. Corni and R. Tonini, "Some aspects of blistering and exfoliation of helium–hydrogen coimplanted (100) silicon," *Nucl. Instrum. Methods in Physics Research B*, vol. 186, no. 1–4, pp. 349 – 354, 2002. (cited in pages 61 and 68)

[47] Q.-Y. Tong, R. Scholz, U. Gösele, T.-H. Lee, and others., "A "smarter-cut" approach to low temperature silicon layer transfer," *Applied Physics Letters*, vol. 72, no. 1, 1998. (cited in pages 61 and 62)

[48] B. Zhang, P. Zhang, J. Wang, F. Zhu, *et al.*, "Thermal evolution of defects in crystalline silicon by sequential implantation of B and H ions," *Nuclear Physics Review*, vol. 30, no. 4, 2013. (cited in page 61)

[49] X. Ma, W. Liu, C. Chen, D. Zhan, *et al.*, "A high-quality SOI structure fabricated by low-temperature technology with B^+/H^+ co-implantation and plasma bonding," *Semiconductor science and technology*, vol. 21, no. 7, p. 959, 2006. (cited in page 62)

[50] D. Kilanov, V. Popov, L. Safronov, A. Nikiforov, and R. Sholz, "Hydrogen-induced splitting in silicon over a buried layer heavily doped with boron," *Semiconductors*, vol. 37, no. 6, pp. 620–624, 2003. (cited in pages 61 and 62)

[51] J. Schmittbuhl, F. Schmitt, and C. Scholz, “Scaling invariance of crack surfaces,” *Journal of Geophysical Research: Solid Earth*, vol. 100, no. B4, pp. 5953–5973, 1995. (cited in page 65)

[52] S. Santucci, K. J. Måløy, A. Delaplace, J. Mathiesen, A. Hansen, J. O. Haavig Bakke, J. Schmittbuhl, L. Vanel, and P. Ray, “Statistics of fracture surfaces,” *Phys. Rev. E*, vol. 75, p. 016104, Jan 2007. (cited in page 65)

[53] F. Plouraboué, P. Kurowski, J.-P. Hulin, S. Roux, and J. Schmittbuhl, “Aperture of rough cracks,” *Phys. Rev. E*, vol. 51, pp. 1675–1685, Mar 1995. (cited in page 65)

[54] J. Schmittbuhl and K. J. Måløy, “Direct observation of a self-affine crack propagation,” *Phys. Rev. Lett.*, vol. 78, pp. 3888–3891, May 1997. (cited in pages 36 and 65)

[55] C. Lu, D. Vere-Jones, and H. Takayasu, “Avalanche behavior and statistical properties in a microcrack coalescence process,” *Phys. Rev. Lett.*, vol. 82, pp. 347–350, Jan 1999. (cited in pages 36 and 65)

[56] J. Grisolia, *Evolution thermique des défauts introduits par implantation ionique d’hydrogène ou d’hélium dans le silicium et le carbure de silicium*. PhD thesis, Université Paul-Sabatier Toulouse III - France, 2000. (cited in page 66)

[57] C. Bonafos, D. Mathiot, and A. Claverie, “Ostwald ripening of end-of-range defects in silicon,” *Journal of Applied Physics*, vol. 83, no. 6, 1998. (cited in page 66)

3 | Thermal Smoothening

Contents

As discussed in chapter 2, *Si* surfaces obtained by splitting show high topographic variations especially at high spatial frequencies (at the atomic level). Thus, one important step in SOI fabrication is the reduction of surface roughness. To this end, two processes are commonly used in the SOI manufacturing, the chemical-mechanical polishing (*CMP*) and the smoothening by thermal annealing at high temperature.

In this chapter, we will investigate the roughness evolution, by means of AFM, of silicon surfaces during annealing. Again, we will quantify the spectral evolution of surface topography through the *PSD* functions. Then, we will propose a predictive model, based on the Mullins-Herring (M-H) diffusion equation, to describe the evolution of the surface topography of silicon during thermal annealing as a function of time and temperature. We will also discuss the influence of the experimental conditions (annealing atmosphere, initial surface morphology) onto the smoothening of these surfaces during rapid thermal annealing (*RTA*). Then, we will explore the limitations of this smoothening technique. Finally, a MatLab® code allowing the simulation of the surface evolution for during thermal treatment (couple time - temperature) will be presented.

3.1 | Surface self-diffusion

Providing thermal energy to a crystal by heating, under appropriate atmosphere conditions, leads to the reconstruction of its surface so as to reduce its free surface energy [1]. Surface morphology can be modified through the transport of material based on several mechanisms which have been listed and investigated by Herring [2] and Mullins [3]. Figure 3.1 shows a schematic of the different possible transport mechanisms: surface self-diffusion, evaporation/condensation and volume (bulk) diffusion. As the atmosphere is never perfectly pure, chemical reactions of the surface with external molecules may alter its morphology, thus they must be taken into account (see Figure 3.1 (d)).

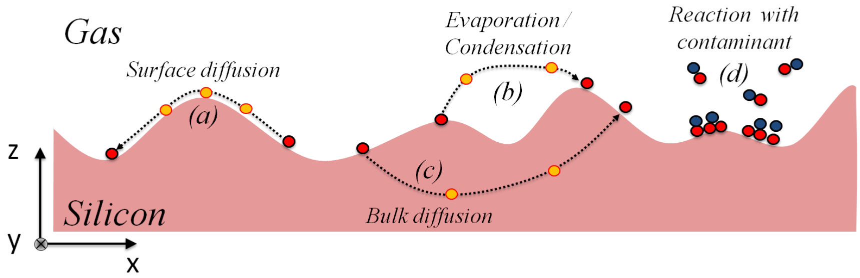

Fig. 3.1: Schematic of different matter transport mechanisms: (a) Surface self-diffusion, (b) Evaporation/condensation, (c) Bulk diffusion and (d) Chemical reaction with external molecules.

The relationship between time and characteristic lengths of the changes on the surface through those mechanisms can be described by simple scaling laws [2]. Indeed, the characteristic time τ associated to the surface evolution depends on the system size L, according to the scaling law $\tau \sim L^z$, where z is named the dynamic exponent and is usually written as $z = \alpha/\beta$, α being the roughness exponent and β being the growth exponent which respectively describe the evolution of the RMS value as a function of the system dimensions and of time [4]. A maximum value of the dynamic exponent, $z = 4$, is obtained for surface self-diffusion while $z = 2$ and $z = 3$ for evaporation/condensation and bulk diffusion, respectively. This means that surface self-diffusion is the most efficient mechanism for material transport to reduce surface roughness. Hence, most of the techniques used to reduce surface topography variations at high spatial frequencies (up to few microns length) are based on surface self-diffusion. One of them consist in annealing at high temperature in inert or reducing atmosphere [5–7]. Thus, the understanding of the atomic-scale mechanisms describing surface self-diffusion on silicon surface, at high temperatures is of great scientific and technological interest.

Surface self-diffusion was macroscopically described by Mullins in terms of the continuum surface model [8]. Mullins' theory treats the shape evolution of surfaces under the capillary forces arising from surface curvatures, in the case of surfaces of low curvature and isotropic surface energy [8]. Indeed, when surface diffusion is supposed to be the only mechanism operating, shape transformation occurs through atoms flux (j) along the surface which is driven by the surface gradients of the Gibbs-Thomson chemical potential, $\mu(\kappa) = \kappa\gamma\Omega$, where κ is the local curvature, γ is the surface tension, and Ω is the atomic volume. The flux of atoms, at the surface, is thus given by,

$$j = -\left(\frac{D_s \gamma \Omega \nu_s}{k_B Tan}\right) \frac{\partial \kappa}{\partial \zeta} \tag{3.1}$$

where D_s the surface diffusion coefficient, γ_s is the surface energy, Ω is the molecular volume, ν_s the number of atoms per unit area of the surface, ζ is arc-length along the surface, T_{an} is the annealing absolute temperature and k_B is the Boltzmann constant.

Since the increase in the number of atoms per unit area is given by $-\partial j/\partial \zeta$, we obtain the normal velocity $\nu_n = \frac{\partial h(\vec{x},t)}{\partial t}$, which describes the vertical displacement of the surface,

$$\nu_n = \frac{D_s \gamma \Omega \nu_s}{k_B T} \frac{\partial^2 \kappa}{\partial \zeta^2} \tag{3.2}$$

Indeed, the normal velocity ν_n at a given point of the surface, is proportional to the Laplacian of κ and thus rewrites as $\nu_n = \nu_4 \frac{\partial^2 \kappa}{\partial \zeta^2}$. The parameter ν_4 depends on both the material characteristics and the annealing temperature through the relationship: $\nu_4 = D_s \gamma_s \upsilon \Omega^2 / k_B T$, where υ is the atomic density. It is worth noting that this constant is directly proportional to D_s.

Now, assuming that the surface profile is defined by a function $h(\vec{x}, t)$, where $\vec{x}$ is the horizontal coordinate and t is time, Mullins [8] has shown that equation 3.2 can be written as a nonlinear, fourth-order partial differential equation for $h(\vec{x}, t))$, as follows,

$$\frac{\partial h(\vec{x},t)}{\partial t} = -\nu_4 \frac{\partial}{\partial x}\left[\chi \frac{\partial}{\partial x}\left(\chi^3 \frac{\partial^2 h(\vec{x},t)}{\partial x^2}\right)\right] \tag{3.3}$$

with, $\chi(\vec{x}, t) = \left[1 + \left(\frac{\partial h(\vec{x},t)}{\partial x}\right)^2\right]^{-1/2}$

In most crystalline systems, γ_s is much larger than typical interfacial energies γ_i. Then, the small-slope approximation, $\kappa \sim \frac{\partial^2 h(\vec{x},t)}{\partial^2}$ $(\chi \sim 1)$, may be used, resulting in the following linear equation for the evolution of the surface profile $h(\vec{x}, t)$, named the Mullins-Herring (M-H) equation [4, 8, 9].

$$\frac{\partial h(\vec{x},t)}{\partial t} = -\nu_4 \frac{\partial^4 h(\vec{x},t)}{\partial x^4} \tag{3.4}$$

This simple model allows one to describe how an isotropic crystalline surface showing asperities of low aspect ratios (low curvatures) evolves during thermal annealing. Actually, this model is still valid for surface asperities whose aspect ratio is smaller than 8% [10, 11]. Although this theory is valid only for isotropic surfaces above the surface roughening temperature T_R, it has been used to interpret phenomena below T_R, because of its mathematical convenience in analyzing experimental data [6, 12, 13].

Even if the M-H equation (Eq. 3.4) is deterministic, there is some inherent randomness of the system. Indeed, surface self-diffusion can be seen as adatoms jumping between adjacent adsorption sites on the surface and thus it is a probabilistic process. This randomness can be described by a stochastic term ($\eta(\vec{x},t)$ added to the right-hand side of the M-H equation) [4, 14],

$$\frac{\partial h(\vec{x},t)}{\partial t} = -\nu_4 \frac{\partial^4 h(\vec{x},t)}{\partial x^4} + \eta(\vec{x},t) \tag{3.5}$$

where $\eta(\vec{x},t)$ is a non-conservative noise (NCN) which is uncorrelated in space and time (Eq. 3.5 is commonly called the «noisy M-H equation»). In case of rapid thermal annealing (RTA) at high temperature, this term can be related to the surface evolution due to the oxidation-evaporation of silicon, which is due to the presence of some oxygen contamination at the atmosphere [14]. Since this phenomenon is considered to take place randomly at the silicon surface, it can be described by the NCN term. The space-average of this NCN must be zero ($\langle\eta(\vec{x},t)\rangle = 0$). Its correlator, describing the spatial correlation of the NCN, can be written as $\langle\eta(\vec{x},t)\eta(\vec{x}',t')\rangle = 2\Delta_{NCN}\delta^d(\vec{x}-\vec{x}')\delta^d(t-t')$ [4, 14].

Many authors have experimentally studied surface self-diffusion through the shape transformation of periodic superficial silicon structures during annealing at high temperatures. The first experimental study of the kinetics of surface evolution during annealing at high temperature of such periodic surfaces was performed by Blakely *et al.* [15]. Afterward, Keeffe *et al.* [12] investigated the gradual change of periodic atomic step arrays on (001)-oriented Si surfaces caused by annealing. The evolution of the steps amplitudes were studied through different microscopy methods. They observed that it decays following an exponential law of the fourth order, indicating that under their experimental conditions, self-surface diffusion was mainly responsible for the mass transport.

More recently, Kuribayashi *et al.* [16] investigated the shape transformation of micron-sized silicon trenches during high temperatures (between 900 and 1100 °C) in hydrogen ambient using scanning electron microscopy (SEM) and AFM. The time dependence of the curvatures of the upper corners of trenches, observed by SEM, is consistent with $\kappa \propto (\nu_4\, t)^{-1/4}$ as expected for the Mullins' theory. Moreover, a dramatic decrease of the surface roughness (analyzed by AFM and comparing RMS values) is observed. The shape transformation of silicon trenches under equivalent experimental conditions (temperatures commonly used are between 900 and 1150 °C and pressure varies from 10 to 40 $Torr$) has been studied by many authors, yielding very similar results [6, 17]. Figure 3.2 shows typical trenches evolution during annealing at high temperatures.

Furthermore, numerical simulations based on Mullins' theory have been performed in order to treat the shape transformation of an entire trench profile [13, 18]. Figure 3.2 (c) shows typical profiles obtained by simulation of the thermal evolution of trenches compared with the experimental observed profiles. All simulations confirm that surface

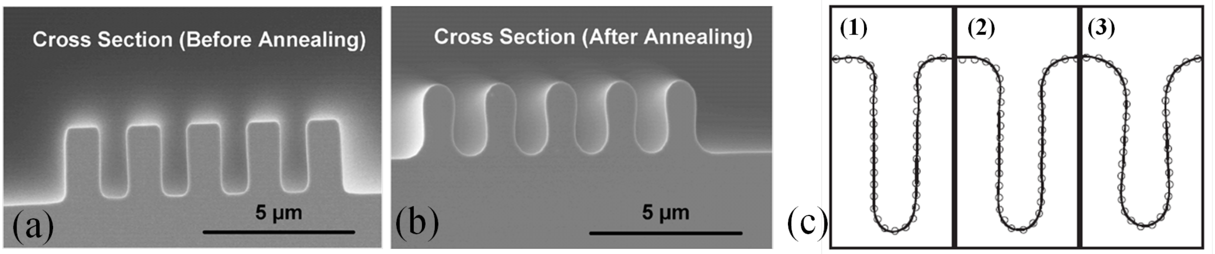

Fig. 3.2: Cross sectional SEM micro-graphs of Si trenches, (a) before and (b) after hydrogen annealing at $1100\,^{\circ}\mathrm{C}$ and $10\,Torr$ for $5\,\mathrm{min}$ [17]. (c) Calculated trench profiles (solid curves) are compared with experimental profiles (open circles) extracted from SEM images.Trenches were annealed in H_2 at $1000\,^{\circ}\mathrm{C}$ for (1) $30\,\mathrm{s}$, (2) $180\,\mathrm{s}$, and (3) $600\,\mathrm{s}$ [13].

self-diffusion is the dominant mechanism driving shape transformation. These simulations also show that the low curvature approximation does not hold for micron-sized trenches with high aspect-ratios ($> 8\%$). Moreover, these simulations show that the high aspect ratio patterns, after a transient stage, adopt a specific «universal» shape which is mathematically well-specified [18].

Even if these investigations are pertinent to describe the kinetics of Si trenches during annealing, only one spatial frequency, corresponding to the period of structures, is actually studied. Hereafter, we propose an original and general approach allowing the assessment of the thermal evolution of Si surfaces of given roughnesses. Indeed, our work takes into account the spectral evolution, over a large spatial bandwidth, of the surface roughness due to surface self-diffusion mechanisms.

3.2 | Smoothening by Rapid Thermal Annealing

3.2.1 | Experimental procedure and samples

Silicon surfaces can undergo a roughening transition from a faceted to a rough surface above the roughening temperature (T_R), where surface self-diffusion can be seen as isotropic [19, 20]. For example, for (001)-oriented Si surfaces, T_R is approximately $1050\,^{\circ}\mathrm{C}$ [21–23]. The thermal treatments investigated here are done at high enough temperatures so that surface diffusion can be assumed to be isotropic. Considering annealing times of few seconds (typical RTA duration), thermal annealing above T_R leads to characteristic lengths ($\lambda_D = \sqrt[4]{\nu_4 t}$ where ν_4 is the surface diffusion rate of adatoms for a given temperature) of at least a few micrometers [12, 24]. Thus, in order to observe the evolution of a surface topography during RTA at high temperatures, it is important to use a starting material whose initial topography shows high vertical variations at those characteristic lengths.

In the Smart Cut™ process, the fracture of silicon induced by ion implantation is used to transfer thin silicon films. This fracture leads to a surface showing fractal characteristics with a low roughness exponent ($\alpha = 0.85 \pm 0.1$, see section 2.2 in chapter 2). Moreover, as discussed previously, the evolution of hydrogenated defects induced by implantation and responsible for the silicon fracture, lead to the formation of *micro-cracks* with size-distributions in the range of a few micrometers which determine the roughness of the post-fracture silicon surfaces [25]. It makes post-fracture SOI surfaces a very suitable object to study the impact of rapid thermal annealing on the surface topography.

A set of $300\,mm$-in-diameter SOI wafers was fabricated by the Smart Cut™ process. All «finishing steps» were omitted in order to obtain post-splitting SOI wafers. The implantation induced damage region was removed by a thermal oxidation followed by the chemical etching of the oxide. Thus, the initial surfaces present typical morphological features of post-splitting surfaces, but the implantation induced damages were removed when the oxide layer was chemically etched. Then, wafers were annealed in a mixture of hydrogen and argon ambient (20% and 80%, respectively) at a pressure of $760\,Torr$ and annealing temperatures of 1050 °C, 1100 °C, 1150 °C, 1200 °C and 1250 °C, for six different durations, from 0 s-plateau to 90 s. Actually, the equivalent thermal budget of the 0 s-plateau, corresponds to that of ramp-up to the target temperature followed by ramp-down. The wafers were fed into the annealing chamber at 700 °C, the temperature ramp-up and ramp-down were both $50\,°\mathrm{C}/s$. Experiments were performed in a rapid thermal processing system *Helios XP* from Mattson.

3.2.2 | Results

The surface roughness of each annealed wafer was characterized by means of AFM. In order to cover the spatial bandwidth of interest (from $0.067\,\mu m^{-1}$ to $128\,\mu m^{-1}$) multiple images with sizes of $2\times2\,\mu m^2$, $10\times10\,\mu m^2$, and $30\times30\,\mu m^2$ (512×512 pixels) were recorded.

Figure 3.3 shows typical AFM images in $30\times30\,\mu m^2$ obtained from the samples before and after the *RTA* process. In figure 3.3 (a) we can observe that before *RTA* the fractured silicon surface presents a micro-roughness with a high vertical amplitude. Moreover, profiles from the figure evidence that topography variations present characteristic lengths between $100\,nm$ and $4\,\mu m$. Additionally, figure 3.4 shows typical AFM images of $2\times2\,\mu m^2$.

Figure 3.3 (b) shows the roughness of fractured silicon wafer after 0 s-plateau *RTA* process at 1200 °C (ramp up to 1200 °C followed by the ramp down). We note that the amplitude of vertical variations of the surface considerably decreases while the lower characteristic length increases up to $0.5\,\mu m$. Figure 3.3 (c) evidences a larger decrease of the vertical variations amplitude of the surface after 90 s *RTA* process, while its characteristic length increases up to $3\,\mu m$.

The roughness of a surface is usually described by its *RMS* value. *RMS* is the standard deviation of $h(\vec{x}, t)$ which is composed of discrete points describing the local height surface.

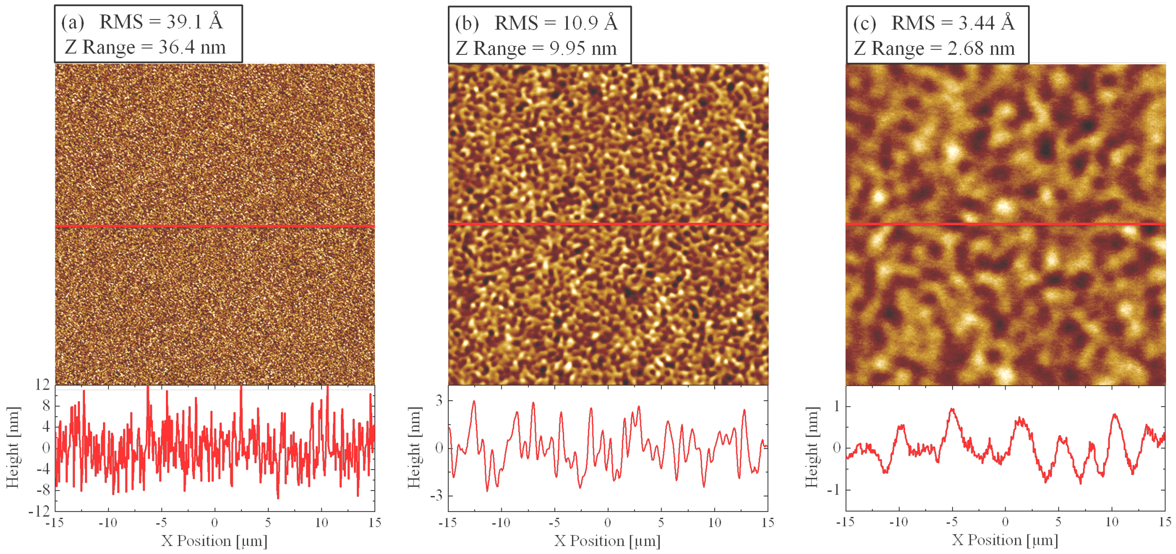

Fig. 3.3: Images obtained by AFM of the surface roughness: (a) before any thermal annealing (just after surface preparation), (b) after thermal annealing corresponding to 0 s-plateau at 1200 °C and (c) after 90 s-plateau annealing at 1200 °C. (Scan size: $30 \times 30\, \mu m^2$ with 512×512 pixels). Bottom insets shows profiles extracted from the AFM images and show the characteristics lengths of each images.

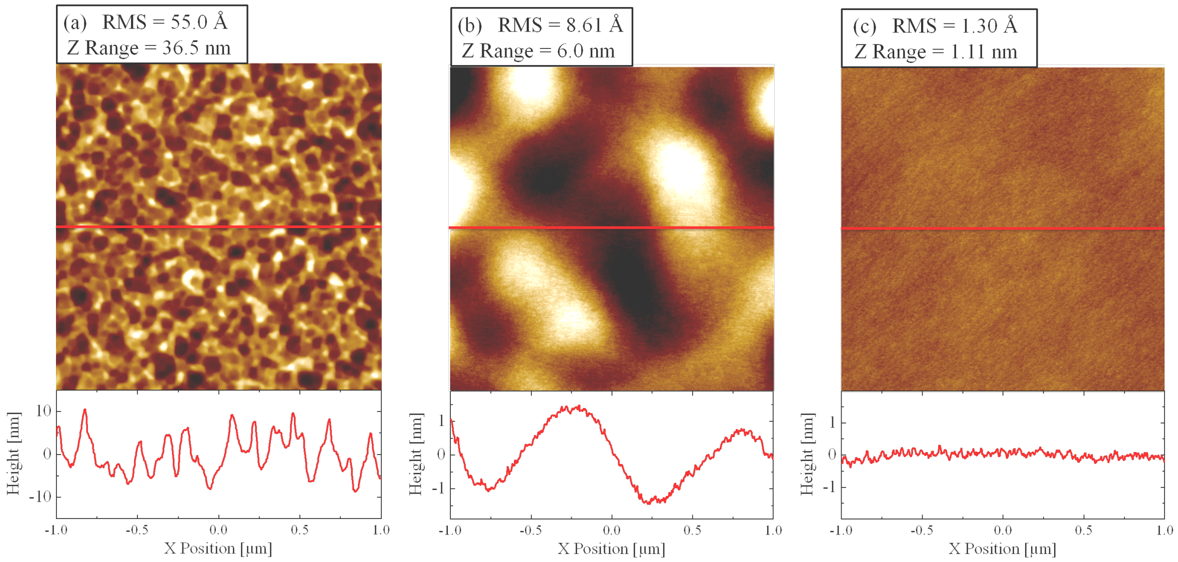

Fig. 3.4: Images obtained by AFM of the surface roughness: (a) before any thermal annealing (just after surface preparation), (b) after thermal annealing corresponding to 0 s-plateau at 1200 °C and (c) after 90 s-plateau annealing at 1200 °C. (Scan size: $2 \times 2\, \mu m^2$ with 512×512 pixels). Bottom insets shows profiles extracted from the AFM images evidencing the characteristics lengths of each images.

This well-known quantity provides a measurement for the overall roughness of the surface regardless of its spatial distribution and relevant lengths (see section 1.1.2 in chapter 1).

Figure 3.5 shows the variation of the *RMS* values of surfaces as a function of the annealing duration, at 1200 °C. It can be observed that the *RMS* decreases as a power-law of the annealing time with a growth exponent $\beta = -0.25 \pm 0.02$. This value is in perfect agreement with self-diffusion theory which predicts an exponent equal to $\beta = -1/4$ [4, 8, 9].

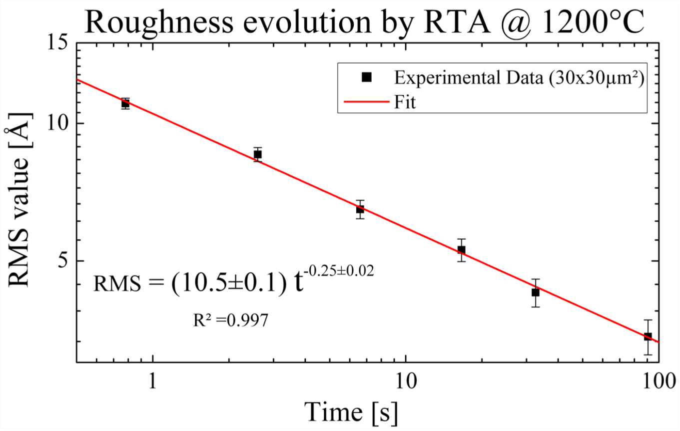

Fig. 3.5: Evolution of the *RMS* surface roughness as a function of annealing duration. *RMS* values are obtained from $30 \times 30\,\mu m^2$ AFM images. The *RMS* value decreases as a power-law of the annealing time with an exponent equal to -0.25 ± 0.02 which is in perfect agreement with self-diffusion theory ($\beta = 1/4$) [4, 8, 9].

Figure 3.6 shows the time-evolution of the *two-dimensional PSD* (PSD_{2D}) functions obtained from AFM $30 \times 30\,\mu m^2$ images of the annealed surfaces. Basically, we can observe two different behaviors. On the one hand, the amplitude of the PSD_{2D} functions rapidly decreases with the spatial frequency roughly from $0.5\,\mu m^{-1}$ up to $2\,\mu m^{-1}$. On the other hand, we can note an asymptotic behavior of the PSD_{2D} function amplitude. Indeed, the PSD_{2D} amplitude still decreases with increasing the spatial frequency but much more slowly.

Furthermore, we can observe at least two characteristic cut-off frequencies; the first one (between $0.3\,\mu m^{-1}$ and $1\,\mu m^{-1}$), which will be named diffusion-frequency (f_D), corresponds to the lowest spatial frequency impacted by the thermal smoothening. In fact, for lower spatial frequencies the amplitude of the PSD_{2D} function remains unchanged, implying that surface variations whose characteristic length corresponds to spatial frequencies lower than diffusion-frequency are not altered by the thermal annealing, under our experimental conditions. Indeed, f_D corresponds to the frontier between this unchanged region and another region in which PSD_{2D} amplitude decreases rapidly (see regions I and II in Fig. 3.7). The value of f_D depends on the annealing conditions and corresponds to the diffusion length of the system for a given thermal budget.

The second cut-off frequency (between $0.7\,\mu m^{-1}$ and $2.5\,\mu m^{-1}$), named noise-frequency (f_N) below, is also defined as a limit between two regions (see region II and III in Fig. 3.7) with different diffusion behaviors. Indeed, for frequencies lower than f_N (and higher than

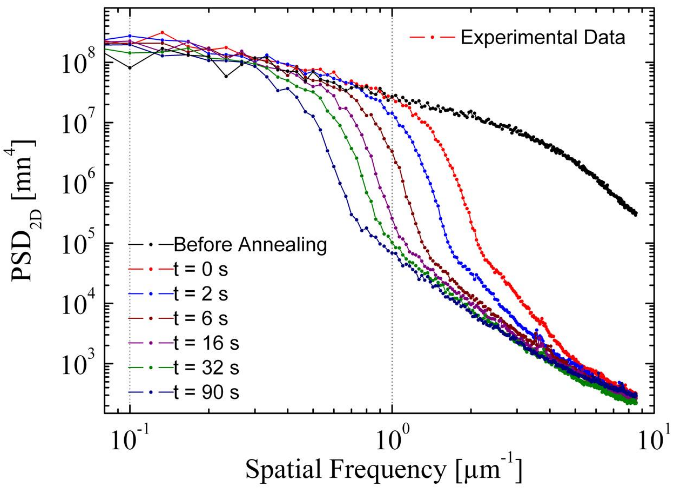

Fig. 3.6: PSD_{2D} functions describing the silicon surface topography of annealed wafers by *RTA* at $1200\,°\mathrm{C}$ for several durations.

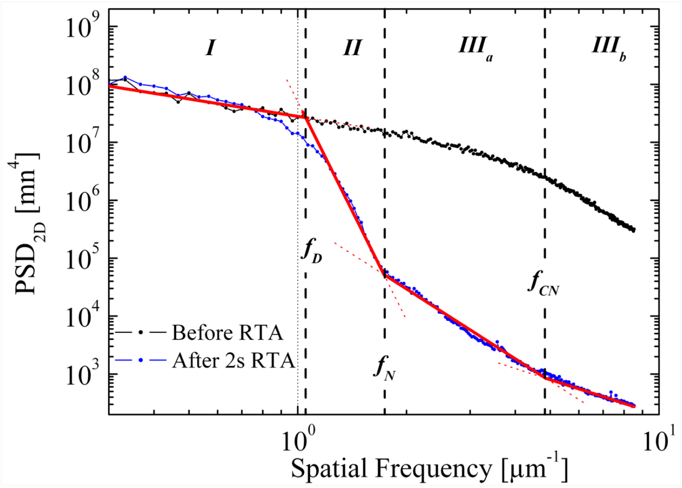

Fig. 3.7: Schematic representation of the PSD_{2D} function of annealed surface ($2\,\mathrm{s}$ at $1200\,°\mathrm{C}$). Four regions with different scaling behaviour are evidenced. These regions are separated by : diffusion-frequency (f_D), noise-frequency (f_N) and conservative noise frequency (f_{CN}).

the diffusion frequency, see region *II* in Fig. 3.7), we observe a dramatic reduction of the PSD_{2D} amplitude as function of the spatial frequency. The observed roughness exponent α (calculated from the slope of the PSD_{2D} function) in this region, is equal to 1.5 ± 0.1 and agrees well with a surface diffusion phenomenon which belongs to the *MBE* (Molecular Beam Epitaxy) universality scaling class [4, 14]. Indeed, this scaling class predicts scaling behavior with exponents $\alpha = 3/2$, $\beta = 3/8$ and $z = 4$ [26, 27]. Besides, for frequencies higher than f_N, the amplitude of the PSD_{2D} function of surfaces after thermal annealing, progressively decreases with the spatial frequency, reaching values considerably lower than the initial PSD_{2D} function amplitude. It means that surface variations with very small characteristic lengths are efficiently smoothened during thermal annealing. However, the observed roughness exponent is much smaller than the one corresponding to a surface self-diffusion phenomenon (see region *III* in Fig. 3.7). This suggests that, for spatial frequencies higher than f_N, some additional thermally activated phenomena takes place at the surface. The possible origin of such phenomena is discussed below.

From the noisy M-H model (Eq. 3.5), one can calculate the PSD_{2D} functions describing the spectral evolution of a surface during annealing. Let $H(f,t)$ be the Fourier transform of the height functions $h(x,t)$, where f is the spatial frequency, the general solution on the Fourier space of Eq. 3.5 can be written as,

$$\frac{\partial H(\vec{f},t)}{\partial t} = -\nu_4 f^4 H(\vec{x},t) \tag{3.6}$$

we can thus solve Eq. 3.6 for $h(\vec{x})_{t=0} = h_0$ and then we have,

$$h(\vec{x},t) = h_0 e^{-\nu_4 f^4 t} + \int\limits_0^t \eta(\vec{x},t') e^{-\nu_4 f^4 (t-t')}\, dt' \tag{3.7}$$

Now, the mean square can be estimated as follows (note that $\langle h(\vec{x},t)\rangle = 0$ permits to eliminate the cross term),

$$\langle h(\vec{x},t_1) h(\vec{x},t_2)\rangle = h_0^2 e^{-2\nu_4 f^4 t} + \int\limits_0^{t_1}\int\limits_0^{t_2} \langle \eta(\vec{x},t_1)\eta(\vec{x},t_2)\rangle\, e^{-\nu_4 f^4 (t_1+t_2-2t)}\, dt_1\, dt_2 \tag{3.8}$$

writing $t_2 = t_1 + \tau$, we obtain,

$$\langle h(\vec{x},t_1) h(\vec{x},t_2)\rangle \simeq h_0^2 e^{-2\nu_4 f^4 t} + \frac{1}{\nu_4 f^4}\left(1 - e^{-2\nu_4 f^4 t}\right) \int\limits_0^{\infty} \langle \eta(\vec{x})_{t=0}\, \eta(\vec{x})_{t=\tau}\rangle\, dt \tag{3.9}$$

Now, knowing that $\langle \eta(\vec{x},t)\rangle = 0$ and $\langle \eta(\vec{x},t)\eta(\vec{x}',t')\rangle = 2\Delta_{NCN}\delta^d(\vec{x}-\vec{x}')\delta^d(t-t')$, Eq. 3.9 rewrites,

$$\left\langle h^2(\vec{x},t)\right\rangle \simeq h_0^2 e^{-2\nu_4 f^4 t} + \frac{\Delta_{NCN}}{\nu_4 f^4}\left(1 - e^{-2\nu_4 f^4 t}\right) \tag{3.10}$$

Finally, we can estimate the evolution of the PSD_{2D} function. It gives the explicit form of PSD_{2D}, describing the time-evolution of the surface height as a function of the spatial frequency (Eq. 3.13).

$$PSD\left[h(\vec{x},t)\right]_t = PSD\left(h(\vec{x},t)\right)_{t=0} e^{-2\nu_4 f^4 t} + \frac{\Delta}{(2\pi)^4 \nu_4 f^4}\left(1 - e^{-2\nu_4 f^4 t}\right) \tag{3.11}$$

where $\Delta = (\Delta x)^2 \Delta_{NCN}$. Δx is the sampling period of the Fourier transform and is used as a normalization term for the PSD_{2D} functions. It is worth noting that the evolution of the PSD_{2D} function of a surface in the simple M-H model is given by the first term on the right hand-side of the Eq. 3.11.

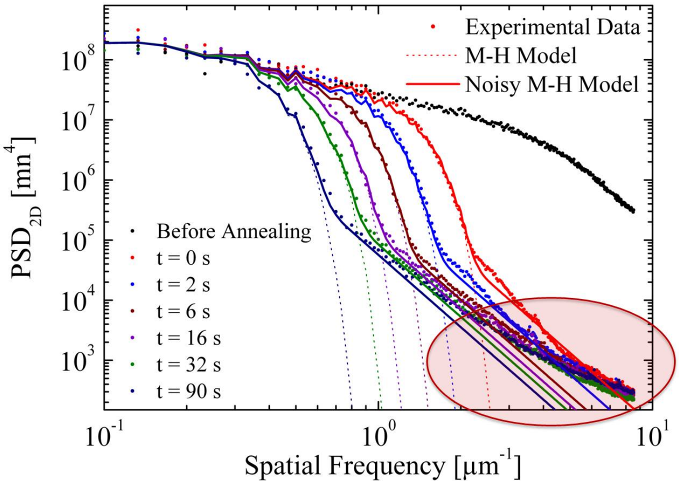

Fig. 3.8: PSD_{2D} spectra of silicon surfaces annealed by *RTA* at 1200 °C during different times. Experimental data (points) are compared to the M-H model (dashes) and to the noisy M-H model (solid lines).

Figure 3.8 shows a comparison between the PSD_{2D} functions obtained from the experimental data (points), those from the simple M-H model (dashes) and those from the noisy M-H model (solid lines). We can note that, for spatial frequencies lower than f_N, PSD_{2D} functions obtained experimentally are well-approximated by both, simple and noisy M-H models. Nevertheless, for spatial frequencies higher than f_N, the amplitude of the PSD_{2D} functions obtained from a simple M-H model, decreases too fast and does not describe the actual evolution of the annealed surfaces. Whereas, the noisy M-H model accurately describes the evolution of the amplitude of the PSD_{2D} functions over the whole spatial bandwidth, for annealing durations up to 2 s. However, it can be noted that the noisy M-H model does not describe the PSD_{2D} functions at high frequencies for annealing duration larger than 2 s. This suggests that the *NCN* term introduced in the noisy M-H model well-described the physical phenomena taking place during the thermal smoothening process at the early stages of the *RTA*, but not for longer times. Therefore, further investigation seems to be necessary to understand the physical mechanisms driving the smoothening behavior at spatial frequencies higher than f_N.

3.2.3 | Extended M-H model

Figure 3.9 shows a zoom on the high frequencies domain (higher than f_N) of the PSD_{2D} function of a surface annealed at 1200 °C during 2 s. It can be observed that the PSD_{2D} function has two different slopes over this spatial frequency range, separated by a characteristic spatial frequency which will be named conservative-noise frequency (f_{CN}) in the following. This suggests that two different phenomena drive the surface evolution at such high frequencies. The slope values of the PSD_{2D} functions are equal to -4 for frequencies lower than f_{CN} (see region (a) in Fig. 3.9) and equal to -2 for frequencies higher than f_{CN} (see region (b) in Fig. 3.9). These slopes can be related to non-conservative and conservative processes, respectively [26, 28, 29].

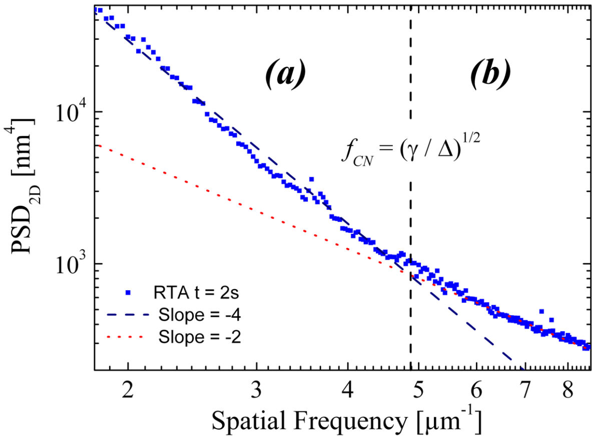

Fig. 3.9: High frequency range of the PSD_{2D} function of annealed surfaces (2 s at 1200 °C). Two scaling regimes are evidenced, separated by a characteristic frequency (f_{CN}).

Thus, to describe the evolution of the full PSD_{2D} spectrum, we propose to introduce a second stochastic term into the noisy M-H diffusion equation (Eq. 3.5). The proposed model is described by the following equation.

$$\frac{\partial h(\vec{x},t)}{\partial t} = -\nu_4 \nabla^4 (h(\vec{x},t)) + \eta(\vec{x},t) + \eta_d(\vec{x},t) \tag{3.12}$$

Where the stochastic term $\eta_d(\vec{x},t)$ defines a «mass conservative» noise (CN) in the system. Indeed, thermal fluctuations change the height of the surface at a given position (by moving adatoms into or away from that position). Every increase (decrease) of the surface height in a particular position is associated to the opposite in another nearby position on the surface. Therefore the integral of the CN over the surface must remain zero at every time. It can be easily verified that any noise term with zero-average ($\langle \eta_d(\vec{x},t) \rangle = 0$) and with correlator $\langle \eta_d(\vec{x},t)\eta_d(\vec{x}',t') \rangle = 2\gamma_{CN} \nabla^2 \delta^d(\vec{x}-\vec{x}')\delta^d(t-t')$ satisfies the requirement of mass conservation [4, 30, 31]. In conclusion, the added CN term describes the evolution of the surface due to the thermal fluctuation of the adatoms on the silicon surface. We can solve Eq. 3.12 in Fourier space, following the same procedure than that used to solve Eq. 3.5, we can thus write,

$$PSD\left[h(\vec{x},t)\right]_t = PSD\left(h(\vec{x},t)\right)_{t=0} e^{-2\nu_4 f^4 t} + \frac{\Delta}{(2\pi)^4 \nu_4 f^4}\left(1 - e^{-2\nu_4 f^4 t}\right) + \frac{\gamma}{(2\pi)^4 \nu_4 f^2}\left(1 - e^{-2\nu_4 f^4 t}\right) \tag{3.13}$$

where $\Delta = (\Delta x)^2 \Delta_{NCN}$ and $\gamma = (\Delta x)^2 \gamma_{CN}$.

Furthermore, we can study the competition between conservative $\eta_d(\vec{x},t)$ and non-conservative $\eta(\vec{x},t)$ noises. Indeed, the following rescaling conversion can be applied: $\vec{x} \to b\vec{x}$ and $t \to b^{zt}$. We obtain $\eta(\vec{x},t) \to \Delta^{1/2}\eta(\vec{x},t)b^{-(d+z)/2}$ and $\eta_d(\vec{x},t) \to \gamma_d^{1/2}\eta_d(\vec{x},t)b^{-(d+z+2)/2}$ [4]. Then, it is easy to calculate the characteristic length scale which is given by,

$$L_{CN} = \left(\frac{\gamma_{CN}}{\Delta_{NCN}}\right)^2 \tag{3.14}$$

The characteristic frequency ($f_{CN} = 1/L_{CN}$) separates two scaling regimes describing two different phenomena. Indeed, for $f >> f_{CN}$ (*i.e.*, $L << L_{CN}$), thermal fluctuations (conservative noise) dominate surface evolution, while for $f << f_{CN}$ (*i.e.*, $L >> L_2$), the deposition/evaporation noise dominates. It has been observed that f_{CN} increases with the annealing duration (see high frequencies domain in Fig. 3.8). It suggests that the NCN contribution to the PSD_{2D} amplitude decreases with time.

3.2.4 | Model validation

Experimental PSD_{2D} functions can be now compared to the proposed model. Actually, we fit experimental data by Eq. 3.13 using three fitting parameters D_s, Δ and γ. Since D_s depends only on the temperature, we use a common D_s for all times for a given temperature. Then, the fit is performed for each time using Δ and γ as parameters. Moreover, by fitting the experimental curves with the simple M-H model over the low frequencies range of PSD_{2D} function (frequencies lower than f_N), we can unambiguously obtain the value of the D_s coefficient for each temperature. Then, using a constant D_s value for each temperature, the time-evolution of the PSD_{2D} function can be fitted varying Δ_{NCN} and γ_{CN} as parameters.

Figure 3.10 shows the comparison between the experimental PSD_{2D} functions and the curves obtained by the model proposed in this work. It can be observed that this model accurately describes the time-evolution of the silicon surfaces during RTA for any process duration. Moreover, it is remarkable that the model well-describes the evolution of the PSD_{2D} functions over the whole measured spatial bandwidth. Thus, it is clear that we have set up a predictive model able to describe the spectral evolution of the surface topography of silicon during rapid thermal annealing for any temperature and any duration.

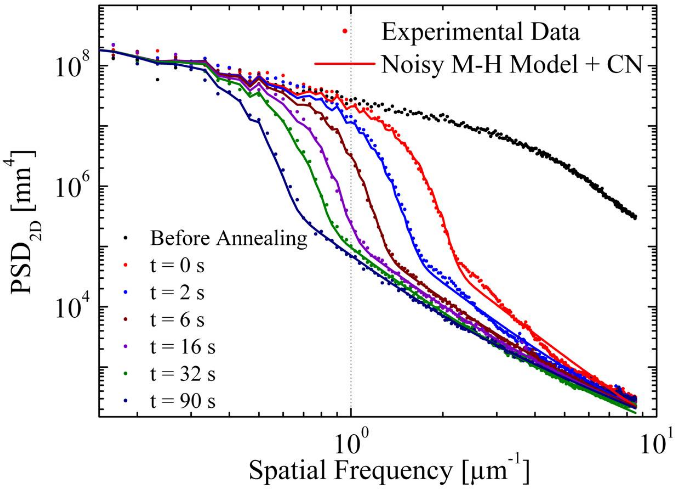

Fig. 3.10: PSD_{2D} functions of surfaces of SOI wafers annealed by *RTA* at $1200\,°\mathrm{C}$ for different times. Experimental data (points) are compared to the new proposed model (solid lines).

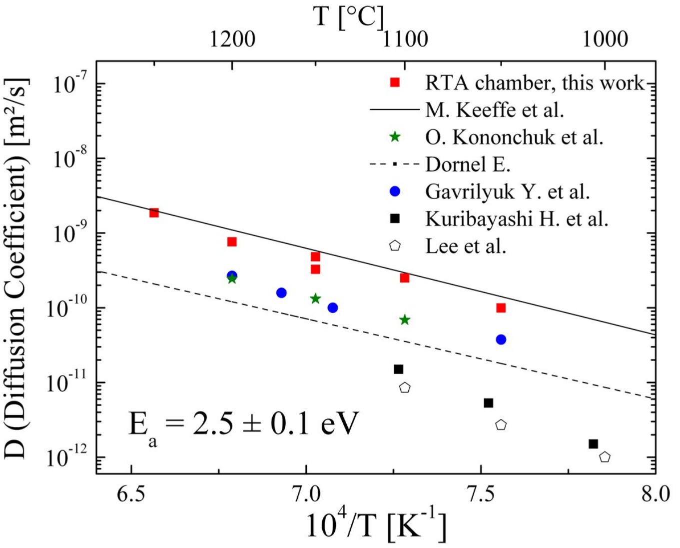

Fig. 3.11: Surface diffusivity coefficient of crystal silicon (100) obtained from the rapid thermal annealing (*RTA*) experiment compared with literature data [10, 12, 16, 17, 24, 32].

Figure 3.11 shows the temperature-dependence of the silicon surface diffusivity as extracted from our experiments by the performed fittings. The values of D_s follows an Arrhenius-type law with an activation energy of $Ea = 2.5 \pm 0.1\,eV$ and a pre-exponential factor of $0.3\,m^2 s^{-1}$. These values are in a very good agreement with most of the literature data obtained from the measurement of the transformation of the shape of periodic superficial silicon structures [10, 12, 24, 32]. For example, Lee M. *et al.* studied the transformation of silicon profiles by surface diffusion using annealing temperatures around $1050\,°\mathrm{C}$ and reported diffusivities with an activation energy of about $Ea = 2.26\,eV$ [17].

3.2.4.1 Stochastic terms evolution

We have also studied the time and temperature evolution of the stochastic terms introduced within the M-H model. Figure 3.12 shows the time and temperature evolutions of these terms (Δ_{NCN} and γ_{CN}). We do not observe any significant change of the non-conservative noise coefficient (Δ_{NCN}) with the annealing temperature. Nevertheless, it can be noted that Δ_{NCN} decreases with time as $t^{-1/2}$. Based on these observations, we can speculate that the non-conservative noise is a result of etching (silicon oxidation followed by oxide desorption) of the silicon surfaces by residual oxygen in the process chamber. Residual oxygen can be consumed through silicon oxidation and purged by the Ar/H_2 flow, thus resulting in a decrease of the noise coefficient over time [33].

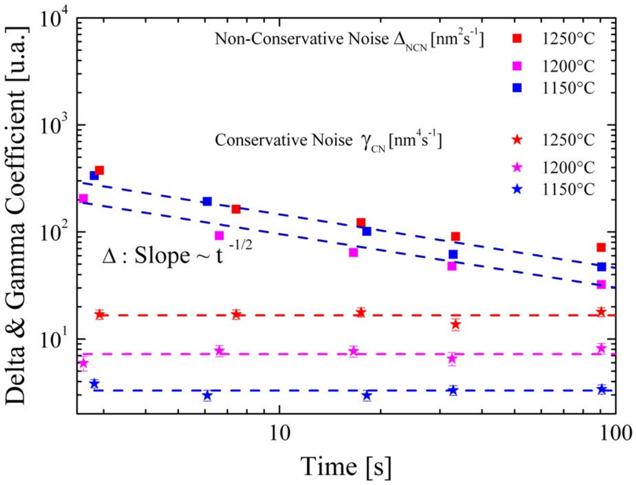

Fig. 3.12: Plot of the noise coefficients Δ_{NCN} and γ_{CN} (conservative noise and non-conservative respectively) as a function of annealing time. For different annealing temperatures.

Besides, we can observe in figure 3.12 that the CN coefficient (γ_{CN}), which describes the thermal fluctuations of the surface, remains constant over the time. It can be also noted that γ_{CN} increases with the annealing temperature what is in agreement with thermal activated fluctuations. Moreover, figure 3.13 shows the evolution of γ_{CN} as a function of the annealing temperature. This evolution can be fitted by an Arrhenius-type law with a pre-exponential factor $A \sim 3.9 \times 10^{11}\, nm^4$ and an activation energy of $3.1 \pm 0.1\, eV$. This again indicates a thermal activated phenomenon, in agreement with our proposal to inject in the model some conservative noise describing thermal fluctuations.

In order to verify our hypothesis concerning the origin of the NCN, we now investigate how smoothening of the surface changes with the oxygen contamination in the process chamber. The equipment we used to perform the RTA process does not control the oxygen amount present in the annealing chamber. In fact, it is too low (less than $10\, ppb$) to be measured during the process. We think that it is reasonable to suppose that the oxygen

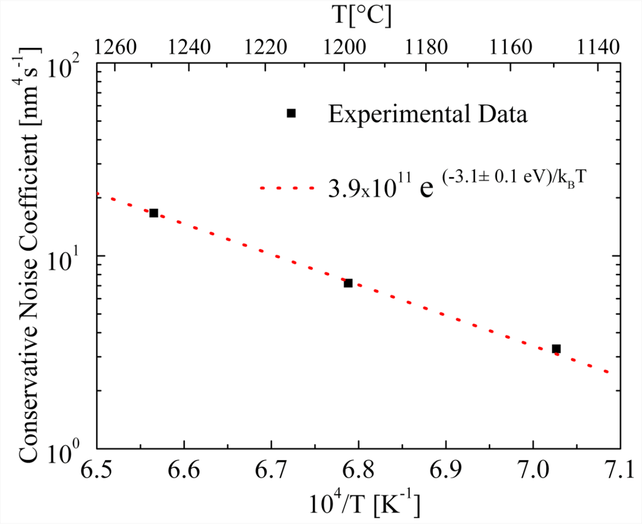

Fig. 3.13: Arrhenius plot of conservative noise coefficient (γ) describing the thermal fluctuations of the system. The activation energy is approximately $3.1\,eV$.

contamination results from the opening of the tool's door when the wafers are fed into the chamber. Comparison between one and several sequences of opening/closing the chamber during the annealing has to be done. Thus, we have performed annealings whose thermal budget were equivalent but during which the tool's door has been opened several times. Table 3.1 summarizes the experimental conditions used to study the impact of the chamber opening onto the smoothening mechanisms.

Sample Number	*Total Process Time*	*Number of Openings*
1 – 2 – 3	60 s – 2×30 s – 4×15 s	1 – 2 – 4
4 – 5 – 6	90 s – 3×30 s – 6×15 s	1 – 3 – 6

Tab. 3.1: Summary of the experimental conditions used to study the impact of the oxygen contamination introduced into the process chamber by opening the tool's door. All annealing were performed at 1200 °C.

The surface topography of the annealed wafers was measured by AFM with scan size of $30 \times 30\,\mu m^2$. The PSD_{2D} functions obtained from the recorded images are shown in figure 3.14 (a). Comparing the low frequencies domain of the PSD_{2D} allows us to confirm that the characteristic frequency of diffusion f_D, which only depends on the thermal budget, is the same for samples 1, 2 and 3 (4, 5 and 6, respectively). Anyway, no significant differences are observed between PSD_{2D} functions obtained from the different samples. Hence, to confirm whether the opening of the chamber when feeding wafers, favors oxygen contamination within the process chamber, further analysis of the high frequencies domain of the samples spectra is needed.

Smaller AFM images ($2 \times 2\,\mu m^2$) were then recorded. Figure 3.14 (b) shows the PSD_{2D}

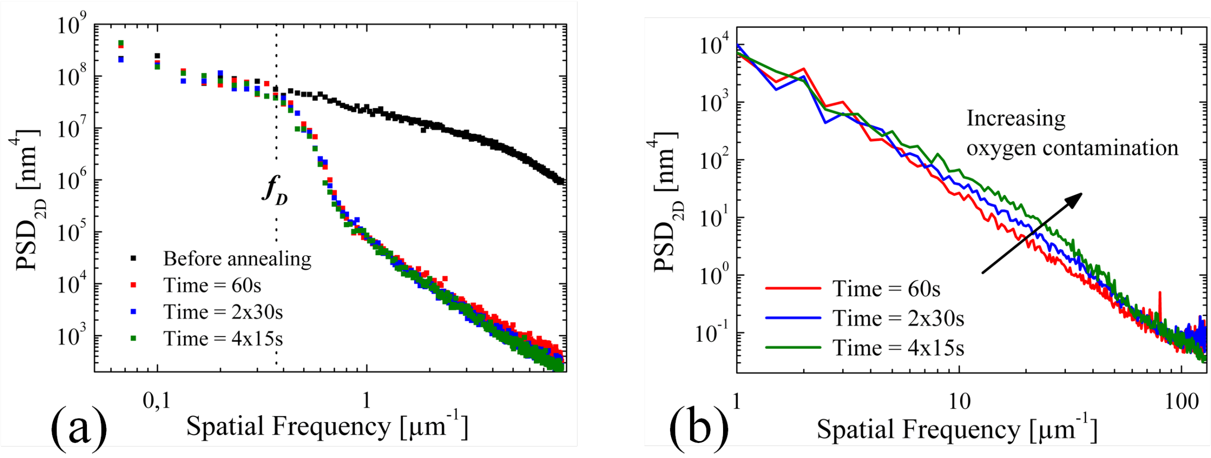

Fig. 3.14: PSD_{2D} functions obtained from AFM recorded images of annealed surfaces ($60\,\mathrm{s}$, $2\times30\,\mathrm{s}$ and $4\times15\,\mathrm{s}$ at $1200\,°\mathrm{C}$) (a) corresponding to $30\times30\,\mu m^2$ images. (b) Zoom on the high frequency domain of the PSD_{2D} functions.

functions obtained from these images. It is now possible to observe that a large number of opening/closing sequences of the chamber has an impact on the spectral foot-print of the annealed surface topography. Indeed, we can note that as the number of openings increases, the amplitude of the PSD_{2D} functions increases over a spatial frequency range from $5\,\mu m^{-1}$ up to $50\,\mu m^{-1}$.

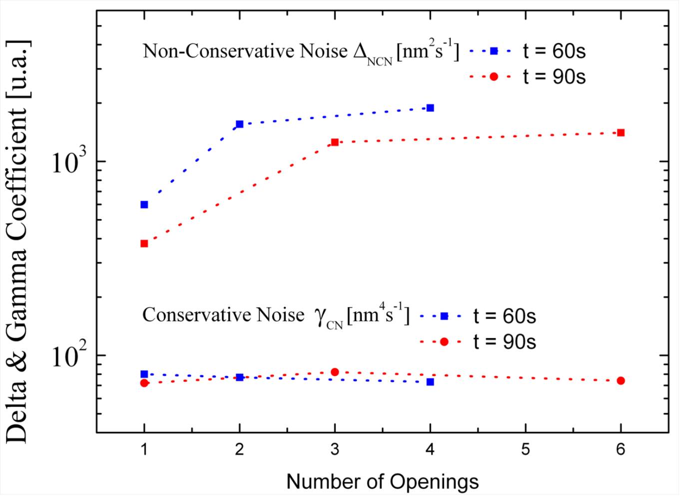

Fig. 3.15: Plot of the noise coefficients Δ_{NCN} and γ_{CN} (conservative noise and non-conservative respectively) as a function of openings number of the chamber door. The annealing temperature was $1200\,°\mathrm{C}$.

These observations are in agreement with our proposal for the origin of the non-conservative noise. Moreover, there is a cut-off frequency ($f = 50\,\mu m^{-1}$) above which no difference is observed between the different PSD_{2D} functions. It means that from this cut-off frequency, the topography evolution is driven exclusively by the conservative noise.

Moreover, using the fitting method we have previously explained, we can extract the values of the noise coefficients corresponding to each experimental condition (different number of openings). Figure 3.15 shows the values of these coefficients versus the number of openings. We can observe that γ_{CN} remains nearly constant what confirms the thermal origin of the conservative noise. On the other side, Δ_{NCN} increases with the number of openings of the process chamber. This suggests once again that the term described by a non-conservative noise we have introduced into the model, is related to some oxygen contamination introduced when feeding wafers into the process chamber. Nevertheless, precise measurements of oxygen partial pressure are necessary to quantitatively investigate the relationship between the amount of oxygen within the chamber and the NCN coefficients.

3.2.5 | Impact of experimental settings

After setting up the predictive model of the thermal evolution of silicon surfaces, we investigate now the influence of some experimental factors on the kinetics of surface diffusion.

3.2.5.1 Starting material

One of the experimental parameters to investigate is the influence of the implantation induced damage zone on surface diffusion. Actually, the wafers used previously as starting material were post-splitting SOI wafers whose damage zone was removed. Hence, in order to study the impact of the damaged zone on the thermal smoothening, we have fabricated supplementary samples whose damaged zone was not removed.

Then, we have performed annealing at 1200 °C for different durations (between 0 and 90 s). Again, the thermal evolution of these surfaces was studied by AFM. The PSD_{2D} functions obtained from such images are compared to the prediction of our extended model (see Fig. 3.16 (a)). We observe that the experimental PSD_{2D} functions can be fitted by the extended model using almost the same self-diffusivity values than for samples without implantation damaged zone. This suggests that diffusion kinetics is not affected by the H-induced defects located close to the surface.

Figure 3.16 (b) shows the evolution of Δ_{NCN} and γ_{CN} coefficients as a function of the annealing time. We observe that the values obtained for Δ_{NCN} are almost 10 times larger in presence of H-induced defects. On the contrary, γ_{CN} values are just slightly larger in that case. Since we have shown that Δ_{NCN} is related to the oxygen contamination, it is reasonable to speculate that larger oxygen contamination present onto the post-splitting surfaces. We think that this contamination results from the rapid growth of native oxide layer in the case of post-splitting wafers.

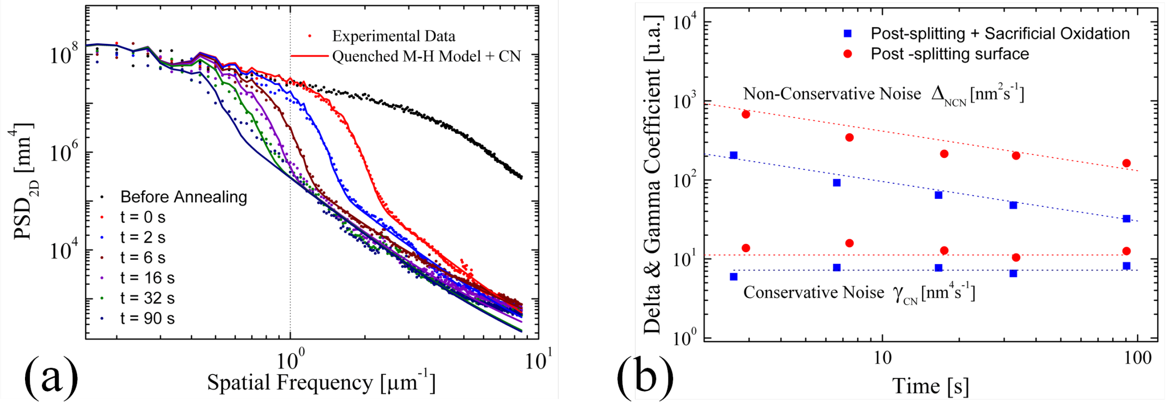

Fig. 3.16: (a) PSD_{2D} functions describing surface thermal evolution of samples whose implantation damaged zone was not removed. (b) Plot of the noise coefficients (Δ_{NCN} and γ_{CN}) extracted by fitting the experimental PSD_{2D} functions by the extended model. The annealing temperature was $1200\,°\mathrm{C}$ and its duration was between $0\,\mathrm{s}$ and $90\,\mathrm{s}$.

3.2.5.2 Annealing atmosphere

The annealing studied so far were done under a mixture of hydrogen and argon (20% and 80%, respectively). We have also performed annealing at $1250\,°\mathrm{C}$ for different durations under pure argon for comparison. Figure 3.17 (a) shows the experimental PSD_{2D} functions and their simulations using the extended model. Since the surface spectra are very similar to those obtained under a mixture of H_2 and Ar, the diffusivity values extracted by fitting are unaffected by the presence or not of H_2 in the gas.

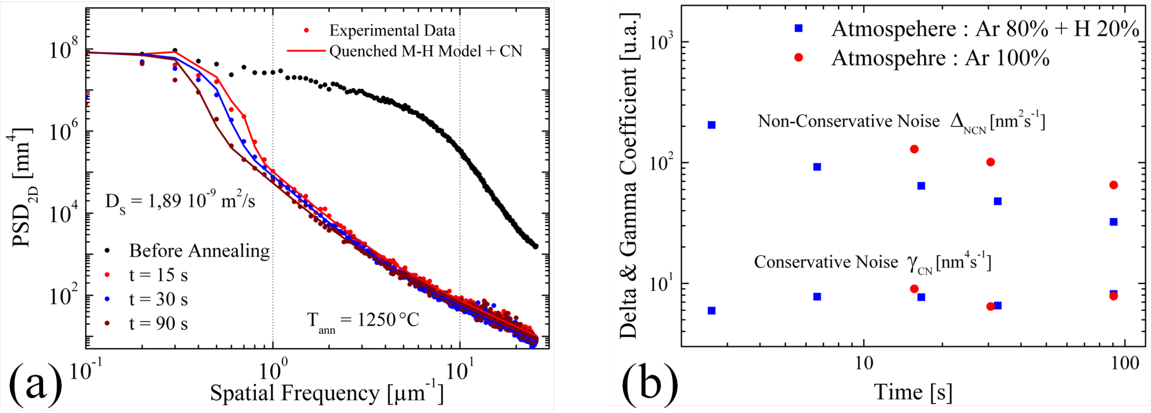

Fig. 3.17: (a) PSD_{2D} functions describing surface thermal evolution of samples using annealing atmosphere containing only Ar. (b) Noise coefficients (Δ_{NCN} and γ_{CN}) extracted by fitting the experimental PSD_{2D} functions by the extended model. The annealing temperature was $1200\,°\mathrm{C}$ and its duration was 15s, 30s and $90\,\mathrm{s}$.

Moreover, figure 3.17 (b) shows that the γ_{CN} values are also unaffected by H_2. Then, the conservative noise coefficient only depends on the annealing temperature. However, we also note that Δ_{NCN} values are somewhat larger when using an Ar than when using a gas mixture ($Ar + H$) although following the same trend. Then, we can conclude that the presence of H_2 in the gas mixture has no impact on how fast the oxygen contamination is consumed. However, H_2 reduce the initial oxygen contamination within the chamber.

Finally, we can conclude that, under our experimental conditions, including hydrogen in the atmosphere has no influence on the kinetics of surface self-diffusion although it may help reducing the oxygen contamination within the process chamber.

3.2.5.3 Buried oxide

Finally, we have also investigated whether the presence of the oxide layer buried within the SOI wafers (BOx) has an impact on the smoothening process. To do that, we have studied the smoothening of the *donor* wafers used in the Smart Cut™ process. Indeed, after fracture, donor wafers present similar morphology features than post-splitting SOI wafers. We have observed that for annealing at 1200 °C, the presence of a buried oxide layer does not have any influence on the smoothening kinetics of the silicon surfaces.

3.3 | Simulation of thermal annealing

Based on the extended model we have previously proposed, we are able to simulate the thermal evolution of surfaces during annealing.

3.3.1 | Simulation code

The simulation code was developed using standard data processing tools under MatLab®. Basically, the simulation consists of four principal steps. First, it is necessary to convert the AFM image into a square matrix containing the height values at each image pixel. The second step consists in the calculation of the PSD_{2D} function of this image. This is done by considering the sampling period and the module of the discrete Fourier transform (DFT_{2D}) of the matrix and by performing a radial average. Then, we can calculate the PSD_{2D} function (see section 1.1 in chapter 1). At this point, the information concerning the phase of the DFT_{2D} of the matrix is recorded. Once the PSD_{2D} function is obtained, the extended diffusion model is used to calculate the thermal evolution of the surface. Finally, the image of the surface after thermal annealing can be reconstructed using the new PSD_{2D} and the phase information recorded on the second step.

Figure 3.18 summarize the operating steps of the simulation code.

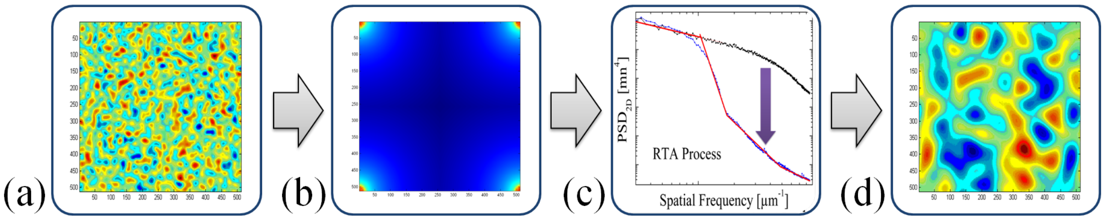

Fig. 3.18: Schematic of the simulation program allowing the reconstruction of the exact morphology of surfaces which would be annealed. (a) Conversion of initial AFM image into text file containing the height information, (b) calculation of the discrete Fourier transform of the surface, (c) estimation of the corresponding PSD_{2D} function and application of the extended diffusion model, (d) reconstruction of the annealed surface.

3.3.2 | Numerical applications

3.3.2.1 Process improvement

One of the main applications of this code is to provide a robust tool to assist the procedure commonly employed in the improvement of the thermal smoothening process. In industry, the continual improvement of process is a critical issue. For example, the reduction of annealing temperature or duration while keeping the same surface quality is very important. Using our simulation code, we just need an AFM image to study the impact of the reduction of the annealing time and/or temperature on the final surface roughness. Figure 3.19 shows the simulation of the evolution of a surface for an annealing temperature of 1100 °C obtained by simulation. As expected, the morphology and the RMS values obtained by simulation are in perfect agreement with those obtained experimentally. Moreover, several annealing processes can be simulated using a single sample and obtain as much information as if we had actually performed several annealing treatments. It is evident that simulations are much less time-consuming and that we can save an important quantity of starting materials.

The proposed simulation code can thus be used as a support to help the continual improvement of the *RTA* process involved in the Smart Cut™ technology. Moreover, this simulation tool permits to save development time and significantly reduce the cost of the process improvement.

3.3.2.2 *RTA* limit roughness

An interesting application of this simulation program is the theoretical exploration of the smoothening limit (if any) provided by *RTA* process. Indeed, the lowest roughness that can be reached by *RTA* can be estimated from the extended model (Eq. 3.13) using times values long enough. Figure 3.20 shows the evolution of the *RMS* value of a post-splitting surface for annealing treatments at 1150 °C, 1200 °C and 1250 °C. We observe that for annealing

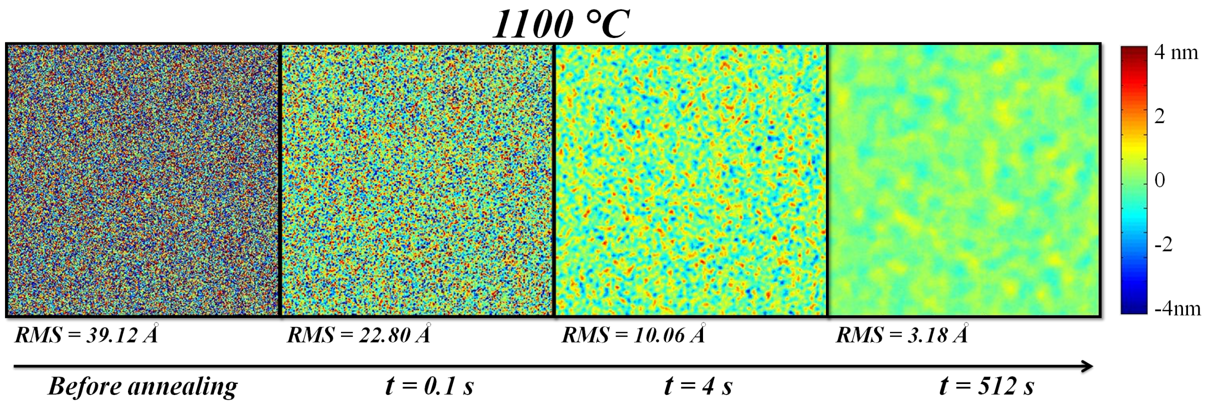

Fig. 3.19: Simulation of the surface topography evolution during a thermal annealing at 1100 °C for different process durations. Simulation were performed from a single AFM image.

durations smaller than approximately 1000 s, the RMS value decreases as a power-law of the time for all of the simulated process. Then, we note a saturation of the smoothening for longer durations. Since the non-conservative noise decreases with time and the conservative noise depends only on the annealing temperature (see section 3.2.4.1), we suggest that the saturation of the RMS value is only related to the conservative noise.

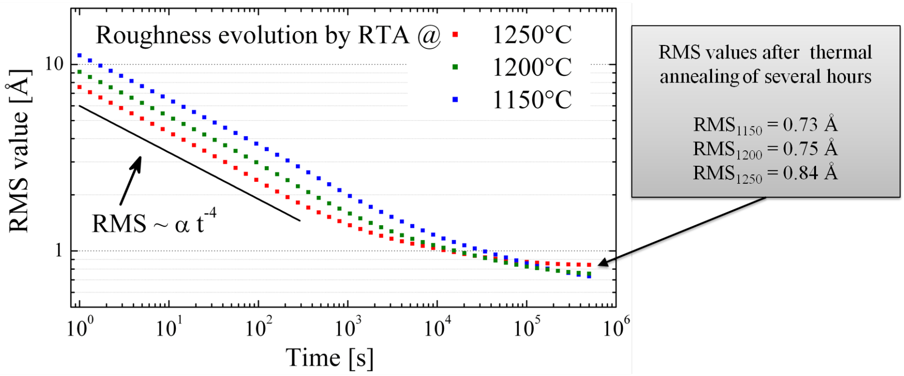

Fig. 3.20: Evolution of the RMS value (corresponding to a $30 \times 30\,\mu m^2$ AFM image) for different annealing temperatures ($T_{ann} = 1150\,°\mathrm{C}$, $1200\,°\mathrm{C}$ and $1250\,°\mathrm{C}$). Annealing duration is simulated up to $t = 140\,h$.

Moreover, it has been shown that the conservative noise is proportional to the annealing temperature. This is in agreement with the observed RMS values. Indeed, the theoretical limit of this value is $RMS = 0.73\,\text{Å}$ for $T_{ann} = 1150\,°\mathrm{C}$ while it is $RMS = 0.84\,\text{Å}$ for $T_{ann} = 1250\,°\mathrm{C}$.

Thus, in order to obtain smoother surfaces, one should favor thermal annealing at lower temperatures which limits the contribution of the conservative noise to the final roughness. However, for low temperatures, the process times are extremely long. Then, two steps annealing processes may be considered. Actually, a high temperature annealing followed by a low temperature annealing should allow to reach lower RMS values while using process times compatible with the industry. Furthermore, if the annealing temperature is lower than the roughening temperature (approximately 1050 °C for (001)-oriented Si), the annealing should leads to a faceted surface which could be atomically flat [23]. Additional requirement to reach smoother surfaces is to use an ultra-clean process chamber and ultra-pure gas flow which reduces the oxygen contamination and then limits the contribution of the non-conservative noise to the surface roughness evolution [34].

3.3.2.3 Shallow holes

Another interesting application is the simulation of the evolution of the morphology of peculiar structures on surfaces. Here, we study the thermal evolution of shallow holes which are surface defects that can sometimes be found on the surface of SOI wafers. In this case, the main objective of such simulations is to determine what kind of holes can be removed by thermal treatments.

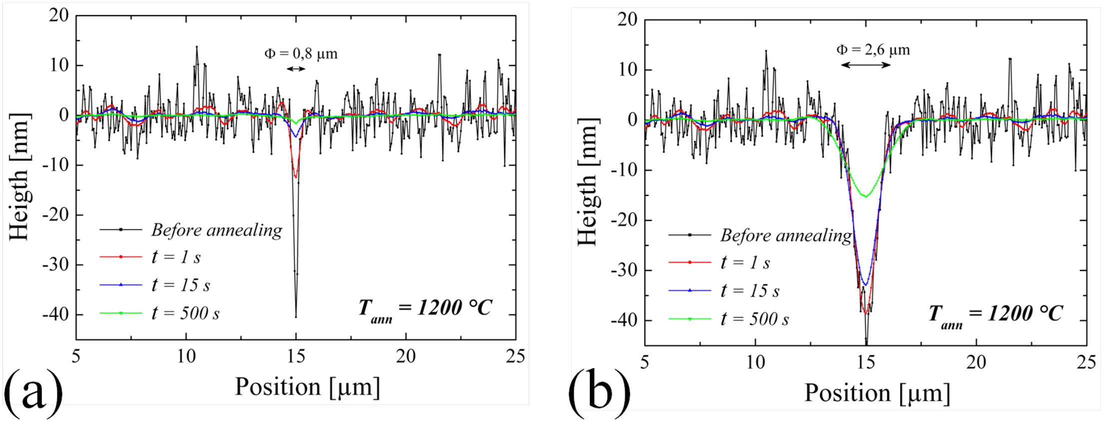

Fig. 3.21: Profiles describing the morphology evolution of holes present onto the annealed surface. Thermal annealing at $T_{ann} = 1200\,°\mathrm{C}$ is simulated for durations going from $1\,\mathrm{s}$ up to $500\,\mathrm{s}$. Initial hole depth is fixed to $40\,nm$ and its diameter varies from $0.8\,\mu m$ to $2.6\,\mu m$.

Figure 3.21 shows the evolution of two characteristics shallow holes which initial depth was fixed to $40\,nm$ and its diameters were $0.8\,\mu m$ and $2.6\,\mu m$ respectively. We observe that for the larger hole, even if its depth is reduced, a $15\,nm$-depth hole is still present after annealing at 1200 °C during 500 s. On the contrary, the narrower hole is almost completely removed after the same annealing.

Figure 3.22 shows the thermal evolution of the ratio final/initial depths for shallow holes which initial diameters range from $0.25\,\mu m$ to $3\,\mu m$ and their initial depth was fixed to $50\,nm$. We observe that for holes whose diameter is smaller than $1\,\mu m$, their depth rapidly starts decreasing and it is almost completely vanished after few or several tens of seconds. This evidences that deep holes with small diameters can be rapidly reduced whereas holes

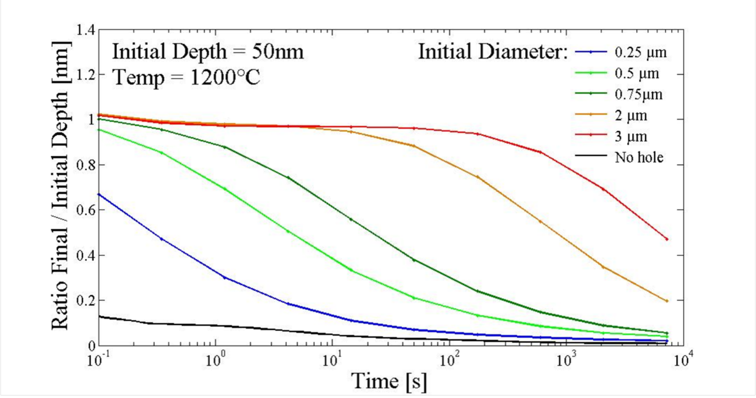

Fig. 3.22: Evolution of the ratio of final/initial depth of shallow holes during thermal annealing at $1200\,°C$ for different initial diameters.

with larger diameters remain almost unchanged during annealing. Hence, only surfaces with shallow holes whose diameter is smaller than approximately $1\,\mu m$ can be smoothened using annealing conditions such as those typically used in the semi-conductor industry (annealing temperature between $1000\,°C$ and $1300\,°C$ and time between few seconds and few tens of minutes).

Besides, we have experimentally observed that in some cases shallow holes are observed on SOI wafers even after the thermal annealing involved in the manufacturing process. Indeed, two types of shallows holes still exist after annealing, the «minor» shallow holes (depth between $20\,Å$ to $40\,Å$ and diameter between $0.2\,\mu m$ and $0.3\,\mu m$) and the «major» shallow holes (depth between $40\,Å$ to $60\,Å$ and diameter between $2\,\mu m$ and $3\,\mu m$). To understand the origin of these holes, we can proceed following an inverse simulation path. Actually, we can simulate the evolution of holes of different dimensions and infer the characteristics of the initial holes at the origin of those experimentally observed after annealing.

Figure 3.23 (a) shows the experimental profile obtained by AFM on a «major» shallow hole (black line) compared to the simulated profile resulting from the annealing at $T_{ann} = 1200\,°C$ for 60 s of a $50\,nm$-deep hole of initial diameter $2.5\,\mu m$ (red line). The AFM profile was vertically shifted ($+15\,nm$) to make the comparison easier. We note that the morphology of both holes is very similar, their diameter is approximately $5\,\mu m$ while their depth is $3.5\,nm$. This evidence that the simulated holes may be at the origin of the experimentally observed holes.

Figure 3.23 (b) shows the evolution of the «depth of holes» as a function of their initial diameter, after a given thermal annealing (60 s at $1200\,°C$), for holes of initial depths between $5\,nm$ and $15\,nm$. It can be inferred that «minor» shallow holes originates from holes with an initial depth of at least $8\,nm$ and up to $15\,nm$. We also observe that «major» shallow holes only slightly evolve during thermal annealing, due to their large diameter. It is worth noting that the maximum aspect ratio of considered shallow holes is about 6%, meaning

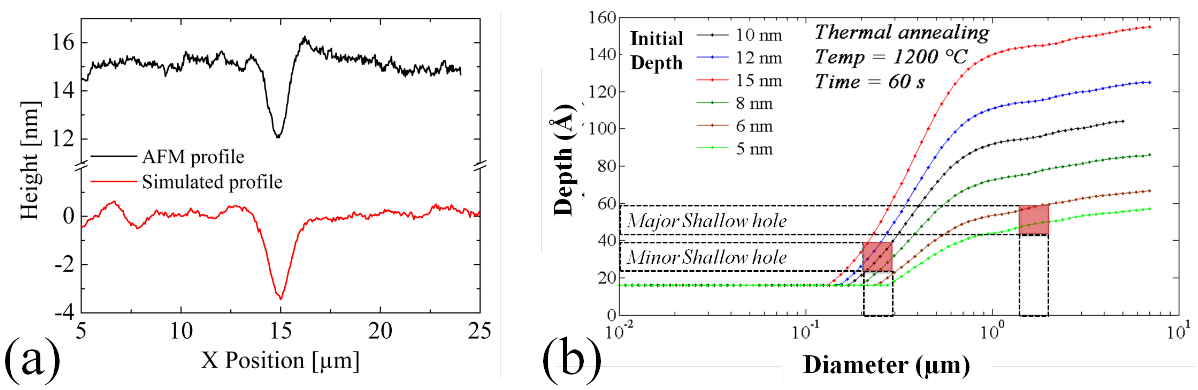

Fig. 3.23: (a) Comparison between measured AFM profile of a major shallow hole and that obtained from the thermal evolution of a hole with a initial diameter of $2.5\,\mu m$ and $50\,nm$-depth. (b) Curves describing the depth evolution of shallow holes after a thermal annealing, for different initial depths as a function of the initial diameter. The simulated annealing was done at $T_{ann} = 1200\,°\mathrm{C}$ during $60\,\mathrm{s}$.

that for all of them, the small curvature approximation is still suitable to describe their thermal evolution. Shallow holes are rather rare on the SOI wafer surfaces, it is thus very difficult to obtain experimental images of this type of defect. Then, more experimental data is required to further investigate the origin of shallow holes. Nevertheless, we can conclude that before annealing (just after the splitting processes), deep holes ($8\,nm$ and up to $15\,nm$) of micro-metric diameters must be present on the SOI wafer surface.

Conclusions

In this chapter, «smoothening», *i.e.*, surface self-diffusion of silicon adatoms on rough SOI wafers was investigated by means of AFM and quantified using PSD_{2D} functions. Three spectral regions can be differentiated through different diffusion behaviors. In the first spectral region (frequencies lower than f_D), no change in the amplitude of the PSD_{2D} functions is observed during annealing (see region I in Fig. 3.7). This suggests that no diffusion phenomenon affects the surface morphology over this spatial bandwidth. In the second region (spatial frequencies between f_D and f_N), the reduction of the amplitude of the PSD_{2D} function during annealing shows a scaling behavior characteristic of surface self-diffusion, evidencing that it is the predominant transport mechanism impacting this spatial bandwidth (see region II in Fig. 3.7). Over the third region (spatial frequencies higher than f_N), two phenomena are observed. For spatial frequencies between f_N and f_{CN}, the surface evolves through an oxidation-evaporation mechanism while for frequencies higher than f_{CN}, it evolves through the thermal fluctuation of adatoms (see regions III_a and III_b in Fig. 3.7 respectively).

The introduction of two stochastic terms, describing the surface thermal fluctuations and the oxidation-evaporation phenomenon, respectively corresponding to a conservative and a non-conservative noises into the simple M-H equation, allows the set up of a predictive model describing the evolution of the surface morphology during high temperature annealing in reducing atmosphere. Very good agreement between our experimental data, describing both the roughness evolution of the surface and the kinetics of surface self-diffusion, and data obtained from this extended model, was obtained. The temperature-dependence of the self-diffusivity of silicon follows an Arrhenius-type law with an activation energy of $Ea = 2.5 \pm 0.1\,eV$ and a pre-exponential factor of approximately $0.3\,m^2 s^{-1}$, in agreement with most values reported in the literature. We have also studied the time and temperature evolutions of the parameters describing the stochastic terms we have introduced into the model. Using this extended model, we can predict the observed decrease of each spatial frequency of the PSD_{2D} amplitude during annealing and this, over a very large spatial bandwidth.

Finally, a predictive simulation code was developed. This simulation tool should permit to save development time and significantly reduce the cost of exploring and developing process improvements. The limits of the smoothening process by RTA has also been explored. We inferred that, to obtain smoother surfaces, one may consider lower annealing temperatures in order to limit the contribution of the thermal fluctuations to the final roughness. Additionally, one can use ultra-pure experimental conditions limiting oxygen contamination of the surface. We have also investigated the thermal evolution and origin of shallow holes that are sometimes observed at the silicon surfaces. We concluded that deep holes (80 Å and up to 150 Å) of micro-metric diameters are present on the post-splitting SOI wafer surfaces, giving rise to the shallow holes observed at the annealed surfaces. Moreover, holes whose diameter is smaller than approximately $1\,\mu m$ can be «smoothened» using annealing conditions such as those typically used in the semi-conductor industry.

In summary, rapid thermal smoothening is a very effective process to reduce surface roughness of the top Si layer of SOI wafers for spatial frequencies higher f_D (few microns in typical experimental conditions) without affecting lower spatial frequencies. This is very suitable for limiting the variability of V_t within transistors processed on FD-SOI wafers.

Bibliography

[1] C. Herring, *Structure and Properties of Solid Surfaces*, ch. The use of Classical Macroscopic Concepts in Eurface-Energy problems. University of Chicago Press, 1953. (cited in page 77)

[2] C. Herring, "Effect of change of scale on sintering phenomena," *Journal of Applied Physics*, vol. 21, no. 4, 1950. (cited in page 78)

[3] W. W. Mullins, "Flattening of a nearly plane solid surface due to capillarity," *Journal of Applied Physics*, vol. 30, no. 1, 1959. (cited in page 78)

[4] A. L. Barabasi and H. E. Stanley, *Fractal Concepts In Surface Growth.* Cambridge Press, 1995. (cited in pages 11, 12, 13, 78, 79, 80, 84, 85, 88, 89, 109, 117 and 118)

[5] L. Zhong, A. Hojo, Y. Matsushita, Y. Aiba, K. Hayashi, R. Takeda, H. Shirai, H. Saito, J. Matsushita, and J. Yoshikawa, "Evidence of spontaneous formation of steps on silicon (100)," *Phys. Rev. B*, vol. 54, pp. R2304–R2307, Jul 1996. (cited in page 78)

[6] R. Hiruta, H. Kuribayashi, S. Shimizu, K. Sudoh, and H. Iwasaki, "Evolution of surface morphology of Si-trench sidewalls during hydrogen annealing," *Applied Surface Science*, vol. 237, no. 1–4, pp. 63 – 67, 2004. Proceedings of the Seventh International Symposium on Atomically Controlled Surfaces, Interfaces and Nanostructures. (cited in pages 78, 79 and 80)

[7] H. Kuribayashi, M. Gotoh, R. Hiruta, R. Shimizu, K. Sudoh, and H. Iwasaki, "Observation of Si (100) surfaces annealed in hydrogen gas ambient by scanning tunneling microscopy," *Applied surface science*, vol. 252, no. 15, pp. 5275–5278, 2006. (cited in page 78)

[8] W. W. Mullins, "Theory of thermal grooving," *Journal of Applied Physics*, vol. 28, no. 3, 1957. (cited in pages 78, 79 and 84)

[9] C. Herring, "Effect of change of scale on sintering phenomena," *Journal of Applied Physics*, vol. 21, no. 4, 1950. (cited in pages 79 and 84)

[10] E. Dornel, *Évolution morphologique par diffusion de surface et application à l'étude du démouillage de films minces solides.* PhD thesis, Univertité Joseph Fourier, Grenoble, 2007. (cited in pages 79 and 90)

[11] J. Cahn and J. Taylor, "Overview n113 surface motion by surface diffusion," *Acta Metallurgica et Materialia*, vol. 42, no. 4, pp. 1045 – 1063, 1994. (cited in page 79)

[12] M. E. Keeffe, C. Umbach, and J. M. Blakely, "Surface self-diffusion on Si from the evolution of periodic atomic step arrays," *Journal of Physics and Chemistry of Solids*, vol. 55, no. 10, pp. 965 – 973, 1994. (cited in pages 79, 80, 81 and 90)

[13] K. Sudoh, H. Iwasaki, H. Kuribayashi, R. Hiruta, and R. Shimizu, "Numerical study on shape transformation of silicon trenches by high-temperature hydrogen annealing," *Japanese Journal of Applied Physics*, vol. 43, no. 9A, pp. 5937–5941, 2004. (cited in pages 79, 80 and 81)

[14] H. Liu, W. Zhou, Q.-M. Nie, and Q.-H. Chen, "Depinning transition of the quenched Mullins - Herring equation: A short-time dynamic method," *Physics Letters A*, vol. 372, no. 47, pp. 7077 – 7080, 2008. (cited in pages 80 and 85)

[15] J. Blakely and H. Mykura, "Surface self diffusion and surface energy measurements on platinum by the multiple scratch method," *Acta Metallurgica*, vol. 10, no. 5, pp. 565 – 572, 1962. (cited in page 80)

[16] H. Kuribayashi, R. Hiruta, R. Shimizu, K. Sudoh, and H. Iwasaki, "Shape transformation of silicon trenches during hydrogen annealing," *Journal of Vacuum Science and Technology A*, vol. 21, no. 4, 2003. (cited in pages 80 and 90)

[17] M.-C. M. Lee and M. Wu, "Thermal annealing in hydrogen for 3-D profile transformation on silicon-on-insulator and sidewall roughness reduction," *Microelectromechanical Systems, Journal of*, vol. 15, no. 2, pp. 338–343, 2006. (cited in pages 80, 81 and 90)

[18] M. F. Castez, "Surface-diffusion-driven decay of patterns: beyond the small slopes approximation," *Journal of Physics: Condensed Matter*, vol. 22, no. 34, p. 345007, 2010. (cited in pages 80 and 81)

[19] W. K. Burton, N. Cabrera, and F. Frank, "The growth of crystals and the equilibrium structure of their surfaces," *Philosophical Transactions of the Royal Society of London. Series A, Mathematical and Physical Sciences*, vol. 243, pp. 299–358, 1951. (cited in page 81)

[20] J. Heyraud, J. Métois, and J. Bermond, "The roughening transition of the Si(113) and Si(110) surfaces – an in situ, real time observation," *Surface Science*, vol. 425, no. 1, pp. 48 – 56, 1999. (cited in page 81)

[21] E. van Vroonhoven, H. J. Zandvliet, and B. Poelsema, "A quantitative evaluation of the dimer concentration during the (2×1) - (1×1) phase transition on Ge(001)," *Surface Science*, vol. 574, no. 2-3, pp. L23–L28, 2005. (cited in page 81)

[22] V. Ignatescu, *Engineering surface morphology at the atomic level with applications in electronic materials*. PhD thesis, Cornell University, 2007. (cited in page 81)

[23] T. Doi, M. Ichikawa, and S. Hosoki, "Observation of Si(001) surface topography at temperatures below 1140°Cusing a reflection electron microscope," *Phys. Rev. B*, vol. 55, pp. 1864–1870, Jan 1997. (cited in pages 81 and 99)

[24] Y. L. Gavrilyuk, Y. S. Kaganovjkii, and V. G. Lifshits, "Diffusive mass transfer on the (111) and (100) surfaces of silicon single crystals," *Sov. Phys. Crystallogr.*, vol. 26, no. 3, 1981. (cited in pages 81 and 90)

[25] S. Personnic, K. K. Bourdelle, F. Letertre, A. Tauzin, *et al.*, "Impact of the transient formation of molecular hydrogen on the microcrack nucleation and evolution in H-implanted Si (001)," *Journal of Applied Physics*, vol. 103, no. 2, pp. –, 2008. (cited in page 82)

[26] E. Darvish and A. A. Masoudi, "Kinetic surface roughening for the Mullins - Herring equation," *Journal of Mathematical Physics*, vol. 50, no. 1, p. 013304, 2009. (cited in pages 37, 85 and 88)

[27] J. M. López, M. A. Rodríguez, and R. Cuerno, “Power spectrum scaling in anomalous kinetic roughening of surfaces,” *Physica A: Statistical Mechanics and its Applications*, vol. 246, no. 3–4, pp. 329 – 347, 1997. (cited in page 85)

[28] A. Röthlein, F. Baumann, and M. Pleimling, “Symmetry-based determination of space-time functions in nonequilibrium growth processes,” *Phys. Rev. E*, vol. 74, p. 061604, Dec 2006. (cited in page 88)

[29] K. A. Takeuchi, M. Sano, T. Sasamoto, and H. Spohn, “Growing interfaces uncover universal fluctuations behind scale invariance,” *Scientific Reports*, vol. 1, no. 34, 2011. (cited in page 88)

[30] J. Villain, “Continuum models of crystal growth from atomic beams with and without desorption,” *Journal de physique I*, vol. 1, no. 1, pp. 19–42, 1991. (cited in page 88)

[31] P. Politi, G. Grenet, A. Marty, A. Ponchet, and J. Villain, “Instabilities in crystal growth by atomic or molecular beams,” *Physics Reports*, vol. 324, no. 5–6, pp. 271 – 404, 2000. (cited in page 88)

[32] O. Kononchuk, D. Landru, and C. Veytizou, “Novel trends in SOI technology for CMOS applications,” *Solid State Phenomena*, vol. 156-158, pp. 69–76, 2010. (cited in page 90)

[33] B. Mohadjeri, M. R. Baklanov, E. Kondoh, and K. Maex, “Oxidation and roughening of silicon during annealing in a rapid thermal processing chamber,” *Journal of Applied Physics*, vol. 83, no. 7, 1998. (cited in page 91)

[34] R. Kuroda, T. Suwa, A. Teramoto, R. Hasebe, S. Sugawa, and T. Ohmi, “Atomically flat silicon surface and silicon/insulator interface formation technologies for (100) surface orientation large-diameter wafers introducing high performance and low-noise metal-insulator-silicon FETs,” *Electron Devices, IEEE Transactions on*, vol. 56, no. 2, pp. 291–298, 2009. (cited in page 99)

4 | Thermal Oxidation

Contents

Thermal oxidation is one of the technological steps involved in the Smart Cut™ process which could impact the roughness and the thickness uniformity of the final silicon layers. Indeed, before implantation, thermal oxidation is performed in order to grow the buried oxide (BOx) layer of the SOI wafers. Moreover, the final thickness of the silicon layer is often adjusted through a sacrificial thermal oxidation.

Thus, in this chapter, we will experimentally investigate the evolution of the surface roughness during the thermal oxidation of silicon. After a rapid presentation of the state of the art, we will use the characterization techniques and methods presented in chapter 1 (see section 1.1.3) to study the impact of the thermal oxidation conditions (time and temperature) on the thickness uniformity and the surface roughness of the grown oxide layer.

4.1 | State of the art

4.1.1 | Oxide growth

The theoretical framework generally accepted to describe the growth of silicon oxide has been proposed by Deal and Grove and is commonly named «DG model» [1]. This model considers the diffusion of oxidant species (O_2) through a silicon oxide film from the surface and toward the Si/SiO_2 interface. The oxidation process is described by a steady-state regime where the gradient of the oxidant species is constant over the oxide film and a reaction between O_2 and Si molecules, taking place at the Si/SiO_2 interface. Based on this description, they have established the well-known linear-parabolic law describing the oxide layer thickness evolution during the oxidation process, usually written as,

$$Th(t) = \frac{A}{2}\left[\sqrt{1+\frac{t+\tau}{A^2/4B}}-1\right] \tag{4.1}$$

where $Th(t)$ is the thickness of the oxide layer, B/A is the linear coefficient which characterizes the initial linear rate growth, and B is the parabolic coefficient which governs the diffusion limited regime. These coefficients follow Arrhenius-type laws given by,

$$\left(\frac{B}{A}\right)_{Dry} = C_{B/A}\, e^{-E_{B/A}eV/k_BT} \quad and \quad (B)_{Dry} = C_B\, e^{-E_BeV/k_BT} \tag{4.2}$$

with $C_{B/A} = 3.71\times10^6\,\mu m/h$, $E_{B/A} = 2\,eV$, $C_B = 772\,\mu m^2/h$ and $E_B = 1.23\,eV$, in the dry oxidation case. Additionally, an initial time offset τ can be necessary to take into account the eventual presence of an initial oxide layer. Similar relationships are valid for wet oxidation.

While the DG model well-describes the oxidation kinetics at long times, it does not explain the unexpectedly fast growth rate of oxide at the very initial stage of the oxidation process, when using dry O_2. Based on the DG model, Massoud *et al.* [2] have proposed a more sophisticated model, where the limiting factor at the first stage of oxidation is the reaction rate of Si and O_2 and not the oxygen diffusion through the oxide layer. Following this model, the thickness evolution of thin oxide layers is given by,

$$\frac{\partial Th(t)}{\partial t} = \frac{B}{2Th(t)+A} + Ce^{-Th(t)/L} \tag{4.3}$$

Additionally, to further improve the description of this initial oxidation stage, a «Si emission model» has been recently proposed and tested with success [3–5]. This model states that Si atoms are emitted from the Si/SiO_2 interface during the oxidation process in order to reduce stress at this interface. Indeed, when the oxide film is thin enough, the Si atoms diffuse through the oxide to the surface. When on the surface, Si atoms can desorb into the atmosphere by forming SiO molecules or react with the oxidants and thus contribute to the oxidation. This model well-describes the faster oxide growth observed when the oxide layer is very thin.

4.1.2 | Roughness evolution during oxidation

The evolution of the surface roughness of the oxide layer during oxidation has been much less examined. Most authors have studied the roughness evolution of the Si/SiO_2 interface rather than the SiO_2 surface during oxidation [6, 7].

Omi *et al.* [8] have studied the roughening of the Si/SiO_2 interface during thermal oxidation of silicon at 1200 °C under dry conditions. Analyzing AFM images, they found that the roughening characteristics of dry oxidation depends on the concentration of oxygen gas (O_2 partial pressure). More recently, they have shown that, for $T_{Ox} > 1250\,^{\circ}\mathrm{C}$, the interface is not roughened but smoothed instead during oxidation [9]. This evolution of the interface roughness can be written,

$$\frac{\partial h(\vec{x},t)}{\partial t} = \mu\nabla^2 h(\vec{x},t) - D\nabla^4 h(\vec{x},t) + G|\nabla h(\vec{x},t)| + \nu(\vec{x},t) \tag{4.4}$$

where μ, D and G are constants. The $G|\nabla h(\vec{x},t)|$ term describes the stress effect on the instability of the interface [10]. The linear terms $\nabla^2 h(\vec{x},t)$ and $\nabla^4 h(\vec{x},t)$ describe, respectively, the surface tension and surface diffusion which both tend to smooth the surface, and $\nu(\vec{x},t)$ is a stochastic term describing the noise in the system. This equation is also known as the linear growth equation [11]. A competition between the linear terms $\nabla^2 h(\vec{x},t)$ and $\nabla^4 h(\vec{x},t)$ generates a characteristic length $L_{Ox} = \sqrt{\frac{D}{\mu}}$. Eq. 4.4 well reproduces the experimental data of the roughness evolution of the Si/SiO_2 interface during thermal oxidation at high temperatures ($T_{Ox} > 1050\,^{\circ}\mathrm{C}$) [9, 11].

The scaling law governing this roughness evolution has also been studied [6], and shows that at small spatial scales ($< 100\,nm$) the RMS of the interface increases with the observation scale (with a roughness exponent α between 0.3 and 0.5) which is typical of fractal surfaces. This characteristic is consistent with the *Familiy-Vicsek* scaling relation (see section 1.1 in chapter 1) which is typical of far-from-equilibrium processes [12, 13].

When the initial surface is rough, the Si/SiO_2 interface tends to become smoother during oxidation because of thermodynamics. Indeed, the Gibbs free energy required to maintain surface structures with high aspect ratio is also high. On the contrary, smooth interfaces are observed to be roughened during oxidation. It is suggested that stress at interface irregularities causes modifications of the local reaction rate over the interface. Consequently, the interfacial roughness generally increases with the oxidation time [14], *i.e.*, with oxide thickness. Additionally, it has been shown that the roughness of the Si/SiO_2 interface is strongly dependent on the oxide thickness but not on the oxidation process itself (dry or wet) [14, 15].

Besides, the roughness evolution of the SiO_2 surface has been investigated by Ohsawa *et al.* [16]. Surface roughness increases only in the early oxidation stage, when the oxide is thinner than $10\,nm$ (see Fig. 4.1 (a)). It is proposed that emitted Si atoms are oxidized at the vicinity of the SiO_2 surface leading to a local volume expansion of the material, thus contributing to the evolution of roughness.

Figure 4.1 (b) summarizes and illustrates the mechanisms driving the surface roughness evolution, taking into account Si emission. Actually, when the oxide is very thin (see Fig. 4.1 ($b1$)), the Si atoms emitted from the interface diffuse through the oxide film out to the atmosphere in the form of SiO gas. Hence, the oxidation rate is increased because

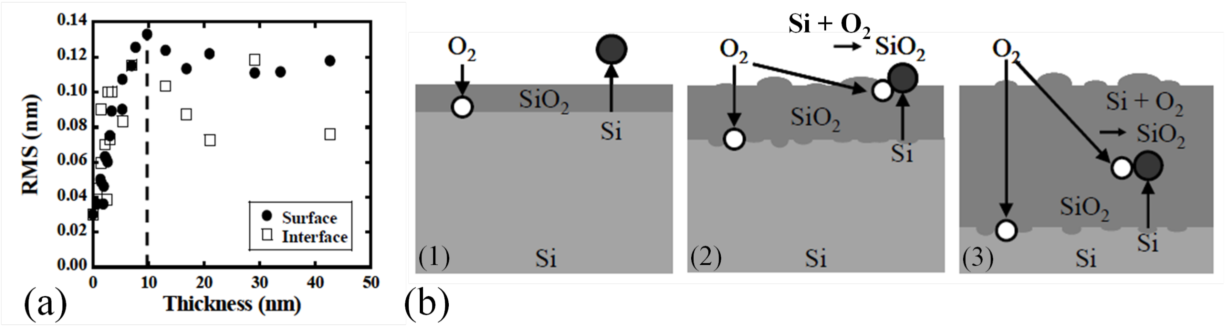

Fig. 4.1: (a) Evolution of *RMS* values of the SiO_2 surface and the Si/SiO_2 interface obtained from $200\times200\,nm^2$ AFM images. (b) Schematic illustration of the roughening model on SiO_2 surface by Si emission when the oxide thickness is (1) very thin, (2) thin, and (3) thick. The open circles are O_2 molecules, and the filled circles are Si atoms. (adapted from [16]).

there is no stress build-up at the interface. As the oxide layer gets thicker, some of the Si atoms can be oxidized nearby the surface, before reaching it (see Fig. 4.1 $(b2)$). This oxidation increases the roughness of the surface by volume expansion. Later on, for thicker oxide layers ($> 10\,nm$), the emitted Si atoms are oxidized in the film far from the surface (see Fig. 4.1 $(b3)$). At this point, the diffusion of Si atoms becomes harder and stress accumulates at the interface, reducing the oxidation rate. The surface roughness does not increase anymore because the SiO_2 layer can absorb the volume expansion isotropically. This «Si emission model» well-explains the experimental observations of the roughness evolution of the oxide surface during thermal oxidation [16–18]. Moreover, it is consistent with the observed change of behavior seen above and below the critical thickness of $10\,nm$.

4.2 | Experimental Methods

The principal objective of the experiments described hereafter was to investigate the evolution of the roughness and thickness uniformity of oxide layers obtained by thermal oxidation of silicon surfaces of different initial roughnesses. For that, we have prepared four different groups of wafers differing by their surface morphologies. The first group (*S1*), consists of mirror-polished (100) Si Cz wafers, we will refer as «smooth» surfaces. The second group (*S2*), consists of mirror-polished Si wafers which have been annealed at 1200 °C during several hours, we will refer as «very smooth» surfaces. Additionally, two other groups of samples were prepared from SOI wafers fabricated by the Smart Cut™ process. The third group (*R1*), consists of post-splitting SOI wafers which have been annealed at 1200 °C during $30\,s$, we will refer as «rough» surfaces. Finally, the fourth group (*R2*), consists of post-splitting SOI wafers without any additional treatment, we will refer as «very rough» surfaces. All wafers were finally cleaned by standard *RCA* process. Then, we have studied the dry and wet oxidations of these different wafers.

The thickness of the grown SiO_2 layers was measured by ellipsometry (SE) following two different protocols. First, the mean value of the thickness was obtained from the averaging of 121 measurements performed following a polar distribution across the wafer. Second, the thickness variations were obtained through linear scans across the wafer using different sampling periods ($\Delta x_1 = 30\,\mu m$, $\Delta x_2 = 300\,\mu m$ and $\Delta x_3 = 2420\,\mu m$). The number of points per profile was fixed at $N = 121$, 14 profiles were recorded for each sampling period (see section 1.1.3 in chapter 1). The surface roughness of the oxide layer was characterized by AFM. Since the roughness evolution is expected to occur at high spatial frequencies, we have recorded AFM images with size of $1 \times 1\,\mu m^2$.

For dry oxidation, the wafers were oxidized in a mixture composed of O_2 and N_2 (99.8% and 0.2% respectively) at a pressure of $760\,Torr$ and oxidation temperatures of 850 °C, 950 °C and 1035 °C. Five different process durations, between 2 min and 1500 min, have been performed. Oxidation was carried out in a conventional vertical furnace (*Telformula* from Tokyo Electron). The wafers were fed into the furnace at 600 °C, then, the temperature was raised with a rate of 5 °C/min up to the target temperature. Experimental conditions are summarized in Table 4.1.

Initial morphology	*Temperature* [°C]	*Process time* [*min*]
$S1$ – $R2$	850	2 – 15 – 180 – 900 – 1500
$S1$ – $R2$	950	2 – 15 – 180 – 900 – 1500
$S1$ – $R2$	1035	2 – 15 – 180 – 900 – 1500

Tab. 4.1: Summary of the experimental conditions, applied to each group (corresponding to initial morphology), to study the impact of time and temperature of the oxidation, on surface roughness and thickness uniformity evolution.

For wet oxidation, the wafers were oxidized in an atmosphere composed of H_2O, O_2 and N_2 (79.8%, 20% and 0.2% respectively) at a pressure of $760\,Torr$ and oxidation temperatures of 950 °C, 1050 °C and 1150 °C. Oxidation times were 2 min, 10 min, 50 min and 480 min. Again, the oxidation processes were carried out using the *Telformula* furnace. The initial temperature at which the wafers were fed into the furnace and the ramp-up were similar to those used for dry oxidation. Experimental conditions are listed in table 4.2.

Initial morphology	*Temperature* [°C]	*Process time* [*min*]
$S1$ – $S2$ – $R1$ – $R2$	950	2 – 10 – 50 – 480
$S1$ – $S2$ – $R1$ – $R2$	1050	2 – 10 – 50 – 480
$S1$ – $S2$ – $R1$ – $R2$	1150	2 – 10 – 50 – 480

Tab. 4.2: Summary of the experimental conditions used to study the impact of wet oxidation on the surface roughness. Those conditions have been performed for each group of wafers.

4.3 | Results and discussion

4.3.1 | Thickness evolution

4.3.1.1 Dry Oxidation

Figure 4.2 shows the time-evolution of the mean oxide thicknesses of oxidized mirror-polished *Si* wafers (*S1*), compared to the predictions from the *DG* model. For oxidation times longer than 100 s, the *DG* model accurately predicts the thickness evolution of these oxide layers. The values used for linear (B/A) and parabolic (B) coefficients are those given by the literature [1]. However, for shorter times, the oxidation kinetics is faster than predicted by the *DG* model. Considering the limit of the model (Eq. 4.1) when t tends to zero, the linear approximation describing the oxide growth for very thin layers writes,

$$Th(t) = \frac{B}{A}(t + \tau) \tag{4.5}$$

Actually, the experimental values can be fitted assuming the existence of an initial oxide layer of 5 nm (τ equal to few minutes). Then, we evidence that the *DG* model does not predict both kinetics, for layers thinner and thicker than 10 nm, simultaneously.

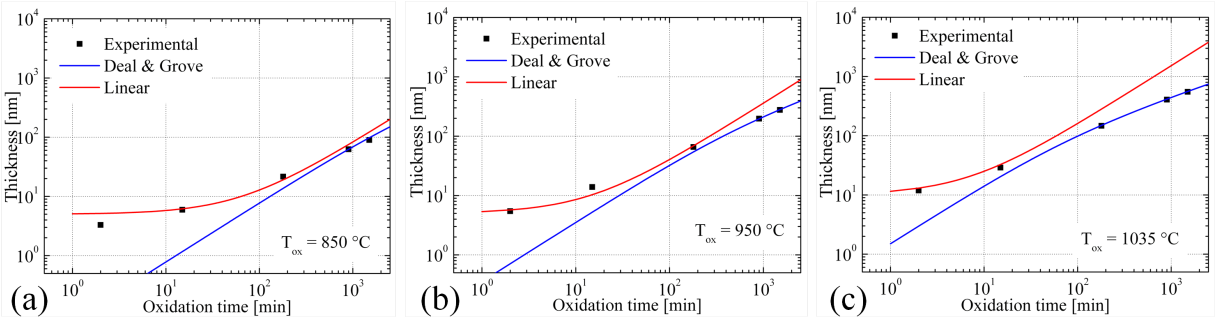

Fig. 4.2: Comparison between thicknesses measured by ellipsometry (points), and that obtained from Deal and Grove model (blue line). Dry oxidation has been performed using mirror-polished *Si* wafers.

Figure 4.3 shows the evolution of the thickness of the oxide layer grown on mirror-polished (*S1*) by dry oxidation. It is compared to values predicted by the Massoud *et al.* model [2]. We observe that this model accurately predicts the thickness evolution during dry oxidation also for thin oxide layers. This suggests that oxidation rate is indeed limited by the oxidation reaction rate when the oxide layer is thinner than $10\,nm$.

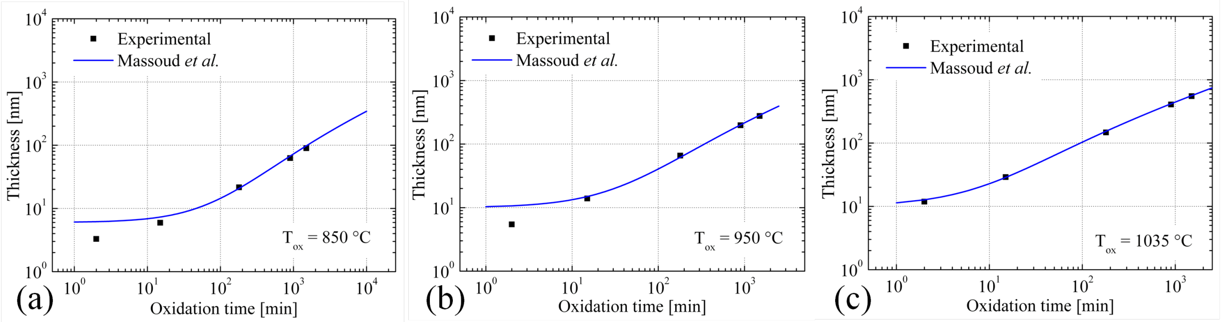

Fig. 4.3: Comparison between thicknesses measured by ellipsometry (points), and that obtained from Massoud *et al.* model (blue line). Dry oxidation has been performed using mirror-polished Si wafers.

These results are in agreement with most of those presented in the literature [2, 19]. Similar results are obtained when comparing the thickness evolution of oxide layers grown on initially very rough (*R2*) surfaces. However, for short oxidation times the oxide growth rate is larger on rough Si surfaces than on smooth surfaces.

Figure 4.4 shows the evolution of the oxide thickness as a function of the oxidation time for both Si mirror polished wafers (*S1*) and post-splitting SOI wafers (*R2*). We observe that the oxide layers grown on rough surfaces are significantly thicker than those grown on smooth surfaces for oxidation times shorter than 15 min. We also note that these differences increase when the oxidation temperature decrease. For oxidation times longer than 15 min (thickness larger than $10\,nm$) the measured thicknesses are identical on both surface morphologies.

Since the oxidation process is limited by the reaction rate at the first stage of the process, it is reasonable to suppose that the oxidation reaction is faster on rougher surfaces. We can also note that, independently on the initial morphology, the thicknesses of the oxide layer are identical for times longer than 180 min. This indicates that for layers thicker than $30\,nm$ the oxidation kinetics is only limited by oxygen diffusion.

Figure 4.5 shows the thickness variations observed after oxidation of smooth wafers (*S1*). The profiles obtained using the smallest sampling period ($\Delta x = 30\,\mu m$), are very similar whatever the oxidation time. For profiles recorded using $\Delta x = 300\,\mu m$ only slight differences can be observed.

Actually, when using the largest sampling period ($\Delta x = 2420\,\mu m$) and thus probing the entire diameter of the wafers, we note important variations of the thickness profiles which

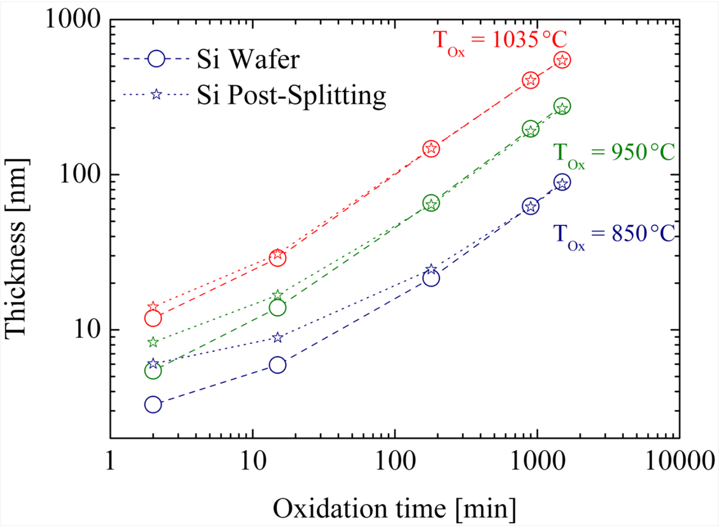

Fig. 4.4: SiO_2 thickness for dry oxidation of Si wafers with mirror-polished (circles) and post-splitting-like (stars) initial surfaces.

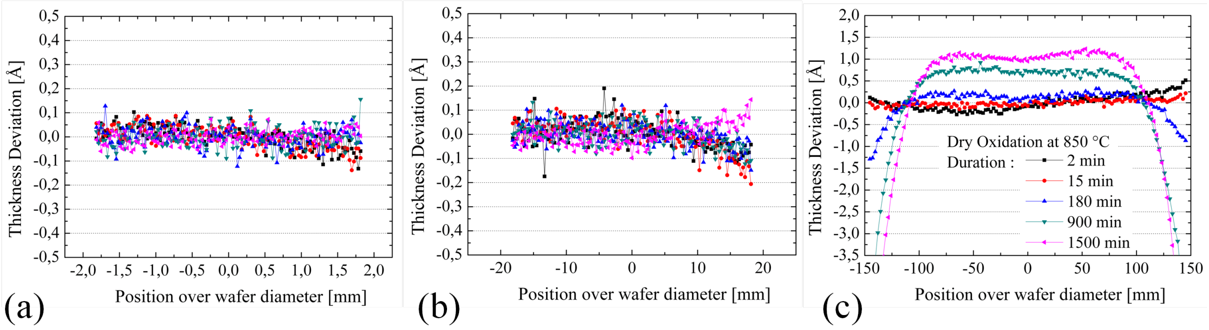

Fig. 4.5: Thickness of oxide layers for dry oxidation measured by *SE* using three different sampling periods: (a) $\Delta x_1 = 30\,\mu m$, (b) $\Delta x_2 = 300\,\mu m$ and (c) $\Delta x_3 = 2420\,\mu m$.

increase with oxidation time. These large thickness variations at the wafer scale results from a thermal gradient over the wafers during the oxidation process. This gradient is inherent to the furnace architecture. Indeed, in the vertical furnaces used in this experiment, gas flow is injected by the top of the tube and then the gas moves down between the tube and the edge of the wafers. Since the injected gas is slightly colder than wafers, the edge of the wafers is cooled down and slows down the oxidation rate.

Figure 4.6 shows PSD_{1D} functions corresponding to the profiles (a) and (b) shown in figure 4.5 (*i.e.*, in the central part of the wafers). For spatial frequencies ranging from $1 \times 10^{-4}\,\mu m^{-1}$ to $2 \times 10^{-2}\,\mu m^{-1}$, the amplitude of the PSD_{1D} functions is very low and remains almost unchanged during oxidation. We also note that the PSD_{1D} function is nearly horizontal, which is typical of a random signal. The thickness of the oxide layer, over this spatial bandwidth, is perfectly uniform. This means that the oxidation rate is nearly constant across the surface of the oxidized wafers.

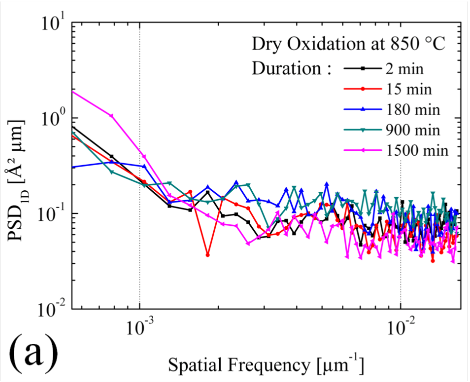

Fig. 4.6: PSD_{1D} describing thickness variations corresponding to profiles presented in Fig. 4.5 using different sampling periods: (a) $\Delta x_1 = 30\,\mu m$ and (b) $\Delta x_2 = 300\,\mu m$.

4.3.1.2 Wet Oxidation

Figure 4.7 shows the evolution of the thickness mean values obtained for mirror-polished wafers (*S1*) under wet oxidation conditions and compares them to the predictions of the *DG* model, for different oxidation temperatures.

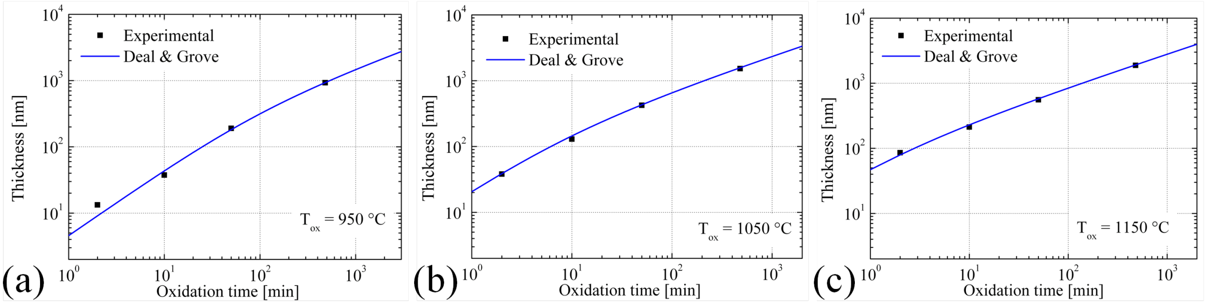

Fig. 4.7: Comparison between thicknesses measured by ellipsometry (points), and obtained from the Deal and Grove model (blue line). Wet oxidation was performed using mirror-polished *Si* wafers (*S1*).

Experimentally, the kinetics of wet oxidation of *S1*, *S2*, *R1* and *R2* wafers seems identical. The *DG* model is able to describe this thickness evolution, with no need to introduce any refinement. Indeed, the short and fast oxidation regime during which the simple, only diffusion limited, *DG* model does not suffice, only lasts 2 min, the time needed to grow a $10\,nm$-thick oxide layer under the conditions of wet oxidation. For this reason, wet oxidation is well-described by the *DG* model.

Finally, the thickness of an oxide layer, grown under both dry and wet oxidations, is always extremely uniform for spatial frequencies from $1 \times 10^{-4}\,\mu m^{-1}$ to $2 \times 10^{-2}\,\mu m^{-1}$ and does not depend on the initial roughness of the *Si* surface, at least for oxide layers thicker than $10\,nm$.

4.3.2 | Roughness evolution

4.3.2.1 Dry Oxidation

Figure 4.8 shows AFM images of SiO_2 surfaces before (Fig. 4.8 (a)) and after dry oxidation at $T_{Ox} = 850\,°C$ of mirror-polished wafers ($S1$) for different durations (b) 2 min, (c) 180 min and (d) 1500 min. The surface morphology evolves as the oxidation time increases: the roughness of the SiO_2 surface increases and surface features with lateral sizes of about few tens of nanometers develop. Our observations confirm previously reported results [14, 17].

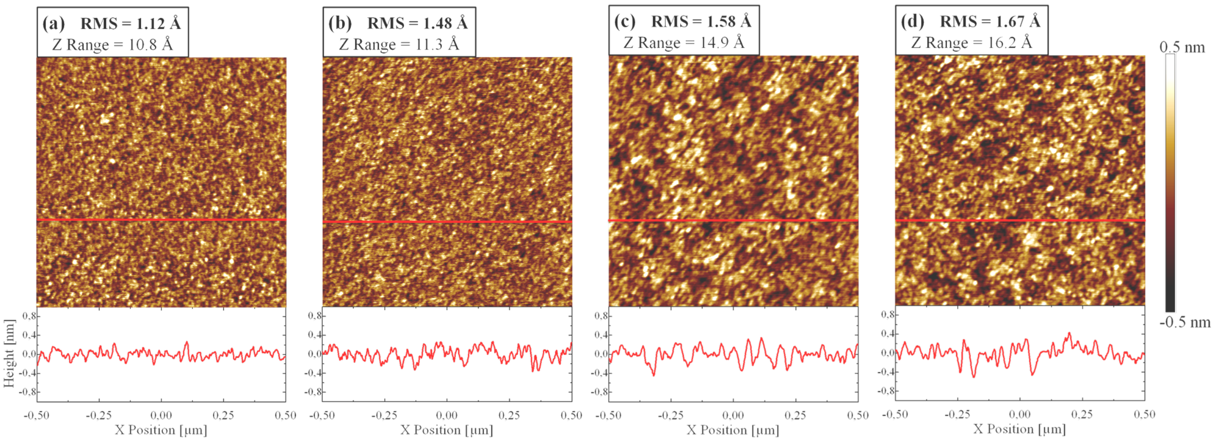

Fig. 4.8: Surface topography of oxidized mirror-polished Si wafers recorded by AFM ($10 \times 10\,\mu m^2$; 512×512 pixels). Corresponding to (a) before oxidation, after dry oxidation at $850\,°C$ during (b) 2 min, (c) 180 min, and (d) 1500 min. The bottom insets shows characteristic surface profiles for each image.

Figure 4.9 shows the time-evolution of the RMS values of the SiO_2 surfaces for wafers from groups $S1$ and $R2$ (smooth and rough). For initially smooth Si surfaces, the SiO_2 roughness increases only during the initial stage of oxidation, when the oxide layer is thinner than $10\,nm$ and then stays constant as the oxide grows. According to Ohsawa *et al.* the evolution of the roughness of initially smooth Si surfaces can be explained by considering the oxidation of the Si atoms emitted from the Si/SiO_2 interface toward the surface. This phenomenon contributes to the roughening of this SiO_2 surface [16].

For initially rough Si surfaces, they first smoothen during the early stage of oxidation then remain constant. Moreover, we do not observe significant impact of the oxidation temperature on this behavior.

Figure 4.10 shows the PSD_{2D} functions describing the roughness evolution of both (a) smooth ($S1$), and (b) rough ($R2$) wafers during dry oxidation.

For smooth surfaces, oxidation results in a slight increase of the amplitude of PSD_{2D} functions for spatial frequencies approximately between $50\,\mu m^{-1}$ and $200\,\mu m^{-1}$ (see red circle in Fig. 4.10 (a)). This increase is related to the appearance of the surface features

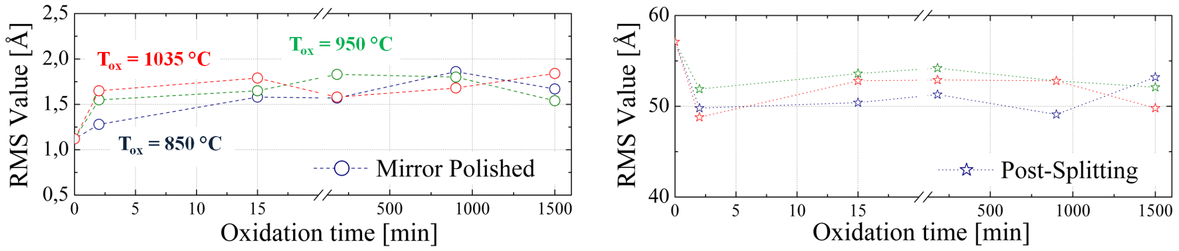

Fig. 4.9: *RMS* values extracted from AFM images recorded from oxidized surfaces for dry oxidation, using experimental conditions summarized in table 4.1.

observed on AFM images. This confirms that the sizes of these features are between 5 nm and 20 nm. The decrease of the reaction rate at the interface due to local stress effects, resulting in a nonuniform oxidation process [10, 15], is though to explain this behavior.

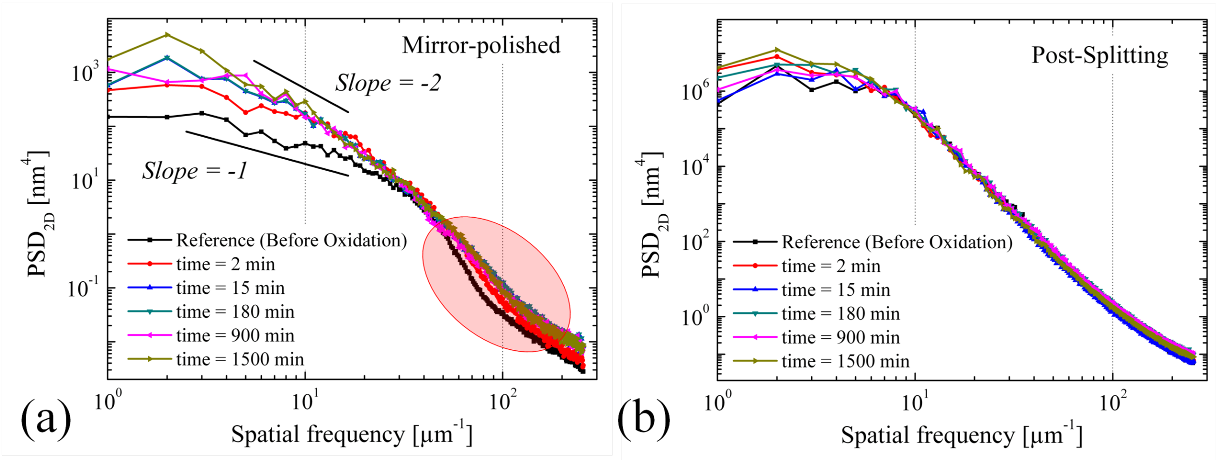

Fig. 4.10: PSD_{2D} functions describing the topography evolution of Si wafers during dry oxidation at 850 °C for (a) smooth and (b) rough initial surfaces.

For spatial frequencies between 1 μm^{-1} and 30 μm^{-1}, the increase of the amplitude of PSD_{2D} functions with oxidation time is much more visible (see left-side of the spectra in Fig. 4.10 (a)). As oxidation proceeds, the slope of the PSD_{2D} functions also changes from -1 for the initial surface to -2 after long times oxidation. The roughness exponents (α) extracted from these slopes vary from -0.5 for initial surfaces to 0 for oxidized surfaces. The first scaling behavior ($\alpha = -0.5$) is typical of chemical-mechanical polishing process used to smooth the Si mirror-polished wafers (the surface roughness varies randomly over this spatial bandwidth). For $\alpha = 0$ the scaling behavior follows the *Edwards-Wilkinson* equation,

$$\frac{\partial h(\vec{x},t)}{\partial t} = \mu \nabla^2 h(\vec{x},t) + \nu(\vec{x},t) \tag{4.6}$$

which derives from the «linear theory» [11] and Eq. 4.4 This equation is usually used to describe the surface roughness evolution during chemical vapor deposition [11, 20].

Finally, we suggest that the roughness evolution of smooth surfaces during dry oxidation can be predicted by using of the *Edwards-Wilkinson* equation.

For rough surfaces, the amplitude of the spectra remains unchanged whatever the oxidation times and temperatures, at least under our experimental conditions. Even if it is commonly accepted that rough surfaces are smoothed during thermal oxidation [14, 21], we have not noticed any evolution along our experiments. We believe that our initial «very rough» surfaces (*R2*) are simply too rough, thus the possible smoothening resulting from the thermal oxidation cannot be detected under our experimental conditions.

4.3.2.2 Wet Oxidation

AFM images were recorded from the different types of surfaces oxidized using the experimental conditions summarized in table 4.2. The *RMS* values obtained from the AFM images are shown in figure 4.11. We observed that, independently on the roughness of the initial surface, the *RMS* value remains almost constant during oxidation for the times considered in our experiments. Moreover, no clear influence of the oxidation temperature is observed.

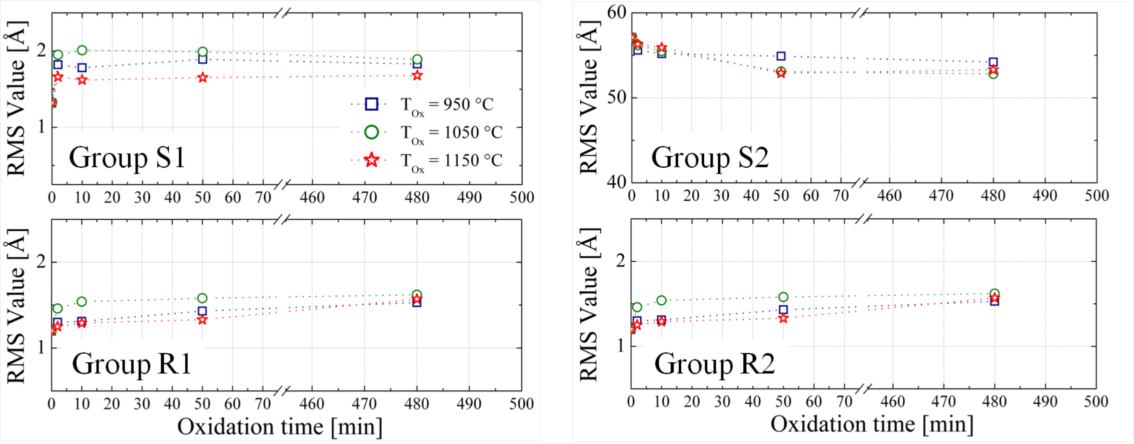

Fig. 4.11: *RMS* values calculated from AFM images recorded from oxidized surfaces for dry oxidation, using experimental conditions summarized in table 4.1.

Since the oxidation rate under wet conditions is significantly larger than that for dry oxidation, the «critical» thickness of 10 nm (where limiting mechanism changes) is reached at the very beginning of the oxidation process. Thus, the thicknesses we have investigated are all beyond this critical value.

The spectra extracted from the AFM images are shown in figure 4.12. The PSD_{2D} functions describing the initial surfaces show different slopes. The mirror-polished surfaces (*S1*) shows a slope equal to -1 while the rough surfaces (*R1*) and very smooth surfaces (*S2*) show slopes equal to -3 and -1.5, respectively.

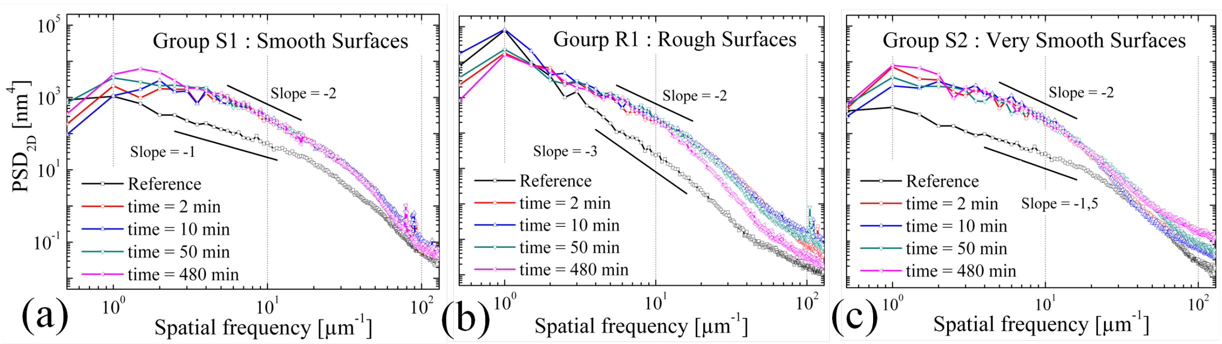

Fig. 4.12: PSD_{2D} functions describing the topography evolution of Si wafers during wet oxidation at 1050 °C for initial surfaces presenting different roughnesses: (a) «smooth» surfaces, (b) «rough» surfaces and (c) «very smooth» surfaces. Note that common vertical axis is used at the left.

After wet oxidation, the slope of all these PSD_{2D} functions is equal to -2. Actually, all these PSD_{2D} functions can be superimposed over the whole spectral bandwidth. For the initially «smooth» surfaces, group *S1*, the surface gets rougher during wet oxidation, impacting spatial frequencies between $1\,\mu m^{-1}$ and $50\,\mu m^{-1}$ (see Fig. 4.12 (a)). For the initially «rough» surfaces (*R1*), wet oxidation increases the amplitude of the PSD_{2D} function for spatial frequencies lying between $2\,\mu m^{-1}$ and $100\,\mu m^{-1}$ (see Fig. 4.12 (b)). Finally, for «very smooth» surfaces (*S2*), the surface is roughened between $0.5\,\mu m^{-1}$ and $30\,\mu m^{-1}$ (see Fig. 4.12 (c)). Additionally, for initially «very rough» surfaces (*R2*) no changes in the amplitude of the PSD_{2D} function are observed (not shown). Thus, it is remarkable that independently of the initial surface morphology, the scaling behavior observed after thermal oxidation is quite similar. This shows that the final roughness of the SiO_2 surface is independent on the initial roughness of the Si surface, if this roughness is not too large.

Moreover, PSD_{2D} functions observed after wet oxidation are very similar to those obtained after dry oxidation. This strongly suggests that the physical mechanisms involved in the roughening processes during wet and dry oxidations are probably identical and that it can be described by the continuum equation at the case of the *Edwards-Wilkinson* model [6].

4.3.2.3 Sacrificial oxidation step in the Smart Cut™ process

Otherwise, we have characterized several wafers sampled during the fabrication of SOI by the Smart Cut™ process. For example, we have characterized the oxide surface topographies before and after the sacrificial oxidation step used to adjust the thickness of Si top layer to specifications. Figure 4.13 shows the superimposition of the PSD_{2D} functions obtained from AFM images of $1\times1\,\mu m^2$ and $30\times30\,\mu m^2$ before and after such an oxidation step. We observed that after oxidation, the SiO_2 surface gets slightly rougher than it was for spatial frequencies approximately between $2\,\mu m^{-1}$ and $70\,\mu m^{-1}$. Thus, oxidation steps such as those involved in the fabrication of SOI wafers using the Smart Cut™ process, have an impact on the roughness over this specific spatial bandwidth.

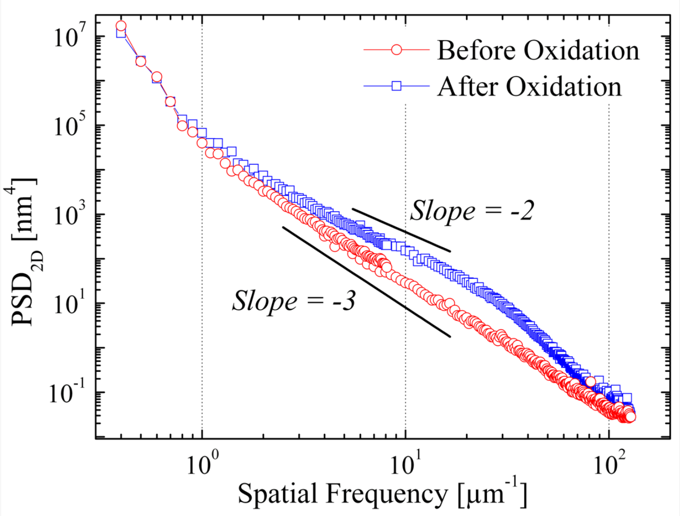

Fig. 4.13: Typical PSD_{2D} functions before and after oxidation step involved in the fabrication of SOI wafers.

Here, only the increase of the roughness of the SiO_2 surface is evidenced. However, we have demonstrated that for spatial frequencies higher than $2\,\mu m^{-1}$ the thickness variations of the top Si layer of SOI wafers are larger than topographic variations of the layer (see section 1.3 in chapter 1) evidencing that, over this spatial bandwidth, roughness of interfaces delimiting the Si layer (Si/SiO_2 and Si/air interfaces) are of same order of magnitude. Thus, we suggest that thermal oxidation can affect the thickness uniformity of the top silicon layer on the spatial bandwidth established above.

Conclusions

In this chapter, we have experimentally investigated the impact of time and temperature on the thickness uniformity and the surface roughness of the oxide layer grown by both dry and wet oxidations. We have confirmed that roughening of the oxide surface only takes place during the early stage of the oxidation process, *i.e.*, for oxide thicknesses smaller than $10\,nm$. Moreover, the roughness evolution during oxidation shows a scaling behavior well explained by the continuum theory and more specifically by the *Edwards-Wilkinson* equation. The spectral footprint of oxidized surfaces is found to be similar whatever the initial surface morphology, pointing out that physical mechanisms involved in dry and wet oxidations are probably identical. Finally, we have identified the spatial bandwidth over which the thermal oxidation process, involved in the Smart Cut™ technology, have an influence on the final thickness uniformity of the top silicon layer of SOI wafers.

Bibliography

[1] B. E. Deal and A. S. Grove, “General relationship for the thermal oxidation of silicon,” *Journal of Applied Physics*, vol. 36, no. 12, pp. 3770–3778, 1965. (cited in pages 107 and 112)

[2] H. Z. Massoud, J. D. Plummer, and E. A. Irene, “Thermal oxidation of silicon in dry oxygen growth-rate enhancement in the thin regime : Experimental results,” *Journal of The Electrochemical Society*, vol. 132, no. 11, pp. 2685–2693, 1985. (cited in pages 108 and 113)

[3] S. Ogawa, A. Yoshigoe, S. Ishidzuka, Y. Teraoka, and Y. Takakuwa, “Consumption kinetics of Si atoms during growth and decomposition of very thin oxide on Si (001) surfaces,” *Thin solid films*, vol. 508, no. 1, pp. 169–174, 2006. (cited in page 108)

[4] M. Uematsu, H. Kageshima, and K. Shiraishi, “Unified simulation of silicon oxidation based on the interfacial silicon emission model,” *Japanese Journal of Applied Physics*, vol. 39, no. Part 2, No. 7B, pp. L699–L702, 2000. (cited in page 108)

[5] M. Uematsu, H. Kageshima, and K. Shiraishi, “Simulation of wet oxidation of silicon based on the interfacial silicon emission model and comparison with dry oxidation,” *Journal of Applied Physics*, vol. 89, no. 3, 2001. (cited in page 108)

[6] T. Yoshinobu, A. Iwamoto, K. Sudoh, and H. Iwasaki, “Scaling of Si/SiO_2 interface roughness,” *Journal of Vacuum Science Technology B: Microelectronics and Nanometer Structures*, vol. 13, no. 4, pp. 1630–1634, 1995. (cited in pages 108, 109 and 119)

[7] L. Lai and E. A. Irene, “Limiting Si/SiO_2 interface roughness resulting from thermal oxidation,” *Journal of Applied Physics*, vol. 86, no. 3, pp. 1729–1735, 1999. (cited in page 108)

[8] H. Omi, H. Kageshima, and M. Uematsu, “Scaling and universality of roughening in thermal oxidation of Si(001),” *Phys. Rev. Lett.*, vol. 97, p. 016102, Jul 2006. (cited in page 108)

[9] H. Omi, H. Kageshima, T. Kawamura, M. Uematsu, Y. Kobayashi, S. Fujikawa, Y. Tsusaka, Y. Kagoshima, and J. Matsui, “Stability-instability transition of reaction fronts in thermal oxidation of silicon,” *Phys. Rev. B*, vol. 79, p. 245319, Jun 2009. (cited in page 109)

[10] G. Grinstein, Y. Tu, and J. Tersoff, “Stability of solid state reaction fronts,” *Phys. Rev. Lett.*, vol. 81, pp. 2490–2493, Sep 1998. (cited in pages 109 and 117)

[11] A. L. Barabasi and H. E. Stanley, *Fractal Concepts In Surface Growth.* Cambridge Press, 1995. (cited in pages 11, 12, 13, 78, 79, 80, 84, 85, 88, 89, 109, 117 and 118)

[12] F. Family and T. Vicsek, “Scaling of the active zone in the eden process on percolation networks and the ballistic deposition model,” *Journal of Physics A: Mathematical and General*, vol. 18, no. 2, p. L75, 1985. (cited in pages 12 and 109)

[13] J. Krug and H. Spoh, *Solids far from Equilibrium*, ch. Growth and morphology and defects, p. 479. Cambridge University Press, 1991. (cited in page 109)

[14] S. Fang, W. Chen, T. Yamanaka, and C. Helms, “The evolution of (001) Si/SiO_2 interface roughness during thermal oxidation,” *Journal of The Electrochemical Society*, vol. 144, no. 8, pp. 2886–2893, 1997. (cited in pages 109, 116 and 118)

[15] A. Carim and R. Sinclair, “The evolution of Si/SiO_2 interface roughness,” *Journal of The Electrochemical Society*, vol. 134, no. 3, pp. 741–746, 1987. (cited in pages 109 and 117)

[16] K. Ohsawa, Y. Hayashi, R. Hasunuma, and K. Yamabe, “Roughness increase on surface and interface of SiO_2 grown on atomically flat Si (111) terrace,” in *Journal of Physics: Conference Series*, vol. 191, p. 012031, IOP Publishing, 2009. (cited in pages 109, 110 and 116)

[17] K. Yamabe, K. Ohsawa, Y. Hayashi, and R. Hasunuma, “2-D roughening of SiO_2 thermally grown on atomically flat Si surface,” *ECS Transactions*, vol. 19, no. 2, pp. 427–442, 2009. (cited in pages 110 and 116)

[18] F. Iacona, V. Raineri, F. La Via, and E. Rimini, “Roughness of thermal oxide layers grown on ion implanted silicon wafers,” *Journal of Vacuum Science Technology B: Microelectronics and Nanometer Structures*, vol. 16, pp. 619–627, Mar 1998. (cited in page 110)

[19] R. M. C. de Almeida, S. Goncalves, I. J. R. Baumvol, and F. C. Stedile, “Dynamics of thermal growth of silicon oxide films on Si,” *Phys. Rev. B*, vol. 61, pp. 12992–12999, May 2000. (cited in page 113)

[20] J. T. Drotar, Y.-P. Zhao, T.-M. Lu, and G.-C. Wang, “Surface roughening in low-pressure chemical vapor deposition,” *Phys. Rev. B*, vol. 64, p. 125411, Sep 2001. (cited in page 118)

[21] W. H. Juan and S. W. Pang, “Controlling sidewall smoothness for micromachined si mirrors and lenses,” *Journal of Vacuum Science and Technology B*, vol. 14, no. 6, 1996. (cited in page 118)

5 | Chemical Mechanical Polishing

Contents

Chemical Mechanical Polishing (*CMP*) has emerged as a key technology to achieve both global and local planarity of wafer surfaces. Indeed, the *CMP* process is one of the most important techniques of topography reduction in the semi-conductor industry. In this chapter, we will experimentally investigate the impact of several parameters, such as the slurry nature, the initial surface topography, and the presence of implantation induced damages onto the thickness uniformity, and the roughness evolution of the processed Si surfaces.

5.1 | State of the art

The *CMP* is a very complex process which includes a large number of variables, such as the initial wafer geometry and material, the process parameters (pressure, velocity, duration) and parameters linked to the process equipment (nature of slurry, roughness of the pad, etc.). In this process, both mechanical and chemical mechanisms occur. *CMP* can be thought as a chemically assisted mechanical polishing, in which material removal is primarily due to a three-body contact. Indeed, the wafer surface is softened or modified by the chemical solution, and then, the soft surface layer is removed by abrasive particles held by a polishing pad. Several analysis consider those two mechanisms separately, but actually, both mechanisms can also interact with each other [1]. Figure 5.1 shows a schematic illustration of a typical *CMP* tool. It is composed of a rotating platen, carrying the polishing pad, and a rotating holder, carrying the material to be polished. During *CMP* processes, the silicon wafer to be polished, which rotates on its axis, is pressed face-down against a rotating polishing pad while a slurry containing a combination of chemicals, fluids, and abrasive particles is deposited on the pad.

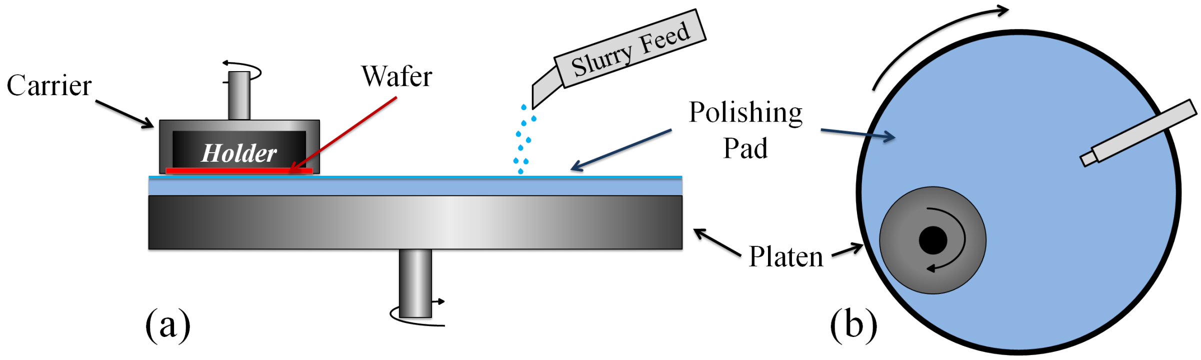

Fig. 5.1: Schematic diagram of typical rotating *CMP* tool. (a) side-view and (b) top-view.

5.1.1 | Material removal

In the literature, four main models intend to describe the various mechanisms, at the particle scale which may occur during a *CMP* process . The first model presented hereafter is empirical and attempts to identify the role of several experimental parameters. The second one presents *CMP* as a chemical erosion process enhanced by stress. The third model assumes that the surface wafer is mechanically plowed by abrasive particles, and links the removal rate to the indentation depth of abrasives into the wafer surface. Finally, the fourth adds a chemical contribution which may significantly impact the material removal rate.

5.1.1.1 Empirical model

Depending on the polishing parameters used during *CMP*, the material removal rate (*MRR*) required to achieve a global planarization varies [1–3]. The *MRR* is often described by the *Preston's* equation [4], as follows,

$$MRR = K_P \, P \, V_r \tag{5.1}$$

Where K_P is the *Preston* coefficient, which depends on the properties of the slurry, on the polishing pad, and on the nature of the polished surface. P is the pressure applied on the carrier (holder), and V_r is the linear relative velocity between the polishing pad and the carrier. *Preston's* equation is an empirical law initially proposed for describe glass polishing. For most of the experimental data, especially in dielectric *CMP*, *Preston's* law provides a reasonably good fit to the data. Although this well-known equation 5.1 allows controlling macroscopically the amount of removed material, it does not take into account the process parameters related to the slurry and the pad. Hence, *Preston*'s equation has been revised by several authors [5,6] evidencing a non-linear dependency of the *MRR* on pressure and velocity. Although this model does not describe the removal mechanisms, it provides some intuition on how to handle a *CMP* process.

5.1.1.2 Stress enhanced Erosion model

Based on *Preston*'s formula, Zhang *et al.* [5] have proposed an equation accounting for the normal and shear stress acting on the contact area between the wafer surface and the abrasive particles. Following the same approach, Zhao *et al.* [6] evidenced the non-linear dependence of material removal on the pressure they have observed is related to the contact area between the wafer and the pad. Hence, they argued that the number of abrasive particles involved in material removal increases with the contact area following a non-linear law. Since the *MRR* is linearly related to the number of abrasive particles, the material removal rate will be non-linear versus pressure.

These revised models pointed out other parameters which impact the *MRR* of the *CMP*. However, there are still many other parameters which should be taken into account such as the change of the force applied on the abrasive particles when increasing the contact area.

5.1.1.3 Indentation mechanism models

Liu *et al.* [7] propose to consider the deformation over the wafer-abrasive interface. To do that, they take into account the adherence of the abrasive particle to the surface, which is related to the hardnesses of the wafer and of the pad, as well as the bending of the abrasive particles. Cook *et al.*, [8] also accounted for the wafer deformation and have found that the removal rate was inversely proportional to the Young's modulus of the wafer material. These investigations clearly highlight that the local deformation of the wafer is also an important parameter to be taken into account when modeling the *MRR* during a *CMP* process.

5.1.1.4 Chemical mechanisms

It has been also reported that the polishing pad together with the composition of the slurry and the applied pressure, have large influences on *MRR* [1,9,10]. Kaufman *et al.* [9] investigated the polishing of tungsten-covered silicon wafers. They have evidenced that material removal in *CMP* occurs as a consequence of a combination of chemical reactions of the slurry with the wafer surface materials and mechanical interactions with the abrasive particles. Indeed, a softened layer is created by chemical reaction, which is removed by the repeated sliding, rolling, or indentation of the abrasive particles against the wafer surface.

Several studies also pointed out the strong impact of the *pH* of the slurry on the *MRR*, showing the importance of chemical reactions [11, 12].

This brief review shows that material removal has been widely investigated at the «particle scale». Most considerations are based on two-body contact approaches. At this point we recommend reading the Ph.D thesis by S. Yeruva [13].

In order to have a global picture of material removal during *CMP*, numerous authors have investigated phenomena taking place at different spatial scales. On the one hand, the impact of surface features and die-pattern has been studied. At these scales, several semi-empirical models which attribute the topographical variations to the pressure non-uniformity and the macroscopic deformation of the pad, have been proposed [14–16]. Besides, physical models have also been reported. These models assumed that a slurry film exists between the surface of the wafer and the pad, and developed pressure equations based on fluid mechanics in order to predict the pressure non-uniformity [17] [18]. On the other hand, some wafer-scale models have been suggested [19–22]. Most of these models assume a solid-solid contact between the wafer and the pad to consider the pressure distribution. Additionally, these models establish that non-uniformities of the material removal, at the wafer scale, are related to the distribution of the applied pressure and to the velocity across the wafer, inherent to the configuration of the *CMP* equipment. Models at these three different scales are discussed in detail in the Ph.D. thesis by Luo [23].

5.2 | Experimental procedure and samples

Hereafter, we investigate the influence of different slurries on the planarization kinetics using a *CMP* process, for two different initial surfaces morphologies (rough and very rough). SOI (100)-oriented 300 mm-in-diameter wafers have been used as the starting material. In that way, the thickness variations of the top silicon layer can be characterized by means of spectroscopic ellipsometry (*SE*). All «finishing steps» of the SOI fabrication were omitted in order to start with post-splitting (fractured) surfaces, but a standard *RCA* cleaning process was performed. The wafers were then prepared into three groups. For the first group, no additional preparation step was performed. This group will be noted «very rough» surfaces below. For the second group («very rough-like» surfaces), the implantation-induced damaged region was removed by means of thermal oxidation followed by the chemical dissolution of the oxide layer. Finally, for the third group of samples («rough» surfaces), thermal annealing was performed, after removal of implantation-induced damaged region (at 1200 °C, 30 s) on post-splitting wafers in order to obtain smoother surfaces.

Three different slurries were used: i) The *EPL*-2361 («Slurry 1»), initially developed for Copper removal, allows achieving very small material removal rates on SOI. ii) The

Glanzox (named «Slurry 2») consisting of colloidal silica dispersed in a liquid, permitting to achieve very high quality polished surfaces. iii) The «Slurry 3» is a new slurry developed at CEA/LETI, we investigated its impact on the surface roughness of polished wafers.

Most of *CMP* treatments have been performed at CEA/LETI in collaboration with C. Euvrard and M. Rivoire. The experimental conditions used in the experiment are summarized in table 5.1.

Sample Group	*Sample number*	*Slurry*	*Removal* [*nm*]
Very rough surfaces	1 – 2 – 3 – 4	*EPL-2301*	5 – 10 – 20 – 30
Very rough surfaces	1 – 2 – 3 – 4	*Glanzox*	10 – 20 – 30 – 90
Very rough surfaces	1 – 2 – 3 – 4	*Slurry* 3	10 – 20 – 30 – 90
Very rough-like surfaces	1 – 2 – 3 – 4 – 5 – 6	*EPL-2301*	4 – 6 – 8 – 10 – 20 – 30
Very rough-like surfaces	1 – 2 – 3 – 4 – 5 – 6	*Glanzox*	4 – 6 – 8 – 10 – 20 – 30
Rough surfaces	1 – 2 – 3 – 4 – 5 – 6	*EPL-2301*	2 – 4 – 6 – 8 – 10 – 13
Rough surfaces	1 – 2 – 3 – 4 – 5	*Glanzox*	4 – 6 – 8 – 10 – 13
Rough surfaces	1 – 2 – 3 – 4	*Slurry* 3	4 – 6 – 10 – 13

Tab. 5.1: Summary of the experimental conditions performed in the study of the *CMP* parameters' process influence on the thickness uniformity and surface roughness of SOI wafers.

Since these slurries have different compositions, the process parameters must be specifically set for each. To be able to compare them, we have fixed the material removal rates, then have adjusted the process parameters (pressure distribution, relative velocity) accordingly.

Figure 5.2 shows the evolution of removed material as a function of the polishing time. For slurry 1, we used a very slow removal rate ($0.5\,\text{Å}s^{-1}$) while for slurry 2 the removal rate was equal to $10\,\text{Å}s^{-1}$. For slurry 3, the removal rate was dependent on the topography of the polished surface. Thus, we have used a slow removal rate ($0.5\,\text{Å}s^{-1}$) for smooth surfaces and a faster removal rate ($10\,\text{Å}s^{-1}$) to polish rough surfaces.

After polishing, the top silicon layer thickness and the surface roughness of the processed wafers were also characterized. The thickness was measured by *SE* (see section 1.1.3 in chapter 1), while the surface roughness was imaged by means of AFM.

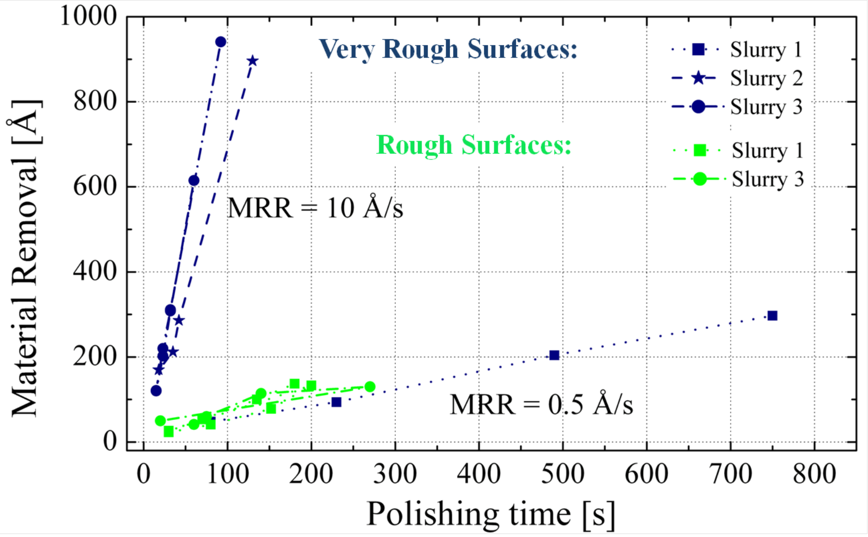

Fig. 5.2: Experimental values of material removal for smooth and rough surfaces using slurries 1, 2 and 3, as a function of polishing time.

5.3 | Results and discussion

5.3.1 | Thickness uniformity

Since the material removal rate is not perfectly uniform across the whole wafer, thickness variations of the top silicon layer tend to increase during a *CMP* process. Figure 5.3 shows typical profiles observed on SOI wafers after polishing, over the three spatial bandwidth measurable by *SE*. Depending on the observation scale (defined by the sampling period), three different trends are observed. For the smaller sampling period ($\Delta x_1 = 30\,\mu m$), the measured profiles are very similar before and after polishing. For a $\Delta x_2 = 300\,\mu m$, slight differences are observed after removal of $10\,nm$. For profiles recorded with $\Delta x_3 = 2420\,\mu m$, significant differences are seen which increase with the amount of removed material.

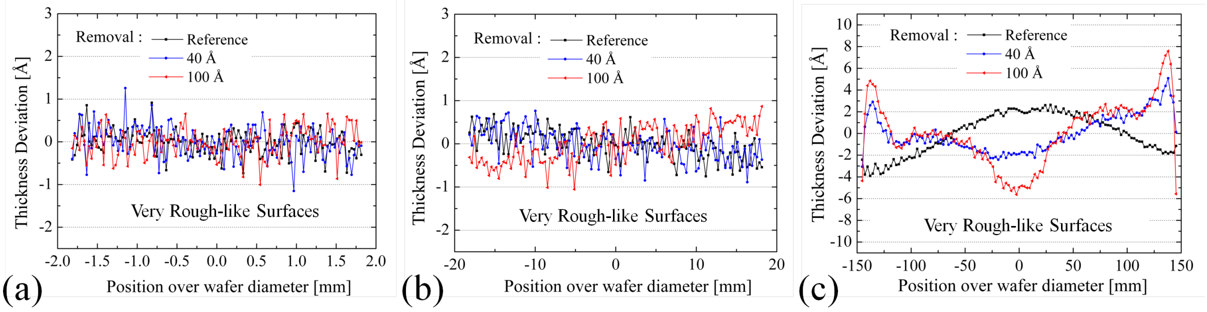

Fig. 5.3: Thickness profiles from *SE* measurement of SOI wafers with «very rough-like» surfaces treated by *CMP* using slurry 1, for three sampling period: (a) $\Delta x_1 = 30\,\mu m$, (b) $\Delta x_2 = 300\,\mu m$, (c) $\Delta x_3 = 2420\,\mu m$.

Figure 5.4 presents the PSD_{1D} functions, split along different frequency bandwidths, corresponding to the thickness variations observed after the removal by CMP of 30 nm of Si using slurry 1 and 2.

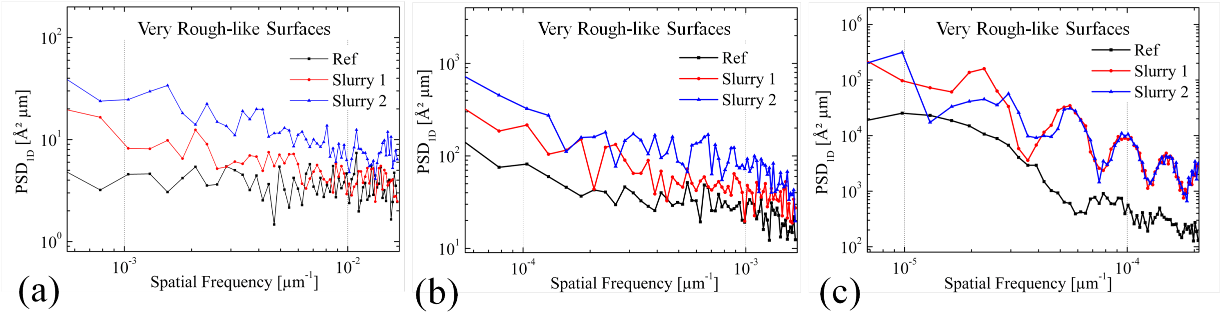

Fig. 5.4: PSD_{1D} functions corresponding to thickness variations of top silicon layer of «very rough-like» wafers before and after CMP process for slurries 1 and 2.

For low frequencies (see figure 5.4 (c)), the amplitude of the PSD_{1D} function is dramatically larger after polishing using both slurries. The peaks, actually contributing to the thickness variations, are those located between the spatial frequencies of approximately 1×10^{-5} and 3×10^{-5}. The additional peaks, seen at higher frequencies, are artifacts (harmonics) introduced by the numerical calculation of the PSD_{1D} function.

At higher frequencies (figure 5.3 (a-b)), the PSD_{1D} amplitudes are also larger after CMP using both slurries the slurry 2 resulting in the largest amplitude increase. Moreover, for slurry 1, the PSD_{1D} amplitude remains almost constant for spatial frequencies approximately lying between $6\times10^{-3}\,\mu m^{-1}$ and $2\times10^{-2}\,\mu m^{-1}$.

These results show that the slurry 2 generates a degradation on the thickness uniformity over the whole spatial bandwidth covered by SE. Alternatively, the use of slurry 1 does not degrade the thickness uniformity for spatial frequencies higher than $6\times10^{-3}\,\mu m^{-1}$.

Slurry 1 and 2 have different compositions and then the process parameters used during the CMP treatment (pressure distribution, relative velocity) were different. Since the non-uniformity of the material removal over the wafer is believed to be due to these parameters (wafer-scale CMP models [24]), we suggest that the thickness variations we measure are probably due to the pressure distribution and the relative velocity between the polished wafer and the pad during our experiments.

5.3.2 | Roughness evolution

5.3.2.1 Starting material: Post-Splitting surfaces

Figure 5.5 shows $30\times30\,\mu m^2$ AFM images of the surface topography of post-splitting SOI wafers («very rough» surfaces) processed by CMP. Smaller AFM images ($1\times1\,\mu m^2$) were also recorded. Figure 5.5 (a) shows the surface morphology before treatment. Figures 5.5 (b-c) shows images of the surface after polishing using slurry 1. The height variations are reduced during the *CMP* process. This reduction takes place from the top of the surface. Indeed, the «peaks» on the surface morphology are reduced while the «holes» remain. After removal of 30 nm of Si, most of the holes on the surface have disappeared. Nevertheless, nano-scratches are visible (see Fig. 5.5 (c)).

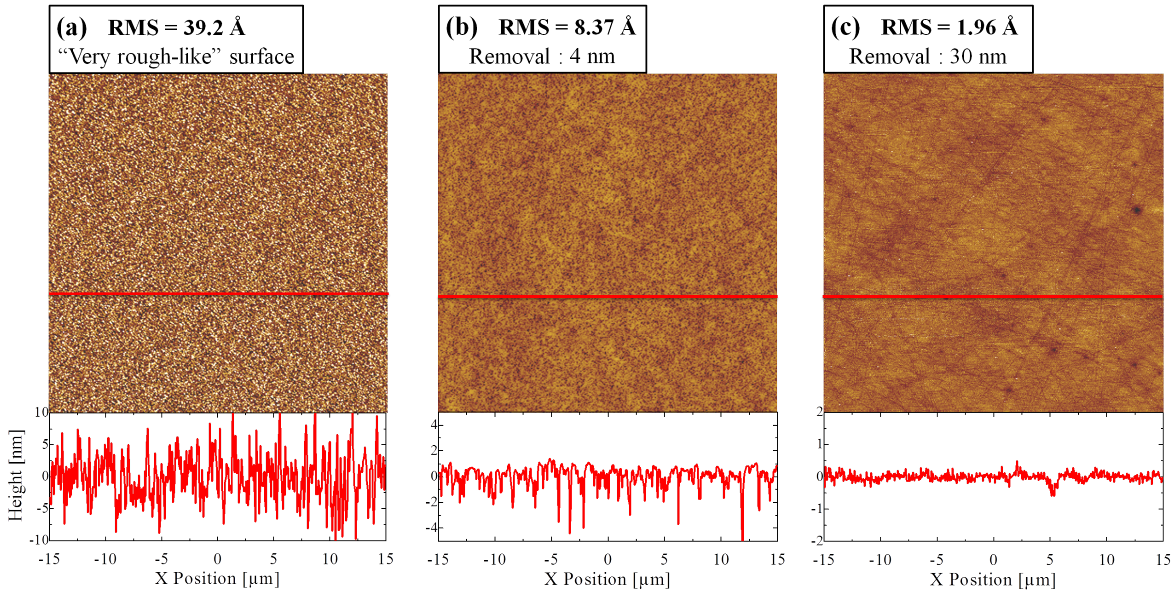

Fig. 5.5: Typical AFM Images ($30\times30\,\mu m^2$; 512×512 pixels) of post-splitting SOI wafers («very rough» surfaces) before (a) and after *CMP* process using slurry 1. Images shown correspond to the minimal : $4\,nm$ (b) and the maximal : $30\,nm$ (c) material removal. The bottom insets shows surface profiles along the red line on the AFM images.

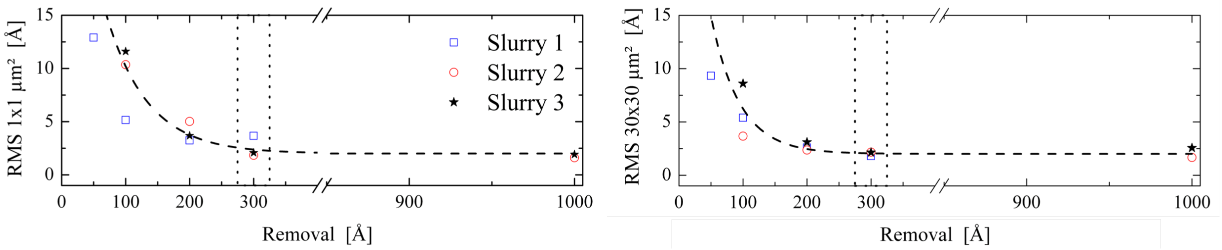

Fig. 5.6: Evolution of the *RMS* value with the amount of removed material during a *CMP* process. The values are obtained from the AFM images recorded on post-splitting SOI wafers after polishing. Sizes of recorded images were: (a) $1\times1\,\mu m^2$ and (b) $30\times30\,\mu m^2$.

Figure 5.6 shows the *RMS* values obtained from AFM images of post-splitting («very rough» surfaces) wafers polished using the experimental conditions presented in table 5.1. The *RMS* values obtained from both scan sizes ($1\times1\,\mu m^2$ and $30\times30\,\mu m^2$) show a similar behavior. In both cases, the RMS decreases during CMP for removals up to $300\,nm$. In order to evidence this effect, the plotted range is limited to $15\,nm$ and thus the initial RMS value (39.2 Å) is out of this range. When removing more material, the RMS value remains almost constant. It is also observed that the lowest roughness is reached when using slurry 2.

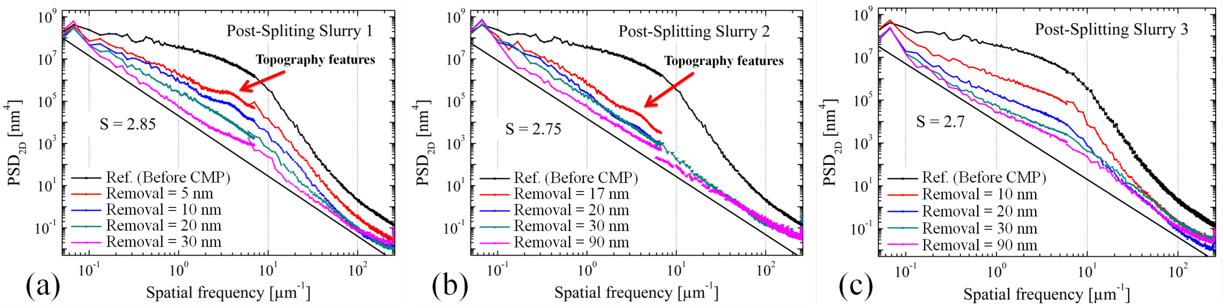

Fig. 5.7: PSD_{2D} functions describing the topography evolution of a Si surface during a CMP process performed on post-splitting SOI wafers («very rough» surfaces) using (a) slurry 1, (b) slurry 2 and (c) slurry 3.

The PSD_{2D} functions describing the surfaces before and after the CMP process were calculated from the AFM images. Figure 5.7 shows the spectral evolution of the roughness for post-splitting wafers polished using the three different slurries. It shows the superimposition of the PSD_{2D} functions obtained from two AFM scan sizes.

The PSD_{2D} functions describing the surfaces after removal of very thin layers (see red curve in Fig. 5.7 (a) and (c)) are nearly parallel to the PSD function corresponding to the surface before the CMP process (black curve). At the beginning of the polishing of «very rough» surfaces, the reduction of the PSD amplitude is almost equal for all spatial frequencies. This suggests that, at this stage, the material removal of Si can be seen as a random process.

For slurries 1 and 2 a «bump» is observed for material removals smaller than $20\,nm$ over spatial frequencies lying between 3 and $8\,\mu m^{-1}$. This «bump» corresponds to topographic features of sizes between 100 and $300\,nm$. These surface features are typical of post-splitting surfaces (see section 2.2 in chapter 2). This «bump» is not observed slurry 3. However, for an identical amount of removed material, surfaces polished using slurry 3 show higher roughnesses.

Finally, we can conclude that for damaged post-splitting surfaces and for large enough amounts of removed material, the CMP process using slurries 1 and 2 leads to very smooth surfaces. When using slurry 3 rougher surfaces are obtained. Additionally, we can point out that for larger material removals, the PSD_{2D} functions tend to follow a fractal behavior with a slope $S \sim 2.8 \pm 0.1$. This suggests that for large enough removals, the morphology of the polished surfaces has the same scaling behavior.

5.3.2.2 Starting material: Post-Splitting damage-free surfaces

In order to study whether implantation induced defects present near the surface of SOI post-splitting wafers, have an influence on the *CMP* process, we have performed a study similar to the previous one but on post-splitting SOI wafers from which the damaged region was removed using a thermal oxidation followed by a chemical etching of the oxide layer («very rough-like» surfaces). We have demonstrated in chapter 4 that thermal oxidation does not modify the spectrum of «very rough» surfaces. Thus, «very rough-like» surfaces show very similar surface morphology than post-splitting SOI wafers.

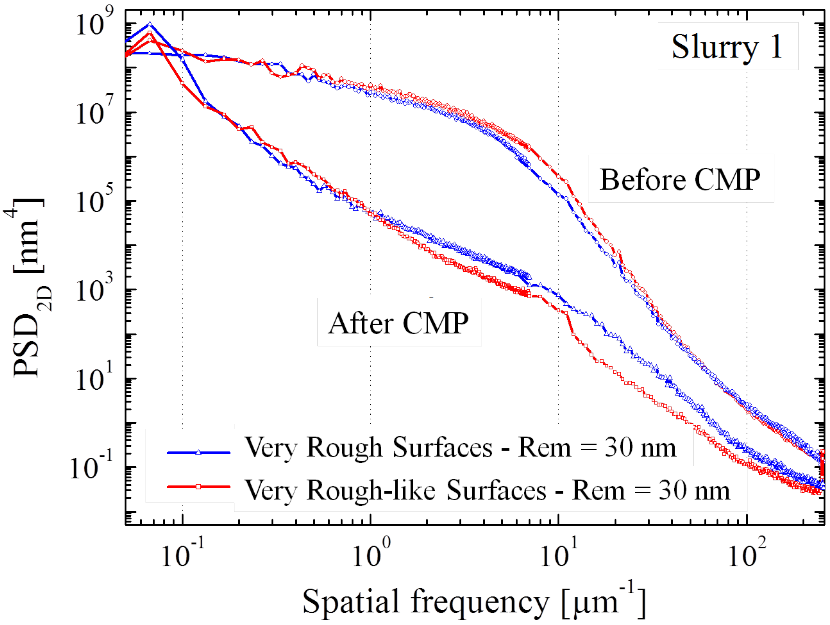

Fig. 5.8: Comparison of the PSD_{2D} functions describing the topography of the «very rough» surfaces and «very rough-like» surfaces before and after a *CMP* process using slurry 1. 30 nm was removed by *CMP*.

In terms of *RMS*, no differences have been observed between these two materials.

Figure 5.8 shows the superimposition of the *PSD* functions describing «very rough» and «very rough-like» surfaces before and after the *CMP* process (30 nm material removal). Before *CMP*, the *PSD* function describing the «very rough» surface shows slightly larger values than that describing the «very rough-like» surface. On the contrary, after the *CMP* process, the «very rough» surface shows lower *PSD* amplitudes. These results suggest that the smoothing by *CMP* is somehow faster when the *Si* crystal is still damaged by the hydrogen implantation.

Since the PSD_{2D} functions describing both materials after the *CMP* process have very similar slopes ($S \sim 2.8 \pm 0.1$), we can infer that their scaling behavior is also very similar. We can then suggest that their roughness evolution should be dominated by the same phenomena.

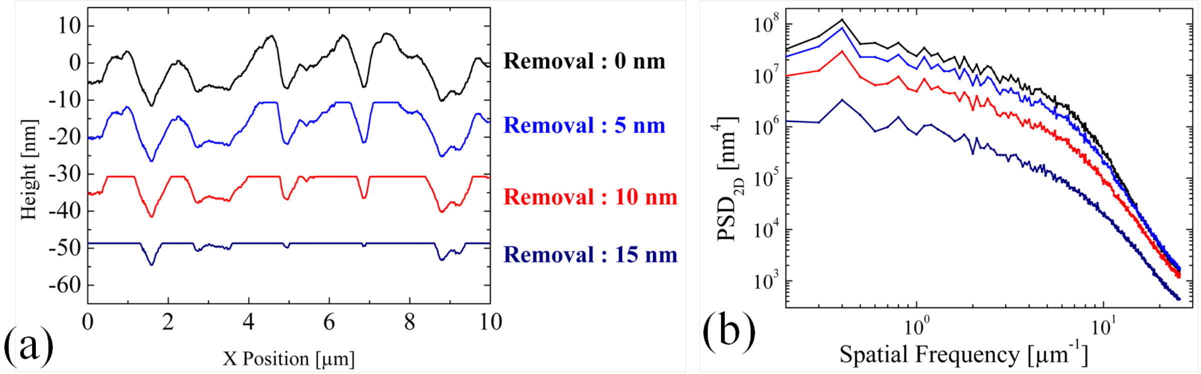

Fig. 5.9: Numerical simulation reproducing material removal as a horizontal take off of the surface. (a) Profile evolution for increasing amount of material removal (note that profiles are shifted following the height axis to ease the observation) and (b) PSD_{2D} corresponding to the presented profiles. The values of material removal correspond to the height removed from the top of the profiles.

Assuming that the phenomena dominating roughness evolution of «very rough» and «very rough-like» surface are identical, we have tried to numerically reproduce this material removal. We suppose that, at first stage of the *CMP* process, the material removal can be described by some horizontal «lift-off». First, we identify the highest value of the surface which is set as the reference (zero removal). Then, for a target amount of removed material (R_M), we can set the maximum height value of the surface by subtracting R_M from the reference (see Fig. 5.9 (a)).

We have simulated the roughness evolution following this approach. Figure 5.9 (a) shows the evolution of typical surface profiles for increasing amount of removed material. The *PSD* functions associated to these surfaces are shown in figure 5.9 (b). The *PSD* amplitudes decrease as the amount of removed material increase. The *PSD* functions obtained by this simulation are almost parallel to the initial *PSD* function. Thus, the simulation of the evolution of these *PSD* functions are in agreement with the experimental *PSD* functions we have obtained for removals smaller than $20\,nm$ on rough surfaces. Thus, in the case of rough surfaces and for small amounts of removed material (short times), the *CMP* process can be seen as some horizontal «lift-off» of the surface.

5.3.2.3 Starting material: Annealed post-splitting surfaces

Hereafter, we study the roughness evolution during *CMP* of wafers with «rough» and damaged surfaces. Figure 5.10 shows $30 \times 30\,\mu m^2$ AFM images obtained before and after

CMP for different amounts of removed material. Again, smaller AFM images ($1\times1\,\mu m^2$) have also been recorded.

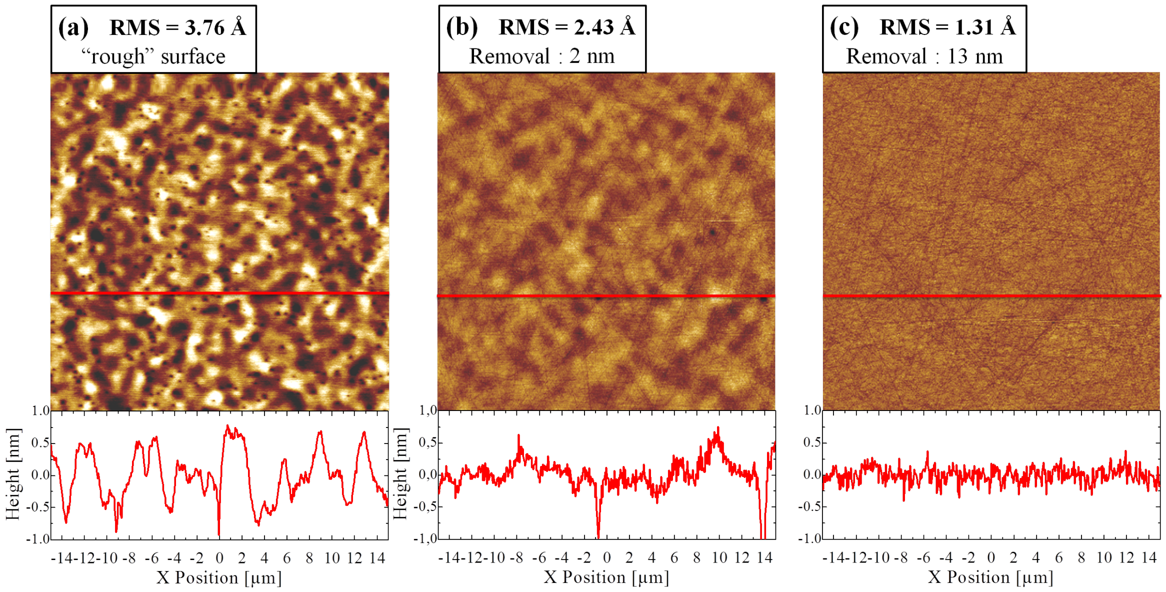

Fig. 5.10: Typical AFM Images ($30\times30\,\mu m^2$; 512×512 pixels) of annealed post-splitting SOI wafers («rough» surface) before (a) and after *CMP* process using slurry 1. Images shown correspond to the minimal ($2\,nm$) (b) and the maximal ($13\,nm$) material removal.

Figure 5.10 (a) shows the surface morphology before polishing. Figures 5.5 (b-c) show the surfaces after polishing using the slurry 1, after $2\,nm$ and $13\,nm$ removals respectively. As expected, we observe that the height variations are reduced during *CMP* process. Peaks on the surface are firstly reduced while holes remains. Note that the height scale is identical for the three shown images, contrary to AFM images shown in the case of «very rough-like» surfaces (shown in Fig. 5.8). This evidences that the roughness reduction is much slower in the case of the «rough» surfaces.

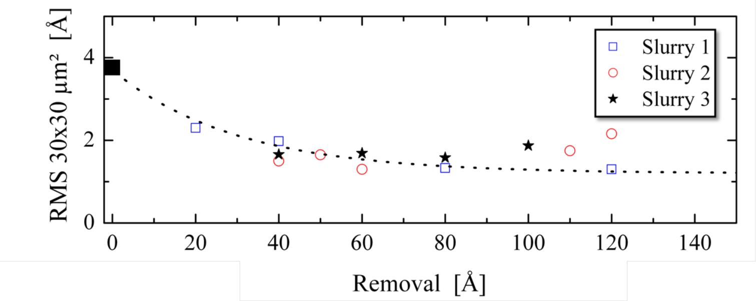

Fig. 5.11: Evolution of the *RMS* value with the material removal amount during *CMP* process. The values are calculated from AFM images recorded from annealed post-splitting SOI wafers («rough» surface) after polishing.

Figure 5.11 shows the evolution of the *RMS* values. They all rapidly decrease on the beginning, whatever the slurry during *CMP* (for material removal smaller than $4\,nm$). Later on, for slurry 1, the *RMS* value slowly decreases. For the slurry 2 and 3, the *RMS* value decreases for removals smaller than $8\,nm$ then increases for larger removals.

Figure 5.12 shows the PSD_{2D} functions extracted from the $30 \times 30\,\mu m^2$ AFM images of surfaces polished using slurry 1 and 2.

For slurry 1 (see Fig. 5.12 (a)) and for spatial frequencies lower than $1\,\mu m^{-1}$, the amplitude of the PSD_{2D} function continuously decreases during *CMP*.

For spatial frequencies higher than $1\,\mu m^{-1}$, the behavior of the PSD_{2D} function depends on the amount of removed material. Indeed, at the beginning, the PSD_{2D} amplitude increases and follows a power-law of the spatial frequency with an exponent approximately equal to -2.2. Later on, for $6\,nm$ and $8\,nm$ removals, a «bump» develops at spatial frequencies around $7\,\mu m^{-1}$ (see inset in Fig. 5.12 (a)). Finally, after $10\,nm$ removal, the PSD_{2D} function recovers the power-law characteristics and the amplitude of the PSD_{2D} function is comparable to that observed before the *CMP* process.

Thus, for the *CMP* process using slurry 1 and for amounts of removed material between $6\,nm$ and $8\,nm$, nano-scratches are created on the polished surface, corresponding to the increasing «bump». For larger removals, nano-scratches are etched away and thus the PSD_{2D} function recovers its spectral foot-print (power-law with -2.3 exponent).

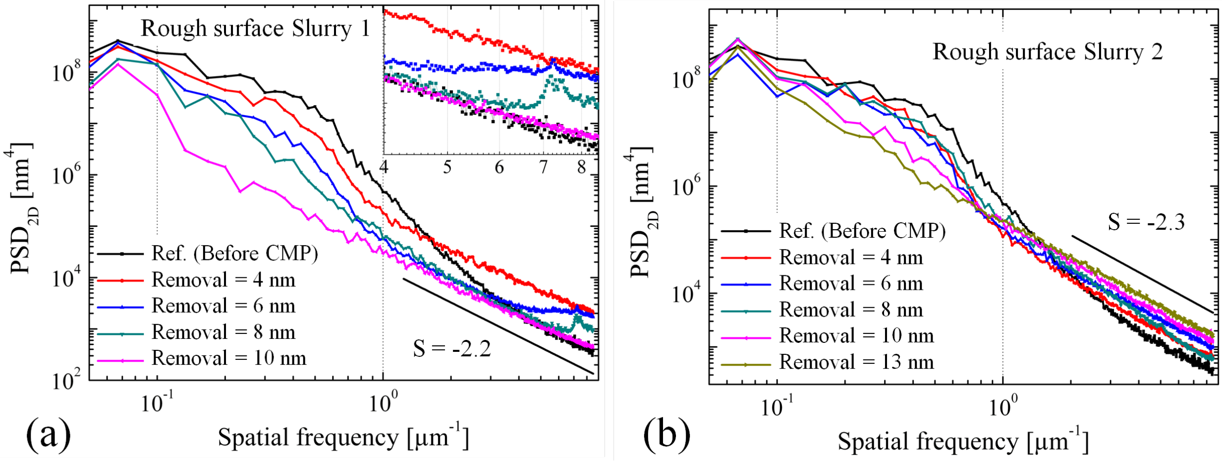

Fig. 5.12: PSD_{2D} functions describing the topography evolution of the surface during *CMP* process performed on annealed post-splitting SOI wafers («rough» surface) using (a) slurry 1 and (b) slurry 2.

For slurry 2, the evolution of the PSD_{2D} function during *CMP* is different (see Fig. 5.12 (b)). Indeed, for spatial frequencies lower than $1\,\mu m^{-1}$, the amplitude decreases much slower than for slurry 1. Moreover, for spatial frequencies higher than $1\,\mu m^{-1}$, the amplitude continuously increases with the amount of removed material, in agreement with the evolution of the *RMS* values. This evidences that the *CMP* process using slurry 2 increases the roughness at high spatial frequencies (higher than $1\,\mu m^{-1}$). Additionally, we observe that the PSD_{2D} function follows a power-law of the spatial frequency with an exponent equal to -2.3 ± 0.1.

It is remarkable that the observed scaling behavior is very similar for both slurries (exponent equal to -2.3 ± 0.1). Hence, we suggest that the mechanisms driving the roughness evolution at high spatial frequencies are similar for both slurries and impose the slope of the PSD_{2D} function at these frequencies.

Whatever the slurry, the contribution of spatial frequencies between $0.1\,\mu m^{-1}$ and $1\,\mu m^{-1}$ on the total roughness variations, is small. However, for spatial frequencies higher than $1\,\mu m^{-1}$ the roughness evolution depends on the slurry. Indeed, for slurry 1 the contribution of these spatial frequencies increases at the beginning of the polishing process. Then, it decreases and reaches an amplitude comparable to that obtained by thermal annealing (surface before *CMP* process). On the contrary, for slurry 2, the contribution of high spatial frequencies continuously increases, evidencing that the polishing process makes the surface rougher at high spatial frequencies. Finally, we conclude that, in the case of «rough» surfaces, the use of slurry 1 permits to reach better results.

Finally, figure 5.13 shows the PSD_{1D} function before and after the *CMP* process for post-splitting wafers without implantation induced defects («very rough-like» surface). In order to evidence the spectral foot-print of the *CMP* process, we plot the PSD_{1D} corresponding to the thickness variations of the top *Si* layer of the SOI wafer (frequencies lower than $2\times10^{-2}\,\mu m^{-1}$) together with that corresponding to the roughness variations. We observe that the *CMP* process degrades the thickness uniformity (for spatial frequencies lower than $6\times10^{-3}\,\mu m^{-1}$) while it improves the roughness (for spatial frequencies higher than $5\times10^{-2}\,\mu m^{-1}$).

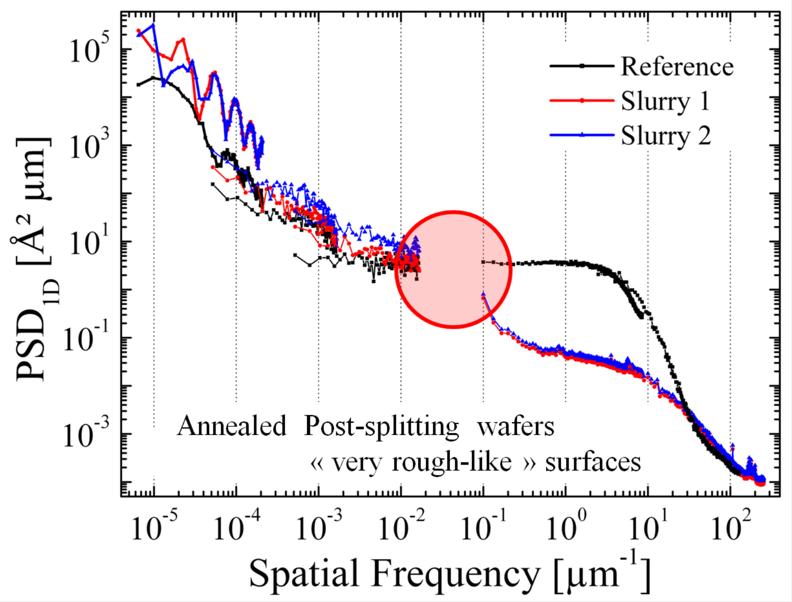

Fig. 5.13: PSD_{1D} functions describing the thickness variation and topography evolution of the surface before and after *CMP* process performed on («very rough-like» surface) using slurry 1.

Conclusions

In this chapter we have experimentally investigated the impact of the *CMP* process on both the thickness uniformity and surface roughness of the top *Si* layer of SOI wafers. We have evidenced that the spectral approach used to investigate the impact of slurry on the final surface roughness can be performed in order to improve the *CMP* process involved in the manufacturing of SOI wafers. We have also shown that the first stage of the material removal can be described as a horizontal «lift-off» of the surface. Besides, the material removal rate is observed to be larger for surfaces including implantation induced defects. Moreover, the spectral foot-print of the process has been obtained. Indeed, it has been evidenced that the *CMP* process leads to an improvement of the roughness of the *Si* surface for high spatial frequencies (device/transistor scale), but a degradation of the thickness uniformity for low spatial frequencies (wafer scale).

Bibliography

[1] J. Luo and D. A. Dornfeld, "Material removal mechanism in chemical mechanical polishing: theory and modeling," *Semiconductor Manufacturing, IEEE Transactions on*, vol. 14, no. 2, pp. 112–133, 2001. (cited in pages 123, 124 and 125)

[2] J. M. Steigerwald, S. P. Murarka, and R. J. Gutmann, *Chemical Mechanical Planarization of Microelectronic Materials*. WILEY-VCH, 2004. (cited in page 124)

[3] D. Dornfeld and D.-E. Lee, *Machine design for precision manufacturing*. Springer, 2008. (cited in page 124)

[4] F. Preston, "The theory and design of plate glass polishing machines," *J. Soc. Glass Tech.*, vol. 11, p. 214, 1927. (cited in page 124)

[5] F. Zhang, A. A. Busnaina, and G. Ahmadi, "Particle adhesion and removal in chemical mechanical polishing and post-CMP cleaning," *Journal of the Electrochemical Society*, vol. 146, no. 7, pp. 2665–2669, 1999. (cited in page 125)

[6] B. Zhao and F. G. Shi, "Chemical mechanical polishing in IC processes: new fundamental insights," in *Proc. Fourth Int. Chemical-Mechanical Planarization for ULSI Multilevel Interconnection Conf., Santa Clara, CA.*, pp. 13–22, 1999. (cited in page 125)

[7] C. W. Liu, T. Dai, W. T. Tseng, and C. F. Yeh, "Modeling of the wear mechanism during chemical-mechanical polishing," *Journal of the Electrochemical Society*, vol. 143, pp. 716–721, 1999. (cited in page 125)

[8] L. M. Cook, "Chemical processes in glass polishing," *Journal of Non-Crystalline Solids*, vol. 120, no. 1–3, pp. 152 – 171, 1990. (cited in page 125)

[9] F. Kaufman, D. Thompson, R. Broadie, M. Jaso, W. Guthrie, D. Pearson, and M. Small, "Chemical-mechanical polishing for fabricating patterned W metal features as chip interconnects," *Journal of the Electrochemical Society*, vol. 138, no. 11, pp. 3460–3465, 1991. (cited in page 125)

[10] H. Liang, F. Kaufman, R. Sevilla, and S. Anjur, "Wear phenomena in chemical mechanical polishing," *Wear*, vol. 211, no. 2, pp. 271–279, 1997. (cited in page 125)

[11] A. Tesar, B. Fuchs, and P. P. Hed, "Examination of the polished surface character of fused silica," *Applied optics*, vol. 31, no. 34, pp. 7164–7172, 1992. (cited in page 126)

[12] V. H. Nguyen, A. Hof, H. Van Kranenburg, P. Woerlee, and F. Weimar, "Copper chemical mechanical polishing using a slurry-free technique," *Microelectronic Engineering*, vol. 55, no. 1, pp. 305–312, 2001. (cited in page 126)

[13] S. B. Yeruva, *Particle scale modeling of material removal and surface roughness in Chemical Mechanical Ploshing*. PhD thesis, University of Florida, 2005. (cited in page 126)

[14] B. Stine, D. Ouma, R. Divecha, D. Boning, J. Chung, D. Hetherington, C. Harwoo, O. Nakagawa, and S.-Y. Oh, "Rapid characterization and modeling of pattern-dependent variation in chemical-mechanical polishing," *Semiconductor Manufacturing, IEEE Transactions on*, vol. 11, pp. 129–140, Feb 1998. (cited in page 126)

[15] T. Tugbawa, T. Park, D. Boning, T. Pan, P. Li, S. Hymes, T. Brown, and L. Camilletti, "A mathematical model of pattern dependencies in Cu CMP processes," in *CMP Symposium, Electrochemical Society Meeting*, pp. 605–615, 1999. (cited in page 126)

[16] T. E., Y. C., and C. H. C., "A mechanical model for DRAM dielectric chemical-mechanical polishing processes," *CMP-MIC Conference*, vol. 13-14 Feb., pp. 258–265, 1997. (cited in page 126)

[17] C. Ouyang, K. Ryu, L. Milor, W. Maly, G. Hill, and Y.-K. Peng, "An analytical model of multiple ILD thickness variation induced by interaction of layout pattern and CMP process," *Semiconductor Manufacturing, IEEE Transactions on*, vol. 13, no. 3, pp. 286–292, 2000. (cited in page 126)

[18] O. Chekina, L. Keer, and H. Liang, "Wear-contact problems and modeling of chemical mechanical polishing," *Journal of the Electrochemical Society*, vol. 145, no. 6, pp. 2100–2106, 1998. (cited in page 126)

[19] D. Wang, J. Lee, K. Holland, T. Bibby, S. Beaudoin, and T. Cale, "Von mises stress in chemical-mechanical polishing processes," *Journal of the Electrochemical Society*, vol. 144, no. 3, pp. 1121–1127, 1997. (cited in page 126)

[20] W.-T. Tseng, Y.-H. Wang, and J.-H. Chin, "Effects of film stress on the chemical mechanical polishing process," *Journal of the Electrochemical Society*, vol. 146, no. 11, pp. 4273–4280, 1999. (cited in page 126)

[21] G. Fu and A. Chandra, "A model for wafer scale variation of material removal rate in chemical mechanical polishing based on viscoelastic pad deformation," *Journal of electronic materials*, vol. 31, no. 10, pp. 1066–1073, 2002. (cited in page 126)

[22] J. Seok, C. P. Sukam, A. T. Kim, J. A. Tichy, and T. S. Cale, "Multiscale material removal modeling of chemical mechanical polishing," *Wear*, vol. 254, no. 3–4, pp. 307 – 320, 2003. (cited in page 126)

[23] J. Luo, *Integrated Modeling Of Chemical Mechanical Planarization/Polishing (CMP) for Integrated Circuit Fabrication: From Particle to Die and Wafer Scales*. PhD thesis, University of California, Berkeley, 2003. (cited in page 126)

[24] X. Xie and D. Boning, "Cmp at the wafer edge–modeling the interaction between wafer edge geometry and polish performance," in *MRS Proceedings*, vol. 867, pp. W5–1, Cambridge Univ Press, 2005. (cited in page 129)

General Conclusions

The control of the thickness uniformity of thin layers and its characterization over different spatial scales, are nowadays very important challenges from a fundamental and industrial point of view. That is why, the main objective of this thesis work was to develop a multi-scale approach to characterize the thickness and the topographical variations of thin silicon layers, and especially to explore their origins.

To address these issues, we have first developed original metrology methods based on the use of the Power Spectral Density (*PSD*) function allowing to compare signals recorded by means of different characterization techniques. This permits investigating thickness and topographical variations of thin silicon layers over a very large spatial bandwidth (from $10\,nm$ up to $300\,mm$). Then, we have studied the relationship between the thickness variations and the roughness of interfaces delimiting the top silicon layer of SOI wafers. It has been shown that depending on the spatial frequency, thickness variations can be deduced from the quantification of the topographical variations of the top surface. Moreover, we have determined the specifics spatial bandwidths over which this approach can be applied.

Since the Smart Cut™ process is particularly related to the splitting, we have reviewed physical phenomena involved in the thermal evolution of defects introduced by ion implantation leading to the splitting. We have also experimentally investigated the impact of implantation conditions on the roughness of the post-splitting surfaces.

Afterwards, we have established the spectral foot-prints of the principal technological steps involved in the Smart Cut™ technology, influencing the thickness uniformity of the final top silicon layer of SOI wafers.

Firstly, we have investigated the evolution of the roughness of silicon wafers during thermal annealing. We have shown that smoothening of silicon surfaces by thermal activated self-diffusion of adatoms can drastically attenuate the contribution of high spatial frequencies to the total roughness. The atomic-scale mechanisms driving this smoothening have been investigated in detail. Two additional mechanisms influencing the roughness evolution during thermal annealing process have been evidenced, the thermal fluctuations of the surface and the oxidation-evaporation phenomenon. Based on our results, a simulation code allowing to reproduce the thermal evolution of silicon surfaces during annealing was developed. This simulation tool permits to significantly reduce the development time and cost of the improvement of the annealing process. We have demonstrated that rapid thermal annealing is a very suitable process to reduce the variability of the physical characteristics within transistors processed on SOI wafer without affecting the matching of these characteristics over the wafer scale.

Then, we have investigated the impact of the thermal oxidation of silicon on the thickness uniformity and the surface roughness of the top silicon layer. It has been demonstrated that the roughness evolution of the surface of the oxide layer only takes place during early stage of the oxidation process, while the oxide thickness is lower than $10\,nm$. The scaling behavior of the oxidation process is observed to be similar whatever the initial surface morphology. Additionally, we have pointed out that spectral foot-print of the silicon oxidation on the roughness evolution, is similar for both oxidation conditions (dry or wet), evidencing that physical mechanisms involved in dry and wet oxidations must be identical.

Moreover, since the scaling behavior of the oxidation process, is observed to be consistent with the *Edwards-Wilkinson* equation, further investigations should permit setting up a predictive model of the surface evolution during thermal oxidation.

Finally, the impact of the chemical-mechanical polishing (*CMP*) on both thickness uniformity and surface roughness of the top silicon layer of SOI wafer, have been experimentally investigated. It has been evidenced that implantation induced defects slightly increases the material removal during *CMP* process. Moreover, we have established the spectral foot-print of the process, showing that the surface roughness is strongly improved for spatial frequencies higher than $5\times10^{-2}\,\mu m^{-1}$. However, a degradation of the thickness uniformity takes place at low spatial frequencies (between $7{\times}10^{-6}\,\mu m^{-1}$ up to $1{\times}10^{-2}\,\mu m^{-1}$). This suggest the *CMP* process is effective to improve the transistor variability, but can deteriorate the matching of transistor characteristics over the SOI wafer.

In a general way, a *CMP* process results from very complex combination of numerous experimental parameters. Further investigations on the impact of these parameters should be possible by using the analysis methods developed in this work.

Now, we have in hands the required metrological machinery to investigate thickness and roughness variations of thin silicon layers over a very large spectral bandwidth [approximately from $3{\times}10^{-6}\,\mu m^{-1}$ to $1{\times}10^{2}\,\mu m^{-1}$] as needed by the semiconductor industry. The metrology techniques and analysis methods developed during this thesis can be applied to the study of any other process impacting the thickness uniformity or the surface roughness of thin layers and this whatever the material and the targeted application.